Einfluss von kurzzeitigem Energiemangel auf die Physiologie neokortikaler Astrozyten

Inaugural-Dissertation

zur Erlangung des Doktorgrades
der Mathematisch-Naturwissenschaftlichen Fakultät
der Heinrich-Heine-Universität Düsseldorf

vorgelegt von
Sara Eitelmann
aus Frankenthal

Düsseldorf, Januar 2023

aus dem Institut für Neurobiologie
der Heinrich-Heine-Universität Düsseldorf

Gedruckt mit der Genehmigung der
Mathematisch-Naturwissenschaftlichen Fakultät der
Heinrich-Heine-Universität Düsseldorf

Berichterstatter:

1. Prof. Dr. Christine Rosemarie Rose

2. Prof. Dr. Patrick Küry

Tag der mündlichen Prüfung: 28.04.2023

Zusammenfassung

Das Hauptmerkmal von Astrozyten ist die Bildung großer, funktioneller Synzytien über Gap Junctions. Diese enge Kopplung ermöglicht unter anderem die Aufrechterhaltung der extrazellulären K^+-Homöostase durch interastrozytäre Umverteilung von K^+. Unter pathophysiologischen Bedingungen kann es jedoch zu einer Störung der K^+-Homöostase kommen, welche mit einer gesteigerten neuronalen Erregbarkeit einhergeht. Dies wird beispielsweise bei ischämischen Schlaganfällen in der sogenannten Penumbra beobachtet. In dieser Region übersteigt der Energiebedarf des Gewebes die verfügbare Energie, sodass die betroffenen Zellen unter hohem metabolischem Stress stehen. Zusätzlich sind die Zellen sich radial ausbreitenden Infarktwellen ausgesetzt, die von einer vorübergehenden Störung der zellulären Ionen-Homöostase begleitet werden. Jede weitere Welle stellt hierbei ein größeres Risiko für irreversiblen Schäden dar. Somit ist es essenziell herauszufinden, welche Parameter die gesunden Zellen vor den schädlichen Faktoren schützen. Inwiefern die intrazelluläre K^+-Konzentration und die Gap Junction-Kopplung der Astrozyten hierbei eine Rolle spielen könnten, ist der Hauptfokus der vorliegenden Arbeit.

Daher wurden zunächst die Auswirkungen eines kurzzeitigen Energiemangels auf die intrazelluläre K^+-Konzentration von Astrozyten untersucht. Mittels eines empirisch-theoretischen Ansatzes wurde berechnet, dass es während des kurzzeitigen Energiemangels von einer intrazellulären K^+-Konzentration unter Ruhebedingungen von 146 mM zu einem K^+-Verlust von rund 43 mM kommt. Zusätzlich wurde nach Reperfusion ein Nettogewinn an K^+ der Astrozyten festgestellt. Dies könnte durch die Verringerung der extrazellulären K^+-Konzentration die Erregbarkeit der Neuronen absenken. Anschließend wurde mithilfe von Ableitungen der Isopotenzialität die Gap Junction-Kopplung erstmals unter pathophysiologischen Bedingungen dynamisch untersucht. Dabei zeigten die Messungen eine schnelle Reduktion der Kopplungsstärke. Darüber hinaus ist diese unempfindlich gegenüber Ischämie-induzierten pH-Änderungen, aber abhängig vom Ca^{2+}-Einstrom.

Zusammengefasst zeigen Astrozyten während einer kurzzeitigen metabolischen Inhibition zum einen eine verzögerte, erhöhte K^+-Aufnahme, welche durch Senkung der neuronalen Erregbarkeit den ATP-Verbrauch der Neuronen reduzieren könnte und somit die Erholung begünstigen könnte. Zum anderen deuten die Daten darauf hin, dass eine Ca^{2+}-abhängige Entkopplung von Astrozyten, benachbarte Astrozyten vor zusätzlichen, durch Gap Junction-vermittelten Ca^{2+}-Anstiegen schützen könnte. Somit zeigt die vorliegende Arbeit, dass Astrozyten maßgeblich dazu beitragen können, Zellschäden in der ischämischen Penumbra zu begrenzen und zu reduzieren.

Inhaltsverzeichnis

1 Physiologie der Astrozyten 1

1.1 Morphologie . . . 2

1.2 Dreiteilige Synapse . . . 2

1.2.1 Glutamat-Homöostase . . . 3

1.2.2 K^+-Homöostase . . . 4

1.3 Neurovaskuläre und neurometabolische Kopplung . . . 6

1.4 Gap Junction-Kopplung . . . 8

1.4.1 Aufbau von Gap Junction-Kanälen . . . 10

1.4.2 Astrozyten-Netzwerke . . . 11

1.4.3 Modulation von Gap Junction-Kanälen . . . 15

1.5 Elektrophysiologische Eigenschaften . . . 17

1.6 Vom Leim zum essenziellen Kommunikationspartner . . . 19

2 Pathophysiologie des ischämischen Schlaganfalls 20

2.1 Die ischämische Penumbra . . . 20

2.2 Zelluläre Folgen von Infarktwellen . . . 21

3 Astrozyten während kurzzeitigem Energiemangel 23

3.1 Störung der astrozytären K^+-Homöostase . . . 24

3.1.1 Simulation von $[K^+]_i$ . . . 24

3.1.2 Anionen-Lücke . . . 27

3.2 Schnelle Veränderung der astrozytären Kopplung . . . 28

3.2.1 Isopotenzialität von neokortikalen Astrozyten . . . 29

3.2.2 Schnelle Reduktion der Kopplungsstärke . . . 30

3.2.3 Ca^{2+}-abhängige Verringerung der Kopplung . . . 32

3.3 Rolle von Astrozyten bei der Ausbreitung von ischämischen Schäden . . . 34

4 Literaturverzeichnis 36

Anhang

I Publikationen und Manuskripte 48

I.I Eitelmann et al., eingereicht bei Front Cell Neurosci. . . . 49

I.II Eitelmann et al., 2022. Int J Mol Sci. . . . 76

I.III Stephan et al., 2021. Front Cell Neurosci. . . . 95

I.IV Eitelmann et al., 2020. Int J Mol Sci. . . . 111

1 Physiologie der Astrozyten

Bei Vertebraten stellt das Gehirn den zentralen Integrationsort komplexer Informationen dar. Um diese vielschichtige Aufgabe zu bewältigen, verfügt das Gehirn über eine Vielzahl an spezialisierten Zellen (Abbildung 1). Schätzungsweise 86 Milliarden der 170 Milliarden Zellen im adulten Gehirn sind **Neurone** (Azevedo et al., 2009). Dies sind elektrisch erregbare Zellen, die Signale in Form von Aktionspotenzialen empfangen und weiterleiten können. Den Neuronen steht fast die gleiche Anzahl an **Gliazellen** gegenüber, welchen in der Vergangenheit ausschließlich die Rolle des stillen Beobachters zugeschrieben wurde. Das Konzept der „Glia“ (griechisch für „Leim“) wurde Mitte des 19. Jahrhunderts vom deutschen Mediziner Rudolph Virchow aufgestellt (Virchow, 1856). In der schriftlichen Sammlung seiner Vorlesungen aus dem Jahr 1856 beschrieb Virchow Gliazellen als „Bindegewebe, das im Gehirn […] eine Art Nervenkitt bildet, in den die Elemente des Nervensystems eingebettet sind“. Diese anfängliche Sichtweise hat sich allerdings von Gliazellen als einer reinen Zwischenmasse zu einer heterogenen Population von Zellen weiterentwickelt.

Heute ist bekannt, dass die Untergruppen von Gliazellen einzigartige, spezialisierte Funktionen übernehmen. So sind beispielsweise **Oligodendrozyten** für die Myelinisierung von Axonen und **Mikroglia** für die Immunabwehr des Gehirns verantwortlich (Bunge, 1968; Baumann and Pham-Dinh, 2001; Dheen et al., 2002; Farber and Kettenmann, 2005). Die vorliegende Arbeit fokussiert sich auf die Physiologie einer weiteren Untergruppe: den **Astrozyten**.

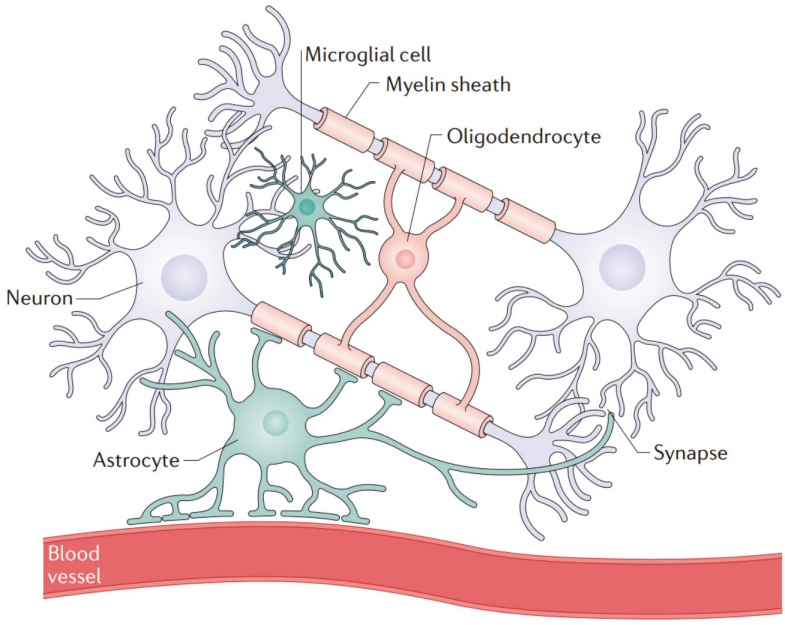

Abbildung 1. Schematische Darstellung verschiedener Zelltypen im Gehirn. Astrozyten (grün, unten) stehen auf einer Seite mit Blutgefäßen (rot) und auf der anderen Seite mit Neuronen (lila) in engem Kontakt. Für die Myelinisierung der Axone wird durch Oligodendrozyten (orange) verantwortlich. Die Mikroglia (grün, oben) sind in Nähe der Neurone lokalisiert. Modifiziert mit Genehmigung aus Hanani and Spray, 2020.

1.1 Morphologie

Astrozyten machen rund 10–12 % der gesamten Zellen im zentralen Nervensystem aus (Sun et al., 2017). Die Bezeichnung „Astrozyt“ erhielten sie aufgrund ihrer sternförmigen Erscheinung von dem ungarischen Anatomen Mihály von Lenhossék (von Lenhossék, 1895). Mit der Weiterentwicklung histologischer Techniken wurde jedoch deutlich, dass Astrozyten eine wesentlich heterogenere Morphologie aufweisen (Andriezen, 1893; Koelliker, 1899; Ramón y Cajal, 1913; Río-Hortega, 1920). So ergaben sich verschiedene neuroanatomische Untergruppen entsprechend ihrer Lage, darunter die **fibrösen** und die **protoplasmatischen** Astrozyten. Fibröse Astrozyten liegen in der weißen Substanz vor und zeichnen sich durch eine Vielzahl an langen Ausläufern aus, wobei ihre Endigungen als perivaskuläre oder subpiale Endfüße spezialisiert sind (Lundgaard et al., 2014).

In der grauen Substanz hingegen befinden sich die protoplasmatischen Astrozyten. Diese zeichnen sich durch ihre eher schwammförmige Morphologie aus (Bushong et al., 2002b; Ogata and Kosaka, 2002). Diese entsteht durch die Ausbildung von bis zu zehn primären Ausläufern, die sich weiter in sekundäre und tertiäre Ausläufer verzweigen. Die Ausläufer machen dabei etwa 95 % des Gesamtvolumens aus. Zusätzlich überlappen die Ausläufer benachbarter protoplasmatischer Astrozyten nur minimal, was zu einer Gliederung einzelner Astrozyten in separaten Bereichen führt (Abbildung 1; Bushong et al., 2002b).

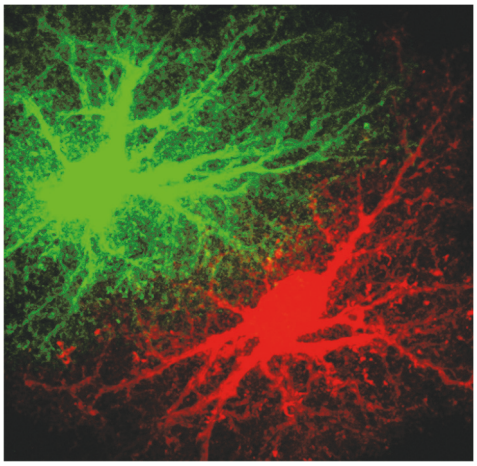

Abbildung 2. Morphologie protoplasmatischer Astrozyten. Aufnahme eines konfokalen Mikroskops benachbarter, gefüllter Astrozyten (grün: Luzifer gelb; rot: Alexa 568). Protoplasmatische Astrozyten weisen eine charakteristische schwammartige Morphologie auf und sind in nicht-überlappende Bereiche organisiert. Modifiziert mit Genehmigung aus Bushong et al., 2002a.

1.2 Dreiteilige Synapse

Während sich protoplasmatische Astrozyten also in abgegrenzten Bereichen organisieren, umgeben ihre feinen Ausläufer die Strukturen anderer Zellen. So reichen die astrozytären Ausläufer auch in die unmittelbare Umgebung von Neuronen, wobei ein einzelner Astrozyt

im Maushirn über 140.000 Synapsen umhüllen kann (Bushong et al., 2002b; Oberheim et al., 2009). Der Abstand zwischen Synapsen und astrozytären Ausläufern beträgt hierbei nur wenige hundert Nanometer (Medvedev et al., 2014). Studien aus dem späten 20. Jahrhundert lieferten erste Hinweise auf einen Informationsaustausch zwischen diesen Zelltypen (Kettenmann et al., 1984; Cornell-Bell et al., 1990). Dies führte schlussendlich zur Entwicklung des Konzepts der **dreiteiligen Synapse**, bestehend aus prä- sowie postsynaptischem Neuron und perisynaptischem Astrozyten (Abbildung 3; Araque et al., 1999).

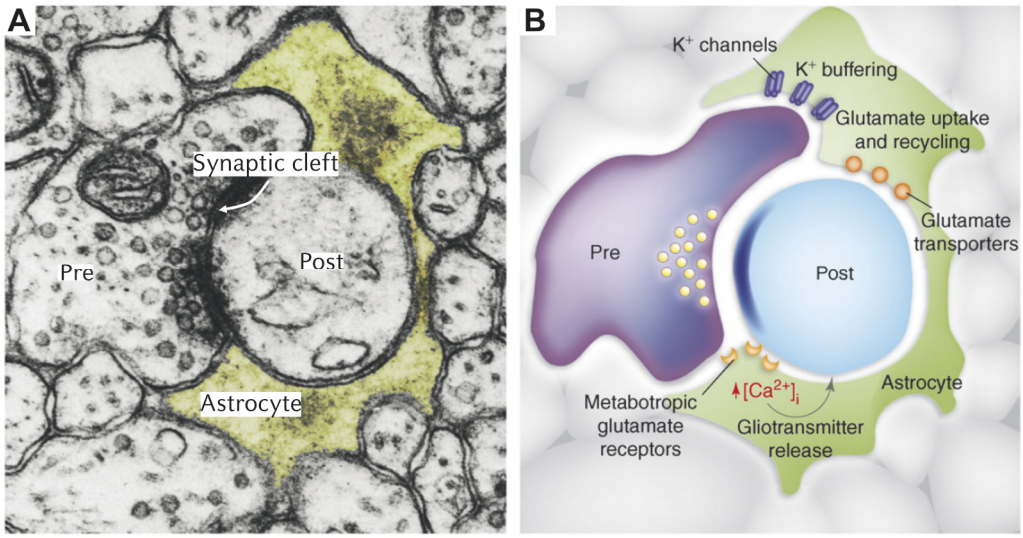

Abbildung 3. Dreiteilige Synapse. A) Elektronenmikroskopische Aufnahme eines prä- und eines postsynaptischen Neurons, welche von einem Astrozyten (gelb) umhüllt werden. **B)** Innerhalb der dreiteiligen Synapse nehmen Astrozyten wichtige Funktionen ein, unter anderem die Aufnahme von überschüssigem Glutamat und K^+. Modifiziert mit Genehmigung aus Halassa et al., 2007.

1.2.1 Glutamat-Homöostase

Dieser enge Kontakt ermöglicht es Astrozyten unter anderem, die **Neurotransmitter-Homöostase** im Extrazellularraum zu regulieren (Parpura and Verkhratsky, 2012; Murphy-Royal et al., 2017). Dabei ist der wichtigste exzitatorische Neurotransmitter im zentralen Nervensystem die Aminosäure **Glutamat**. Dieser aktiviert beispielsweise ionotrope Glutamat-Rezeptoren wie den N-Methyl-D-Aspartat (NMDA)-Rezeptor, was einen Einstrom von Ca^{2+} in die postsynaptischen Neuronen zur Folge hat. Eine erhöhte Akkumulation resultiert in einem exzessiven Ca^{2+}-Einstrom und in eine andauernde Depolarisation der Neuronen (Curtis et al., 1959). Dies kann schlussendlich durch Aktivierung von Proteasen, Endonukleasen und Lipasen zur Apoptose des Neurons führen (Berdichevsky et al., 1983; Ricci et al., 2009). Der neurotoxische Effekt infolge dieser

Glutamat-vermittelten Prozesse wird auch **Exzitotoxizität** genannt (Kristián and Siesjö, 1998; Choi, 2020).

Die astrozytäre Aufnahme von Glutamat erfolgt durch die Expression verschiedener Transporter an ihren peripheren Ausläufern. Dazu gehören beispielsweise der Glutamat-Transporter 1 und der Glutamat/Aspartat Transporter 1 (Perego et al., 2000; Murphy-Royal et al., 2015). Darüber hinaus können Astrozyten die Verfügbarkeit dieser Transporter je nach neuronaler Aktivität steuern (Pannasch et al., 2014). Dies geschieht über die variable Abdeckung von Synapsen durch astrozytäre Ausläufer (Xu-Friedman et al., 2001; Genoud et al., 2006; Bernardinelli et al., 2014b). Studien aus dem Hippokampus zeigten, dass dieses An- und Abziehen im Minutenbereich erfolgen kann (Haber and Murai, 2006; Bernardinelli et al., 2014a). Astrozyten können somit durch die astrozytäre Glutamat-Aufnahme die synaptische Transmission modulieren und ein „Überschwappen" an benachbarte Synapsen verhindern (Tzingounis and Wadiche, 2007).

1.2.2 K^+-Homöostase

Eine weitere wichtige Funktion der Astrozyten innerhalb der dreiteiligen Synapse ist die Aufrechterhaltung der **extrazellulären K^+-Homöostase** (Verkhratsky and Nedergaard, 2018). Unter Ruhebedingungen liegt die extrazelluläre K^+-Konzentration ($[K^+]_e$) bei 3 mM, welche bei der Generierung eines Aktionspotenzials transient um maximal 1 mM erhöht wird (Bradbury and Kleeman, 1967; Adelman and Fitzhugh, 1975; Katzman, 1976; Somjen, 1979). Letzteres geschieht infolge der K^+-Ausschüttung während der Repolarisation. Bei einem epileptischen Anfall kann die $[K^+]_e$ sogar bis zu einem Höchstwert von 12 mM ansteigen (Bradbury and Kleeman, 1967; Katzman, 1976; Heinemann and Lux, 1977; Somjen, 1979). Die Akkumulation von K^+ im Extrazellularraum führt zu einer Depolarisation der neuronalen Membran und zu einer erhöhten Ausschüttung von Neurotransmittern (Gage and Quastel, 1965; Erulkar and Weight, 1977; Malenka et al., 1981). Dies geht einher mit einer gesteigerten Erregbarkeit, wofür beispielsweise bei hippokampalen Neuronen ein Anstieg der $[K^+]_e$ um 5 mM ausreichend ist (Voskuyl and Ter Keurs, 1981; Balestrino et al., 1986; Kreisman and Smith, 1993).

Die Regulation der $[K^+]_e$ ist somit essenziell für die neuronale Funktion. Bereits 1965 postulierte Hertz, dass Astrozyten maßgeblich an der Entfernung von K^+ aus dem Extrazellularraum beteiligt sind und zudem durch die Manipulation der $[K^+]_e$ die neuronale Aktivität steuern (Hertz, 1965). Die treibende Kraft für die K^+-Aufnahme stellt hierbei die elektromotorische Kraft (EMK) dar. Diese ist die Differenz zwischen dem

Membranpotenzial (E_M) und dem K^+-Gleichgewichtspotenzial (E_K) der astrozytären Membran ($EMK_k = E_M - E_K$). So ergibt sich bei einer positiven EMK ein K^+-Ausstrom und bei einer negativen EMK ein K^+-Einstrom (Kandel et al., 2021).

Der K^+-Strom über die Membran hängt von deren **Permeabilität für K^+** (P_K) ab (Ransom and Goldring, 1973; Kimelberg et al., 1979). Diese entsteht hauptsächlich durch die hohe Expression an passiven K^+-Kanälen, wie den einwärts gleichrichtenden K^+ (K_{ir})- und den Zwei-Porendomänen-K^+ (K_{2P})-Kanälen (Abbildung 4; Butt and Kalsi, 2006; Pasler et al., 2007; Seifert et al., 2009; Mathie et al., 2010). Die K^+-Aufnahme wird durch den $Na^+/K^+/2Cl^-$-Cotransporter 1 (NKCC1) und die Na^+/K^+-ATPase (NKA) bewerkstelligt (Abbildung 4; Balestrino and Somjen, 1986; Ransom et al., 2000; D'Ambrosio et al., 2002; Hertz et al., 2015). Letztere nutzt den Abbau von ATP, um 2 K^+ im Austausch von 3 Na^+ in die Zellen zu bringen (Larsen et al., 2019). Unter physiologischen Bedingungen ergibt sich so aus dem Zusammenspiel zwischen aktivem Einwärtstransport und passivem Ausstrom eine intrazelluläre K^+-Konzentration ($[K^+]_i$) zwischen 120 und 150 mM (Kimelberg et al., 1979; Hansen, 1985; Rimmele and Chatton, 2014).

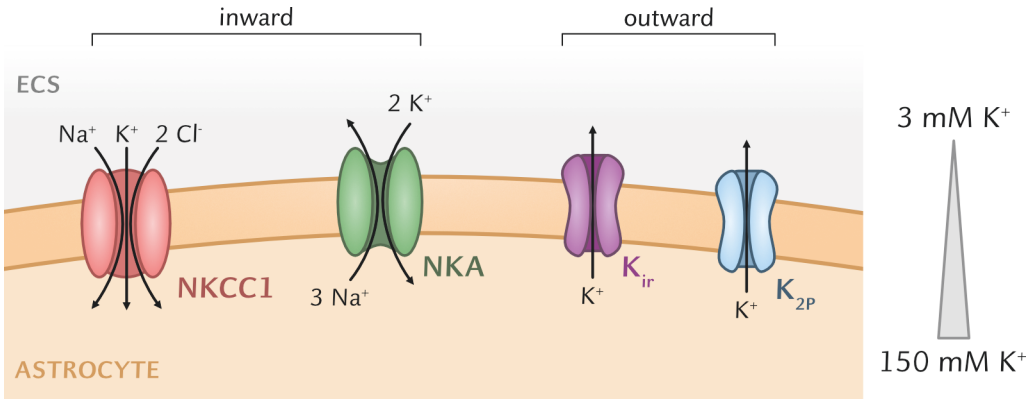

Abbildung 4. K^+-Strom über die Astrozyten-Membran. Der Einwärtstransport von K^+ wird über den $Na^+/K^+/2Cl^-$-Cotransporter 1 (NKCC1) und die Na^+/K^+-ATPase (NKA) bewerkstelligt. Die Aufnahme von K^+ geschieht über den einwärts gleichrichtenden K^+ (K_{ir})- und den Zwei-Porendomänen-K^+ (K_{2P})-Kanal. Durch die Kombination aus aktivem Einwärtstransport und passivem Ausstrom ergibt sich ein elektrochemischer Gradient in Richtung Extrazellularraum (ECS). Unpublizierte Abbildung, Werte für K^+ aus Eitelmann et al., 2022, erstellt von S. Eitelmann.

Somit ist die $[K^+]_i$ rund 40- bis 50-fach höher als die $[K^+]_e$. Diese asymmetrische Verteilung führt schlussendlich zur Ausbildung von E_M. Dieses liegt bei Astrozyten bei rund -85 mV (Zhou et al., 2006; Kafitz et al., 2008; Wang and Bordey, 2008).

E_K hingegen ist das Potenzial, bei dem netto kein K^+-Strom über die Membran fließt. Dieses kann mithilfe der Nernst-Gleichung (Gleichung 1) bestimmt werden.

$$E_K = \frac{RT}{F} \ln \left[\frac{[K^+]_e}{[K^+]_i}\right], \quad (1)$$

wobei R die ideale Gaskonstante, T die absolute Temperatur, $[K^+]_{e/i}$ die Konzentration von K^+ extra- oder intrazellulär und F die Faraday'sche Konstante ist.

Nach Gleichung 1 ergibt sich für neokortikale Astrozyten unter Ruhebedingungen ein E_K von circa -100 mV (nach Eitelmann et al., 2022). Somit ist E_M (~ -85 mV) positiver als E_K (~ -100 mV) und die EMK positiv. Dies bedeutet, dass K^+ unter Ruhebedingungen aus den Astrozyten strömt. Kommt es jedoch zu einer gesteigerten neuronalen Aktivität und folglich zu einer erhöhten $[K^+]_e$, wird E_K positiver als E_M, wodurch eine einwärtsgerichtete Kraft für K^+ entsteht. Diese begünstigt die astrozytäre K^+-Aufnahme über die passiven K^+-Kanäle. Das aufgenommene K^+ wird anschließend interastrozytär umverteilt, worauf in einem späteren Kapitel näher eingegangen wird (Kapitel 1.4). Somit können Astrozyten über ihre charakteristischen Membraneigenschaften Abweichungen in der $[K^+]_e$ und damit einhergehend die neuronale Erregbarkeit regulieren.

1.3 Neurovaskuläre und neurometabolische Kopplung

Die astrozytären Ausläufer umhüllen neben Synapsen auch nahezu alle Blutgefäße (Abbildung 5; Barros and Deitmer, 2010; Foo et al., 2011). Dabei bilden die astrozytären **Endfüße** ein Geflecht um die Endothelzellen der Blutgefäße aus. So ergibt sich zwischen Blutgefäßen und Gehirn die **Blut-Hirn-Schranke**. Diese stellt eine Diffusionsbarriere dar, welche den Austausch von potenziell schädlichen Substanzen wie beispielsweise Neurotransmittern und Xenobiotika aus dem Blut ins Gehirn verhindert (Abbott, 2002). Über ihre Endfüße nehmen Astrozyten Wasser, Ionen und Stoffwechselprodukte aus dem Blut auf und geben umgekehrt zytotoxische Substanzen, überschüssiges Wasser und Ionen ins Blut ab (Nedergaard et al., 2003; Strohschein et al., 2011). Der bidirektionale Wasserfluss über die Membran wird durch die Aquaporin-4-Kanäle in den peripheren Ausläufern vermittelt (Satoh et al., 2007). Diese spielen eine Rolle bei der Regulation des Volumens und der Osmolarität des Extrazellularraums und damit auch die Wasserflüsse über die Blut-Hirn-Schranke.

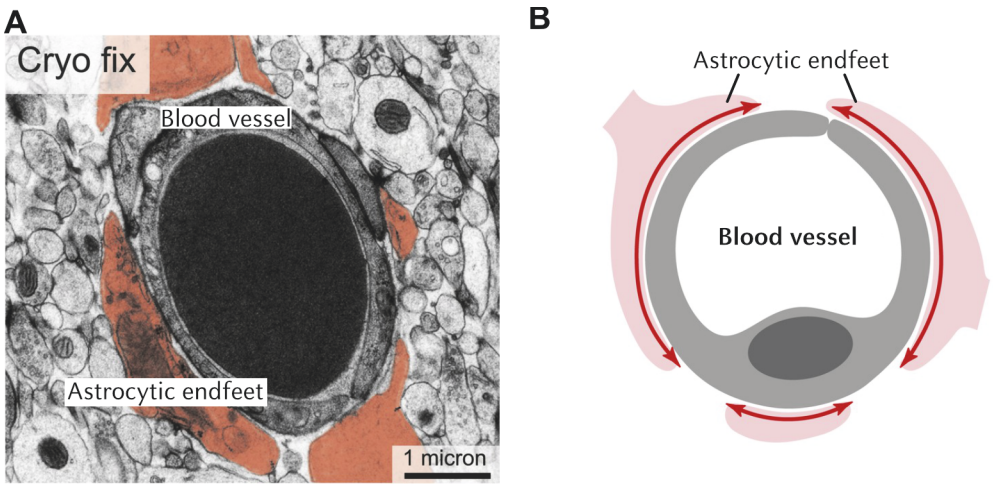

Abbildung 5. Astrozytäre Ausläufer umhüllen Blutgefäße. A) Elektronenmikroskopische Aufnahme einer Blutkapillare, welche von astrozytären Endfüßen (orange) umhüllt wird. **B)** Schema der astrozytären Abdeckung der Endfüße (rot) von Blutgefäßen. Modifiziert mit Genehmigung aus Korogod et al., 2015.

Astrozyten stellen somit eine Zwischenstation zwischen Blutgefäßen und Neuronen dar, wobei die Gesamtheit als **neurovaskuläre Einheit** bezeichnet wird (Leybaert et al., 2007; Iadecola, 2017). Dies bietet die Grundlage für die neuronale Versorgung an Sauerstoff und Glukose.

In Abhängigkeit von der neuronalen Aktivität können Astrozyten gefäßverengende oder gefäßerweiternde Substanzen freisetzen (Gordon et al., 2007). Hierbei kann eine Erhöhung des Blutflusses zu einer verbesserten Versorgung an Sauerstoff führen. Dies geschieht beispielsweise infolge eines Glutamat-vermittelten Ca^{2+}-Einstroms, der zur Freisetzung von vasodilativen Substanzen wie Prostaglandinen führt.

Darüber hinaus exprimieren Astrozyten an den Endfüßen Transporter wie den Glukose-Transporter 1 (GLUT-1), wodurch sie **Glukose** direkt aus dem Blut aufnehmen können (Morgello et al., 1995; Vannucci et al., 1997). Glukose ist das wichtigste metabolische Substrat und essenziell für die Produktion von **Adenosintriphosphat** (ATP), dem Energieträger der Zellen. Neuronale Synapsen sind zwar Hauptverbraucher an zellulärem ATP, haben jedoch nicht die Ressourcen, um dies bei gesteigerter Aktivität selbst schnell und effizient herzustellen (Ricci et al., 2009). Nach dem Konzept des **Astrozyten-Neuronen-Laktat-Shuttles** versorgen Astrozyten Neuronen mit dem Metabolit **Laktat** (Abbildung 6; Pellerin and Magistretti, 1994; Magistretti et al., 1999; Schurr et al., 1999). Dies ist ein intermediäres Stoffwechselprodukt, welches für die oxidative ATP-Produktion in Neuronen verwendet wird. Bei erhöhter Aktivität schütten Neuronen Glutamat aus, welches von Astrozyten aufgenommen wird (Clements et al., 1992; Pellerin and Magistretti, 1994). Dies ruft einen Na^{+}-Cotransport in den Astrozyten hervor und

aktiviert somit deren NKA (Pellerin and Magistretti, 1997). Dies führt wiederum zur Stimulation der Glykolyse, d. h. die Glukose-Umwandlung und die Laktat-Produktion (Chatton et al., 2000).

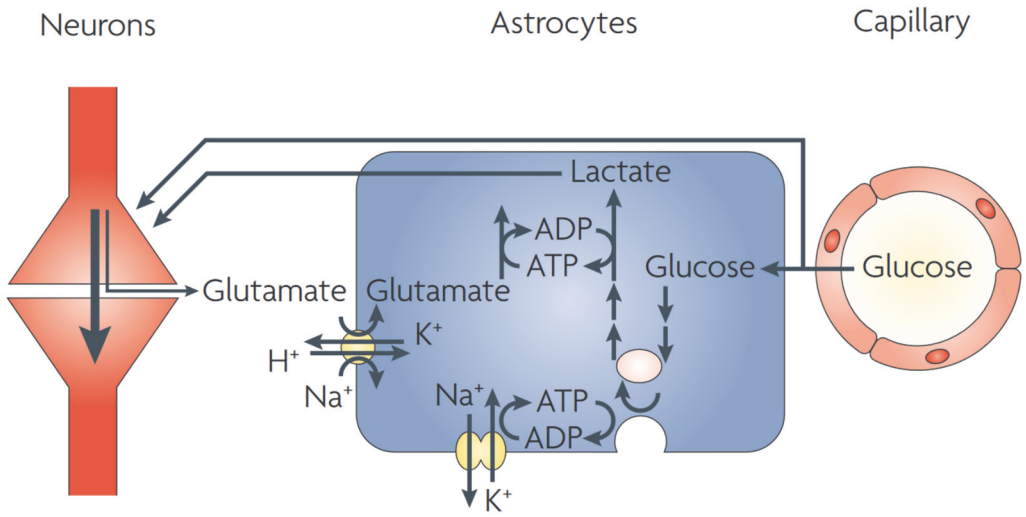

Abbildung 6. Astrozyten-Neuronen-Laktat-Shuttle. In Reaktion auf eine erhöhte glutamaterge neuronale Aktivität nehmen Astrozyten vermehrt Glutamat auf. Dies führt zu einem gesteigerten Energiebedarf der Astrozyten, wodurch die Glukose-Aufnahme aus dem Blut gefördert wird. Anschließend wird Glukose zu Laktat umgewandelt und zum Neuron transportiert. Modifiziert mit Genehmigung aus Giaume et al., 2010.

Eine alternative Energiequelle geht aus dem **Glutamat-Glutamin-Zyklus** hervor (Hertz et al., 1999; Daikhin and Yudkoff, 2000). Nach astrozytärer Glutamat-Aufnahme wird dies zu **Glutamin** synthetisiert, welches anschließend wieder zurück zu Neuronen transportiert wird. Diese können schlussendlich Glutamin über die Phosphat-aktivierte Glutaminase wieder zu Glutamat umwandeln (Kvamme et al., 2000).

Insgesamt können Astrozyten die lokale Verfügbarkeit an Stoffwechselsubstraten als Reaktion auf neuronale Aktivität erhöhen und somit die Energieversorgung der Neuronen sicherstellen.

1.4 Gap Junction-Kopplung

Astrozyten spielen durch die Aufnahme von Neurotransmittern, Ionen und Metaboliten eine große Rolle bei der Aufrechterhaltung homöostatischer Prozesse. Die effiziente Umverteilung erfolgt über **Gap Junctions**, welche die Zytoplasmen benachbarter Astrozyten funktionell koppeln (Bennett et al., 1991; Nagy and Dermietzel, 2000; Giaume et al., 2010). Die Ausbildung von Gap Junction-Kanälen führt dazu, dass biochemisch aktive Substanzen von Orten hoher Konzentration zu Orten niedriger Konzentration entlang des elektrochemischen Gradienten transportiert werden können. Dieses Prinzip der räumlichen

Pufferung wurde bereits Mitte des 20. Jahrhunderts für K^+ vorgeschlagen (Abbildung 7; Hertz, 1965; Orkand et al., 1966; Kofuji and Newman, 2004; Wallraff et al., 2006). Diesem Prinzip nach nehmen Astrozyten im ersten Schritt überschüssiges K^+ im Extrazellularraum auf, das von Neuronen freigesetzt worden ist. Dadurch entsteht ein elektrochemischer K^+-Gradient innerhalb des Synzytiums, der größer zwischen den Astrozyten ist als zwischen Astrozyten und Extrazellularraum. Daraufhin wird K^+ solange über Gap Junctions verteilt bis K^+ im Extrazellularraum wieder so gering ist, dass K^+ entlang des elektrochemischen Gradienten herausdiffundieren kann.

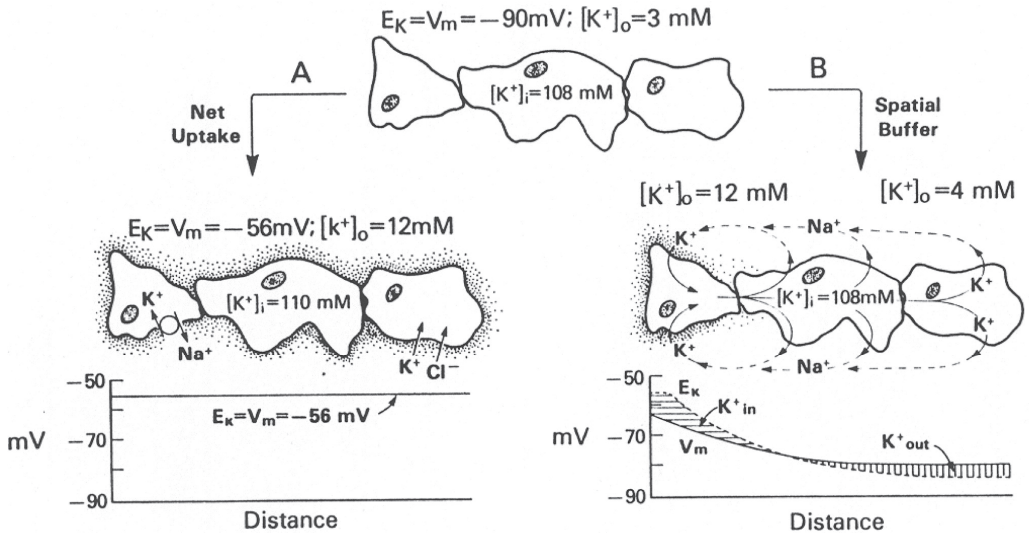

Abbildung 7. Schema der astrozytären Regulation der K^+-Homöostase. Gap junction-gekoppelte Astrozyten weisen unter Ruhebedingungen (d.h. bei einer extrazellulärer K^+-Konzentration ($[K^+]_o$) von 3 mM) ein stark negatives Membranpotential (V_M) auf von rund -90 mV. **A)** Aufnahme von K^+ aus dem Extrazellularraum. Oben: Steigt die $[K^+]_o$, dann nehmen Astrozyten über die Na^+/K^+-ATPase oder den $Na^+/K^+/Cl^-$-Kotransporter 1 K^+ auf. Unten: V_M bleibt hierbei innerhalb des Synzytiums konstant. **B)** Räumliche Pufferung von K^+. Oben: Lokale Erhöhung von K^+ führt zu einer Depolarisation der Astrozyten-Membran, welche sich innerhalb des Synzytiums verteilt. Unten: Die lokalen Unterschiede von $[K^+]_o$ führen zu einem K^+-Transport in Richtung niedrigerem $[K^+]_o$. Mit Genehmigung aus Orkand, 1986.

So kann unter anderem durch Gap Junction-vermittelte Umverteilung von K^+ die synaptische Transmission moduliert werden (Pannasch et al., 2011; Chever et al., 2016). Des Weiteren wird über die astrozytäre Kopplung der Metaboliten-Transport über weitere Entfernungen von Blutgefäßen zu Neuronen gewährleistet (Giaume et al., 1997; Rouach et al., 2008; Giaume et al., 2010).

Im Folgenden wird zunächst darauf eingegangen, wie Gap Junctions aufgebaut sind.

1.4.1 Aufbau von Gap Junction-Kanälen

Die kleinste strukturelle Einheit der Gap Junction-Kanäle bildet die Proteinfamilie der **Connexine** (Cx; Abbildung 8; Beyer et al., 1990; Pannasch and Rouach, 2013). Diese organisieren sich in Hexameren, welche **Connexone** genannt werden (Abbildung 8A; Nagy and Dermietzel, 2000). Diese Connexone bewegen sich in kleinen Gruppen lateral entlang der Membran, bis sie sich mit weiteren Connexonen aggregieren und *plaques* bilden (Ebihara, 2003). Anschließend können die Connexone benachbarter Astrozyten aneinander andocken und so die interzellulären Gap Junction-Kanäle bilden (Abbildung 7A). Diese ermöglichen die Diffusion von Molekülen mit einer Masse <1,2 kDa (Laird, 2006; Giaume et al., 2010). Die jeweilige Selektivität und Öffnungswahrscheinlichkeit eines jeden Gap Junction-Kanals ist abhängig von der Cx-Zusammensetzung (Bruzzone and Giaume, 1999). Dabei können Connexone homomer, d. h. aus den gleichen Cx-Isoformen, oder heteromer, d. h. aus unterschiedlichen Cx-Isoformen aufgebaut sein. Die Gap Junction-Kanäle wiederum können zusätzlich homotypisch (gleicher Connexon-Aufbau) oder heterotypisch (ungleicher Connexon-Aufbau) sein.

Bislang wurden 20 verschiedene Cx-Isoformen im murinen Gehirn entdeckt (Dermietzel and Spray, 1993; Rackauskas et al., 2010). Diese besitzen grundsätzlich die gleiche Tertiärstruktur, die aus vier Transmembrandomänen, zwei extrazellulären und einer intrazellulären Schleife sowie den zytoplasmatischen NH_2 (N)- und COOH (C)-Termini besteht (Abbildung 8B; Beyer et al., 1990). Die Länge des C-Terminus variiert jedoch innerhalb der Cx-Isoformen und bestimmt somit die Größe der Cxs (Laird, 2006). Abhängig von ihrem mutmaßlichen Molekulargewicht werden sie kategorisiert und benannt, beispielweise besitzt Cx27 eine Masse von 27 kDa (Beyer et al., 1990; Willecke et al., 2002).

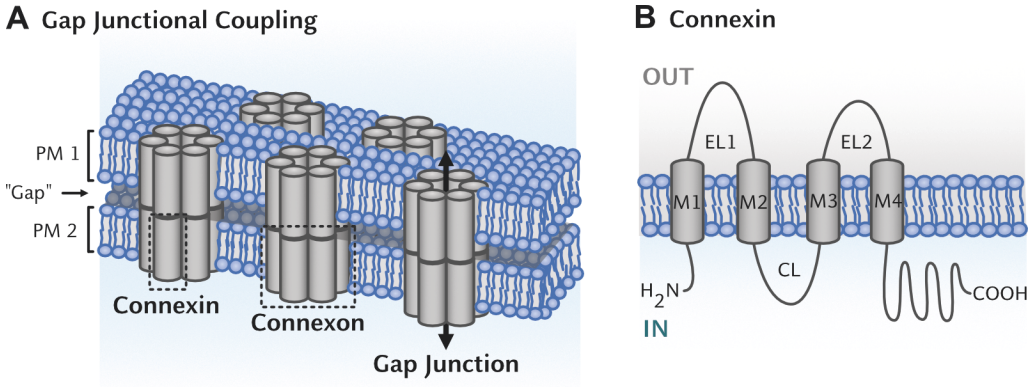

Abbildung 8. Aufbau von Gap Junction-Kanälen. A) Zwei Connexon-Paare (Hexamere von Connexinen) bilden einen intrazellulären Kanal (Gap Junction), der die Diffusion von Ionen und kleinen Molekülen ermöglicht. B) Membrantopologie eines Cxs. Cxs besitzen zwei extrazelluläre Schleifen (EL1-2), eine zytoplasmatische Schleife (CL), vier Transmembranhelices (M1-4) sowie einen N- und einen C-Terminus. Modifiziert mit Genehmigung aus Stephan et al., 2021.

Die in Astrozyten am häufigsten exprimierten Isoformen sind Cx43 und Cx30, wobei die Expression abhängig vom Entwicklungsstadium und der jeweiligen Gehirnregion ist (Dermietzel et al., 1989; Dahl et al., 1996; Nagy et al., 1999; Nagy et al., 2004). Während Cx43 bereits in frühen Stadien exprimiert wird, ist Cx30 erst in der dritten postnatalen Woche vorhanden (Kunzelmann et al., 1999; Nagy and Rash, 2000). Darüber hinaus unterscheidet sich die vorherrschende Cx-Isoform beider Formen von Gehirnregion zu Gehirnregion. Während Cx43 im Hippokampus stärker ausgeprägt ist, sind im Neokortex beide Isoformen gleich stark exprimiert (Griemsmann et al., 2015).

1.4.2 Astrozyten-Netzwerke

Astrozyten bilden durch die Gap Junction-Kopplung ausgedehnte, anatomisch abgegrenzte Synzytien, die auch als **Netzwerke** bezeichnet werden (Giaume et al., 2010). In einem Review aus 2021 beschreibe ich verschiedenste Techniken zur Untersuchung solcher Astrozyten-Netzwerke (Stephan et al., 2021*). Unter anderem kann hierfür die Beladung des Netzwerkes mithilfe eines **Tracers** genutzt werden (Abbildung 9A; Binmöller and Müller, 1992; Houades et al., 2006; Griemsmann et al., 2015; Eitelmann et al., 2020). Dabei wird die Diffusion von Molekülen innerhalb des Netzwerkes nachgeahmt. Im Speziellen wird zunächst ein einzelner Astrozyt mit einem Tracer gefüllt. Dieser wird über die Rückfüllung einer Pipette in die Zelle injiziert und diffundiert in benachbarte Gap Junction-gekoppelte Zellen. Dabei sind Tracer entweder autofluoreszierend oder können mit einem fluoreszierenden Konjugat markiert werden. Einer der ersten verwendeten Tracer ist Luzifer gelb (Kawata et al., 1983). Als autofluoreszierendes Molekül ermöglicht es eine direkte Beobachtung der Tracer-Diffusion innerhalb der Gap Junction-gekoppelten Zellen. Luzifer gelb ist jedoch nur gering permeabel für Cx30-basierte Gap Junctions und ist daher nur begrenzt anwendbar (Rackauskas et al., 2007). Alternativ können zwei nicht fluoreszierende Tracer, N-Biotinyl-L-Lysin (Biocytin) und N-(2-Aminoethyl)-Biotinamid-Hydrochlorid (Neurobiotin), zur Untersuchung der Astrozyten-Kopplung verwendet werden (Horikawa and Armstrong, 1988; Huang et al., 1992). Hierbei ist für die Visualisierung eine anschließende histochemische Färbung erforderlich, z. B. mit Farbstoff-markiertem Avidin (Livnah et al., 1993).

---

*Stephan, J., **Eitelmann, S.**, & Zhou, M. (2021). *Approaches to Study Gap Junctional Coupling.* Frontiers in Cellular Neuroscience, 15, 640406. https://doi.org/10.3389/fncel.2021.640406.

Die Diffusion eines Tracers ist jedoch nicht immer uniform. So können je nach primärem Diffusionsgradienten die Form und die Ausrichtung von Astrozyten-Netzwerken variieren. Bei der Form unterscheidet man zwischen **isotropen Netzwerken**, bei denen die Diffusion in allen Richtungen gleich ist und in **anisotropen Netzwerken**, welche eine präferierte Tracer-Diffusion entlang einer bestimmten Achse zeigen (Abbildung 9B).

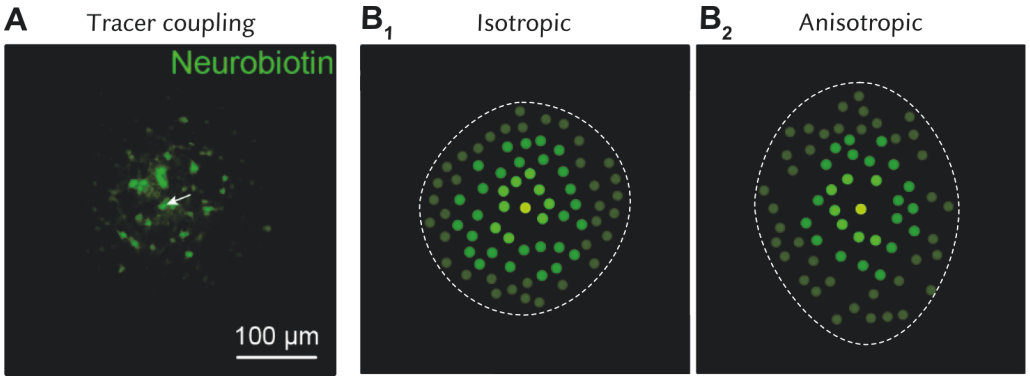

Abbildung 9. Diffusion von Tracern innerhalb Gap Junction-gekoppelter Netzwerke. A) Visualisierung der Gap Junction-Kopplung mithilfe des Tracers Neurobiotin. **B)** *In silico*-Netzwerke, welche ein isotropes (B_1) und ein anisotropes (B_2) Netzwerk zeigen. Modifiziert mit Genehmigung aus Eitelmann et al., 2019.

Sphärische Astrozyten-Netzwerke mit einer isotropen Tracer-Diffusion wurden beispielsweise in den neokortikalen Schichten IV und V sowie in ausreichender Entfernung zur Pyramidenschicht im *stratum radiatum* des Hippokampus entdeckt (Houades et al., 2006). Im Gegensatz dazu zeigen vor allem Astrozyten-Netzwerke in sensorischen Systemen eine Tracer-Kopplung mit präferierter Diffusionsrichtung. Dabei zeigen die astrozytären Netzwerke eine starke Korrelation zur anatomisch-funktionellen Organisation der Neuronen. So zeigten Studien in Regionen des somatosensorischen Kortex und im Thalamus, die in Tönnchen aufgeteilt sind, eine präferierte Diffusion des Tracers entlang der Tönnchen im Vergleich zu den Septen (Houades et al., 2008; Claus et al., 2018). In diesen Systemen könnte die Formierung der Topografie der Astrozyten-Netzwerke in Korrelation zur neuronalen Organisation begünstigend für den Transport von Metaboliten sowie für die Regulation der synaptischen Transmission sein.

Welche Faktoren die Ausbildung von anisotropen Netzwerken steuern, ist jedoch nicht vollständig geklärt. Zum einen zeigten Studien im Hippokampus und in der lateralen superioren Olive (LSO), dass die Netzwerk-Form bzw. die Anisotropie mit der Morphologie der Astrozyten korreliert (Anders et al., 2014; Augustin et al., 2016).

Zum anderen zeigte ich in einer Studie aus dem Jahr 2020, dass die Ausrichtung anisotroper Astrozyten-Netzwerke aktivitätsabhängig ist (Eitelmann et al., 2020*). Hierbei wurde die zuvor genannte LSO untersucht (Abbildung 10; Tollin, 2003; Kandler et al., 2009). Diese ist als Kern des auditorischen Hirnstamms entscheidend für die Lokalisierung von Schallquellen. Eine Besonderheit der auditorischen Hirnstammkerne ist, dass die Neurone eine tonotope Organisation aufweisen, d. h. sie entlang ihrer sensitivsten Frequenz von hohen (medial) zu niedrigen (lateral) Frequenzen organisiert sind. Hierbei werden Neurone innerhalb isofrequenter Bänder durch den gleichen schmalbandigen Frequenzbereich stimuliert (Abbildung 10A_1; Kandler et al., 2009). Entsprechend sind die Dendriten entlang dieser Bänder ausgerichtet und weisen eine schmale Morphologie auf (Sanes et al., 1992; Rietzel and Friauf, 1998). In einer vorangegangenen Studie wurde gezeigt, dass Astrozyten-Netzwerke, in Korrelation zur neuronalen Organisation, eine Anisotropie in Richtung der isofrequenten Bänder aufweisen (Abbildung 10A_2; Augustin et al., 2016).

Die Breite der isofrequenten Bänder im Maushirn erfährt bis zum Einsetzen des Hörens am 12. postnatalen Tag eine deutliche Verfeinerung (Kandler et al., 2009; Friauf et al., 2019). Dies erfolgt maßgeblich durch die Cochlea-getriebene Spontanaktivität (Tritsch et al., 2007). Hierbei verursachen Mutationen in verschiedenen Genen, die beispielsweise für den spannungsaktivierten Ca^{2+}-Kanal 1.3 ($Ca_V1.3$) oder den Ca^{2+}-Sensor Otoferlin in den inneren Haarzellen der Cochlea kodieren, eine erbliche Taubheit (Abbildung 10B). Studien mit *knock-out* (KO) Mäusen, bei denen diese Mutationen vorliegen, haben gezeigt, dass die tonotope Organisation der neuronalen Schaltkreise durch den Entzug der spontanen Cochlea-Aktivität beeinträchtigt ist (Hirtz et al., 2012; Müller et al., 2019).

---

*Eitelmann, S., Petersilie, L., Rose, C. R., & Stephan, J. (2020). *Altered Gap Junction Network Topography in Mouse Models for Human Hereditary Deafness.* International journal of molecular sciences, 21(19), 7376. https://doi.org/10.3390/ijms21197376

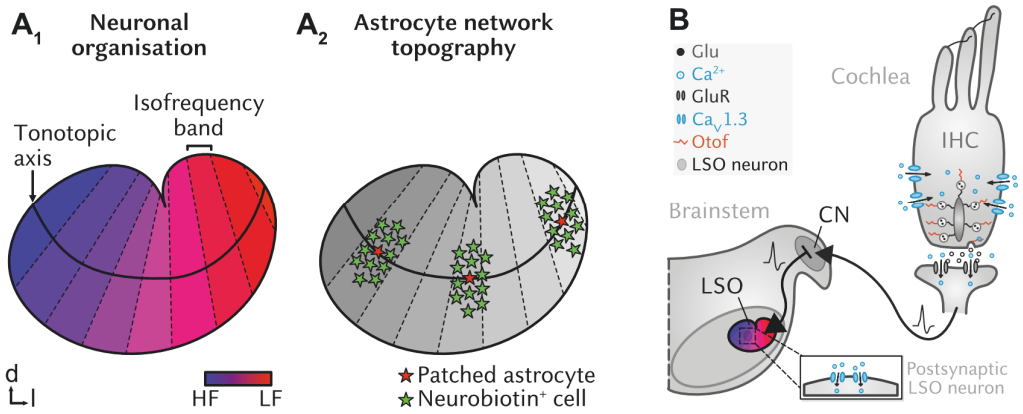

Abbildung 10. Zelluläre Organisation in der lateralen superioren Olive. A) Schematische Darstellung der neuronalen Organisation und der astrozytären Netzwerk-Topografie in der lateralen superioren Olive (LSO). Neurone sind in isofrequenten Bändern entsprechend ihrer Sensitivität von hoher (HF) bis niedriger Frequenz (LF) organisiert. Orthogonal dazu ergibt sich die tonotope Achse (A_1). Die Astrozyten-Netzwerke sind entlang der isofrequenten Bänder und entsprechend orthogonal zur tonotopen Achse organisiert (A_2). **B)** Ipsilaterale Verschaltung zu LSO-Neuronen. Der Ca^{2+}-Einstrom vermittelt über den Ca^{2+}-Sensor Otoferlin die Exozytose in den inneren Haarzellen (IHCs). Die spannungsabhängigen Ca^{2+}-Kanäle 1.3 ($Ca_V1.3$) führen zu einer Glutamat-Freisetzung in den IHCs und zu einem Ca^{2+}-Einstrom in die postsynaptischen LSO-Neuronen. Modifiziert mit Genehmigung aus Eitelmann et al., 2020.

Inwiefern die Abwesenheit der spontanen Cochlea-Aktivität auch zu einer Beeinträchtigung der astrozytären Netzwerk-Topografie führt, war unklar. Dafür wurden in dieser Studie die oben genannten Mausmodelle für erbliche Taubheit – $Ca_V1.3$- und Otoferlin-KO-Mäuse – verwendet und Tracer-Beladungen zur Visualisierung der Gap Junction-Kopplung genutzt (Abbildung 11A_1,B_1,C_1). Darüber hinaus wurde ein halbautomatischer Ansatz zur Bestimmung der Isotropie und Ausrichtung des Netzwerkes verwendet (Abbildung 11A_2, B_2,C_2,D; Eitelmann et al., 2019). Zunächst zeigte sich, dass in den KO-Mäusen analog zu den Wildtyp-Mäusen eine Anisotropie der Netzwerke vorliegt. Dies spricht dafür, dass die Spontanaktivität nicht für die Form der astrozytären Netzwerke verantwortlich ist. Interessanterweise zeigten die Daten, dass die Ausrichtung der Netzwerke in den KO-Mäusen verändert ist. So weisen die anisotropen Astrozyten-Netzwerke in den KO-Mäusen eine präferierte Ausrichtung nicht orthogonal, sondern entlang der tonotopen Achse auf. Dies deutet darauf hin, dass neuronale Aktivität aus der Peripherie während der frühen postnatalen Entwicklung für eine korrekte Ausrichtung der Astrozyten-Netzwerke in der LSO notwendig ist.

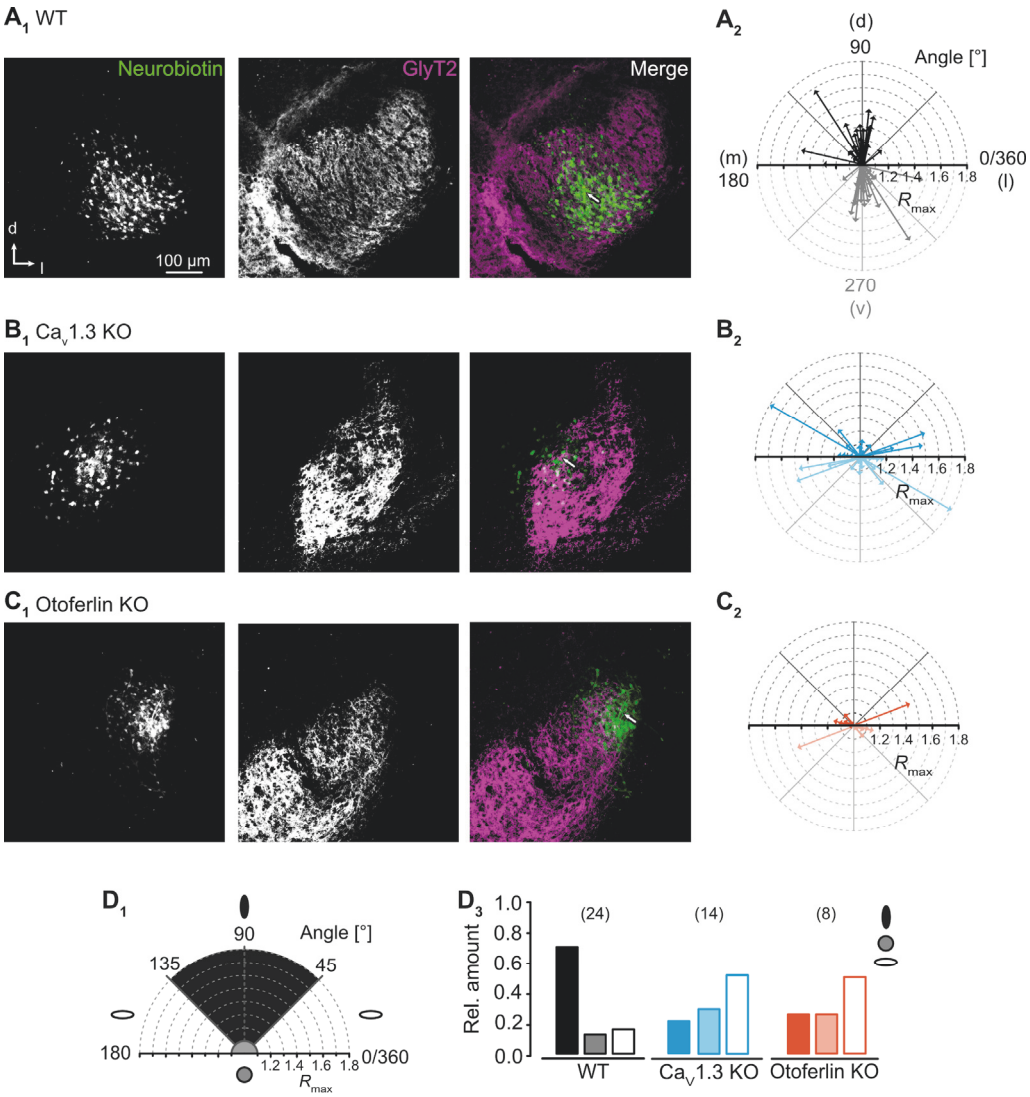

Abbildung 11. Aktivitätsabhängige Veränderung der Gap Junction-Kopplung. Visualisierung der Tracer-Kopplung in Wildtyp (WT; A_1), $Ca_V1.3$ *knock-out* (KO; B_1) und Otoferlin KO (C_1) Mäusen. Neurobiotin wurde über die Patch-Pipette in die gekoppelten Zellen eingebracht. Glycin-Transporter (GlyT) 2-Antikörperfärbungen wurden zur Hervorhebung der lateralen superioren Olive verwendet. Die semi-automatische Analyse ergab, dass Astrozyten-Netzwerke in WT orthogonal zur tonotopen Achse orientiert sind (A_2; D), während Netzwerke in den KO-Mäusen überwiegend entlang der tonotopen Achse orientiert sind (A_2+B_2; D). Dennoch waren alle Tracer-gekoppelten Netzwerke vorzugsweise anisotrop. Modifiziert mit Genehmigung aus Eitelmann et al., 2020.

1.4.3 Modulation von Gap Junction-Kanälen

Anatomisch-funktionelle sowie aktivitätsabhängige Faktoren innerhalb der Entwicklung führen dazu, dass Astrozyten-Netzwerke eine präferierte Diffusionsrichtung aufweisen. Die **Leitfähigkeit der Gap Junctions** (g_j) ist jedoch nicht statisch, sondern kann dynamisch reguliert werden (Willecke et al., 2002; Giaume et al., 2021). Dies geschieht über verschiedenste Mechanismen, beispielsweise über **spannungssensitive** oder **chemische Modulation** (Bukauskas and Verselis, 2004; Sosinsky and Nicholson, 2005; Nielsen et al., 2012).

Bei der spannungssensitiven Modulation wirken sich Änderungen der transjunktionalen Spannung (V_j), also der Differenz der Spannungen zweier Gap Junction-gekoppelter Zellen, auf g_j aus (Harris, 2001; Bukauskas and Verselis, 2004). Wenn die Spannung über beiden Zellmembranen identisch ist, ist $V_j = 0$, und folglich g_j maximal. Ändert sich jedoch die Spannung über eine der beiden Zellmembranen, ergibt sich $V_j > 0$ und es kommt zu einer Reduktion von g_j. Dabei sind grundsätzlich sind alle Gap Junctions spannungssensitiv. So reagieren auch Gap Junction-Kanäle, die aus den Astrozyten-spezifischen Cx43 und/oder Cx30 gebildet sind, auf Änderungen in V_j (Manthey et al., 2001). Studien mit HeLaCx43- and Novikoff-Zellen konnten zeigen, dass ein V_j von 30 mV zu einer Reduktion von g_j auf 65 % des maximalen Wertes führt (Bukauskas and Verselis, 2004).

Bei der chemischen Modulation führt die Bindung Ionen oder andere chemisch wirkende Moleküle zu einer Veränderung in g_j (Bukauskas and Verselis, 2004). Dies kann jedoch im Kontrast zum spannungssensitiven Mechanismus zu einer kompletten Reduktion von g_j führen. Diese Modulation kann direkt oder indirekt über ein anderes intermediäres Molekül erfolgen. So kann beispielsweise die dynamische Interaktion mit Proteinkinasen (a, c oder Mitogen-aktiviert) zur Phosphorylierung des C-Terminus führen (Lampe and Lau, 2000; Laird, 2006; Márquez-Rosado et al., 2012; Solan and Lampe, 2014).

Eine Änderung des intrazellulären pH-Werts (pH_i) führt zu einer Modulation von g_j (Turin and Warner, 1977; Spray et al., 1981; Bukauskas and Peracchia, 1997). Unter physiologischen Bedingungen liegt der astrozytäre pH_i bei etwa 7,0-7,3, was einer intrazellulären H^+-Konzentration von 40-80 nM entspricht (Deitmer and Rose, 1996). Die Konformationsänderung infolge von direkter Wechselwirkung mit Protonen geschieht in Form eines „Partikel-Rezeptor"-Mechanismus (Morley et al., 1997; Duffy et al., 2002; Bukauskas and Verselis, 2004; Seki et al., 2004). Hierbei fungiert der C-Terminus als Partikel und die zytoplasmatische Schleife als Rezeptor. Ein ähnlicher Mechanismus wurde auch für die spannungssensitiven Änderungen vorgeschlagen (Zhou et al., 1999). Ein kompletter Verlust von g_j liegt entweder bei Ansäuerungen stärker als pH 6.4 oder Alkalisierung größer als 7.6 vor (Swietach et al., 2007; Garciarena et al., 2018).

Eine Erhöhung der $[Ca^{2+}]_i$ führt zur Reduzierung von g_j (Rose and Loewenstein, 1975; Turin and Warner, 1977). Dies geschieht infolge eines Anstiegs im niedrigen µM-Bereich (0.5-1 µM; Crow et al., 1994; Enkvist and McCarthy, 1994; Dekker et al., 1996). Da Cxs keine hochsensitiven Bindestellen für Ca^{2+} besitzen, wird vermutet, dass es eine intermediäre Komponente bei dem Ca^{2+}-abhängige Modulation geben muss (Peracchia and Leverone Peracchia, 2021). Ein vielversprechender Kandidat hierfür ist das

Ca^{2+}-bindende Molekül **Calmodulin** (CaM; Qin et al., 1999; Peracchia et al., 2000). Hierbei wurde gezeigt, dass die zytoplasmatische Schleife von Cx43 über CaM-Bindestellen verfügt (Saimi and Kung, 2002). Studien mit CaM-Inhibitoren und CaM-Mutanten unterstützen diese Hypothese (Peracchia et al., 2000; Peracchia, 2004; Zou et al., 2014). Hierbei soll die Interaktion zwischen CaM und Cx einem korkartigen Mechanismus folgen (Abbildung 12; Peracchia et al., 2000; Peracchia, 2020). Demnach bilden CaM-Moleküle bei Ca^{2+}-Bindung eine physische Blockade der zytoplasmatischen Cx-Öffnung.

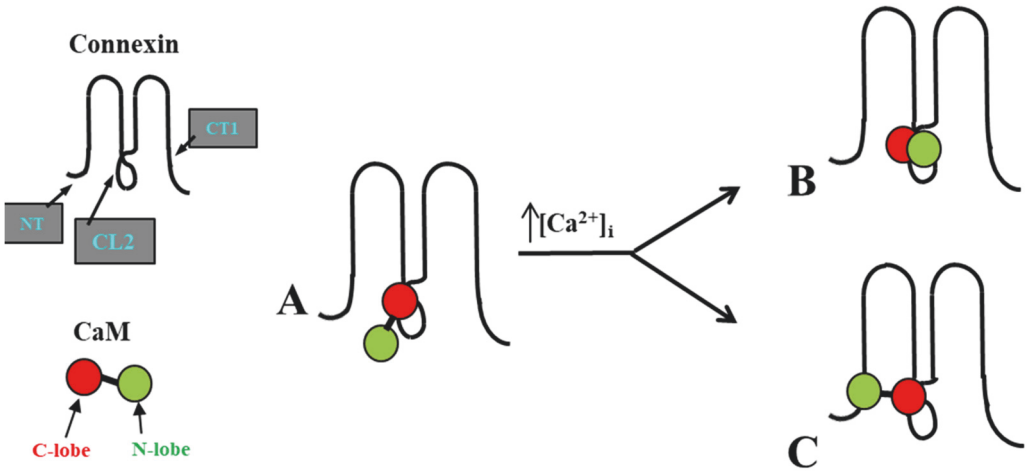

Abbildung 12. Schema des Calmodulin (CaM)-Kork-Modells. Nach dieser Hypothese ist CaM über das C-Ende an der zytoplasmatischen Schleife (CL2) der Connexine verankert (A). Eine Erhöhung der $[Ca^{2+}]_i$ führt zu einer Schließung der Pore durch Bindung innerhalb der zytoplasmatischen Schleife (B) oder an den N-Terminus (C). Modifiziert mit Genehmigung aus Peracchia and Leverone Peracchia, 2021

1.5 Elektrophysiologische Eigenschaften

Innerhalb dieser Netzwerke sind die Astrozyten nicht nur chemisch gekoppelt, sondern auch **elektrisch**. Wenn ein einzelner Astrozyt einer Verschiebung von $[K^+]_i$ ausgesetzt ist, diffundiert K^+ aus den gekoppelten Zellen in die betroffene Zelle. Da K^+ der wichtigste Bestimmungsfaktor von E_M in Astrozyten ist, spiegelt sich dies wiederum in einer Angleichung von E_M zwischen gekoppelten Zellen wider („**Isopotenzialität**"). So ermöglicht die hohe interastrozytäre Kopplung, Abweichungen in $[K^+]_i$ zu puffern (Ma et al., 2016; Kiyoshi et al., 2018).

Während Neurone unter Ruhebedingungen ein E_M von rund -70 mV aufweisen, ist das E_M von Astrozyten wie bereits erwähnt deutlich hyperpolarisierter (Du et al., 2016). Unter Ruhebedingungen liegt das astrozytäre E_M typischerweise bei etwa -85 mV (Nedergaard et al., 2003; Wang and Bordey, 2008). Dies geht einher mit einem R_M im niedrigen MΩ-Bereich (Zhou et al., 2006; Ma et al., 2014; Du et al., 2015). Um die elektrophysiologischen Membraneigenschaften zu bestimmen, kann die

Patch-Clamp-Technik verwendet werden (Neher and Sakmann, 1976). Dabei wird eine Pipette mit einer Lösung gefüllt, deren Zusammensetzung im Regelfall dem intrazellulären Milieu der zu messenden Zelle entspricht (Abbildung 13A). Anschließend wird durch Überdruck ein Membranfleck („Patch“) an die Pipette gezogen, wodurch ein Eingangswiderstand (R_{In}) im GΩ-Bereich („GΩ-seal“) erzeugt wird und die Zelle im *cell-attached*-Modus abgeleitet werden kann (Abbildung 13B$_1$). Weiterführend kann ein erneuter, kurzer Überdruck genutzt werden, um die Membran zu öffnen. Nun kann die Zelle im *whole-cell*-Modus gemessen werden (Abbildung 13B$_2$). Hierbei kann entweder E vorgegeben werden und I gemessen werden (*voltage clamp*) oder andersherum (*current clamp*).

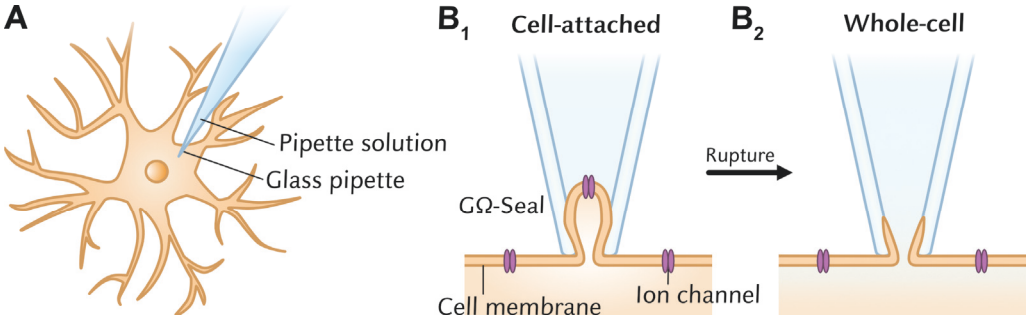

Abbildung 13. Schematische Darstellung der Patch-Clamp-Technik. A) Eine Pipette wird auf die Zellmembran platziert. **B)** Durch leichten Unterdruck wird die Membran zur Pipette gezogen, wodurch eine Dichtung im GΩ-Bereich erreicht wird und die Zelle im *cell-attached*-Modus abgeleitet werden kann (B$_1$). Applikation eines kurzen, starken Überdrucks führt zur Öffnung der Membran und ermöglicht die Ableitung im *whole-cell*-Modus (B$_2$). Unpublizierte Abbildung, erstellt von S. Eitelmann.

Bei elektrophysiologischen Messungen können verschiedene Merkmale von Astrozyten zur Identifikation genutzt werden. Zum einen kann der fluoreszierende Farbstoff Sulforhodamin 101 verwendet werden, der unter definierten Bedingungen nur von Astrozyten aufgenommen wird (Abbildung 14A; Nimmerjahn et al., 2004; Kafitz et al., 2008). Zum anderen kann auf das charakteristische passive Strommuster der Astrozyten geprüft werden (Du et al., 2015). Dafür wird das Verhältnis zwischen Strom und Spannung (I/V) bestimmt. Im *voltage clamp*-Modus werden hierfür Spannungsstufen appliziert und der resultierende Strom gemessen (Abbildung 14B$_1$). Ausgereifte Astrozyten weisen hauptsächlich passive K^+-Ströme auf, was zu einer linearen I/V-Beziehung führt (Abbildung 14B$_2$; Zhou et al., 2006; Kafitz et al., 2008).

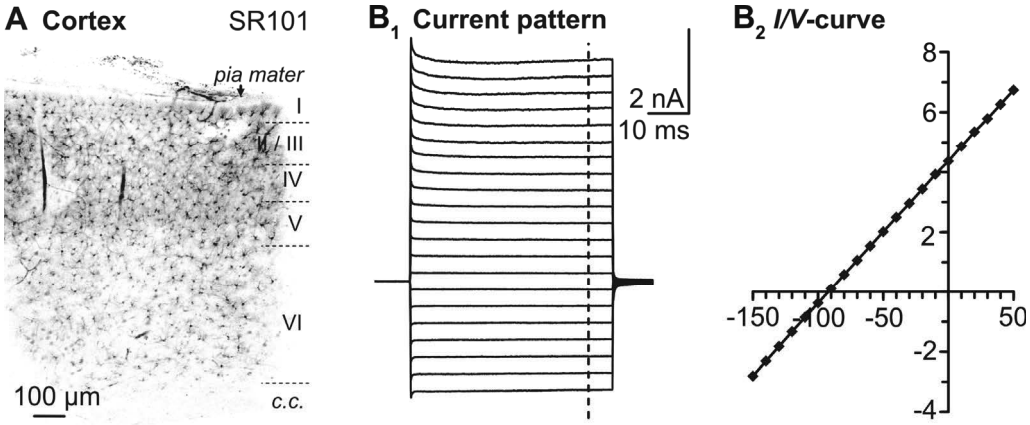

Abbildung 14. Elektrophysiologie eines neokortikalen Astrozyten. A) Sulforhodamin 101-Färbungen der neokortikalen Astrozyten im murinen Akutschnitt. **B)** Resultierende Stromstufen bei Applikation von Spannungsstufen (B_1). Das Diagramm zeigt das lineare Verhalten der *I/V*-Beziehung eines passiven Astrozyten (B_2). Unpublizierte Abbildung, erstellt von S. Eitelmann.

1.6 Vom Leim zum essenziellen Kommunikationspartner

Klassischerweise ging man davon aus, dass Astrozyten lediglich als Leim innerhalb des Gehirns dienen. Heute weiß man, dass Astrozyten als Teil der dreiteiligen Synapse neuronale Signale integrieren und die synaptische Übertragung modulieren. Außerdem versorgen Astrozyten Neurone mit essenziellen Stoffwechselprodukten. Durch die Ausbildung großer ausgedehnter Netzwerke über Gap Junctions können verschiedene Moleküle wie Neurotransmitter, Ionen und Metabolite effizient umverteilt werden. Des Weiteren kann die interastrozytäre Diffusion dynamisch infolge von Änderungen in der V_j, pH_i und $[Ca^{2+}]_i$ moduliert werden. Darüber hinaus besitzen Astrozyten einzigartige elektrophysiologische Eigenschaften wie ein stark hyperpolarisiertes E_M, das auf Ionenschwankungen mit Hyper- oder Depolarisation reagiert. Diese Punkte demonstrieren, dass Astrozyten als Kommunikationspartner für Neuronen eine essenzielle Rolle bei der Signalübertragung im Gehirn spielen.

2 Pathophysiologie des ischämischen Schlaganfalls

Astrozyten sind die Hauptkontrolleure homöostatischer Prozesse im zentralen Nervensystem. Es gibt jedoch immer mehr Hinweise darauf, dass eine Fehlfunktion der Astrozyten eine wichtige Rolle bei neurologischen Erkrankungen spielt – so auch bei der Pathophysiologie von **ischämischen Schlaganfällen**.

Das Gehirn ist besonders anfällig für ischämische Bedingungen, denn gemessen an seiner Größe ist das Gehirn das Organ mit dem höchsten Energiebedarf (Attwell et al., 2010). Das menschliche Gehirn macht 2 % des Körpergewichts aus, wobei es 20–25 % der Gesamtenergie verbraucht. Unter physiologischen Bedingungen wird dieser massive Energiebedarf durch die strikte Regulation des zerebralen Blutflusses und somit die Versorgung an Glukose und Sauerstoff gedeckt. Wie bereits erwähnt spielen Astrozyten hierbei eine zentrale Rolle durch Vasomodulation oder aktivitätsabhängige Bereitstellung von Metaboliten.

2.1 Die ischämische Penumbra

Bei ischämischen Schlaganfällen führen Blutgerinnsel zu einem Verschluss einer Hirnarterie und folglich zu einer Reduktion des ZBFs (Dirnagl et al., 1999). Im ischämischen Kern liegt nur noch ein zerebraler Blutfluss unter 20 % vor, was zu irreparablen Schäden der betroffenen Zellen führt (Jennett et al., 1966; Hossmann, 1994). Daran angrenzend befindet sich mit einem Blutfluss von 20–40 % die **Penumbra** (Astrup et al., 1981; Heiss and Graf, 1994). Zellen in dieser Region leiden unter metabolischem Stress, können sich aber potenziell durch Reperfusion wieder erholen. Daher stellt die Penumbra das erfolgreichste Ziel für eine Therapie dar (Mehta et al., 2007).

Eine der wichtigsten Merkmale der ischämischen Penumbra sind spontan auftretende **Infarktwellen** (Abbildung 15; Somjen, 2001; Dreier, 2011). Diese Infarktwellen werden durch den Energiemangel im ischämischen Kern initiiert, der zu einer Dysfunktion der NKA und damit zu einem Zusammenbruch der Ionen-Homöostase führt (Rossi et al., 2007; Moskowitz et al., 2010; van Putten et al., 2021). Infolgedessen kommt es zur spontanen Depolarisation der neuronalen Zellmembran (Moskowitz et al., 2010). Anschließend breiten sich diese depolarisierenden Infarktwellen mit einer Geschwindigkeit von 2-8 mm/min radial aus (Hartings et al., 2003; Dreier and Reiffurth, 2015). Diese sind durch die Depolarisation und damit einhergehend den erhöhten Energiebedarf eine zusätzliche,

erhebliche metabolische Belastung für die Zellen. So kommt es zusätzlich nach jeder weiteren Infarktwelle zu einer progressiven Reduktion des ZBFs und schlussendlich zu einer Vergrößerung des ischämischen Kerns (Mies et al., 1993; Dijkhuizen et al., 1999; Shin et al., 2006).

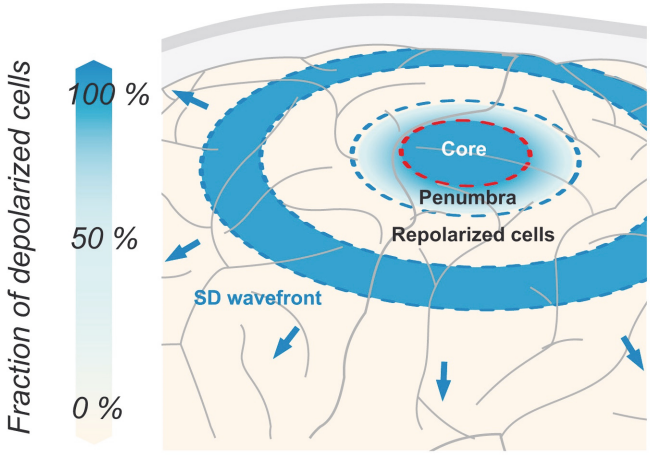

Abbildung 15. Ausbreitung von Infarktwellen. In der Kernregion bleiben die Zellen aufgrund des starken Energiemangels depolarisiert. Radial davon breiten sich Infarktwellen (*SD wavefront*) aus. Modifiziert mit Genehmigung aus Dreier and Reiffurth, 2015.

2.2 Zelluläre Folgen von Infarktwellen

Infarktwellen führen zu deutlichen Beeinträchtigung grundlegender zellulärer Prozesse (Abbildung 16; Dreier, 2011; Pietrobon and Moskowitz, 2014; van Putten et al., 2021). Zum einen weisen Astrozyten eine verringerte Glutamat-Aufnahme auf, wodurch es zu einer Überstimulation der postsynaptischen Glutamat-Rezeptoren kommt und folglich zu einer Glutamat-vermittelten Exzitotoxizität (Mori et al., 2004; Giffard and Swanson, 2005). Zum anderen führt der Mangel an Sauerstoff und Glukose zu einer reduzierten ATP-Produktion, was einhergeht mit einem Zusammenbruch der Ionen-Gradienten (Bambrick et al., 2004; Pietrobon and Moskowitz, 2014). Diese Störung führt zusätzlich zu einer Erhöhung von $[Ca^{2+}]_i$, welche eine weitere Glutamat-Freisetzung auslösen kann und somit zur Exzitotoxizität beiträgt (Rakers and Petzold, 2017; Gerkau et al., 2018). Des Weiteren kommt es zu einer Erhöhung von $[Na^{+}]_i$ und einer Ansäuerung in Astrozyten und Neuronen (Pietrobon and Moskowitz, 2014; Dreier and Reiffurth, 2015; Gerkau et al., 2018; Meyer et al., 2022). Die Änderungen der Ionen-Konzentrationen gehen einher mit einer intrazellulären Hyperosmolarität und folglich eines Wasser-Einstroms in die Zellen (Kraig and Nicholson, 1978; Vorísek and Syková, 1997; Mazel et al., 2002; Windmüller et al., 2005).

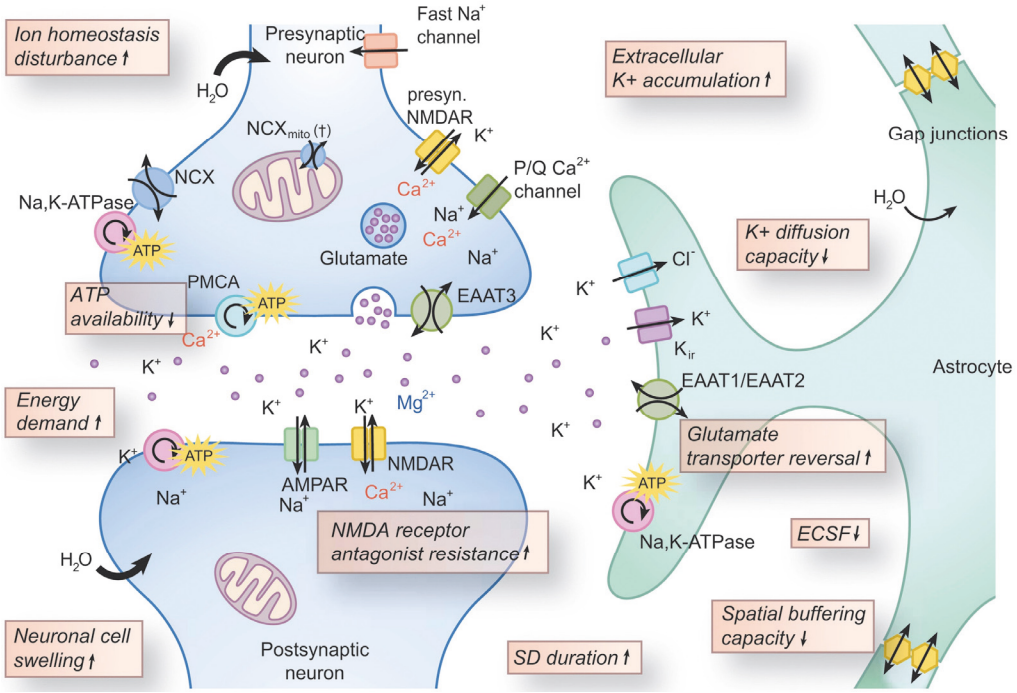

Abbildung 16. Auswirkungen von Infarktwellen auf Zellen in der Penumbra. Während Infarktwellen erfahren die Zellen der dreiteiligen Synapse (blau: Neuron; grün: Astrozyt) zelluläre Störungen wie einen Zusammenbruch der Ionen-Homöostase und gleichzeitig ein Schwellen von neuronalen Somata sowie eine Verkleinerung des Extrazellularraums. Modifiziert mit Genehmigung aus Dreier and Reiffurth, 2015.

Somit stellt der Verlust der astrozytären Funktionen eine große Belastung für die Zellen während ischämischer Bedingungen dar. Zusätzlich scheinen Astrozyten weniger sensitiv gegenüber ischämischen Bedingungen zu sein als Neuronen, wie bei Studien im ischämischen Kern beobachtet worden ist (Thoren et al., 2005). Hierbei wurde gezeigt, dass in der frühen Phase der Reperfusion ein Teil der Astrozyten im Gegensatz zu den Neuronen noch metabolisch aktiv ist.

Aus all diesen Punkten kristallisiert sich heraus, dass der Erhalt der astrozytären Funktionen eine kritische Rolle bei der Pathophysiologie von ischämischen Bedingungen spielt.

3 Astrozyten während kurzzeitigem Energiemangel

Aus den vorangegangenen Kapiteln geht hervor, dass Astrozyten unter physiologischen Bedingungen durch Glutamat- und K^+-Aufnahme die neuronale Erregbarkeit und die synaptische Transmission regulieren können. Zusätzlich stellen sie die Energieversorgung von Neuronen durch die Bereitstellung von Glukose sicher. Die interastrozytäre Umverteilung dieser Neurotransmitter, Ionen und Metabolite wird über die Gap Junction-Kopplung bewerkstelligt. Während den pathophysiologischen Bedingungen eines ischämischen Schlaganfalls kommt es zu sich radial ausbreitenden Infarktwellen, die von der ischämischen Kernregion ausgehend die Penumbra infiltrieren und einher gehen mit einer Störung der extrazellulären K^+-Homöostase. Dabei stellt jede weitere Welle eine zusätzliche Belastung der Zellen der Penumbra dar. Somit ist es essenziell herauszufinden, welche Faktoren die Zellschäden limitieren könnten.

Da Astrozyten hauptverantwortlich sind für die Regulierung der K^+-Menge im Extrazellularraum, stellt eine Änderung der astrozytären $[K^+]_i$ eines der frühsten Anzeichen einer Infarktwelle dar (Pietrobon and Moskowitz, 2014). Die Methoden zur Bestimmung von $[K^+]_i$ sind jedoch sehr limitiert. Somit war nicht bekannt, wie sich $[K^+]_i$ im zeitlichen Verlauf bei kurzzeitigen ischämischen Bedingungen ändert. Da die Gap Junction-Kopplung der Astrozyten hauptverantwortlich für die Umverteilung von Ionen (und insbesondere K^+) ist, wurde zusätzlich vermutet, dass die astrozytäre Kopplung eine kritische Rolle bei der Weiterleitung von potenziell schädlichen Faktoren spielen könnte. Dazu wurde bereits in früheren Studien gezeigt, dass es bei andauerndem Energiemangel zu einer Entkopplung kommt (Vera et al., 1996; Lee et al., 2016). Ob sich die Kopplungsstärke schon bei kurzzeitigen ischämischen Bedingungen verändert, war nicht bekannt.

Um herauszufinden, inwiefern Astrozyten bei der Begrenzung von ischämischen Schäden eine Rolle spielen könnten, wurden in den vorliegenden Studien die Folgen eines kurzzeitiger Energiemangel auf die $[K^+]_i$ (Eitelmann et al., 2022) und in der Gap Junction-Kopplung (Eitelmann et al, eingereicht) untersucht. Die Ergebnisse und Erkenntnisse aus diesen Studien sind im Folgenden zusammengefasst.

3.1 Störung der astrozytären K^+-Homöostase

Eines der frühesten Anzeichen für die Entwicklung einer depolarisierenden Infarktwelle ist eine Störung in der K^+-Homöostase (Pietrobon and Moskowitz, 2014). Unter physiologischen Bedingungen stellt die Regulation der extrazellulärem K^+-Homöostase eine der wichtigsten Funktionen von Astrozyten dar. Jedoch sind Astrozyten im ischämischen Kern nicht mehr in der Lage, die übermäßigen Mengen an $[K^+]_e$ zu puffern (Hansen, 1985; Somjen, 2005; van Putten et al., 2021). Bei einem Anstieg der $[K^+]_e$ über 12–16 mM ruft dies letztlich depolarisierende Infarktwellen hervor (Erecińska and Silver, 1994; Petzold et al., 2005; Maslarova et al., 2011; Du et al., 2018). Dies geht einher mit einer Verringerung der $[K^+]_i$, welche zusätzlich zu einer Steigerung von $[K^+]_e$ beiträgt (Du et al., 2018).

In der folgenden Studie war es mein Ziel, den kompletten zeitlichen Verlauf der astrozytären, intrazellulären K^+-Homöostase während eines kurzzeitigen Energiemangels zu bestimmen (Eitelmann et al., 2022*).

3.1.1 Simulation von $[K^+]_i$

Die Bestimmung der astrozytären $[K^+]_i$ im zeitlichen Verlauf ist jedoch nicht trivial. Genetisch-kodierte oder chemische $[K^+]_i$-Indikatoren sind verfügbar, aber es mangelt an geeigneten Techniken für *in situ*-Experimente (Rimmele and Chatton, 2014; Bischof et al., 2017; Wellbourne-Wood et al., 2017; Shen et al., 2019). Weitere Studien näherten sich diesem Problem, indem mathematische Modelle zur Bestimmung der $[K^+]_i$ verwendetet wurden (Kimelberg et al., 1979; Breslin et al., 2018; Du et al., 2018; Kalia et al., 2021). In der vorliegenden Studie wurde ein empirisch-theoretischer Ansatz verwendet, bei dem experimentell erhobene Daten zur Berechnung von $[K^+]_i$ genutzt wurden. Für die Berechnung von $[K^+]_i$ wurde die Goldman-Hodgkin-Katz-Gleichung (Gleichung 2) verwendet.

$$E_M = \frac{RT}{F} \ln \frac{P_K[K^+]_e + P_{Na}[Na^+]_e}{P_K[K^+]_i + P_{Na}[Na^+]_i}, \quad (2)$$

wobei *R* die ideale Gaskonstante, *T* die absolute Temperatur, *F* die Faraday'sche Konstante, $[X^z]_{e/i}$ die Konzentration des Ions X extra- oder intrazellulär mit der Valenz z und $P_{K/Na}$ die Permeabilität für jeweils K^+ oder Na^+ ist.

---

*Eitelmann, S., Stephan, J., Everaerts, K., Durry, S., Pape, N., Gerkau, N. J., & Rose, C. R. (2022). *Changes in Astroglial K^+ upon Brief Periods of Energy Deprivation in the Mouse Neocortex.* International Journal Of Molecular Sciences, 23(9), 4836. https://doi.org/10.3390/ijms23094836.

Diese eignet sich zum einen, da die P_K der Astrozyten-Membran unter physiologischen Bedingungen im Vergleich zu der P_{Na} deutlich größer ist (Ransom and Goldring, 1973; Kimelberg et al., 1979). Zum anderen wurde gezeigt, dass die passiven Eigenschaften der astrozytären Membran während ischämischen Bedingungen unverändert bleiben (Xie et al., 2008; Du et al., 2018).

Alle anderen Parameter (E_M, $[K^+]_e$, α, $[Na^+]_{e/i}$) wurden experimentell bestimmt. Dafür wurden Astrozyten des somatosensorischen Neokortex (Schicht II/III) aus Akutschnitten der Maus zwischen den postnatalen Tagen 14-21 untersucht. Die ischämischen Bedingungen wurden während einer Infarktwellen in der Penumbra durch kurzzeitige Inhibition des Metabolismus nachgeahmt („**chemische Ischämie**"; Gerkau et al., 2018; Engels et al., 2021; Meyer et al., 2022). Bei der chemisch-induzierten Ischämie wird das Präparat für 2 min mit einer Glukose-freien artifiziellen Cerebrospinalflüssigkeit (ACSF) perfundiert, die zusätzlich den Zytochrom-c-Oxidase-Inhibitor Natriumazid (NaN_3; 5mM) und das nicht metabolisierbare Glukose-Analogon 2-Desoxyglukose (2-DG; 2mM) enthält. Infolgedessen kommt es zu einer Änderung im intrazellulären ATP-Gehalt, analog zu dem Verlust, der während der Generierung von Infarktwellen beobachtet wird (Mies et al., 1993; Lerchundi et al., 2019; Lerchundi et al., 2020). Zum anderen wurde im Vergleich zwischen *in situ*- und *in vivo*-Experimenten bestätigt, dass die Ionen-Veränderungen mit diesem Protokoll nachgebildet werden können (Gerkau et al., 2018).

Des Weiteren wurden E_M und α mithilfe der Patch-Clamp-Technik gemessen, die $[K^+]_e$ und die $[Na^+]_e$ mit Ionen-sensitiven Mikroelektroden und $[Na^+]_i$ in Weitfeld-Imaging-Experimenten mithilfe des Na^+-Indikators SBFI. Dabei ergibt die Bestimmung von P_K/P_{Na} für neokortikale Astrozyten ein α von 0.010, welches niedriger ist als das für Astrozyten aus der hippokampalen CA1 Region (0.015; Stephan et al., 2012).

Zur Berechnung der $[K^+]_i$ wurden die experimentell bestimmten Verläufe von E_M, $[K^+]_e$, $[Na^+]_e$ und $[Na^+]_i$ gemittelt (Abbildung 17A). Anhand Gleichung 2 ergibt sich so der $[K^+]_i$-Verlauf während der chemischen Induktion einer Ischämie (Abbildung 17B). Hierbei zeigt sich zunächst ein Ruhewert von $\mathbf{[K^+]_i = 146\ mM}$. Dieser Wert liegt etwas höher im Vergleich zu dem zuvor genäherten $[K^+]_i$ von 133 mM in kultivierten, kortikalen Astrozyten der Maus (Rimmele and Chatton, 2014). Jedoch wurde während der Experimente dieser Studie eine höhere $[K^+]_e$ verwendet, was zu einer Depolarisation der Zellen und entsprechend zu einer niedrigeren $[K^+]_i$ führt.

Der chemischen Induktion der Ischämie folgt ein maximaler Verlust an K^+ von **43 mM** rund 100 s nach Reperfusion. Dies ist hauptsächlich auf die Dysfunktion der NKA

zurückzuführen (Rimmele and Chatton, 2014; Gerkau et al., 2018). Zusätzlich könnte hierbei die Aktivierung von astrozytären Glutamat-Transportern zur Verringerung der $[K^+]_i$ beitragen.

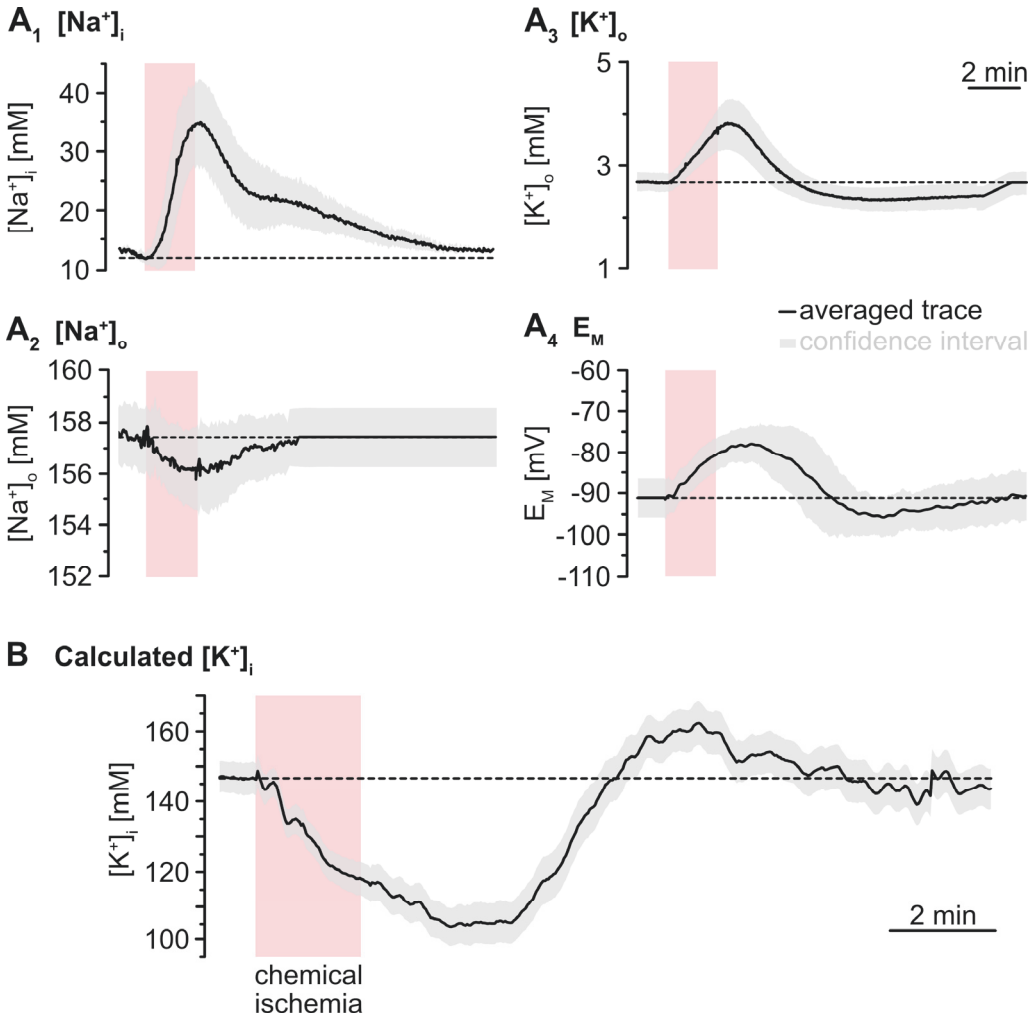

Abbildung 17. Simulation des zeitlichen Verlaufs der astrozytären $[K^+]_i$ während der kurzzeitigen, chemischen Induktion einer Ischämie. A) Zeitlich gemittelter Verlauf der experimentell bestimmten Daten von $[Na^+]_{i/e}$ (A_{1+2}), $[K^+]_e$ (A_3) und E_M (A_4). **B)** Mithilfe der Goldman-Hodgkin-Katz-Gleichung wurde mit den Spuren aus (A) der zeitliche Verlauf von $[K^+]_i$ berechnet. Modifiziert mit Genehmigung aus Eitelmann et al., 2022.

Überraschenderweise konnten wir eine verzögerte Aufnahme von K^+ von **16 mM** berechnen, welche circa 6 min nach Reperfusion eintritt und sich wieder langsam auf den anfänglichen Ruhewert erholt. Dies deutet darauf hin, dass die NKA nach der metabolischen Inhibition aufgrund der immer noch erhöhten $[Na^+]_i$ anhaltend aktiviert bleibt (Ransom et al., 2000; Xie et al., 2008; Gerkau et al., 2018). Zusätzlich könnte die verzögerte K^+-Aufnahme aufgrund der erhöhten Aktivität des NKCC1s vorliegen (Engels et al., 2021). Die K^+-Aufnahme über den initialen Wert steht in Korrelation zu einer verminderten $[K^+]_e$. Folglich führt dies höchstwahrscheinlich zu einer Hyperpolarisation der Neuronen und

gleichzeitig einer reduzierten neuronalen Erregbarkeit (Bellot-Saez et al., 2017). Dies könnte einen neuroprotektiven Effekt mit sich bringen, der den ATP-Verbrauch der Neuronen reduziert und somit die Erholung nach dem metabolischen Stress begünstigt.

3.1.2 Anionen-Lücke

Die Ab- und Zunahme der $[K^+]_i$ erfordert einen intrazellulären Ausgleich des **Kationen/Anionen-Gleichgewichts** gemäß der Bewahrung der Elektroneutralität (Hansen, 1985). Den ermittelten Daten zufolge kompensiert der Na^+-Strom circa 50 % des K^+-Stroms. So muss es a) beim initialen K^+-Verlust einen zusätzlichen Anionen-Ausstrom oder Kationen-Einstrom und b) bei der verzögerten K^+-Aufnahme einen Anionen-Einstrom oder Kationen-Ausstrom geben.

Es wurde vermutet, dass die Konzentrationsänderungen des Anions **HCO_3^-** hierzu beitragen könnten. Daher wurde zusätzlich der extrazelluläre pH-Wert (pH_e) und pH_i experimentell bestimmt, um die intra- sowie extrazelluläre Konzentration von HCO_3^- ($[HCO_3^-]_{i/e}$) zu berechnen (nach Henderson-Hasselbalch sowie Kaila et al., 1990; Abbildung 18A). Daraus ergibt sich, dass die Verringerung von $[HCO_3^-]_i$ teilweise zur Wahrung der Elektroneutralität beiträgt, jedoch die Anionen-Lücke während der verzögerten K^+-Aufnahme sogar vergrößert (Abbildung 18B).

Neben HCO_3^- könnte **Cl^-** zur Anionen-Lücke beitragen. Des Weiteren ist der Cl^--Strom über die Membran mit der Transmembranbewegung von Wasser gekoppelt und führt somit zum Anschwellen von Astrozyten unter ischämischen Bedingungen (Kimelberg, 2005; Risher et al., 2010). Eine vorausgegangene Studie konnte mithilfe Fluoreszenz-Lebensdauer-Imaging zeigen, dass die Änderungen der $[Cl^-]_i$ infolge einer 2- oder 5-minütigen, chemisch-induzierten Ischämie minimal sind (Engels et al., 2021). Jedoch wurden hier nur die Konzentrationsänderungen kurz nach der Behandlung untersucht. So könnte es 6 min nach der Reperfusion zu einem verstärkten Cl^--Einstrom und gleichzeitig zu einem Anschwellen der Astrozyten kommen.

Eine solche Anionen-Lücke wurde auch bereits in vorherigen Studien unter ischämischen Bedingungen entdeckt (Kraig and Nicholson, 1978; Walz and Mukerji, 1988; Leis et al., 2005; Windmüller et al., 2005; Hyzinski-García et al., 2014). Diese vermuteten zusätzlich die Beteiligung von anionischen Osmolyten wie Glutamat oder Aspartat.

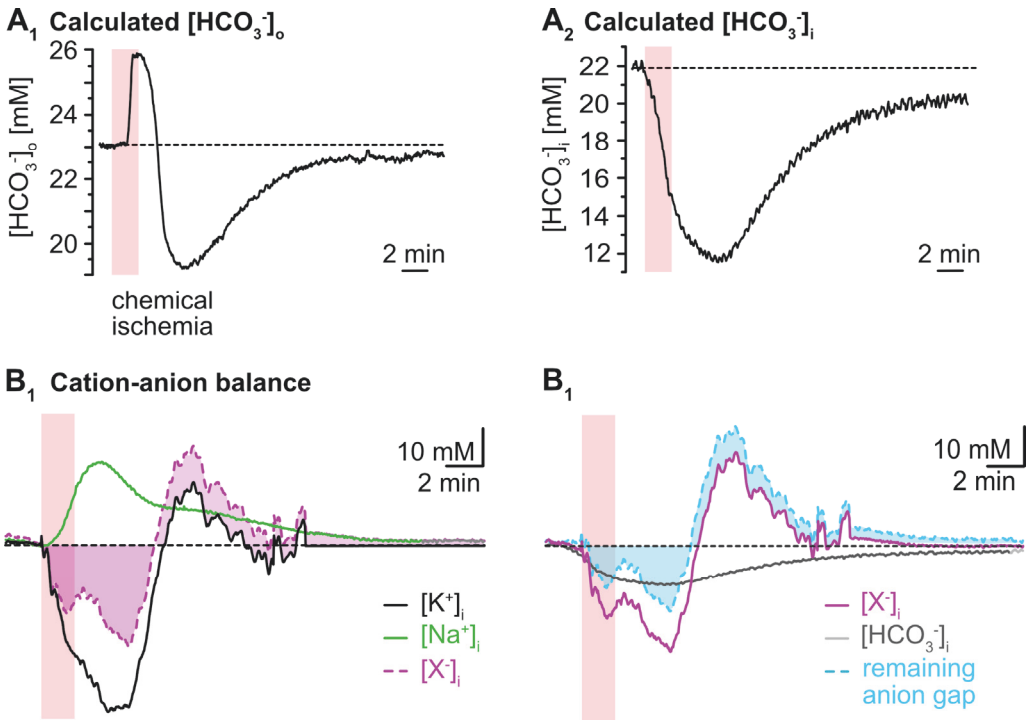

Abbildung 18. Astrozytäre Anionen-Lücke während der chemischen Induktion einer Ischämie. A) Berechnete Verläufe von $[HCO_3^-]_e$ und $[HCO_3^-]_i$. **B)** Subtraktion der gemittelten Kurve von $[K^+]_i$ (schwarz) und $[Na^+]_i$ (grün) während chemisch-induzierter Ischämie zeigt eine biphasische Anionen-Lücke (magenta; B_1). Weitere Subtraktion von $[HCO_3^-]_i$ (schwarz) verringert die Anionen-Lücke in der anfänglichen Phase, wobei sie in der Erholungsphase vergrößert wird (cyan; B_2). Modifiziert mit Genehmigung aus Eitelmann et al., 2022.

3.2 Schnelle Veränderung der astrozytären Kopplung

Astrozyten erfahren somit unter akutem metabolischem Stress eine Störung ihrer K^+-Homöostase. Jede weitere depolarisierende Infarktwelle führt folglich zu einer zusätzlichen Belastung der Zellen und zu einer höheren Chance von irreversiblen Schäden (Mies et al., 1993; Dijkhuizen et al., 1999; Shin et al., 2006). Somit ist es essenziell herauszufinden, welche Parameter die Weiterleitung solcher schädlichen Faktoren beeinflussen. Vorausgegangene Studien konnten zeigen, dass die astrozytäre Gap Junction-Kopplung sensitiv auf anhaltenden Energiemangel reagiert. So konnte in kultivierten Astrozyten gezeigt werden, dass eine 16-stündige Inhibition der oxidativen Phosphorylierung, und damit einhergehend eine Reduzierung des intrazellulären ATPs, zu einer starken Reduktion der Tracer-Diffusion zwischen Gap Junction-gekoppelten Zellen führt (Vera et al., 1996). Ähnlich hierzu zeigten auch hippokampale Astrozyten in Akutschnitten eine beeinträchtigte Tracer-Diffusion nach 30-minütiger Unterversorgung mit Glukose (Lee et al., 2016). Die hierbei verwendeten Protokolle ahmen jedoch hauptsächlich den anhaltenden Zusammenbruch des Energiestoffwechsels der ischämischen Kernregion nach (Moskowitz et al., 2010; van Putten et al., 2021). Darüber hinaus erfahren Astrozyten

hierbei einen Anstieg des pH_i und der $[Ca^{2+}]_i$ – beides Modulatoren der astrozytären Kopplung (Giaume et al., 2021).

In der folgenden Studie untersuchte ich, ob sich die Kopplungsstärke der Astrozyten auch unter kurzzeitigem Energiemangel verändert (Eitelmann et al., eingereicht*).

3.2.1 Isopotenzialität von neokortikalen Astrozyten

Zur Bestimmung der astrozytären Kopplung kann wie bereits beschrieben ein gepatchter Astrozyt mit einem Tracer beladen werden, was in der Regel eine gute Methode zur Visualisierung von Astrozyten-Netzwerken darstellt. Hierbei werden die Astrozyten jedoch für mindestens 10 min gefüllt und zu einem definierten Zeitpunkt aufgenommen bzw. fixiert, was eine zeitliche Auflösung und damit eine dynamische Beobachtung der Kopplung nicht zulässt. Da das Ziel dieser Studie die dynamische Untersuchung von Veränderungen der Gap Junction-Kopplung im niedrigen Minutenbereich war, wurde ein rein elektrophysiologischen Ansatz genutzt (Kiyoshi et al., 2018; Ma et al., 2016; Stephan et al., 2021). Im Speziellen wurde eine Patch-Clamp-basierte Technik verwendet, welche auf der Isopotenzialität von astrozytären Synzytien beruht (Abbildung 19). Hierbei wird eine K^+-freie Pipetten-Lösung (0 mM K^+) genutzt und die Diffusion innerhalb des Synzytiums gemessen. Dafür wird zunächst ein GΩ-*seal* erzeugt und die Zelle im *current clamp*-Modus abgeleitet. Der anschließende Durchbruch des Patches führt zu einem anfänglichen Abfall von E_M. Dieser Wert spiegelt das E_M unter Ruhebedingungen der gepatchten Astrozyten wider. Anschließend führt die Dialyse von 0 mM K^+ zu einer Depolarisation von E_M. Je stärker E_M depolarisiert ist, desto geringer ist die Kopplungsstärke und umgekehrt.

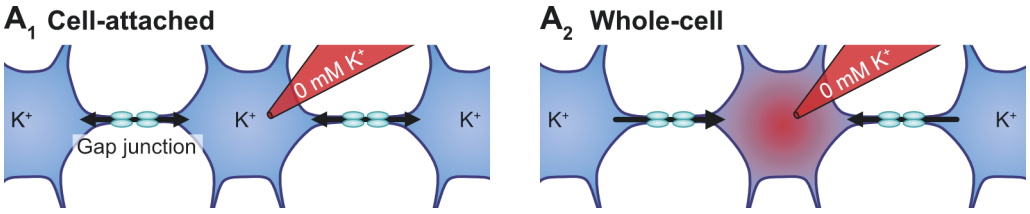

Abbildung 19. Prinzip der Isopotenzialitäts-Messungen zur Bestimmung der Gap Junction-Kopplung. Schematische Darstellung der Dialyse eines Gap Junction-gekoppelten Astrozyten mit einer K^+-freien Pipetten-Lösung (0 mM K^+). Hierbei wird die Veränderung der $[K^+]_i$ des gepatchten Astrozyten in Abhängigkeit der Kopplungsstärke Wgepuffert. In einem Modifiziert mit Genehmigung aus Eitelmann et al., eingereicht.

*Eitelmann, S., Everaerts, K., Petersilie, L., Rose, C. R. & Stephan, J. *Ca^{2+}-dependent rapid uncoupling of astrocytes upon brief metabolic stress.* Eingereicht bei Front Cell Neurosci im Januar 2023.

So wurde im ersten Schritt die Isopotenzialität von Astrozyten des somatosensorischen Neokortex (Schicht II/III) aus murinen Akutschnitten der Maus im Alter von 14-21 postnatalen Tagen unter physiologischen Bedingungen gemessen. Hierbei konnte gezeigt werden, dass neokortikale Astrozyten ein initiales E_M von circa -87 mV aufweisen (Abbildung 20A$_1$). Dies entspricht dem klassisch hochnegativem E_M der Astrozyten (Eitelmann et al., 2022). Die anschließende Dialyse mit 0 mM K^+ ergibt eine Depolarisation zu rund -80 mV. Um die Kopplung mit anderen Gap Junction-gekoppelten Zellen zu bestätigen, wurden die gepatchten Astrozyten zusätzlich mit dem Tracer Neurobiotin gefüllt. Daraus ergibt sich, dass ein Astrozyt, der nach Dialyse mit 0 mM K^+ ein E_M von -80 mV aufweist, mit rund 11 Nachbarn gekoppelt ist (Abbildung 20A$_2$). Dies bestätigt den Trend einer Studie, die für hippokampale Astrozyten eine Kopplung mit circa 8 Nachbarn eine Depolarisation zu -74 mV ermitteln konnte (Ma et al., 2016; Kiyoshi et al., 2018). Analog wurde die Isopotenzialität von Astrozyten unter Verwendung des Gap Junction-Blockers Carbenoxolon (CBX) geprüft. Hierbei depolarisierte das astrozytäre E_M gegen Null (Abbildung 20B$_1$). Zusätzlich wurde mithilfe der Tracer-Beladung die entkoppelnde Wirkung von CBX bestätigt (Abbildung 20B$_2$).

Daraus ergibt sich, dass die neokortikalen, Gap Junction-gekoppelten Astrozyten die Dialyse mit 0 mM K^+ kompensieren können und somit die Isopotenzialität innerhalb des Synzytiums wahren.

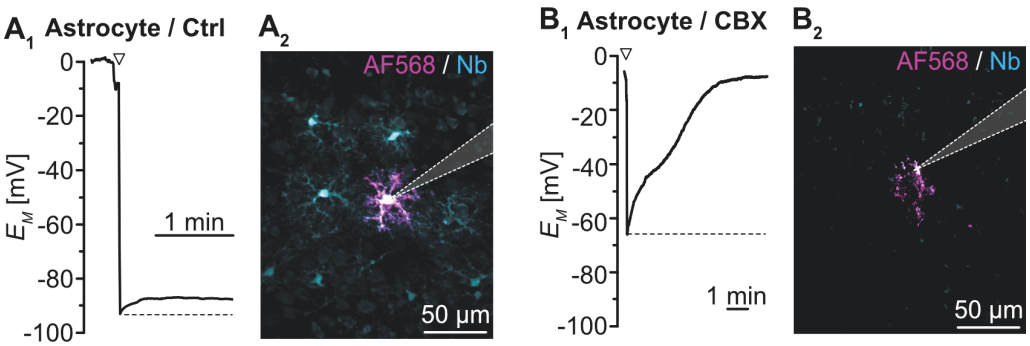

Abbildung 20. Isopotenzialität kortikaler Astrozyten. A) Messung der Isopotenzialität von Gap Junction-gekoppelten Astrozyten. Dialyse mit K^+-freier Pipetten-Lösung wird durch gekoppelte Zellen gepuffert. Die Öffnung des *patches* ist mit einem offenen Dreieck angezeigt. **B)** Messung der Isopotenzialität von ungekoppelten Astrozyten. In einem einzelnen Astrozyten ersetzt die K^+-freie Pipetten-Lösung den endogenen K^+-Gehalt, was zu einer Depolarisation von E_M in Richtung Null führt. Modifiziert mit Genehmigung aus Eitelmann et al., eingereicht.

3.2.2 Schnelle Reduktion der Kopplungsstärke

Mit der Erkenntnis, dass die Messungen der Isopotenzialität eine effiziente Methode zur Analyse der Gap Junction-Kopplung neokortikaler Astrozyten darstellen, wurden die

Effekte auf die Kopplung infolge von kurzzeitigem Energiemangel untersucht. Hierfür wurde das zuvor beschriebene Protokoll zur 2-minütigen chemischen Induktion einer Ischämie verwendet.

Aus der vorangegangenen Studie geht hervor, dass dieses Protokoll zu einer Depolarisation der astrozytären Membran führt (Eitelmann et al., 2022). So stellt diese den Grundwert der Isopotentialitäts-Messungen dar. Daher wurde zunächst die Depolarisation mittels *cell attached*-Messungen bestimmt. Diese erlauben es, ohne Effekt der Pipetten-Lösung E_M zu bestimmen. Daraus ergibt sich, dass die chemisch-induzierte Ischämie zu einer Depolarisation von -87 mV auf -73 mV führt (Abbildung 21A,C_1). Somit stellt letzteres das initiale E_M für Messungen der Isopotenzialität während chemischer Ischämie dar.

Die Messungen der Isopotenzialität zeigen eine schnelle Depolarisation der Astrozyten auf -45 mV innerhalb von 14 s (Abbildung 21B, C_2). Dieses E_M ist signifikant größer als das E_M der *cell attached*-Messungen, was bedeutet, dass die beobachtete Depolarisation der Isopotentialitäts-Messungen eine Reduktion der Isopotentialität des Synzytiums und somit eine Verringerung der Kopplungsstärke zeigt (Abbildung 21C_1).

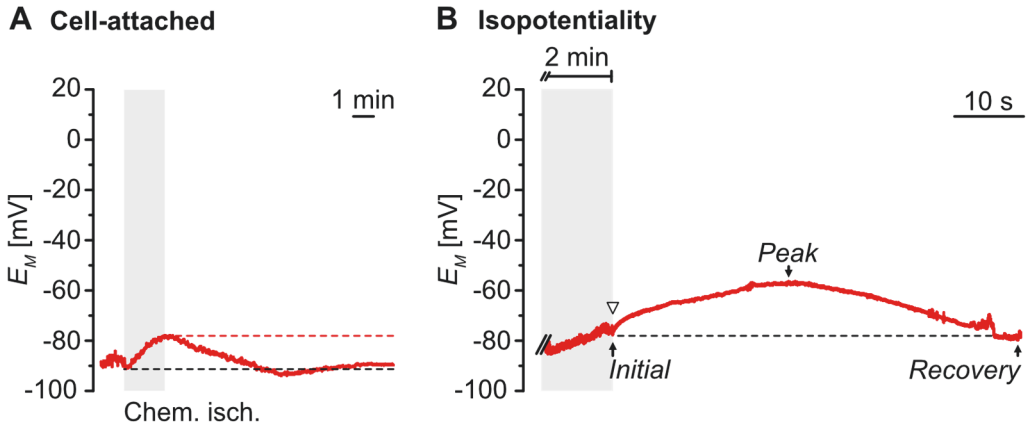

Abbildung 21. Schnelle Entkopplung neokortikaler Astrozyten während kurzzeitiger, chemischer Ischämie. A) *Cell-Attached*(CA)-Messungen von Astrozyten des somatosensorischen Kortex Schicht II/III während 2-minütiger, chemischer Induktion einer Ischämie. **B)** Messungen der Isopotenzialität. Die Änderungen in E_M der Isopotentalitäts-Messungen infolge des kurzzeitigen Energiemangels sind größer als die Änderungen im *cell-attached*-Modus. Die offenen Dreiecke weisen auf den Zeitpunkt der Öffnung des Patches hin. Die rote gestrichelte Linie zeigt die maximale Depolarisation durch Induktion der chemischen Ischämie an. Die schwarzen gestrichelten Linien zeigen die initialen Werte von E_M an. Modifiziert mit Genehmigung aus Eitelmann et al., eingereicht.

Hiermit konnten erstmals schnelle Änderungen der Gap Junction-Kopplung von Astrozyten unter pathophysiologischen Bedingungen dynamisch aufgenommen werden. Diese

Ergebnisse zeigen, dass selbst kurzzeitiger metabolischer Stress zu einer schnellen Reduktion der Kopplungsstärke in neokortikalen Astrozyten führt.

3.2.3 Ca^{2+}-abhängige Verringerung der Kopplung

Kurzzeitiger, metabolischer Stress führt zu einer intrazellulären Ansäuerung und einer Erhöhung der $[Ca^{2+}]_i$ (Dreier, 2011; Pietrobon and Moskowitz, 2014; Gerkau et al., 2018). Diese Änderungen des intrazellulären Milieus führen bekanntermaßen zu einer Reduzierung von g_j (Giaume et al., 2021). Daher wurde vermutet, dass die zuvor beobachtete rapide Entkopplung in einem Teil der Astrozyten auf diese beiden Parameter zurückzuführen ist.

Deshalb wurde zunächst die pH-Sensitivität der Gap Junction-Kopplung unter kurzzeitigem metabolischem Stress geprüft. Um eine intrazelluläre Ansäuerung hervorzurufen, wurde der Schnitt mit einer ACSF perfundiert, die eine niedrige $[HCO_3^-]_e$ aufweist (nach Wallraff et al., 2006). Eine 2-minütige Perfusion dieser modifizierten ACSF führt zu der gleichen intrazellulären Ansäuerung (0.26 pH Einheiten) wie die zuvor verwendete chemische Ischämie. Es konnte gezeigt werden, dass diese intrazelluläre Ansäuerung von 0.26 pH Einheiten – ähnlich der Ansäuerung während der chemisch-induzierten Ischämie – zu einer Depolarisation auf -77 mV führt (Abbildung 22A). Dies bedeutet, dass diese Ansäuerung nicht ausreichend ist um die Astrozyten zu entkoppeln. Dahingegen führt eine Erhöhung der Perfusionsdauer auf 5 min und somit eine Verstärkung der Ansäuerung auf 0.45 pH Einheiten zu einer Depolarisation auf -55 mV und somit einer deutlichen Reduktion der Gap Junction-Kopplung (Abbildung 22B). Dies bestätigt, dass eine intrazelluläre Ansäuerung ab einem ausreichenden Wert zu einer Verringerung der Kopplung führen kann. Daraus lässt sich schließen, dass die Verringerung des pH_i während des kurzzeitigen metabolischen Stresses nicht für die Entkopplung der Astrozyten unter den untersuchten Bedingungen verantwortlich ist.

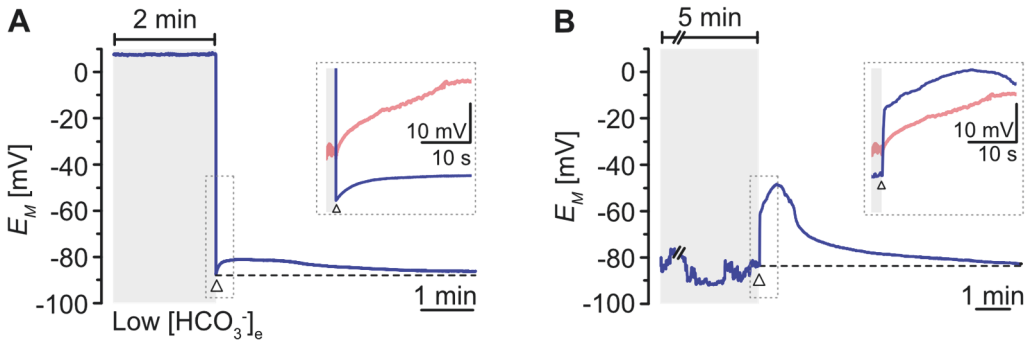

Abbildung 22. pH$_i$-Sensitivität der Isopotentialität neokortikaler Astrozyten. Messungen der Isopotentialität nach Perfusion mit ACSF mit niedrigem [HCO_3^-]$_e$ (blau) für 2 Minuten (A) und für 5 min (B). Die Einschübe zeigen die jeweiligen Messungen im Vergleich zur mittleren Spur der chemisch-induzierten Ischämie (hellrot). Die offenen Dreiecke weisen auf den Zeitpunkt der Öffnung des Patches hin. Die schwarzen gestrichelten Linien zeigen die initialen Werte von E_M an. Modifiziert mit Genehmigung aus Eitelmann et al., eingereicht.

Anschließend wurde getestet, ob eine Änderung in der $[Ca^{2+}]_i$ die beobachtete Reduktion der astrozytären Kopplung hervorrufen könnte. Zuerst wurde die $[Ca^{2+}]$ in der ACSF minimiert (0 $[Ca^{2+}]_e$) um den Ca^{2+}-Einstrom während der chemisch-induzierten abzusenken. Dies ergibt ein maximales E_M von rund -67 mV, welche nicht signifikant unterschiedlich ist zur Depolarisation, die im *cell-attached*-Modus gemessen wurde (Abbildung 23A; vgl. Abbildung 21A). Daraus ergibt sich, dass die Verminderung von $[Ca^{2+}]_e$ die Entkopplung verhindert.

Als nächstes wurden Inhibitoren verwendet, die den Ca^{2+}-Einstrom minimieren (Blocker für NCX (KB-R), NMDA-Rezeptoren (AP5) und TRPV4-Kanäle (HC); Abbildung 23B). Auch hier konnte mit einer Depolarisation auf -68 mV keine Entkopplung festgestellt werden.

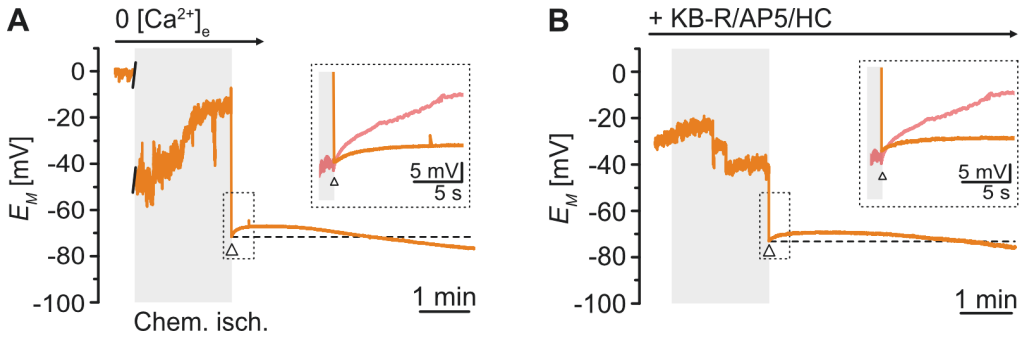

Abbildung 23. Ca^{2+}-abhängige Veränderung der astrozytären Gap Junction-Kopplung während kurzzeitigem Energiemangel. Messungen der Isopotenzialität während der Perfusion mit ACSF, die kein Ca^{2+} enthält (0 Ca^{2+}; A) und mit ACSF, die zusätzlich Inhibitoren des Ca^{2+}-Einstroms enthält (Blocker für NCX (KB-R), NMDA-Rezeptoren (AP5) und TRPV4-Kanäle (HC); B). Die Einschübe zeigen die jeweiligen Messungen im Vergleich zur mittleren Spur der chemisch-induzierten Ischämie (hellrot). Die offenen Dreiecke weisen auf den Zeitpunkt der Öffnung des Patches hin. Die schwarzen gestrichelten Linien zeigen die initialen Werte von E_M an. Modifiziert mit Genehmigung aus Eitelmann et al., eingereicht.

Dies deutet darauf hin, dass die Erhöhung der $[Ca^{2+}]_i$ während kurzzeitigem, metabolischem Stress zu der Reduktion der Gap Junction-Kopplung führt.

3.3 Rolle von Astrozyten bei der Ausbreitung von ischämischen Schäden

In den vorgestellten Studien wurden die pathophysiologischen Veränderungen in der $[K^+]_i$ und der Gap Junction-Kopplung von Astrozyten während kurzzeitigem Energiemangel untersucht.

Zunächst konnte der komplette zeitliche Verlauf von $[K^+]_i$ bestimmt werden. Hierbei wurde für die $[K^+]_i$ neokortikaler Astrozyten ein Wert von 146 mM berechnet. Darüber hinaus wurde eine zusätzliche Aufnahme von K^+ im späteren Zeitverlauf entdeckt, die zu einer Verringerung der neuronalen Aktivität führen kann. Zusätzlich ergab sich eine Diskrepanz des Kationen/Anionen-Gleichgewichts, welches teilweise durch den Strom von HCO_3^- über die Membran zustande kommt. Darüber hinaus könnte es neben der Aufnahme von anionischen Osmolyten auch zu einem Einstrom von Cl^- kommen. Letzteres ist höchstwahrscheinlich mit einem verzögerten Anschwellen der Astrozyten verknüpft. Dies könnte einen neuroprotektiven Effekt mit sich bringen, der den ATP-Verbrauch der Neuronen reduziert und somit die Erholung nach dem metabolischen Stress begünstigt.

Des Weiteren wurden erstmals schnelle Veränderungen der Gap Junction-Kopplung in Astrozyten dynamisch gemessen. So wurde beobachtet, dass während einer kurzzeitigen chemischen Induktion einer Ischämie eine pH_i-insensitive, $[Ca^{2+}]_i$-abhängige Reduktion der Kopplungsstärke der Astrozyten erfolgt. In erster Linie ist solch eine Entkopplung zellprotektiv, da Astrozyten so keine metabolischen Stressfaktoren an die gekoppelten, gesunden Zellen weitergeben können. Entsprechend zeigten Studien, dass die bestehende Gap Junction-Kopplung zu einer Vergrößerung des ischämischen Kerns führt (Lin et al., 1998; Lauritzen et al., 2011). Darüber hinaus gibt es Hinweise darauf, dass eine Reduktion der Cx43-Expression vor gesteigertem Zelltod oder einer Expansion des Insults schützt (Warner et al., 1995; Rawanduzy et al., 1997; Frantseva et al., 2002). Dass eine Verminderung des $[Ca^{2+}]_i$-Anstiegs während einer Infarktwelle neuroprotektive Effekte hat, wird auch von einer jüngsten Studie unterstützt (Rakers and Petzold, 2017). Es gibt zusätzlich Hinweise darauf, dass eine Entkopplung den Transport der Infarktwellen erschwert oder sogar verhindert (Nedergaard et al., 1995; EbrahimAmini et al., 2021). Analog wurde gezeigt, dass die metabolische Inhibition einzelner Cx43-exprimierende Gliom-Zellen zum Zelltod der gekoppelten Nachbarn führt (Lin et al., 1998). Folglich könnte

die Reduktion der Gap Junction-Kopplung die benachbarten Astrozyten vor einem zusätzlichen Gap Junction-vermittelten $[Ca^{2+}]_i$-Anstieg schützen.

Zusammengefasst zeigt die vorliegende Arbeit, dass Astrozyten infolge eines kurzzeitigen Energiemangels – ähnlich zu der Situation während einer Infarktwelle in der Penumbra – eine verzögerte K^+-Aufnahme und eine Ca^{2+}-abhängige schnelle Reduktion der Gap Junction-Kopplung aufweisen. Dies könnte dazu beitragen, weitere Zellschäden, die durch erneutes Auftreten von Infarktwellen entstehen, zu reduzieren und somit die Ausbreitung des ischämischen Kerns zu limitieren.

4 Literaturverzeichnis

Abbott NJ (2002) Astrocyte–endothelial interactions and blood–brain barrier permeability. Journal of Anatomy 200:629-638.

Adelman WJ, Fitzhugh R (1975) Solutions of the Hodgkin-Huxley equations modified for potassium accumulation in a periaxonal space. In: Membranes, Ions, and Impulses, pp 11-28: Springer.

Anders S, Minge D, Griemsmann S, Herde MK, Steinhauser C, Henneberger C (2014) Spatial properties of astrocyte gap junction coupling in the rat hippocampus. Philos Trans R Soc Lond B Biol Sci 369:20130600.

Andriezen WL (1893) The Neuroglia Elements in the Human Brain. Br Med J 2:227-230.

Araque A, Parpura V, Sanzgiri RP, Haydon PG (1999) Tripartite synapses: glia, the unacknowledged partner. Trends Neurosci 22:208-215.

Astrup J, Siesjö BK, Symon L (1981) Thresholds in cerebral ischemia - the ischemic penumbra. Stroke 12:723-725.

Attwell D, Buchan AM, Charpak S, Lauritzen M, Macvicar BA, Newman EA (2010) Glial and neuronal control of brain blood flow. Nature 468:232-243.

Augustin V, Bold C, Wadle SL, Langer J, Jabs R, Philippot C, Weingarten DJ, Rose CR, Steinhauser C, Stephan J (2016) Functional anisotropic panglial networks in the lateral superior olive. Glia 64:1892-1911.

Azevedo FA, Carvalho LR, Grinberg LT, Farfel JM, Ferretti RE, Leite RE, Jacob Filho W, Lent R, Herculano-Houzel S (2009) Equal numbers of neuronal and nonneuronal cells make the human brain an isometrically scaled-up primate brain. J Comp Neurol 513:532-541.

Balestrino M, Somjen GG (1986) Chlorpromazine protects brain tissue in hypoxia by delaying spreading depression-mediated calcium influx. Brain Res 385:219-226.

Balestrino M, Aitken PG, Somjen GG (1986) The effects of moderate changes of extracellular K+ and Ca2+ on synaptic and neural function in the CA1 region of the hippocampal slice. Brain research 377:229-239.

Bambrick L, Kristian T, Fiskum G (2004) Astrocyte Mitochondrial Mechanisms of Ischemic Brain Injury and Neuroprotection. Neurochemical Research 29:601-608.

Barros LF, Deitmer JW (2010) Glucose and lactate supply to the synapse. Brain Res Rev 63:149-159.

Baumann N, Pham-Dinh D (2001) Biology of oligodendrocyte and myelin in the mammalian central nervous system. Physiol Rev 81:871-927.

Bellot-Saez A, Kékesi O, Morley JW, Buskila Y (2017) Astrocytic modulation of neuronal excitability through K+ spatial buffering. Neuroscience & Biobehavioral Reviews 77:87-97.

Bennett MVL, Barrio LC, Bargiello TA, Spray DC, Hertzberg E, Sáez JC (1991) Gap junctions: New tools, new answers, new questions. Neuron 6:305-320.

Berdichevsky E, Riveros N, Sánchez-Armáss S, Orrego F (1983) Kainate, N-methylaspartate and other excitatory amino acids increase calcium influx into rat brain cortex cells in vitro. Neuroscience Letters 36:75-80.

Bernardinelli Y, Muller D, Nikonenko I (2014a) Astrocyte-synapse structural plasticity. Neural Plast 2014:232105.

Bernardinelli Y, Randall J, Janett E, Nikonenko I, König S, Jones EV, Flores CE, Murai KK, Bochet CG, Holtmaat A, Muller D (2014b) Activity-dependent structural plasticity of perisynaptic astrocytic domains promotes excitatory synapse stability. Curr Biol 24:1679-1688.

Beyer EC, Paul DL, Goodenough DA (1990) Connexin family of gap junction proteins. J Membr Biol 116:187-194.

Binmöller FJ, Müller C (1992) Postnatal development of dye-coupling among astrocytes in rat visual cortex. Glia 6:127-137.
Bischof H et al. (2017) Novel genetically encoded fluorescent probes enable real-time detection of potassium in vitro and in vivo. Nat Commun 8:1422.
Bradbury MW, Kleeman CR (1967) Stability of the potassium content of cerebrospinal fluid and brain. Am J Physiol 213:519-528.
Breslin K, Wade JJ, Wong-Lin K, Harkin J, Flanagan B, Van Zalinge H, Hall S, Walker M, Verkhratsky A, McDaid L (2018) Potassium and sodium microdomains in thin astroglial processes: A computational model study. PLoS computational biology 14:e1006151.
Bruzzone R, Giaume C (1999) Connexins and information transfer through glia. Adv Exp Med Biol 468:321-337.
Bukauskas FF, Peracchia C (1997) Two distinct gating mechanisms in gap junction channels: CO2-sensitive and voltage-sensitive. Biophys J 72:2137-2142.
Bukauskas FF, Verselis VK (2004) Gap junction channel gating. Biochim Biophys Acta 1662:42-60.
Bunge RP (1968) Glial cells and the central myelin sheath. Physiol Rev 48:197-251.
Bushong EA, Martone ME, Ellisman MH (2002a) CCDB:1055, rattus norvegicus, protoplasmic astrocyte. In. CIL.
Bushong EA, Martone ME, Jones YZ, Ellisman MH (2002b) Protoplasmic astrocytes in CA1 stratum radiatum occupy separate anatomical domains. J Neurosci 22:183-192.
Butt AM, Kalsi A (2006) Inwardly rectifying potassium channels (Kir) in central nervous system glia: a special role for Kir4.1 in glial functions. J Cell Mol Med 10:33-44.
Chatton JY, Marquet P, Magistretti PJ (2000) A quantitative analysis of L-glutamate-regulated Na+ dynamics in mouse cortical astrocytes: implications for cellular bioenergetics. Eur J Neurosci 12:3843-3853.
Chever O, Dossi E, Pannasch U, Derangeon M, Rouach N (2016) Astroglial networks promote neuronal coordination. Sci Signal 9:ra6.
Choi DW (2020) Excitotoxicity: Still Hammering the Ischemic Brain in 2020. Front Neurosci 14:579953.
Claus L, Philippot C, Griemsmann S, Timmermann A, Jabs R, Henneberger C, Kettenmann H, Steinhauser C (2018) Barreloid Borders and Neuronal Activity Shape Panglial Gap Junction-Coupled Networks in the Mouse Thalamus. Cereb Cortex 28:213-222.
Clements JD, Lester RA, Tong G, Jahr CE, Westbrook GL (1992) The time course of glutamate in the synaptic cleft. Science 258:1498-1501.
Cornell-Bell AH, Finkbeiner SM, Cooper MS, Smith SJ (1990) Glutamate induces calcium waves in cultured astrocytes: long-range glial signaling. Science 247:470-473.
Crow JM, Atkinson MM, Johnson RG (1994) Micromolar levels of intracellular calcium reduce gap junctional permeability in lens cultures. Investigative Ophthalmology & Visual Science 35:3332-3341.
Curtis DR, Phillis JW, Watkins JC (1959) Chemical excitation of spinal neurones. Nature 183:611-612.
D'Ambrosio R, Gordon DS, Winn HR (2002) Differential role of KIR channel and Na(+)/K(+)-pump in the regulation of extracellular K(+) in rat hippocampus. J Neurophysiol 87:87-102.
Dahl E, Manthey D, Chen Y, Schwarz HJ, Chang YS, Lalley PA, Nicholson BJ, Willecke K (1996) Molecular cloning and functional expression of mouse connexin-30,a gap junction gene highly expressed in adult brain and skin. J Biol Chem 271:17903-17910.
Daikhin Y, Yudkoff M (2000) Compartmentation of brain glutamate metabolism in neurons and glia. J Nutr 130:1026s-1031s.
Deitmer JW, Rose CR (1996) pH regulation and proton signalling by glial cells. Prog Neurobiol 48:73-103.

Dekker LR, Fiolet JW, VanBavel E, Coronel R, Opthof T, Spaan JA, Janse MJ (1996) Intracellular Ca2+, intercellular electrical coupling, and mechanical activity in ischemic rabbit papillary muscle: effects of preconditioning and metabolic blockade. Circulation research 79:237-246.

Dermietzel R, Spray DC (1993) Gap junctions in the brain: where, what type, how many and why? Trends Neurosci 16:186-192.

Dermietzel R, Traub O, Hwang TK, Beyer E, Bennett MV, Spray DC, Willecke K (1989) Differential expression of three gap junction proteins in developing and mature brain tissues. Proc Natl Acad Sci U S A 86:10148-10152.

Dheen ST, Hao AJ, Ng YK, Ling EA (2002) Regulatory Factors and Functions of Microglia during Development. Neuroembryology and Aging 1:105-112.

Dijkhuizen RM, Beekwilder JP, van der Worp HB, Berkelbach van der Sprenkel JW, Tulleken KA, Nicolay K (1999) Correlation between tissue depolarizations and damage in focal ischemic rat brain. Brain Res 840:194-205.

Dirnagl U, Iadecola C, Moskowitz MA (1999) Pathobiology of ischaemic stroke: an integrated view. Trends Neurosci 22:391-397.

Dreier JP (2011) The role of spreading depression, spreading depolarization and spreading ischemia in neurological disease. Nat Med 17:439-447.

Dreier JP, Reiffurth C (2015) The stroke-migraine depolarization continuum. Neuron 86:902-922.

Du Y, Ma B, Kiyoshi CM, Alford CC, Wang W, Zhou M (2015) Freshly dissociated mature hippocampal astrocytes exhibit passive membrane conductance and low membrane resistance similarly to syncytial coupled astrocytes. Journal of Neurophysiology 113:3744-3750.

Du Y, Kiyoshi CM, Wang Q, Wang W, Ma B, Alford CC, Zhong S, Wan Q, Chen H, Lloyd EE (2016) Genetic deletion of TREK-1 or TWIK-1/TREK-1 potassium channels does not alter the basic electrophysiological properties of mature hippocampal astrocytes in situ. Frontiers in cellular neuroscience 10:13.

Du Y, Wang W, Lutton AD, Kiyoshi CM, Ma B, Taylor AT, Olesik JW, McTigue DM, Askwith CC, Zhou M (2018) Dissipation of transmembrane potassium gradient is the main cause of cerebral ischemia-induced depolarization in astrocytes and neurons. Exp Neurol 303:1-11.

Duffy HS, Sorgen PL, Girvin ME, O'Donnell P, Coombs W, Taffet SM, Delmar M, Spray DC (2002) pH-dependent intramolecular binding and structure involving Cx43 cytoplasmic domains. J Biol Chem 277:36706-36714.

Ebihara L (2003) Physiology and biophysics of hemi-gap-junctional channels expressed in Xenopus oocytes. Acta Physiologica Scandinavica 179:5-8.

EbrahimAmini A, Bazzigaluppi P, Aquilino MS, Stefanovic B, Carlen PL (2021) Neocortical in vivo focal and spreading potassium responses and the influence of astrocytic gap junctional coupling. Neurobiol Dis 147:105160.

Eitelmann S, Hirtz JJ, Stephan J (2019) A Vector-Based Method to Analyze the Topography of Glial Networks. Int J Mol Sci 20.

Eitelmann S, Petersilie L, Rose CR, Stephan J (2020) Altered Gap Junction Network Topography in Mouse Models for Human Hereditary Deafness. Int J Mol Sci 21.

Eitelmann S, Stephan J, Everaerts K, Durry S, Pape N, Gerkau NJ, Rose CR (2022) Changes in Astroglial K(+) upon Brief Periods of Energy Deprivation in the Mouse Neocortex. Int J Mol Sci 23.

Engels M, Kalia M, Rahmati S, Petersilie L, Kovermann P, van Putten MJ, Rose CR, Meijer HG, Gensch T, Fahlke C (2021) Glial chloride homeostasis under transient ischemic stress. Frontiers in cellular neuroscience:365.

Enkvist MO, McCarthy KD (1994) Astroglial gap junction communication is increased by treatment with either glutamate or high K+ concentration. J Neurochem 62:489-495.
Erecińska M, Silver IA (1994) Ions and energy in mammalian brain. Prog Neurobiol 43:37-71.
Erulkar S, Weight F (1977) Extracellular potassium and trasmitter release at the giant synapse of squid. The Journal of Physiology 266:209-218.
Farber K, Kettenmann H (2005) Physiology of microglial cells. Brain Res Brain Res Rev 48:133-143.
Foo LC, Allen NJ, Bushong EA, Ventura PB, Chung WS, Zhou L, Cahoy JD, Daneman R, Zong H, Ellisman MH, Barres BA (2011) Development of a method for the purification and culture of rodent astrocytes. Neuron 71:799-811.
Frantseva MV, Kokarovtseva L, Perez Velazquez JL (2002) Ischemia-induced brain damage depends on specific gap-junctional coupling. J Cereb Blood Flow Metab 22:453-462.
Friauf E, Krächan EG, Müller NI (2019) Lateral superior olive. The Oxford handbook of the auditory brainstem:329.
Gage P, Quastel D (1965) Dual effect of potassium on transmitter release. Nature 206:625-626.
Garciarena CD, Malik A, Swietach P, Moreno AP, Vaughan-Jones RD (2018) Distinct moieties underlie biphasic H(+) gating of connexin43 channels, producing a pH optimum for intercellular communication. Faseb j 32:1969-1981.
Genoud C, Quairiaux C, Steiner P, Hirling H, Welker E, Knott GW (2006) Plasticity of astrocytic coverage and glutamate transporter expression in adult mouse cortex. PLoS Biol 4:e343.
Gerkau NJ, Rakers C, Durry S, Petzold GC, Rose CR (2018) Reverse NCX Attenuates Cellular Sodium Loading in Metabolically Compromised Cortex. Cereb Cortex 28:4264-4280.
Giaume C, Tabernero A, Medina JM (1997) Metabolic trafficking through astrocytic gap junctions. Glia 21:114-123.
Giaume C, Naus CC, Saez JC, Leybaert L (2021) Glial Connexins and Pannexins in the Healthy and Diseased Brain. Physiol Rev 101:93-145.
Giaume C, Koulakoff A, Roux L, Holcman D, Rouach N (2010) Astroglial networks: a step further in neuroglial and gliovascular interactions. Nat Rev Neurosci 11:87-99.
Giffard RG, Swanson RA (2005) Ischemia-induced programmed cell death in astrocytes. Glia 50:299-306.
Gordon GRJ, Mulligan SJ, MacVicar BA (2007) Astrocyte control of the cerebrovasculature. Glia 55:1214-1221.
Griemsmann S, Hoft SP, Bedner P, Zhang J, von Staden E, Beinhauer A, Degen J, Dublin P, Cope DW, Richter N, Crunelli V, Jabs R, Willecke K, Theis M, Seifert G, Kettenmann H, Steinhauser C (2015) Characterization of Panglial Gap Junction Networks in the Thalamus, Neocortex, and Hippocampus Reveals a Unique Population of Glial Cells. Cereb Cortex 25:3420-3433.
Haber M, Murai KK (2006) Reshaping neuron-glial communication at hippocampal synapses. Neuron Glia Biol 2:59-66.
Halassa MM, Fellin T, Haydon PG (2007) The tripartite synapse: roles for gliotransmission in health and disease. Trends Mol Med 13:54-63.
Hanani M, Spray DC (2020) Emerging importance of satellite glia in nervous system function and dysfunction. Nature Reviews Neuroscience 21:485-498.
Hansen AJ (1985) Effect of anoxia on ion distribution in the brain. Physiol Rev 65:101-148.
Harris AL (2001) Emerging issues of connexin channels: biophysics fills the gap. Q Rev Biophys 34:325-472.

Hartings JA, Rolli ML, Lu XC, Tortella FC (2003) Delayed secondary phase of peri-infarct depolarizations after focal cerebral ischemia: relation to infarct growth and neuroprotection. J Neurosci 23:11602-11610.

Heinemann U, Lux HD (1977) Ceiling of stimulus induced rises in extracellular potassium concentration in the cerebral cortex of cat. Brain Res 120:231-249.

Heiss WD, Graf R (1994) The ischemic penumbra. Curr Opin Neurol 7:11-19.

Hertz L (1965) Possible role of neuroglia: a potassium-mediated neuronal--neuroglial--neuronal impulse transmission system. Nature 206:1091-1094.

Hertz L, Dringen R, Schousboe A, Robinson SR (1999) Astrocytes: glutamate producers for neurons. J Neurosci Res 57:417-428.

Hertz L, Song D, Xu J, Peng L, Gibbs ME (2015) Role of the astrocytic Na+, K+-ATPase in K+ homeostasis in brain: K+ uptake, signaling pathways and substrate utilization. Neurochemical research 40:2505-2516.

Hirtz JJ, Braun N, Griesemer D, Hannes C, Janz K, Lohrke S, Muller B, Friauf E (2012) Synaptic refinement of an inhibitory topographic map in the auditory brainstem requires functional Cav1.3 calcium channels. J Neurosci 32:14602-14616.

Horikawa K, Armstrong WE (1988) A versatile means of intracellular labeling: injection of biocytin and its detection with avidin conjugates. Journal of Neuroscience Methods 25:1-11.

Hossmann KA (1994) Glutamate-mediated injury in focal cerebral ischemia: the excitotoxin hypothesis revised. Brain Pathol 4:23-36.

Houades V, Koulakoff A, Ezan P, Seif I, Giaume C (2008) Gap junction-mediated astrocytic networks in the mouse barrel cortex. J Neurosci 28:5207-5217.

Houades V, Rouach N, Ezan P, Kirchhoff F, Koulakoff A, Giaume C (2006) Shapes of astrocyte networks in the juvenile brain. Neuron Glia Biol 2:3-14.

Huang Q, Zhou D, DiFiglia M (1992) Neurobiotin™, a useful neuroanatomical tracer for in vivo anterograde, retrograde and transneuronal tract-tracing and for in vitro labeling of neurons. Journal of Neuroscience Methods 41:31-43.

Hyzinski-García MC, Rudkouskaya A, Mongin AA (2014) LRRC8A protein is indispensable for swelling-activated and ATP-induced release of excitatory amino acids in rat astrocytes. The Journal of physiology 592:4855-4862.

Iadecola C (2017) The Neurovascular Unit Coming of Age: A Journey through Neurovascular Coupling in Health and Disease. Neuron 96:17-42.

Jennett WB, Harper AM, Gillespie F (1966) Measurement of regional cerebral blood-flow during carotid ligation. The Lancet 288:1162-1163.

Kafitz KW, Meier SD, Stephan J, Rose CR (2008) Developmental profile and properties of sulforhodamine 101--Labeled glial cells in acute brain slices of rat hippocampus. J Neurosci Methods 169:84-92.

Kaila K, Saarikoski J, Voipio J (1990) Mechanism of action of GABA on intracellular pH and on surface pH in crayfish muscle fibres. The Journal of Physiology 427:241-260.

Kalia M, Meijer HGE, van Gils SA, van Putten M, Rose CR (2021) Ion dynamics at the energy-deprived tripartite synapse. PLoS Comput Biol 17:e1009019.

Kandel ER, Koester JD, Mack SH, Siegelbaum SA (2021) Principles of Neural Science, Sixth Edition: McGraw-Hill Education.

Kandler K, Clause A, Noh J (2009) Tonotopic reorganization of developing auditory brainstem circuits. Nat Neurosci 12:711-717.

Katzman R (1976) Maintenance of a constant brain extracellular potassium. Fed Proc 35:1244-1247.

Kawata M, Sano Y, Inenaga K, Yamashita H (1983) Immunohistochemical identification of Lucifer Yellow-labeled neurons in the rat supraoptic nucleus. Histochemistry 78:21-26.

Kettenmann H, Backus KH, Schachner M (1984) Aspartate, glutamate and gamma-aminobutyric acid depolarize cultured astrocytes. Neurosci Lett 52:25-29.
Kimelberg HK (2005) Astrocytic swelling in cerebral ischemia as a possible cause of injury and target for therapy. Glia 50:389-397.
Kimelberg HK, Bowman C, Biddlecome S, Bourke RS (1979) Cation transport and membrane potential properties of primary astroglial cultures from neonatal rat brains. Brain Research 177:533-550.
Kiyoshi CM, Du Y, Zhong S, Wang W, Taylor AT, Xiong B, Ma B, Terman D, Zhou M (2018) Syncytial isopotentiality: A system-wide electrical feature of astrocytic networks in the brain. Glia 66:2756-2769.
Koelliker A (1899) Handbuch der Gewebelehre des Menschen. Archiv für Entwicklungsmechanik der Organismen 9:319-319.
Kofuji P, Newman EA (2004) Potassium buffering in the central nervous system. Neuroscience 129:1045-1056.
Korogod N, Petersen CCH, Knott GW (2015) Ultrastructural analysis of adult mouse neocortex comparing aldehyde perfusion with cryo fixation. eLife 4:e05793.
Kraig RP, Nicholson C (1978) Extracellular ionic variations during spreading depression. Neuroscience 3:1045-1059.
Kreisman NR, Smith ML (1993) Potassium-induced changes in excitability in the hippocampal CA1 region of immature and adult rats. Developmental brain research 76:67-73.
Kristián T, Siesjö BK (1998) Calcium in ischemic cell death. Stroke 29:705-718.
Kunzelmann P, Schroder W, Traub O, Steinhauser C, Dermietzel R, Willecke K (1999) Late onset and increasing expression of the gap junction protein connexin30 in adult murine brain and long-term cultured astrocytes. Glia 25:111-119.
Kvamme E, Roberg B, Torgner IA (2000) Phosphate-activated glutaminase and mitochondrial glutamine transport in the brain. Neurochem Res 25:1407-1419.
Laird DW (2006) Life cycle of connexins in health and disease. Biochem J 394:527-543.
Lampe PD, Lau AF (2000) Regulation of Gap Junctions by Phosphorylation of Connexins. Archives of Biochemistry and Biophysics 384:205-215.
Larsen BR, Stoica A, MacAulay N (2019) Developmental maturation of activity-induced K(+) and pH transients and the associated extracellular space dynamics in the rat hippocampus. J Physiol 597:583-597.
Lauritzen M, Dreier JP, Fabricius M, Hartings JA, Graf R, Strong AJ (2011) Clinical relevance of cortical spreading depression in neurological disorders: migraine, malignant stroke, subarachnoid and intracranial hemorrhage, and traumatic brain injury. J Cereb Blood Flow Metab 31:17-35.
Lee CY, Dallerac G, Ezan P, Anderova M, Rouach N (2016) Glucose Tightly Controls Morphological and Functional Properties of Astrocytes. Front Aging Neurosci 8:82.
Leis JA, Bekar LK, Walz W (2005) Potassium homeostasis in the ischemic brain. Glia 50:407-416.
Lerchundi R, Huang N, Rose CR (2020) Quantitative Imaging of Changes in Astrocytic and Neuronal Adenosine Triphosphate Using Two Different Variants of ATeam. Front Cell Neurosci 14:80.
Lerchundi R, Kafitz KW, Winkler U, Färfers M, Hirrlinger J, Rose CR (2019) FRET-based imaging of intracellular ATP in organotypic brain slices. J Neurosci Res 97:933-945.
Leybaert L, De Bock M, Van Moorhem M, Decrock E, De Vuyst E (2007) Neurobarrier coupling in the brain: adjusting glucose entry with demand. J Neurosci Res 85:3213-3220.
Lin JH, Weigel H, Cotrina ML, Liu S, Bueno E, Hansen AJ, Hansen TW, Goldman S, Nedergaard M (1998) Gap-junction-mediated propagation and amplification of cell injury. Nat Neurosci 1:494-500.

Livnah O, Bayer EA, Wilchek M, Sussman JL (1993) Three-dimensional structures of avidin and the avidin-biotin complex. Proc Natl Acad Sci U S A 90:5076-5080.

Lundgaard I, Osorio MJ, Kress BT, Sanggaard S, Nedergaard M (2014) White matter astrocytes in health and disease. Neuroscience 276:161-173.

Ma B, Xu G, Wang W, Enyeart JJ, Zhou M (2014) Dual patch voltage clamp study of low membrane resistance astrocytes in situ. Mol Brain 7:18.

Ma B, Buckalew R, Du Y, Kiyoshi CM, Alford CC, Wang W, McTigue DM, Enyeart JJ, Terman D, Zhou M (2016) Gap junction coupling confers isopotentiality on astrocyte syncytium. Glia 64:214-226.

Magistretti PJ, Pellerin L, Rothman DL, Shulman RG (1999) Energy on demand. Science 283:496-497.

Malenka RC, Kocsis JD, Ransom BR, Waxman SG (1981) Modulation of parallel fiber excitability by postsynaptically mediated changes in extracellular potassium. Science 214:339-341.

Manthey D, Banach K, Desplantez T, Lee CG, Kozak CA, Traub O, Weingart R, Willecke K (2001) Intracellular domains of mouse connexin26 and -30 affect diffusional and electrical properties of gap junction channels. J Membr Biol 181:137-148.

Márquez-Rosado L, Solan JL, Dunn CA, Norris RP, Lampe PD (2012) Connexin43 phosphorylation in brain, cardiac, endothelial and epithelial tissues. Biochim Biophys Acta 1818:1985-1992.

Maslarova A, Alam M, Reiffurth C, Lapilover E, Gorji A, Dreier JP (2011) Chronically epileptic human and rat neocortex display a similar resistance against spreading depolarization in vitro. Stroke 42:2917-2922.

Mathie A, Al-Moubarak E, Veale EL (2010) Gating of two pore domain potassium channels. J Physiol 588:3149-3156.

Mazel T, Richter F, Vargová L, Syková E (2002) Changes in extracellular space volume and geometry induced by cortical spreading depression in immature and adult rats. Physiol Res 51 Suppl 1:S85-93.

Medvedev N, Popov V, Henneberger C, Kraev I, Rusakov DA, Stewart MG (2014) Glia selectively approach synapses on thin dendritic spines. Philos Trans R Soc Lond B Biol Sci 369:20140047.

Mehta SL, Manhas N, Raghubir R (2007) Molecular targets in cerebral ischemia for developing novel therapeutics. Brain Res Rev 54:34-66.

Meyer J, Gerkau NJ, Kafitz KW, Patting M, Jolmes F, Henneberger C, Rose CR (2022) Rapid Fluorescence Lifetime Imaging Reveals That TRPV4 Channels Promote Dysregulation of Neuronal Na(+) in Ischemia. J Neurosci 42:552-566.

Mies G, Iijima T, Hossmann KA (1993) Correlation between peri-infarct DC shifts and ischaemic neuronal damage in rat. Neuroreport 4:709-711.

Morgello S, Uson RR, Schwartz EJ, Haber RS (1995) The human blood-brain barrier glucose transporter (GLUT1) is a glucose transporter of gray matter astrocytes. Glia 14:43-54.

Mori T, Tateishi N, Kagamiishi Y, Shimoda T, Satoh S, Ono S, Katsube N, Asano T (2004) Attenuation of a delayed increase in the extracellular glutamate level in the peri-infarct area following focal cerebral ischemia by a novel agent ONO-2506. Neurochem Int 45:381-387.

Morley GE, Ek-Vitorín JF, Taffet SM, Delmar M (1997) Structure of connexin43 and its regulation by pHi. J Cardiovasc Electrophysiol 8:939-951.

Moskowitz MA, Lo EH, Iadecola C (2010) The science of stroke: mechanisms in search of treatments. Neuron 67:181-198.

Müller NIC, Sonntag M, Maraslioglu A, Hirtz JJ, Friauf E (2019) Topographic map refinement and synaptic strengthening of a sound localization circuit require spontaneous peripheral activity. J Physiol 597:5469-5493.
Murphy-Royal C, Dupuis J, Groc L, Oliet SHR (2017) Astroglial glutamate transporters in the brain: Regulating neurotransmitter homeostasis and synaptic transmission. J Neurosci Res 95:2140-2151.
Murphy-Royal C, Dupuis JP, Varela JA, Panatier A, Pinson B, Baufreton J, Groc L, Oliet SH (2015) Surface diffusion of astrocytic glutamate transporters shapes synaptic transmission. Nat Neurosci 18:219-226.
Nagy JI, Dermietzel R (2000) Gap junctions and connexins in the mammalian central nervous system. Advances in Molecular and Cell Biology 30:323-396.
Nagy JI, Rash JE (2000) Connexins and gap junctions of astrocytes and oligodendrocytes in the CNS. Brain Res Brain Res Rev 32:29-44.
Nagy JI, Dudek FE, Rash JE (2004) Update on connexins and gap junctions in neurons and glia in the mammalian nervous system. Brain Res Brain Res Rev 47:191-215.
Nagy JI, Patel D, Ochalski PAY, Stelmack GL (1999) Connexin30 in rodent, cat and human brain: selective expression in gray matter astrocytes, co-localization with connexin43 at gap junctions and late developmental appearance. Neuroscience 88:447-468.
Nedergaard M, Cooper AJ, Goldman SA (1995) Gap junctions are required for the propagation of spreading depression. J Neurobiol 28:433-444.
Nedergaard M, Ransom B, Goldman SA (2003) New roles for astrocytes: redefining the functional architecture of the brain. Trends Neurosci 26:523-530.
Neher E, Sakmann B (1976) Single-channel currents recorded from membrane of denervated frog muscle fibres. Nature 260:799-802.
Nielsen MS, Axelsen LN, Sorgen PL, Verma V, Delmar M, Holstein-Rathlou NH (2012) Gap junctions. Compr Physiol 2:1981-2035.
Nimmerjahn A, Kirchhoff F, Kerr JN, Helmchen F (2004) Sulforhodamine 101 as a specific marker of astroglia in the neocortex in vivo. Nat Methods 1:31-37.
Oberheim NA, Takano T, Han X, He W, Lin JH, Wang F, Xu Q, Wyatt JD, Pilcher W, Ojemann JG, Ransom BR, Goldman SA, Nedergaard M (2009) Uniquely hominid features of adult human astrocytes. J Neurosci 29:3276-3287.
Ogata K, Kosaka T (2002) Structural and quantitative analysis of astrocytes in the mouse hippocampus. Neuroscience 113:221-233.
Orkand RK (1986) Glial-Interstitial Fluid Exchange. Annals of the New York Academy of Sciences 481:269-272.
Orkand RK, Nicholls JG, Kuffler SW (1966) Effect of nerve impulses on the membrane potential of glial cells in the central nervous system of amphibia. J Neurophysiol 29:788-806.
Pannasch U, Rouach N (2013) Emerging role for astroglial networks in information processing: from synapse to behavior. Trends Neurosci 36:405-417.
Pannasch U, Vargova L, Reingruber J, Ezan P, Holcman D, Giaume C, Sykova E, Rouach N (2011) Astroglial networks scale synaptic activity and plasticity. Proc Natl Acad Sci U S A 108:8467-8472.
Pannasch U, Freche D, Dallerac G, Ghezali G, Escartin C, Ezan P, Cohen-Salmon M, Benchenane K, Abudara V, Dufour A, Lubke JH, Deglon N, Knott G, Holcman D, Rouach N (2014) Connexin 30 sets synaptic strength by controlling astroglial synapse invasion. Nat Neurosci 17:549-558.
Parpura V, Verkhratsky A (2012) Astrocytes revisited: concise historic outlook on glutamate homeostasis and signaling. Croat Med J 53:518-528.

Pasler D, Gabriel S, Heinemann U (2007) Two-pore-domain potassium channels contribute to neuronal potassium release and glial potassium buffering in the rat hippocampus. Brain Res 1173:14-26.

Pellerin L, Magistretti PJ (1994) Glutamate uptake into astrocytes stimulates aerobic glycolysis: a mechanism coupling neuronal activity to glucose utilization. Proc Natl Acad Sci U S A 91:10625-10629.

Pellerin L, Magistretti PJ (1997) Glutamate uptake stimulates Na+,K+-ATPase activity in astrocytes via activation of a distinct subunit highly sensitive to ouabain. J Neurochem 69:2132-2137.

Peracchia C (2004) Chemical gating of gap junction channels; roles of calcium, pH and calmodulin. Biochim Biophys Acta 1662:61-80.

Peracchia C (2020) Calmodulin-Cork Model of Gap Junction Channel Gating-One Molecule, Two Mechanisms. Int J Mol Sci 21.

Peracchia C, Leverone Peracchia LM (2021) Calmodulin-Connexin Partnership in Gap Junction Channel Regulation-Calmodulin-Cork Gating Model. Int J Mol Sci 22.

Peracchia C, Sotkis A, Wang XG, Peracchia LL, Persechini A (2000) Calmodulin directly gates gap junction channels. J Biol Chem 275:26220-26224.

Perego C, Vanoni C, Bossi M, Massari S, Basudev H, Longhi R, Pietrini G (2000) The GLT-1 and GLAST glutamate transporters are expressed on morphologically distinct astrocytes and regulated by neuronal activity in primary hippocampal cocultures. J Neurochem 75:1076-1084.

Petzold GC, Windmüller O, Haack S, Major S, Buchheim K, Megow D, Gabriel S, Lehmann TN, Drenckhahn C, Peters O, Meierkord H, Heinemann U, Dirnagl U, Dreier JP (2005) Increased extracellular K+ concentration reduces the efficacy of N-methyl-D-aspartate receptor antagonists to block spreading depression-like depolarizations and spreading ischemia. Stroke 36:1270-1277.

Pietrobon D, Moskowitz MA (2014) Chaos and commotion in the wake of cortical spreading depression and spreading depolarizations. Nat Rev Neurosci 15:379-393.

Qin N, Olcese R, Bransby M, Lin T, Birnbaumer L (1999) Ca2+-induced inhibition of the cardiac Ca2+ channel depends on calmodulin. Proc Natl Acad Sci U S A 96:2435-2438.

Rackauskas M, Verselis VK, Bukauskas FF (2007) Permeability of homotypic and heterotypic gap junction channels formed of cardiac connexins mCx30.2, Cx40, Cx43, and Cx45. Am J Physiol Heart Circ Physiol 293:H1729-1736.

Rackauskas M, Neverauskas V, Skeberdis VA (2010) Diversity and properties of connexin gap junction channels. Medicina (Kaunas) 46:1-12.

Rakers C, Petzold GC (2017) Astrocytic calcium release mediates peri-infarct depolarizations in a rodent stroke model. J Clin Invest 127:511-516.

Ramón y Cajal S (1913) Contribución al conocimiento de la neuroglia del cerebro humano.

Ransom BR, Goldring S (1973) Ionic determinants of membrane potential of cells presumed to be glia in cerebral cortex of cat. Journal of neurophysiology 36:855-868.

Ransom CB, Ransom BR, Sontheimer H (2000) Activity-dependent extracellular K+ accumulation in rat optic nerve: the role of glial and axonal Na+ pumps. J Physiol 522 Pt 3:427-442.

Rawanduzy A, Hansen A, Hansen TW, Nedergaard M (1997) Effective reduction of infarct volume by gap junction blockade in a rodent model of stroke. J Neurosurg 87:916-920.

Ricci G, Volpi L, Pasquali L, Petrozzi L, Siciliano G (2009) Astrocyte-neuron interactions in neurological disorders. J Biol Phys 35:317-336.

Rietzel HJ, Friauf E (1998) Neuron types in the rat lateral superior olive and developmental changes in the complexity of their dendritic arbors. Journal of Comparative Neurology 390:20-40.

Rimmele TS, Chatton JY (2014) A novel optical intracellular imaging approach for potassium dynamics in astrocytes. PLoS One 9:e109243.
Río-Hortega P (1920) Estudios Sobre la Neuroglia. La Microglía Y Su Transformación en Células en Bastoncito Y Cuerpos Gránulo-adiposos.
Risher WC, Ard D, Yuan J, Kirov SA (2010) Recurrent spontaneous spreading depolarizations facilitate acute dendritic injury in the ischemic penumbra. J Neurosci 30:9859-9868.
Rose B, Loewenstein WR (1975) Permeability of cell junction depends on local cytoplasmic calcium activity. Nature 254:250-252.
Rossi DJ, Brady JD, Mohr C (2007) Astrocyte metabolism and signaling during brain ischemia. Nat Neurosci 10:1377-1386.
Rouach N, Koulakoff A, Abudara V, Willecke K, Giaume C (2008) Astroglial metabolic networks sustain hippocampal synaptic transmission. Science 322:1551-1555.
Saimi Y, Kung C (2002) Calmodulin as an ion channel subunit. Annual review of physiology 64:289.
Sanes DH, Song J, Tyson J (1992) Refinement of dendritic arbors along the tonotopic axis of the gerbil lateral superior olive. Developmental brain research 67:47-55.
Satoh J, Tabunoki H, Yamamura T, Arima K, Konno H (2007) Human astrocytes express aquaporin-1 and aquaporin-4 in vitro and in vivo. Neuropathology 27:245-256.
Schurr A, Miller JJ, Payne RS, Rigor BM (1999) An increase in lactate output by brain tissue serves to meet the energy needs of glutamate-activated neurons. J Neurosci 19:34-39.
Seifert G, Huttmann K, Binder DK, Hartmann C, Wyczynski A, Neusch C, Steinhauser C (2009) Analysis of astroglial K+ channel expression in the developing hippocampus reveals a predominant role of the Kir4.1 subunit. J Neurosci 29:7474-7488.
Seki A, Duffy HS, Coombs W, Spray DC, Taffet SM, Delmar M (2004) Modifications in the biophysical properties of connexin43 channels by a peptide of the cytoplasmic loop region. Circ Res 95:e22-28.
Shen Y, Wu S-Y, Rancic V, Aggarwal A, Qian Y, Miyashita S-I, Ballanyi K, Campbell RE, Dong M (2019) Genetically encoded fluorescent indicators for imaging intracellular potassium ion concentration. Communications Biology 2:18.
Shin HK, Dunn AK, Jones PB, Boas DA, Moskowitz MA, Ayata C (2006) Vasoconstrictive neurovascular coupling during focal ischemic depolarizations. J Cereb Blood Flow Metab 26:1018-1030.
Solan JL, Lampe PD (2014) Specific Cx43 phosphorylation events regulate gap junction turnover in vivo. Febs Lett 588:1423-1429.
Somjen GG (1979) Extracellular potassium in the mammalian central nervous system. Annu Rev Physiol 41:159-177.
Somjen GG (2001) Mechanisms of spreading depression and hypoxic spreading depression-like depolarization. Physiol Rev 81:1065-1096.
Somjen GG (2005) Ions in the Brain: Normal Function, Seizures, and Stroke. Archives of Neurology 62:503.
Sosinsky GE, Nicholson BJ (2005) Structural organization of gap junction channels. Biochim Biophys Acta 1711:99-125.
Spray DC, Harris AL, Bennett MV (1981) Gap junctional conductance is a simple and sensitive function of intracellular pH. Science 211:712-715.
Stephan J, Eitelmann S, Zhou M (2021) Approaches to Study Gap Junctional Coupling. Frontiers in Cellular Neuroscience 15.
Stephan J, Haack N, Kafitz KW, Durry S, Koch D, Hochstrate P, Seifert G, Steinhauser C, Rose CR (2012) Kir4.1 channels mediate a depolarization of hippocampal astrocytes under hyperammonemic conditions in situ. Glia 60:965-978.

Strohschein S, Huttmann K, Gabriel S, Binder DK, Heinemann U, Steinhauser C (2011) Impact of aquaporin-4 channels on K+ buffering and gap junction coupling in the hippocampus. Glia 59:973-980.

Sun W, Cornwell A, Li J, Peng S, Osorio MJ, Aalling N, Wang S, Benraiss A, Lou N, Goldman SA, Nedergaard M (2017) SOX9 Is an Astrocyte-Specific Nuclear Marker in the Adult Brain Outside the Neurogenic Regions. J Neurosci 37:4493-4507.

Swietach P, Rossini A, Spitzer KW, Vaughan-Jones RD (2007) H+ ion activation and inactivation of the ventricular gap junction: a basis for spatial regulation of intracellular pH. Circ Res 100:1045-1054.

Thoren AE, Helps SC, Nilsson M, Sims NR (2005) Astrocytic function assessed from 1-14C-acetate metabolism after temporary focal cerebral ischemia in rats. J Cereb Blood Flow Metab 25:440-450.

Tollin DJ (2003) The lateral superior olive: a functional role in sound source localization. Neuroscientist 9:127-143.

Tritsch NX, Yi E, Gale JE, Glowatzki E, Bergles DE (2007) The origin of spontaneous activity in the developing auditory system. Nature 450:50-55.

Turin L, Warner A (1977) Carbon dioxide reversibly abolishes ionic communication between cells of early amphibian embryo. Nature 270:56-57.

Tzingounis AV, Wadiche JI (2007) Glutamate transporters: confining runaway excitation by shaping synaptic transmission. Nat Rev Neurosci 8:935-947.

van Putten M, Fahlke C, Kafitz KW, Hofmeijer J, Rose CR (2021) Dysregulation of Astrocyte Ion Homeostasis and Its Relevance for Stroke-Induced Brain Damage. Int J Mol Sci 22.

Vannucci SJ, Maher F, Simpson IA (1997) Glucose transporter proteins in brain: delivery of glucose to neurons and glia. Glia 21:2-21.

Vera B, SanchezAbarca LI, Bolanos JP, Medina JM (1996) Inhibition of astrocyte gap junctional communication by ATP depletion is reversed by calcium sequestration. Febs Lett 392:225-228.

Verkhratsky A, Nedergaard M (2018) Physiology of Astroglia. Physiol Rev 98:239-389.

Virchow R (1856) Gesammelte Abhandlungen zyr wissenschaftlischen Medizin. Verlag von Meidinger Sohn & Comp, Frankfurt.

von Lenhossék M (1895) Der feinere Bau des Nervensystems im Lichte neuester Forschung. Berlin: Fischer's Medicinische Buchhandlung H Kornfield.

Vorísek I, Syková E (1997) Ischemia-induced changes in the extracellular space diffusion parameters, K+, and pH in the developing rat cortex and corpus callosum. J Cereb Blood Flow Metab 17:191-203.

Voskuyl R, Ter Keurs H (1981) Modification of neuronal activity in olfactory cortex slices by extracellular K+. Brain Research 230:372-377.

Wallraff A, Kohling R, Heinemann U, Theis M, Willecke K, Steinhauser C (2006) The impact of astrocytic gap junctional coupling on potassium buffering in the hippocampus. J Neurosci 26:5438-5447.

Walz W, Mukerji S (1988) KCl movements during potassium-induced cytotoxic swelling of cultured astrocytes. Experimental neurology 99:17-29.

Wang DD, Bordey A (2008) The astrocyte odyssey. Prog Neurobiol 86:342-367.

Warner DS, Ludwig PS, Pearlstein R, Brinkhoust AD (1995) Halothane reduces focal ischemic injury in the rat when brain temperature is controlled. The Journal of the American Society of Anesthesiologists 82:1237-1245.

Wellbourne-Wood J, Rimmele TS, Chatton JY (2017) Imaging extracellular potassium dynamics in brain tissue using a potassium-sensitive nanosensor. Neurophotonics 4:015002.

Willecke K, Eiberger J, Degen J, Eckardt D, Romualdi A, Guldenagel M, Deutsch U, Sohl G (2002) Structural and functional diversity of connexin genes in the mouse and human genome. Biol Chem 383:725-737.

Windmüller O, Lindauer U, Foddis M, Einhäupl KM, Dirnagl U, Heinemann U, Dreier JP (2005) Ion changes in spreading ischaemia induce rat middle cerebral artery constriction in the absence of NO. Brain 128:2042-2051.

Xie M, Wang W, Kimelberg HK, Zhou M (2008) Oxygen and glucose deprivation-induced changes in astrocyte membrane potential and their underlying mechanisms in acute rat hippocampal slices. Journal of Cerebral Blood Flow & Metabolism 28:456-467.

Xu-Friedman MA, Harris KM, Regehr WG (2001) Three-dimensional comparison of ultrastructural characteristics at depressing and facilitating synapses onto cerebellar Purkinje cells. J Neurosci 21:6666-6672.

Zhou L, Kasperek EM, Nicholson BJ (1999) Dissection of the molecular basis of pp60(v-src) induced gating of connexin 43 gap junction channels. J Cell Biol 144:1033-1045.

Zhou M, Schools GP, Kimelberg HK (2006) Development of GLAST(+) astrocytes and NG2(+) glia in rat hippocampus CA1: mature astrocytes are electrophysiologically passive. J Neurophysiol 95:134-143.

Zou J, Salarian M, Chen Y, Veenstra R, Louis CF, Yang JJ (2014) Gap junction regulation by calmodulin. FEBS letters 588:1430-1438.

I Publikationen und Manuskripte

Die eingereichten Manuskripte und Publikationen, die in dieser Arbeit vorgestellt werden, sind im Folgenden jeweils in antichronologischer Reihenfolge angefügt. Die *impact*-Faktoren (IF) sind jeweils angegeben. Die Beiträge zu den jeweiligen Studien sind vor dem Anhang aufgeführt.

Eingereichtes Manuskript

I **Sara Eitelmann**, Katharina Everaerts, Laura Petersilie, Christine Rosemarie Rose*, Jonathan Stephan*. *gleichwertiger Beitrag. *Ca^{2+}-dependent rapid uncoupling of astrocytes upon brief metabolic stress.* Eingereicht bei Front Cell Neurosci (26.01.2023; IF 2021: 6.1).

Publikationen

II **Sara Eitelmann***, Jonathan Stephan*, Katharina Everaerts, Simone Durry, Nils Pape, Niklas Jonny Gerkau, Christine Rosemarie Rose. *gleichwertiger Beitrag. *Changes in Astroglial K^+ upon Brief Periods of Energy Deprivation in the Mouse Neocortex.* Int J Mol Sci (2022; IF 2021: 6.2). DOI: 10.3390/ijms23094836.

III Jonathan Stephan, **Sara Eitelmann,** Min Zhou. *Approaches to Study Gap Junctional Coupling.* Front Cell Neurosci (2021; IF 2021: 6.1). DOI: 10.3389/fncel.2021.6404.

IV **Sara Eitelmann,** Laura Petersilie, Christine Rosemarie Rose, Jonathan Stephan. *Altered GJ Network Topography in Mouse Models for Human Hereditary Deafness.*Int J Mol Sci (2020; IF 2020: 5.9). DOI: 10.3390/ijms21197376.

Ca^{2+}-dependent rapid uncoupling of astrocytes upon brief metabolic stress

Sara Eitelmann, Katharina Everaerts, Laura Petersilie, Christine Rosemarie Rose*, Jonathan Stephan*

Institut für Neurobiologie, Heinrich-Heine-Universität Düsseldorf, Düsseldorf, Deutschland

Eingereicht bei Front Cell Neurosci (26.01.2023). IF 2021: 6.1.

Eigener Beitrag

Experimente:
- Alle Patch-Clamp-Messungen zur Isopotenzialität (Abbildung 1+2;4+5)
- Beladungen der Astrozyten-Netzwerke (Abbildung 1)
- *Cell-attached* Patch-Clamp-Messungen (Abbildung 2)

Analyse:
- Alle Patch-Clamp-Messungen zur Isopotenzialität (Abbildung 1+2;4+5)
- *Cell-attached* Patch-Clamp-Messungen (Abbildung 2)
- Statistische Analyse aller Daten

Manuskript:
- Erstellung aller Abbildungen (Abbildung 1-5)
- Beitrag zur Konzeptualisierung und Methodik der Studie
- Beitrag zur Verfassung und Überarbeitung des Manuskripts

frontiers

Ca2+-dependent rapid uncoupling of astrocytes upon brief metabolic stress

Sara Eitelmann[1], Katharina Everaerets[1], Laura Petersilie[1], Christine R. Rose[1*], Jonathan Stephan[1*]

[1]Heinrich Heine University of Düsseldorf, Germany

Submitted to Journal:
Frontiers in Cellular Neuroscience

Specialty Section:
Non-Neuronal Cells

Article type:
Original Research Article

Manuscript ID:
1151608

Received on:
26 Jan 2023

Journal website link:
www.frontiersin.org

In review

Ca^{2+}-dependent rapid uncoupling of astrocytes upon brief metabolic stress

Sara Eitelmann[1], Katharina Everaerts[1], Laura Petersilie[1], Christine R. Rose[1,*] & Jonathan Stephan[1,*]

[1]Institute of Neurobiology, Heinrich Heine University Düsseldorf, Universitätsstraße 1, D-40225 Düsseldorf, Germany

*** Correspondence:**
Corresponding Authors
jonathan.stephan@hhu.de; rose@hhu.de

Keywords: gap junctions, ischemia, isopotentiality, calcium, pH, sodium, neocortex.

In review

Abstract

Astrocytic gap junctional coupling is a major element in neuron-glia interaction. There is strong evidence that impaired coupling is involved in neurological disorders. Reduced coupling was e.g., demonstrated for core regions of ischemic stroke that suffer from massive cell death. In the surrounding penumbra, cells may recover, but recovery is hampered by spreading depolarizations, which impose additional metabolic stress onto the tissue. Spreading depolarizations are characterized by a transient breakdown of cellular ion homeostasis, including pH and Ca^{2+}, which might directly affect gap junctional coupling. To address this question, we examined the effects of brief metabolic stress on coupling strength between astrocytes in mouse neocortical tissue slices. Changes in gap junctional coupling were assessed by recording the syncytial isopotentiality. Moreover, quantitative ion imaging was performed to analyze the mechanisms triggering the observed changes. Our experiments show that a 2-minute perfusion with blockers of glycolysis and oxidative phosphorylation caused a rapid, significant uncoupling of astrocytes. They further indicate that uncoupling was not mediated by the accompanying (moderate) intracellular acidification. Dampening large astrocytic Ca^{2+} increases by either removal of extracellular Ca^{2+} or blocking Ca^{2+} influx, however, prevented uncoupling. Taken together, we conclude that astrocytes, which experience large Ca^{2+} changes upon brief episodes of metabolic stress, also undergo a rapid, Ca^{2+}-dependent uncoupling. Such uncoupling may help to confine and reduce cellular damage in the ischemic penumbra.

1 Introduction

Astrocytes in the mouse brain are coupled via gap junctions mainly composed of connexin (Cx) 43 and Cx30, forming extensive functional syncytia (Giaume et al., 2021; Stephan et al., 2021). This coupling allows the diffusion of ions (e.g., K^+, Na^+, Ca^{2+}) and small molecules including metabolites (e.g., glucose, lactate) between coupled cells. Gap junctions also play an important role in the delivery of energy metabolites to neurons (Rouach et al., 2008). Furthermore, they facilitate the uptake of excess extracellular glutamate and K^+ released upon synaptic activity, thereby regulating neuronal excitability and synaptic plasticity (Pannasch et al., 2011; Hosli et al., 2022). Notably, astrocyte coupling is not static, but dynamically adjusted to the activity and energy demand of neighboring neurons (Rouach et al., 2008).

Astrocytic gap junctional coupling thus emerges as a major element in neuron-glia interaction and communication in the healthy brain (Giaume et al., 2021; Mazaud et al., 2021).

Many pathological conditions, however, result in an uncoupling of astrocytes. For example, coupling is significantly reduced in epilepsy, resulting in an impaired clearance and buffering of K^+. This suggests a causative involvement of an impaired gap junctional coupling in the development of this disease (Boison and Steinhauser, 2018). Uncoupling of gap junctions was also demonstrated in astrocytes exposed to conditions of prolonged metabolic failure, which mimic acute conditions in the core region of an ischemic stroke (Vera et al., 1996; Cotrina et al., 1998; Xu et al., 2010; Lee et al., 2016). The ischemic core is characterized by a dramatic drop in blood flow and an energy supply that is too low to maintain the activity of ion pumps and secondary-active transporters (Struyk, 2005). This results in a breakdown of ion gradients, followed by irreversible cell damage (Rossi et al., 2007; Moskowitz et al., 2010; van Putten et al., 2021).

In the adjacent ischemic penumbra, blood flow is reduced but high enough to initially maintain the viability of neurons and astrocytes. Full recovery is possible, provided that reperfusion is regained in time (Moskowitz et al., 2010). Recovery in the penumbra is, however, jeopardized by waves of spreading depolarizations. These invade the penumbra from the ischemic core, aggravating hypoxia and thereby playing an important role in the gradual expansion of the ischemia core (Dirnagl et al., 1999; Rossi et al., 2007; Lauritzen et al., 2011; Hinzman et al., 2014; Dreier and Reiffurth, 2015). Hallmarks of spreading depolarizations are reversible accumulations of extracellular glutamate and K^+. In both, neurons and astrocytes, this is accompanied by an increase in intracellular Ca^{2+} and Na^+ concentrations ($[Ca^{2+}]_i$, $[Na^+]_i$), by an acidification, as well as a decrease in cellular ATP (Pietrobon and Moskowitz, 2014; Dreier and Reiffurth, 2015; Rakers and Petzold, 2017; Gerkau et al., 2018). Notably, gap junctional conductance is directly sensitive to changes in intracellular pH (pH_i) and $[Ca^{2+}]_i$ (Giaume et al., 2021). However, it is still unclear, if transient ionic alterations such as those that are characteristic for the ischemic penumbra and subject to spreading depolarizations will result in an immediate change in astrocyte coupling.

To address this question, we examined the effects of brief metabolic stress on gap junctional coupling between astrocytes in acute tissue slices of the mouse neocortex. Gap junctional coupling was assessed by recording the syncytial isopotentiality, a direct measure of coupling strength (Stephan et al., 2021). In addition, coupling was analyzed by tracer loading and by imaging the intercellular spread of induced Na^+ elevations. Imaging of astrocyte pH_i and $[Ca^{2+}]_i$ was performed to address the mechanisms triggering the observed changes in gap junctional coupling. Our results demonstrate that neocortical astrocytes uncouple upon strong Ca^{2+} loads evoked by metabolic stress.

2 Materials and Methods

2.1 Ethical approval

The present study was carried out in strict accordance with the institutional guidelines of the Heinrich Heine University Düsseldorf, as well as the European Community Council Directive (2010/63/EU). All procedures were reported to, and approved by, the Animal Welfare Office of the Animal Care and Use Facility of the Heinrich Heine University Düsseldorf (institutional act number: O52/05). Based on the recommendations of the European Commission (Close et al., 1997), mice were anesthetized with CO_2, rapidly decapitated, and their brains were quickly removed. According to the German Welfare Act (TSchG; section 4, paragraph 3), no additional approval was required for *post mortem* removal of brain tissue.

Preview

2.2 Preparation of acute tissue slices and salines

Experiments were carried out using acute parasagittal tissue slices containing layer II/III of the somatosensory cortex from Balb/C mice of both sexes at postnatal days 14-21. Immediately after dissection, brains were transferred into ice-cold (3 ± 1 °C) preparation saline containing (in mM): 130 NaCl, 2.5 KCl, 1.25 NaH_2PO_4, 26 $NaHCO_3$, 0.5 $CaCl_2$, 6 $MgCl_2$, and 10 glucose; pH 7.4, 310 ± 5 mOsm; bubbled with carbogen (95% O_2, 5% CO_2). Thereafter, 250 µm-thick neocortical slices were cut using a vibratome (HM650V, Microtome, Thermo Fisher Scientific, Waltham, MA, USA). For *a priori* identification of astrocytes, slices were incubated for 20 min at 34 °C in preparation saline containing 0.5-1 µM sulforhodamine (SR) 101 (Kafitz et al., 2008). Thereafter, slices were incubated for 10 min at 34 °C in SR101-free standard artificial cerebrospinal fluid (ACSF) containing (in mM): 130 NaCl, 2.5 KCl, 1.25 NaH_2PO_4, 26 $NaHCO_3$, 2 $CaCl_2$, 1 $MgCl_2$, and 10 glucose; pH 7.4, bubbled with carbogen. Afterwards, slices were stored in ACSF at room temperature (21 ± 1 °C) until used for experiments, which were also performed at room temperature. During experiments, slices were constantly perfused with ACSF at a rate of 2.5 ml/min.

All chemicals were purchased from Merck/Sigma-Aldrich (St. Louis, MO, USA) or AppliChem (Darmstadt, Germany), if not stated otherwise. To expose cells to brief metabolic stress, slices were perfused for 2 min with glucose-free ACSF containing the cytochrome C inhibitor sodium azide (NaN_3; 5 mM) and the non-metabolizable glucose analogue 2-deoxyglucose (2-DG; 2 mM) to inhibit cellular ATP production ("chemical ischemia"; Gerkau et al., 2018; Lerchundi et al., 2019; Eitelmann et al., 2022). Gap junctional communication was blocked by perfusing slices with carbenoxolone (CBX, 100 µM). The influence of pH_i on gap junctional coupling was investigated by perfusing slices for either 2 or 5 min with an ACSF containing a lower HCO_3^- concentration ($[HCO_3^-]_e$; 3.6 mM, pH 6.4; cf. Wallraff et al., 2006). To reduce Ca^{2+} entry into astrocytes, KB-R7943 (NCX inhibitor, 50 µM, Abcam, Cambridge, UK), DL-AP5 (NMDA receptor antagonist, 100 µM; StressMarq Biosciences, Cadboro Bay Village, Canada), and HC-067047 (TRPV4 antagonist, 10 µM) were added to the saline. Bath application of blockers was started 15 min prior to and maintained throughout the entire duration of experiments.

2.3 Electrophysiology

Patch-clamp experiments were performed at an upright microscope (E600FN, Nikon, Tokyo, Japan). The microscope was equipped with infrared differential interference contrast optics including a 60x water immersion objective (Fluor 60x/1.00W, DIC H/N2, ∞/0 WD 2.0, Nikon) and an infrared video camera (XC-ST70CE, Hamamatsu Photonics, Herrsching, Germany). Electrophysiological recordings were performed using an EPC10 amplifier and "PatchMaster" software (Harvard Bioscience/HEKA Elektronik, Lambrecht, Germany). Patch pipettes were pulled from borosilicate glass capillaries (GB150(F)-8P, Science Products, Hofheim am Taunus, Germany) at a vertical puller (PC-10 Puller, Narishige International, London, UK) and had a resistance of 3.5-4.5 MΩ. The standard pipette solution contained (in mM): 116 K-methansulfonate, 32 KCl, 10 HEPES (N-(2-hydroxyethyl)piperazine-N'-2-ethanesulfonic acid), 10 NaCl, 4 Mg-ATP, and 0.4 Na_2-GTP; pH 7.3. The offset potential was corrected. Data were analyzed using "OriginPro 2021" (OriginLab Corporation, Northampton, MA, USA).

Syncytial isopotentiality was determined as previously described by the Zhou lab (Ma et al., 2016; Kiyoshi et al., 2018). To this end, a K^+-free pipette solution (0 mM K^+) was used in which K^+ was substituted with an equimolar amount of Na^+. After achieving a GΩ seal, the recording was switched to current-clamp mode and the membrane patch ruptured by applying

In review

negative pressure. This resulted in a rapid drop in the recorded potential reflecting the resting membrane potential (E_M) of the cell. Subsequent dialysis of the cell with 0 mM K^+ led to a decline in E_M to a new steady state level. The latter represents a direct measure of gap junctional coupling, i.e., the ability to equalize the E_M of astrocytes within the functional syncytium ("isopotentiality"). Whole-cell recordings were discarded when input resistance exceeded 30 MΩ.

Changes in astrocytic E_M in response to brief metabolic stress were determined by cell-attached recordings as described before (Eitelmann et al., 2022). Pipettes were filled with standard ACSF and the remaining offset potential was corrected. In cell-attached recordings, the input resistance should be at least 100-fold higher than the membrane resistance (R_M) to ensure reliable measurement of E_M (Perkins, 2006). As R_M of mature astrocytes is about 10 MΩ (Kafitz et al., 2008), an input resistance higher than 1 GΩ was required for cell-attached recordings.

2.4 Tracer coupling

Visualization of gap junctional coupling of astrocytes by tracer loading was done as described earlier (Eitelmann et al., 2019; Eitelmann et al., 2020). Briefly, an astrocyte was recorded in whole-cell configuration for 20 min using a pipette solution that contained the gap junction-impermeable dye Alexa Fluor (AF) 568 (100 µM, Thermo Fisher Scientific/Invitrogen, Carlsbad, CA, USA) and the gap junction-permeable tracer neurobiotin (2%, Vector Laboratories, Burlingame, CA, USA) to visualize the patched astrocyte as well as its coupled neighbors, respectively. Afterwards, slices were fixed at 4 °C with 4% paraformaldehyde overnight after which they were washed three times for 10 min in phosphate buffered saline (PBS) containing NaCl, Na_2HPO_4*2 H_2O, and NaH_2PO_4*H_2O (pH 7.4). Membrane permeabilization was achieved by incubation in 0.25% triton X-100 for 30 min, followed by a wash with PBS. For detection of neurobiotin, slices were then incubated with avidin AF488 (50 µg/ml, Invitrogen) for 3 h. Finally, slices were washed in PBS, transferred on microscope slides (VWR, Radnor, PA, USA) and embedded in mounting medium Mowiol.

Stainings were documented using a confocal system (Eclipse C1, Nikon) equipped with an upright microscope (E600FN, Nikon) and a 60x oil immersion objective (Plan Apo VC 60x/1.40 Oil, ∞/0.17 WD 0.13, Nikon). Confocal images were acquired using "EZ-C1 FreeViewer" software (Nikon). Fluorophores were excited and detected as follows (excitation wavelength / filtered emission wavelength): AF488 (488 nm / 515/30 nm) and AF568 (543 nm / 605/75 nm). Images were further processed using "FIJI" software (Schindelin et al., 2012).

2.5 Imaging of $[Na^+]_i$, pH_i, or $[Ca^{2+}]_i$

To measure changes in $[Na^+]_i$, pH_i, or $[Ca^{2+}]_i$, tissue slices were loaded with the membrane-permeable forms of SBFI (SBFI-AM; sodium-binding benzofuran isophthalate-acetoxymethyl ester, 116.7 µM; Teflabs, Austin, USA), BCECF (BCECF-AM; 2',7'-Bis-(2-Carboxyethyl)-5-(and-6)-Carboxyfluorescein-acetoxy-methyl ester, 125 µM; A.G. Scientific, San Diego, CA, USA) or OGB-1 (OGB-1-AM, Oregon Green 488 BAPTA-1-acetoxymethyl ester; 111 µM; Invitrogen), respectively. Wide field imaging was performed using an upright microscope (Eclipse FN-1, Nikon) equipped with a 40x water immersion objective (Fluor 40×/0.8W, DIC M/N2, ∞/0 WD 2.0, Nikon) and fluorophores were excited using a Polychrome V monochromator (Thermo Fisher Scientific/FEI, Planegg, Germany). Astrocytes were identified by additional SR101-labeling (excitation at 575 nm,

In review

emission collected >590 nm). SBFI was excited at 400 nm and its fluorescence was detected above ~430 nm (409 beam splitter and 510/84 emission filter; Gerkau et al., 2018). BCECF was excited at 458 (isosbestic wavelength) and 488 nm (pH-sensitive wavelength), and its emission was recorded between 511 and 563 nm. OGB-1 was excited at 488 nm, and its emission was collected above 505 nm.

Images of SBFI, BCECF, and OGB-1 fluorescence were acquired at 0.5-1 Hz with an ORCA FLASH 4.0LT camera (Hamamatsu Photonics). Fluorescence was collected from regions of interest (ROIs) representing cell bodies of SR101-positive astrocytes. Emission from individual ROIs was background corrected and SBFI and OGB-1 signals were additionally corrected for bleaching by employing "OriginPro 2019/2021". For BCECF, the fluorescence ratio (F_{458}/F_{488}) was calculated after background correction. Normalization of fluorescence was performed in MS Excel 2016. *In situ* calibration of SBFI, BCECF, and OGB-1 fluorescence was done as described before (Gerkau et al., 2018; Ziemens et al., 2019; Eitelmann et al., 2022). Changes in $[Ca^{2+}]_i$ were analyzed immediately at onset of reperfusion, i.e., 2 min after start of chemical ischemia wash-in.

2.6 Statistics

Each set of experiments was performed on at least three tissue slices taken from at least three different animals. Before further processing, data were tested for outliers using "WinSTAT" (R. Fitch Software, Bad Krozingen, Germany). Subsequently, data were further statistically analyzed using "OriginPro 2021". Normal distribution was assessed using a Shapiro-Wilk test or Kolmogorov Smirnov test for a sample size (n) of <50 or ≥50, respectively (Mishra et al., 2019). In case of normal distribution, independent samples were tested by unpaired Student's t-test or ANOVA test (>2 comparisons), whereas paired samples were tested by paired Student's t-test or repeated measures ANOVA test (>2 comparisons). In the absence of normal distribution, independent samples were tested by Mann-Whitney U test or Kruskal-Wallis H test (>2 comparisons), whereas paired samples were tested by Wilcoxon test or Friedman's ANOVA test (>2 comparisons; Nayak and Hazra, 2011). p represents the error probability: $*p < 0.05$, $**p < 0.01$, $***p < 0.001$. Experimental results are provided as mean ± standard deviation (SD). n represents the number of cells (or experiments) per slice per animal. Data illustrated in box plots show single data points (grey diamonds), mean (square), median (horizontal line), SD (box), and min/max (whiskers).

3 Results

3.1 Isopotentiality of neocortical astrocytes

To measure dynamic changes in gap junctional coupling, we employed an electrophysiological approach based on the isopotentiality of the astrocyte syncytium. Here, diffusion of K^+, and the ability of the astrocyte syncytium to equalize intercellular differences in E_M via gap junctions, provides a direct measure of syncytial coupling (Figure 1A). To this end, we first performed whole-cell patch-clamp recordings using a standard pipette solution containing 148 mM K^+ (Figure 1B). This is close to the estimated intracellular K^+ concentration ($[K^+]_i$) of astrocytes in layer II/III of the somatosensory cortex (146 mM; cf. Eitelmann et al., 2022). Directly upon rupture of the membrane patch, an initial E_M of -87.9 ± 5.8 mV was measured (n = 31/20/15). During the ongoing recording, E_M remained stable at -88.1 ± 5.9 mV (p = 0.694; Figure 1B$_2$). Thus, E_M was essentially unaffected by dialysis of the cytosol with the standard patch pipette solution, which was expected given its near-physiological $[K^+]$. Moreover, the experimentally determined E_M was close to the -89.0 mV predicted by the Goldman-Hodgkin-Katz equation (assuming a relative Na^+/K^+

In review

permeability of 0.010; cf. Eitelmann et al., 2022). Under this resting condition, astrocytes exhibited profound tracer coupling (Figure 1B$_3$).

In contrast, using a pipette saline containing 0 mM K^+ depolarized the astrocytes' E_M within 10-20 s after breakthrough from an initial E_M of -86.6 ± 3.1 mV to a peak E_M of -79.8 ± 4.9 mV (n = 12/10/7, $p = 6 \times 10^{-4}$; Figure 1C$_{1-2}$). This peak E_M was markedly less positive than expected, as the Goldman-Hodgkin-Katz equation predicts a depolarization to +18.8 mV. The striking difference between the experimentally measured and the theoretically predicted E_M suggests that despite dialysis of 0 mM K^+ into the patch-clamped cell, its $[K^+]_i$ was largely maintained by equilibration via gap junctional coupling. Accordingly, astrocyte E_M was kept close to physiological levels, though there was small shift in peak E_M ($p = 4 \times 10^{-4}$; Figure 1G). Like in the preceding experiment, astrocytes were considerably tracer-coupled (Figure 1C$_3$).

To confirm that K^+ exchange within the syncytium limits the depolarizing effect of 0 mM K^+ in the patch pipette, we repeated the isopotentiality recordings in the presence of the gap junction blocker CBX (100 µM; Figure 1D$_1$). When slices were preincubated with CBX, astrocytes depolarized rapidly and E_M essentially collapsed from an initial E_M of -86.7 ± 7.5 mV to a peak E_M of -5.3 ± 3.2 mV (n = 7/7/3, $p = 3 \times 10^{-7}$; Figure 1D$_2$). Thus, blocking gap junctions strongly shifts peak E_M ($p = 3 \times 10^{-17}$; Figure 1G). Tracer coupling from these astrocytes to neighboring cells was not detected, confirming CBX-induced blockage of gap junctions (Figure 1D$_3$).

As further proof of concept, we performed isopotentiality recordings with 0 mM K^+ from cells lacking prominent gap junctional coupling, i.e., from pyramidal neurons in layers II/III and putative NG2 cells. Pyramidal neurons showed a rapid and almost complete depolarization to -9.9 ± 12.7 mV (n = 3/3/3, $p = 2 \times 10^{-4}$; Figure 1E), accompanied by action potential firing immediately after breakthrough, which contrasts astrocyte peak E_M ($p = 5 \times 10^{-14}$; Figure 1G). SR101-negative cells, exhibiting a small, rounded soma and an initial E_M of -69.0 ± 17.3 mV - properties characteristic for NG2 cells - also depolarized rapidly and strongly to -2.5 ± 3.0 mV after establishing the whole-cell configuration, albeit without generating action potentials (n = 3/3/3, p = 0.003; Figure 1F), which similarly contrasts astrocyte peak E_M ($p = 7 \times 10^{-15}$; Figure 1G). As opposed to astrocytes, both pyramidal neurons and putative NG2 cells were thus unable to confer isopotentiality.

Taken together, these results confirm that astrocytes in acutely isolated tissue slices of mouse neocortex, in contrast to pyramidal neurons and presumed NG2 cells, confer syncytial isopotentiality. Furthermore, our data show that the ability of individual astrocytes to counteract depolarization induced by dialysis with a K^+-free pipette solution depends on gap junctional coupling.

3.2 Changes in gap junctional coupling upon brief metabolic stress

Next, we employed isopotentiality recordings to study changes in gap junctional coupling upon brief metabolic stress. The latter was induced by chemical ischemia, i.e., perfusing slices with a glucose-free saline that additionally contained 5 mM NaN_3 and 2 mM 2-DG for 2 min. Importantly, chemical ischemia *per se* causes a depolarization of astrocytes (e.g. Eitelmann et al., 2022), which will overlap with any changes in E_M induced by isopotentiality recordings with 0 mM K^+. Therefore, we first performed cell-attached recordings to determine the magnitude of these changes (Figure 2A$_1$). Upon chemical ischemia, astrocytes depolarized from a baseline level of -86.4 ± 3.6 mV to -72.6 ± 4.9 mV ($p = 2 \times 10^{-7}$, n = 6/6/4; Figure 2A$_{2-3}$). This peak depolarization was reached 28 ± 22 s after the onset of reperfusion with

In review

standard ACSF. Subsequently, astrocytes hyperpolarized to -89.1 ± 4.8 mV ($p = 9 \times 10^{-5}$) before their E_M recovered to -84.5 ± 5.5 mV ($p = 1 \times 10^{-4}$), which is close to their initial baseline (Figure $2A_2$).

We next examined changes in the isopotentiality of the astrocyte network upon metabolic stress. Astrocytes were approached with a patch pipette filled with 0 mM K^+ and a GΩ seal was formed. Subsequently, slices were exposed to chemical ischemia for 2 min and the recording was switched to current-clamp mode to measure E_M. Immediately at onset of reperfusion with standard ACSF, the membrane patch was ruptured, establishing the whole-cell configuration (Figure $2B_1$). Astrocytes exhibited an initial E_M of -69.4 ± 16.3 mV immediately after chemical ischemia induction from which cells depolarized to a peak E_M of -45.4 ± 23.8 mV ($p = 0.004$) within about 14 s ($n = 11/11/9$; Figure $2B_2$). Thus, the peak E_M of astrocytes was more depolarized compared to control ($p = 8 \times 10^{-5}$; Figure $2B_3$). In the following, some cells recovered, whereas others remained or further depolarized indicating different susceptibility for metabolic stress (Figure $2B_2$). Importantly, peak E_M of astrocytes in isopotentiality recordings was more depolarized compared to cell-attached recordings ($p = 0.016$; Figure $2B_3$), indicating that the isopotentiality of the astrocytic syncytium was reduced.

Taken together, our results demonstrate that astrocytes display a rapid reduction in isopotentiality when exposed to a 2-minute period of chemical ischemia. This indicates that astrocytes undergo an immediate reduction in functional gap junctional coupling in response to brief metabolic stress.

3.3 Intercellular sodium diffusion during brief metabolic stress

Our isopotentiality measurements indicated that transient chemical ischemia induces an uncoupling of astrocytes. To further probe for such uncoupling, we analyzed the intercellular spread of Na^+ between astrocytes, which has been shown to diffuse rapidly through gap junctions (Langer et al., 2012). In addition, we determined the length constant λ of intercellular Na^+ diffusion, which is a measure for the effectiveness of Na^+ redistribution within the network and ranges from 31-46 µm depending on the studied brain region (Langer et al., 2012; Augustin et al., 2016; Moshrefi-Ravasdjani et al., 2017; Wadle et al., 2018).

To this end, slices were loaded with the chemical Na^+ indicator SBFI-AM to record changes in astrocytic $[Na^+]_i$. An individual astrocyte was then approached by an electroporation pipette filled with ACSF and stimulated by a single current pulse (1 ms, 30 mV; Figure $3A_1$). As observed earlier (Langer et al., 2012), this electroporation resulted in an immediate and strong $[Na^+]_i$ increase in the stimulated cell ("a_1"). Neighboring cells exhibited delayed, smaller increases in $[Na^+]_i$ ("a_2"-"a_5"; Figure $3A_2$). The peak amplitude of electroporation-induced elevation of $[Na^+]_i$ decreased mono-exponentially with increasing distance to the simulated astrocyte, with a length constant λ ranging from 28-54 µm. The average λ was 38 ± 11 µm ($R^2 = 0.822$, $n = 53/6/5$, Figure $3A_3$), which is close to values reported from astrocytes in the hippocampus and the auditory brainstem (Langer et al., 2012; Augustin et al., 2016; Wadle et al., 2018). This mono-exponential decay suggests passive spread of Na^+ from the stimulated cell to its gap junction-coupled neighbors (cf. (Langer et al., 2012).

Next, astrocytes were exposed to chemical ischemia for 2 min (Figure 3B). As reported before, this results in an astrocytic $[Na^+]_i$ increase (Figure $3B_2$; Gerkau et al., 2018; Eitelmann et al., 2022). Immediately upon reperfusion with standard ACSF, a single astrocyte was subjected to electroporation (see cell "b_1" in Figure $3B_1$). This evoked an additional rapid

In review

$[Na^+]_i$ increase in the stimulated astrocyte as well as in neighboring astrocytes ("b_2"-"b_4"), which overlapped the Na^+ load induced by chemical ischemia (Figure $3B_2$).

To determine the magnitude of the electroporation-induced $[Na^+]_i$ increase independent of the initial chemical ischemia-induced $[Na^+]_i$ increase, the following procedure was employed: First, the second derivative was calculated from each experimental trace. The presence of an inflection point within the first 60 s after electroporation, at which traces bent to the left, was indicative of an additional Na^+ load. After determination of the inflection point, a mono-exponential fit was created from the original trace that covered the 2-minute rising phase of the chemical ischemia-induced Na^+ load until the inflection point. This fit was extrapolated to reveal the presumed kinetics of the chemical ischemia-induced Na^+ load (see red dotted line in Figure $3B_2$). In a final step, the maximum difference between the measured maximum $[Na^+]_i$ and the fit was determined, reflecting the estimated electroporation-induced Na^+ load.

The peak amplitude of the electroporation-induced Na^+ load in each cell was plotted against the distance from the stimulated astrocyte (Figure $3B_3$). Again, data from individual experiments were fitted with mono-exponential decay curves, and it was found that the length constants now ranged from 1 µm (indicating essentially no spread of Na^+) to 40 µm (indicating a spread of Na^+ comparable to that under control conditions; Figure $3B_3$). As a result, the average λ was decreased to 21 ± 15 µm (55%, n = 51/6/5, p = 0.026).

Taken together, these experiments demonstrate that metabolic stress results in a reduction in the passive spread of Na^+ between astrocytes. Since gap junctions are the pathway responsible for the intercellular diffusion of Na^+, this strongly suggests an overall reduction in gap junctional conductance upon brief metabolic stress.

3.4 Influence of pH_i on gap junctional coupling

We next probed for possible modulators that might mediate the observed changes in gap junctional coupling in neocortical astrocytes. Cerebral ischemia is associated with acidosis in the lesion area (Kraig et al., 1985; Smith et al., 1986; Nedergaard et al., 1991). Additionally, previous work has shown that gap junctional conductance is sensitive to intracellular acidification (Wallraff et al., 2006). Thus, rapid reduction in astrocyte coupling might be mediated by changes in their pH. To this end, we performed wide field imaging experiments employing the pH-sensitive dye BCECF (Figure $4A_1$) and found that astrocytes acidified by 0.28 ± 0.01 pH units upon chemical ischemia for 2 min (n = 29/4/3; Figure $4A_{2,5}$). Thereafter, pH_i recovered to a level slightly more acidic than the initial baseline (Figure $4A_2$).

To mimic such intracellular acidosis, slices were then perfused for 2 min with a saline in which $[HCO_3^-]_e$ was reduced to 3.6 mM. This indeed resulted in a comparable transient decrease in astrocytic pH_i by 0.26 ± 0.01 pH units (n = 47/5/3; p = 0.367), followed by recovery to baseline in standard ACSF (Figure $4A_{3,5}$). Isopotentiality recordings in this low $[HCO_3^-]_e$ saline showed that the peak E_M of -76.5 ± 4.9 mV, detected about 15-25 s after onset of reperfusion with standard ACSF, was less depolarized compared to chemical ischemia (n = 9/8/3, p = 0.003; Figure 4D). Taken together, these results indicate that a chemical ischemia-like acidification by about 0.26 pH units is not sufficient to mimic the chemical ischemia-induced reduction of gap junctional coupling between astrocytes.

We also extended the perfusion period of low $[HCO_3^-]_e$ to 5 min, whereupon astrocytes showed a stronger acidification by 0.45 ± 0.05 pH units (n = 27/3/2, $p = 2 \times 10^{-34}$; Figure $4A_{4-5}$). Isopotentiality recordings in which the patch was ruptured after 5 min of low $[HCO_3^-]_e$ showed a significant depolarization from initial E_M of -79.1 ± 9.3 mV to a peak E_M

[in review]

of -55.4 ± 16.8 mV (n = 10/10/4, p = 0.020; Figure 4C$_{1-2}$). The depolarization peaked about 15-30 s after onset of reperfusion with standard ACSF. The peak E_M after 5 min of low $[HCO_3^-]_e$ compared to 2 min (p = 0.009; Figure 4D). Subsequently, six out of ten astrocytes recovered, whereas four astrocytes remained depolarized or depolarized even further (Figure 4C$_2$). Similar to what was observed upon chemical ischemia, this phenomenon was thus readily reversible in roughly half of the cells, whereas the remainder of cells did not recover.

Taken together, these results demonstrate that an intracellular acidification by about 0.45 pH units causes an immediate and robust reduction in the isopotentiality of astrocytes, indicating a reduction in gap junctional coupling and thereby confirming its well-known dependence on pH_i. In addition, our results show that a decrease in pH_i by about 0.26 pH units does not affect the isopotentiality of astrocytes. This strongly suggests that the intracellular acidification of astrocytes that accompanied brief metabolic stress was not responsible for the observed reduction in gap junctional coupling.

3.5 Influence of Ca^{2+} load on gap junctional coupling

In addition to cellular acidification, gap junctions are also modulated by alterations in $[Ca^{2+}]_i$ (Lurtz and Louis, 2007). To determine whether the observed chemical ischemia-induced reduction of gap junction coupling depends on an induced Ca^{2+} load, we performed imaging experiments with the Ca^{2+}-sensitive dye OGB-1 (Figure 5A$_1$). As expected from previous work (e.g., Duffy and MacVicar, 1996; Rakers et al., 2017; Gerkau et al., 2018), we found that the chemical ischemia caused a rapid, transient increase in astrocytic Ca^{2+} (Figure 5A$_2$). The peak amplitude of the $[Ca^{2+}]_i$ increase was about 100 nM (106 ± 109 nM, n = 75/8/6; Figure 5A$_5$).

Next, slices were perfused with a saline devoid of Ca^{2+} (0 $[Ca^{2+}]_e$) to reduce the Ca^{2+} load induced by chemical ischemia. Under these conditions, astrocytes showed an average $[Ca^{2+}]_i$ increase of about 50 nM (47 ± 20 nM; n = 65/6/6; Figure 5A$_3$). This increase was significantly lower than that induced by chemical ischemia alone (p = 0.011; Figure 5A$_5$).

A similar result was obtained when perfusing slices with ACSF containing blockers of NCX (KB-R7943, 50 µM), NMDA receptors (DL-AP5, 100 µM) as well as TRPV4 channels (HC-067047, 10 µM) to reduce chemical ischemia-induced Ca^{2+} influx (Rakers et al., 2017; Gerkau et al., 2018). Here, astrocytes showed an $[Ca^{2+}]_i$ increase by 31 ± 7 nM (n = 92/6/5; Figure 5A$_4$). This was significantly lower than that induced by chemical ischemia without blockers ($p = 2 \times 10^{-9}$) and indistinguishable from the results in 0 $[Ca^{2+}]_e$ (p = 0.058; Figure 5A$_5$). Altogether, both removal of extracellular Ca^{2+} or inhibition of Ca^{2+} entry thus resulted in a reduced Ca^{2+} load in response to chemical ischemia.

To test whether a reduction in the overall Ca^{2+} load would affect the observed changes in gap junctional coupling upon brief metabolic stress, we next performed isopotentiality measurements. In 0 $[Ca^{2+}]_e$, chemical ischemia for 2 min caused a peak depolarization of astrocyte E_M to -66.6 ± 3.8 mV (n = 9/9/3; Figure 5B$_1$). Compared to chemical ischemia in standard $[Ca^{2+}]_e$ the peak E_M was less depolarized (p = 0.011; Figure 5D). All cells showed a complete recovery and subsequent hyperpolarization within the recording period of 5-30 min (Figure 5B$_2$), similar to the hyperpolarization observed in cell-attached recordings (cf. Figure 2A$_{1-2}$).

As observed upon removal of extracellular Ca^{2+}, combined inhibition of NCX, NMDA receptors and TRPV4 channels during chemical ischemia led to a peak E_M of -67.5 ± 5.2 mV (n = 9/9/3, p = 0.003; Figure 5C). Compared to chemical ischemia without these blockers,

In review

peak E_M was reduced ($p = 0.007$), however, it was indistinguishable from the 0 $[Ca^{2+}]_e$ experiment ($p = 0.077$; Figure 5D). Thus, removal of extracellular Ca^{2+} or inhibition of Ca^{2+} entry resulted in a less depolarized peak E_M, which reflects a significant rescue from chemical ischemia-induced uncoupling.

In summary, our results demonstrate that astrocytes exhibit partial uncoupling and are subject to Ca^{2+} loading upon transient chemical ischemia. Dampening Ca^{2+} entry from the extracellular space reduces astrocyte uncoupling significantly, suggesting that uncoupling upon brief metabolic stress was causally related to Ca^{2+} influx.

4 Discussion

In the present study, we employed syncytial isopotentiality recordings and quantitative ion imaging in mouse neocortical tissue slices to analyze the effects of brief metabolic stress on astrocyte gap junctional coupling. Our results show that neocortical astrocytes exhibit an immediate reduction in coupling. While we confirmed a general dependence of astrocytic gap junction coupling on pH_i, the data suggest that the reduced gap junctional coupling upon brief metabolic stress was not mediated by concomitant (moderate) intracellular acidification. Attenuation of changes in $[Ca^{2+}]_i$, however, largely prevented uncoupling, indicating that it was dependent on the induced astrocytic Ca^{2+} load.

4.1 Probing astrocytic gap junctional coupling

As demonstrated here, loading a gap junction-permeable tracer into a single astrocyte via a patch-clamp pipette enables the subsequent visualization of neighboring coupled cells. Tracer coupling is a highly robust and informative approach to demonstrate the topography of networks (Wallraff et al., 2006;Houades et al., 2008; Augustin et al., 2016; Eitelmann et al., 2019). However, it typically requires a tracer loading time of at least 10-20 min and provides a more or less static view on astrocyte coupling. High temporal resolution can be obtained by electrophysiological techniques, and classical studies have provided fundamental insights into the properties of gap junctional coupling between astrocytes and/or other glial cells (Kettenmann and Ransom, 1988; Dermietzel et al., 1991; Giaume et al., 1991).

In the present study, we employed a patch-clamped-based approach in which gap junctional coupling is assessed via recording of astrocyte isopotentiality (Ma et al., 2016; Kiyoshi et al., 2018; Stephan et al., 2021). Here, the rapid exchange of K^+ with neighboring cells is taken as a measure of the coupling strength of a given astrocyte. Previous reports established that the degree of depolarization of a given astrocyte induced by the K^+-free pipette solution is inversely correlated to tracer coupling with neighboring cells (Zhong et al., 2023), which was roughly confirmed here. Our results confirm the applicability of this approach in cortical layer II/III astrocytes. In contrast to pyramidal neurons and presumed NG2 cells, these astrocytes conferred isopotentiality, which could be attenuated by blocking gap junctions with CBX.

4.2 Brief metabolic stress induces rapid changes in astrocyte coupling strength

Several studies have demonstrated that prolonged energy deprivation results in uncoupling of astrocytes. For example, initial experiments on cultured rodent astrocytes revealed a strong reduction of coupling upon inhibition of oxidative phosphorylation for 16 h (Vera et al., 1996). Similarly, a strong decrease in astrocytic coupling strength was observed in hippocampal slices in response to at least 30 min of metabolic stress (Xu et al., 2010; Lee et al., 2016). Such manipulations mimic the sustained breakdown of energy metabolism in the core region of an ischemic stroke, which leads to a breakdown of ion gradients and massive cell damage and death (Rossi et al., 2007; Moskowitz et al., 2010; van Putten et al., 2021).

In review

Here, we addressed the situation in the penumbra surrounding the ischemic core, which undergoes repetitive waves of spreading depolarizations. These spreading depolarizations are characterized by transient accumulation of extracellular glutamate, cellular depolarization and acidification, loss of cellular ATP, and a reversible increase in $[Na^+]_i$ as well as $[Ca^{2+}]_i$ (Chuquet et al., 2007; Murphy et al., 2008; Pietrobon and Moskowitz, 2014; Dreier and Reiffurth, 2015; Rakers and Petzold, 2017; Rakers et al., 2017; Gerkau et al., 2018; Eitelmann et al., 2022). We have recently shown that exposing acute tissue slices to brief chemical ischemia, induced by a 2-minute perfusion with inhibitors of glycolysis and oxidative phosphorylation, mimics the transient changes in $[Na^+]_i$ and $[Ca^{2+}]_i$ seen during passage of a spreading depolarization in the mouse brain after middle cerebral artery occlusion (Gerkau et al., 2018; Meyer et al., 2022). In addition, this metabolic stress leads to a transient increase in extracellular $[K^+]$, a transient depolarization of astrocytes, a transient decrease in their ATP content, and transient extra- and intracellular acidification (Gerkau et al., 2018; Eitelmann et al., 2022), all further characteristics of spreading depolarizations as described above.

Notably, isopotentiality recordings revealed a pronounced decrease in coupling strength evolving already within 10-20 s after a 2-minute perfusion with metabolic inhibitors. This substantial decrease in coupling strength is similar to that found upon 5 minutes of oxygen-glucose deprivation in HeLa cells expressing Cx43, a major component of astrocytic gap junctions (Sahu et al., 2014). Upon reperfusion with standard saline and wash-out of metabolic inhibitors, respectively, about half of the cells quickly repolarized indicating recoupling. The other half of astrocytes, in contrast, exhibited a depolarization that was maintained as long as the recordings lasted (i.e. for at least 5 min to up to 20 min), indicating more persistent uncoupling. This divergence in their ability to recover indicates a different susceptibility of astrocytes to metabolic stress. Such differential susceptibility was also reported in neocortical slices exposed to oxygen-glucose deprivation. In their study, Benesova and colleagues (2009) identified two astrocyte groups of approximately equal size that differed in their response to energy deprivation based on measurements of E_M and cell swelling. Among others, they found differences in astrocytic $K_{ir}4.1$ expression as well as taurine levels between the two groups and speculated that these were causal for the observed heterogeneity (Benesova et al., 2009). Recent single-cell RNA sequencing data furthermore indicated the presence of five astrocyte subpopulations in the mouse forebrain, two of which (AST2 and 3) were dominant in layers II/III (Batiuk et al., 2020). These two subtypes mainly differed in transcripts related to glutamatergic versus GABAergic neurotransmission. This eventually points towards a differential responsiveness to glutamate, which is reminiscent of an increased susceptibility to glutamate-mediated injury as suggested here (Batiuk et al., 2020).

Taken together, our results thus demonstrate that a brief period of chemical ischemia leads to a rapid partial uncoupling of neocortical astrocytes. Moreover, our data show a differential ability to regain coupling afterwards, indicating a different vulnerability of astrocytes to the transient metabolic stress.

4.3 Causes and possible consequences of astrocyte uncoupling

Gap junctional coupling depends on various factors e.g., expression, trafficking, and de-/phosphorylation of connexins as well as changes in pH_i and $[Ca^{2+}]_i$ (Giaume et al., 2021). Here, we found that acidification of astrocytes by 0.45 pH units indeed caused an immediate decrease in gap junctional coupling in all astrocytes investigated, confirming their rapid modulation by such changes in pH_i. In contrast, acidifying astrocytes by only 0.26 pH units, which mimicked the acidification associated with a 2-minute chemical ischemia, had no effect on coupling. This strongly indicates that the uncoupling of astrocytes upon brief metabolic

stress observed in the present study was primarily independent from the (moderate) intracellular acidification induced by this manipulation.

In the present study, $[Ca^{2+}]_i$ imaging experiments revealed an average $[Ca^{2+}]_i$ increase of about 100 nM. Notably, dampening the Ca^{2+} influx from the extracellular space not only reduced the peak $[Ca^{2+}]_i$ change to about 50 nM, but also the peak depolarization in isopotentiality recordings. Thus, our experiments strongly indicate that astrocyte uncoupling depends on the magnitude of the Ca^{2+} load induced by chemical ischemia. This is consistent with former studies reporting that gap junctions close in response to elevation of $[Ca^{2+}]_i$, (Spray et al., 1982; Muller et al., 1996; Cotrina et al., 1998; Lurtz and Louis, 2007; Giaume et al., 2021).

The functional consequences of a Ca^{2+}-dependent reduction in astrocyte coupling upon brief metabolic stress are currently unclear. This is mainly due to conflicting results regarding the functional role of astrocyte gap junctional coupling in the ischemic brain, which may be at least partly related to opposing actions mediated by gap junction channels versus hemichannels (Contreras et al., 2004; Rovegno and Saez, 2018; Liang et al., 2020; Giaume et al., 2021). On the one hand, there are reports showing that Cx43 knock-out mice exhibit larger infarct volumes, suggesting a protective role (Siushansian et al., 2001; Nakase et al., 2003). On the other hand, some studies describe a gap junction-mediated expansion of cell injury (Lin et al., 1998; Lauritzen et al., 2011). In addition, further studies demonstrated that reduced expression or inhibition of Cx43 results in decreased neuronal death and infarct volume (Rawanduzy et al., 1997; Rami et al., 2001; Li et al., 2015). Similarly, the role of astrocytic gap junctional coupling in the ischemic penumbra is debated. There is evidence that they promote the propagation of spreading depolarizations (Nedergaard et al., 1995; Seidel et al., 2016; EbrahimAmini et al., 2021). However, there are also findings that contradict this hypothesis (Theis et al., 2003; Enger et al., 2015).

Gap junctional coupling carries and supports the propagation of intercellular astrocytic Ca^{2+} waves (Haydon, 2001; Verkhratsky and Nedergaard, 2018). The dissemination of an $[Ca^{2+}]_i$ elevation and of other signaling molecules from an injured astrocyte to its neighbors via gap junctions has been proposed to spread the damage in the syncytium (Contreras et al., 2004; Decrock et al., 2009; De Bock et al., 2014). In the present study, we found that brief metabolic stress led to rapid substantial uncoupling of astrocytes experiencing large $[Ca^{2+}]_i$ increases. During passage of spreading depolarizations in the ischemic penumbra, such Ca^{2+}-dependent uncoupling would separate cells from each other thereby preventing additional Ca^{2+} loads arising from neighboring cells. Notably, a recent study showed that dampening of spreading depolarization-evoked astrocytic Ca^{2+} signals results in decreased extracellular glutamate accumulation, reduced spreading depolarization frequency and burden as well as increased neuronal survival after stroke in a mouse model of focal ischemia (Rakers and Petzold, 2017). We thus propose that disconnecting astrocytes may exert a protective role, helping to confine and reduce spreading of cellular damage in the ischemic penumbra.

5 Conflict of Interest

The authors declare no conflict of interest. The funders had no role in the design of the study, in the collection, analyses, or interpretation of data; in the writing of the manuscript, or in the decision to publish the results.

6 Author Contributions

In review

JS, CRR and SE designed experiments. SE, KE, and LP performed experiments and analyzed data. JS, CRR and SE wrote the manuscript. All authors approved the final version.

7 Funding

This research was funded by the Deutsche Forschungsgemeinschaft (DFG), Research Unit 2795 “Synapses under Stress” to C.R.R. (Ro2327/13-1, 13-2).

8 Acknowledgments

We thank Claudia Roderigo and Simone Durry for excellent technical assistance.

9 Data Availability Statement

The data presented in this study are available on request from the corresponding authors.

10 References

Augustin, V., Bold, C., Wadle, S.L., Langer, J., Jabs, R., Philippot, C., Weingarten, D.J., Rose, C.R., Steinhauser, C., and Stephan, J. (2016). Functional anisotropic panglial networks in the lateral superior olive. *Glia* 64, 1892-1911.

Batiuk, M.Y., Martirosyan, A., Wahis, J., De Vin, F., Marneffe, C., Kusserow, C., Koeppen, J., Viana, J.F., Oliveira, J.F., Voet, T., Ponting, C.P., Belgard, T.G., and Holt, M.G. (2020). Identification of region-specific astrocyte subtypes at single cell resolution. *Nat Commun* 11, 1220.

Benesova, J., Hock, M., Butenko, O., Prajerova, I., Anderova, M., and Chvatal, A. (2009). Quantification of astrocyte volume changes during ischemia in situ reveals two populations of astrocytes in the cortex of GFAP/EGFP mice. *J Neurosci Res* 87, 96-111.

Boison, D., and Steinhauser, C. (2018). Epilepsy and astrocyte energy metabolism. *Glia* 66, 1235-1243.

Chuquet, J., Hollender, L., and Nimchinsky, E.A. (2007). High-resolution in vivo imaging of the neurovascular unit during spreading depression. *J Neurosci* 27, 4036-4044.

Close, B., Banister, K., Baumans, V., Bernoth, E.M., Bromage, N., Bunyan, J., Erhardt, W., Flecknell, P., Gregory, N., Hackbarth, H., Morton, D., and Warwick, C. (1997). Recommendations for euthanasia of experimental animals: Part 2. DGXT of the European Commission. *Lab Anim* 31, 1-32.

Contreras, J.E., Sanchez, H.A., Veliz, L.P., Bukauskas, F.F., Bennett, M.V., and Saez, J.C. (2004). Role of connexin-based gap junction channels and hemichannels in ischemia-induced cell death in nervous tissue. *Brain Res Brain Res Rev* 47, 290-303.

Cotrina, M.L., Kang, J., Lin, J.H., Bueno, E., Hansen, T.W., He, L., Liu, Y., and Nedergaard, M. (1998). Astrocytic gap junctions remain open during ischemic conditions. *J Neurosci* 18, 2520-2537.

De Bock, M., Decrock, E., Wang, N., Bol, M., Vinken, M., Bultynck, G., and Leybaert, L. (2014). The dual face of connexin-based astroglial Ca(2+) communication: a key player in brain physiology and a prime target in pathology. *Biochim Biophys Acta* 1843, 2211-2232.

In review

Decrock, E., Vinken, M., De Vuyst, E., Krysko, D.V., D'herde, K., Vanhaecke, T., Vandenabeele, P., Rogiers, V., and Leybaert, L. (2009). Connexin-related signaling in cell death: to live or let die? *Cell Death Differ* 16, 524-536.

Dermietzel, R., Hertberg, E.L., Kessler, J.A., and Spray, D.C. (1991). Gap junctions between cultured astrocytes: immunocytochemical, molecular, and electrophysiological analysis. *J Neurosci* 11, 1421-1432.

Dirnagl, U., Iadecola, C., and Moskowitz, M.A. (1999). Pathobiology of ischaemic stroke: an integrated view. *Trends Neurosci* 22, 391-397.

Dreier, J.P., and Reiffurth, C. (2015). The stroke-migraine depolarization continuum. *Neuron* 86, 902-922.

Duffy, S., and Macvicar, B.A. (1996). In vitro ischemia promotes calcium influx and intracellular calcium release in hippocampal astrocytes. *J Neurosci* 16, 71-81.

Ebrahimamini, A., Bazzigaluppi, P., Aquilino, M.S., Stefanovic, B., and Carlen, P.L. (2021). Neocortical in vivo focal and spreading potassium responses and the influence of astrocytic gap junctional coupling. *Neurobiol Dis* 147, 105160.

Eitelmann, S., Hirtz, J.J., and Stephan, J. (2019). A Vector-Based Method to Analyze the Topography of Glial Networks. *Int J Mol Sci* 20, 2821.

Eitelmann, S., Petersilie, L., Rose, C.R., and Stephan, J. (2020). Altered Gap Junction Network Topography in Mouse Models for Human Hereditary Deafness. *Int J Mol Sci* 21, 7376.

Eitelmann, S., Stephan, J., Everaerts, K., Durry, S., Pape, N., Gerkau, N.J., and Rose, C.R. (2022). Changes in Astroglial K(+) upon Brief Periods of Energy Deprivation in the Mouse Neocortex. *Int J Mol Sci* 23, 4836.

Enger, R., Tang, W., Vindedal, G.F., Jensen, V., Johannes Helm, P., Sprengel, R., Looger, L.L., and Nagelhus, E.A. (2015). Dynamics of Ionic Shifts in Cortical Spreading Depression. *Cereb Cortex* 25, 4469-4476.

Gerkau, N.J., Rakers, C., Durry, S., Petzold, G.C., and Rose, C.R. (2018). Reverse NCX Attenuates Cellular Sodium Loading in Metabolically Compromised Cortex. *Cereb Cortex* 28, 4264-4280.

Giaume, C., Fromaget, C., El Aoumari, A., Cordier, J., Glowinski, J., and Gros, D. (1991). Gap junctions in cultured astrocytes: single-channel currents and characterization of channel-forming protein. *Neuron* 6, 133-143.

Giaume, C., Naus, C.C., Saez, J.C., and Leybaert, L. (2021). Glial Connexins and Pannexins in the Healthy and Diseased Brain. *Physiol Rev* 101, 93-145.

Haydon, P.G. (2001). GLIA: listening and talking to the synapse. *Nat Rev Neurosci* 2, 185-193.

Hinzman, J.M., Andaluz, N., Shutter, L.A., Okonkwo, D.O., Pahl, C., Strong, A.J., Dreier, J.P., and Hartings, J.A. (2014). Inverse neurovascular coupling to cortical spreading depolarizations in severe brain trauma. *Brain* 137, 2960-2972.

Hosli, L., Binini, N., Ferrari, K.D., Thieren, L., Looser, Z.J., Zuend, M., Zanker, H.S., Berry, S., Holub, M., Mobius, W., Ruhwedel, T., Nave, K.A., Giaume, C., Weber, B., and Saab, A.S. (2022). Decoupling astrocytes in adult mice impairs synaptic plasticity and spatial learning. *Cell Rep* 38, 110484.

In review

Houades, V., Koulakoff, A., Ezan, P., Seif, I., and Giaume, C. (2008). Gap junction-mediated astrocytic networks in the mouse barrel cortex. *J Neurosci* 28, 5207-5217.

Kafitz, K.W., Meier, S.D., Stephan, J., and Rose, C.R. (2008). Developmental profile and properties of sulforhodamine 101-Labeled glial cells in acute brain slices of rat hippocampus. *J Neurosci Methods* 169, 84-92.

Kettenmann, H., and Ransom, B.R. (1988). Electrical coupling between astrocytes and between oligodendrocytes studied in mammalian cell cultures. *Glia* 1, 64-73.

Kiyoshi, C.M., Du, Y., Zhong, S., Wang, W., Taylor, A.T., Xiong, B., Ma, B., Terman, D., and Zhou, M. (2018). Syncytial isopotentiality: A system-wide electrical feature of astrocytic networks in the brain. *Glia* 66, 2756-2769.

Kraig, R.P., Pulsinelli, W.A., and Plum, F. (1985). Hydrogen ion buffering during complete brain ischemia. *Brain Res* 342, 281-290.

Langer, J., Stephan, J., Theis, M., and Rose, C.R. (2012). Gap junctions mediate intercellular spread of sodium between hippocampal astrocytes in situ. *Glia* 60, 239-252.

Lauritzen, M., Dreier, J.P., Fabricius, M., Hartings, J.A., Graf, R., and Strong, A.J. (2011). Clinical relevance of cortical spreading depression in neurological disorders: migraine, malignant stroke, subarachnoid and intracranial hemorrhage, and traumatic brain injury. *J Cereb Blood Flow Metab* 31, 17-35.

Lee, C.Y., Dallerac, G., Ezan, P., Anderova, M., and Rouach, N. (2016). Glucose Tightly Controls Morphological and Functional Properties of Astrocytes. *Front Aging Neurosci* 8, 82.

Lerchundi, R., Kafitz, K.W., Winkler, U., Farfers, M., Hirrlinger, J., and Rose, C.R. (2019). FRET-based imaging of intracellular ATP in organotypic brain slices. *J Neurosci Res* 97, 933-945.

Li, X., Zhao, H., Tan, X., Kostrzewa, R.M., Du, G., Chen, Y., Zhu, J., Miao, Z., Yu, H., Kong, J., and Xu, X. (2015). Inhibition of connexin43 improves functional recovery after ischemic brain injury in neonatal rats. *Glia* 63, 1553-1567.

Liang, Z., Wang, X., Hao, Y., Qiu, L., Lou, Y., Zhang, Y., Ma, D., and Feng, J. (2020). The Multifaceted Role of Astrocyte Connexin 43 in Ischemic Stroke Through Forming Hemichannels and Gap Junctions. *Front Neurol* 11, 703.

Lin, J.H., Weigel, H., Cotrina, M.L., Liu, S., Bueno, E., Hansen, A.J., Hansen, T.W., Goldman, S., and Nedergaard, M. (1998). Gap-junction-mediated propagation and amplification of cell injury. *Nat Neurosci* 1, 494-500.

Lurtz, M.M., and Louis, C.F. (2007). Intracellular calcium regulation of connexin43. *Am J Physiol Cell Physiol* 293, C1806-1813.

Ma, B., Buckalew, R., Du, Y., Kiyoshi, C.M., Alford, C.C., Wang, W., Mctigue, D.M., Enyeart, J.J., Terman, D., and Zhou, M. (2016). Gap junction coupling confers isopotentiality on astrocyte syncytium. *Glia* 64, 214-226.

Mazaud, D., Capano, A., and Rouach, N. (2021). The many ways astroglial connexins regulate neurotransmission and behavior. *Glia* 69, 2527-2545.

Meyer, J., Gerkau, N.J., Kafitz, K.W., Patting, M., Jolmes, F., Henneberger, C., and Rose, C.R. (2022). Rapid Fluorescence Lifetime Imaging Reveals That TRPV4 Channels Promote Dysregulation of Neuronal Na(+) in Ischemia. *J Neurosci* 42, 552-566.

In review

Mishra, P., Pandey, C.M., Singh, U., Gupta, A., Sahu, C., and Keshri, A. (2019). Descriptive statistics and normality tests for statistical data. *Ann Card Anaesth* 22**,** 67-72.

Moshrefi-Ravasdjani, B., Hammel, E.L., Kafitz, K.W., and Rose, C.R. (2017). Astrocyte Sodium Signalling and Panglial Spread of Sodium Signals in Brain White Matter. *Neurochem Res* 42**,** 2505-2518.

Moskowitz, M.A., Lo, E.H., and Iadecola, C. (2010). The science of stroke: mechanisms in search of treatments. *Neuron* 67**,** 181-198.

Muller, T., Moller, T., Neuhaus, J., and Kettenmann, H. (1996). Electrical coupling among Bergmann glial cells and its modulation by glutamate receptor activation. *Glia* 17**,** 274-284.

Murphy, T.H., Li, P., Betts, K., and Liu, R. (2008). Two-photon imaging of stroke onset in vivo reveals that NMDA-receptor independent ischemic depolarization is the major cause of rapid reversible damage to dendrites and spines. *J Neurosci* 28**,** 1756-1772.

Nakase, T., Fushiki, S., Sohl, G., Theis, M., Willecke, K., and Naus, C.C. (2003). Neuroprotective role of astrocytic gap junctions in ischemic stroke. *Cell Commun Adhes* 10**,** 413-417.

Nayak, B.K., and Hazra, A. (2011). How to choose the right statistical test? *Indian J Ophthalmol* 59**,** 85-86.

Nedergaard, M., Cooper, A.J., and Goldman, S.A. (1995). Gap junctions are required for the propagation of spreading depression. *J Neurobiol* 28**,** 433-444.

Nedergaard, M., Kraig, R.P., Tanabe, J., and Pulsinelli, W.A. (1991). Dynamics of interstitial and intracellular pH in evolving brain infarct. *Am J Physiol* 260**,** R581-588.

Pannasch, U., Vargova, L., Reingruber, J., Ezan, P., Holcman, D., Giaume, C., Sykova, E., and Rouach, N. (2011). Astroglial networks scale synaptic activity and plasticity. *Proc Natl Acad Sci U S A* 108**,** 8467-8472.

Perkins, K.L. (2006). Cell-attached voltage-clamp and current-clamp recording and stimulation techniques in brain slices. *J Neurosci Methods* 154**,** 1-18.

Pietrobon, D., and Moskowitz, M.A. (2014). Chaos and commotion in the wake of cortical spreading depression and spreading depolarizations. *Nat Rev Neurosci* 15**,** 379-393.

Rakers, C., and Petzold, G.C. (2017). Astrocytic calcium release mediates peri-infarct depolarizations in a rodent stroke model. *J Clin Invest* 127**,** 511-516.

Rakers, C., Schmid, M., and Petzold, G.C. (2017). TRPV4 channels contribute to calcium transients in astrocytes and neurons during peri-infarct depolarizations in a stroke model. *Glia* 65**,** 1550-1561.

Rami, A., Volkmann, T., and Winckler, J. (2001). Effective Reduction of Neuronal Death by Inhibiting Gap Junctional Intercellular Communication in a Rodent Model of Global Transient Cerebral Ischemia. *Experimental Neurology* 170**,** 297-304.

Rawanduzy, A., Hansen, A., Hansen, T.W., and Nedergaard, M. (1997). Effective reduction of infarct volume by gap junction blockade in a rodent model of stroke. *J Neurosurg* 87**,** 916-920.

Rossi, D.J., Brady, J.D., and Mohr, C. (2007). Astrocyte metabolism and signaling during brain ischemia. *Nat Neurosci* 10**,** 1377-1386.

In review

Rouach, N., Koulakoff, A., Abudara, V., Willecke, K., and Giaume, C. (2008). Astroglial metabolic networks sustain hippocampal synaptic transmission. *Science* 322, 1551-1555.

Rovegno, M., and Saez, J.C. (2018). Role of astrocyte connexin hemichannels in cortical spreading depression. *Biochim Biophys Acta Biomembr* 1860, 216-223.

Sahu, G., Sukumaran, S., and Bera, A.K. (2014). Pannexins form gap junctions with electrophysiological and pharmacological properties distinct from connexins. *Sci Rep* 4, 4955.

Schindelin, J., Arganda-Carreras, I., Frise, E., Kaynig, V., Longair, M., Pietzsch, T., Preibisch, S., Rueden, C., Saalfeld, S., Schmid, B., Tinevez, J.Y., White, D.J., Hartenstein, V., Eliceiri, K., Tomancak, P., and Cardona, A. (2012). Fiji: an open-source platform for biological-image analysis. *Nat Methods* 9, 676-682.

Seidel, J.L., Escartin, C., Ayata, C., Bonvento, G., and Shuttleworth, C.W. (2016). Multifaceted roles for astrocytes in spreading depolarization: A target for limiting spreading depolarization in acute brain injury? *Glia* 64, 5-20.

Siushansian, R., Bechberger, J.F., Cechetto, D.F., Hachinski, V.C., and Naus, C.C. (2001). Connexin43 null mutation increases infarct size after stroke. *J Comp Neurol* 440, 387-394.

Smith, M.L., Von Hanwehr, R., and Siesjo, B.K. (1986). Changes in extra- and intracellular pH in the brain during and following ischemia in hyperglycemic and in moderately hypoglycemic rats. *J Cereb Blood Flow Metab* 6, 574-583.

Spray, D.C., Stern, J.H., Harris, A.L., and Bennett, M.V. (1982). Gap junctional conductance: comparison of sensitivities to H and Ca ions. *Proc Natl Acad Sci U S A* 79, 441-445.

Stephan, J., Eitelmann, S., and Zhou, M. (2021). Approaches to Study Gap Junctional Coupling. *Front Cell Neurosci* 15, 640406.

Struyk, A. (2005). Ions in the Brain: Normal Function, Seizures, and Stroke. *Archives of Neurology* 62, 503.

Theis, M., Jauch, R., Zhuo, L., Speidel, D., Wallraff, A., Doring, B., Frisch, C., Sohl, G., Teubner, B., Euwens, C., Huston, J., Steinhauser, C., Messing, A., Heinemann, U., and Willecke, K. (2003). Accelerated hippocampal spreading depression and enhanced locomotory activity in mice with astrocyte-directed inactivation of connexin43. *J Neurosci* 23, 766-776.

Van Putten, M., Fahlke, C., Kafitz, K.W., Hofmeijer, J., and Rose, C.R. (2021). Dysregulation of Astrocyte Ion Homeostasis and Its Relevance for Stroke-Induced Brain Damage. *Int J Mol Sci* 22.

Vera, B., Sanchez-Abarca, L.I., Bolanos, J.P., and Medina, J.M. (1996). Inhibition of astrocyte gap junctional communication by ATP depletion is reversed by calcium sequestration. *FEBS Lett* 392, 225-228.

Verkhratsky, A., and Nedergaard, M. (2018). Physiology of Astroglia. *Physiol Rev* 98, 239-389.

Wadle, S.L., Augustin, V., Langer, J., Jabs, R., Philippot, C., Weingarten, D.J., Rose, C.R., Steinhauser, C., and Stephan, J. (2018). Anisotropic Panglial Coupling Reflects Tonotopic Organization in the Inferior Colliculus. *Front Cell Neurosci* 12, 431.

In review

Wallraff, A., Kohling, R., Heinemann, U., Theis, M., Willecke, K., and Steinhauser, C. (2006). The impact of astrocytic gap junctional coupling on potassium buffering in the hippocampus. *J Neurosci* 26**,** 5438-5447.

Xu, G., Wang, W., Kimelberg, H.K., and Zhou, M. (2010). Electrical coupling of astrocytes in rat hippocampal slices under physiological and simulated ischemic conditions. *Glia* 58**,** 481-493.

Zhong, S., Kiyoshi, C.M., Du, Y., Wang, W., Luo, Y., Wu, X., Taylor, A.T., Ma, B., Aten, S., Liu, X., and Zhou, M. (2023). Genesis of a functional astrocyte syncytium in the developing mouse hippocampus. *Glia*.

Ziemens, D., Oschmann, F., Gerkau, N.J., and Rose, C.R. (2019). Heterogeneity of Activity-Induced Sodium Transients between Astrocytes of the Mouse Hippocampus and Neocortex: Mechanisms and Consequences. *J Neurosci* 39**,** 2620-2634.

11 Figure legends

Figure 1 | Syncytial isopotentiality of cortical astrocytes. A) Schematic drawing illustrating K^+ diffusion within the syncytium under different conditions. In whole-cell configuration, the astrocyte is dialyzed by the K^+-free pipette solution (0 mM K^+). Under resting conditions, $[K^+]_i$ is expected to be partially buffered within the syncytium (A_1). When using the gap junction blocker carbenoxolone (CBX), no buffering occurs and the cytosol is expected to be completely dialyzed (A_2). **B-D)** Experimental evidence for isopotentiality in neocortical astrocytes. E_M was recorded with a pipette solution containing either 148 mM K^+ (B) or 0 mM K^+ (C, D). With 148 mM K^+, there was no difference between initial E_M and E_M determined after a few minutes (B_{1-2}). Simultaneous tracer injection of Alexa Fluor 568 (AF568) and neurobiotin (Nb) into the recorded cell revealed coupling to several neighboring cells (B_3). Upon patching an astrocyte with 0 mM K^+, in contrast, initial E_M depolarized to a new steady-state E_M (C_{1-2}). Again, simultaneous tracer injection revealed coupling to several neighboring cells (C_3). In a slice pre-incubated with CBX (100 µM), 0 mM K^+ resulted in a strong depolarization of the patched astrocyte (D_{1-2}). In addition, tracer injection labeled only the patched cell (D_3). **E-F)** Patching a pyramidal neuron (E) or a presumed NG2 cell (F) with 0 mM K^+ resulted in a strong and multiphasic depolarization. The insets show that the neuron starts firing action potentials during the early phase of depolarization (E), whereas the presumed NG2 cell does not generate action potentials (F). The dashed lines in B_1, C_1, D_1, E, and F indicate the initial E_M, directly after rupturing the membrane patch (arrowheads). Dot plots in B_2, C_2, and D_2 show individual data points (grey diamonds), mean (squares), and SD (whiskers) of initial E_M and peak E_M determined after a few minutes. **G)** Box plots illustrating that uncoupled cells exhibited a strongly depolarized peak E_M in isopotentiality recordings as compared to gap junction-coupled astrocytes under control conditions. Shown are individual data points (grey diamonds), mean (squares), median (horizontal line), SD (box), and min/max (whiskers). Significance levels are indicated by asterisks: ***$p < 0.001$. *n.s.*: not significant.

Figure 2 | Effect of chemical ischemia on astrocyte syncytial isopotentiality. A) Cell-attached (CA) recording of astrocyte E_M. The recording of a single astrocyte in A_1 shows a depolarization followed by a transient hyperpolarization and recovery to the baseline E_M evoked by a 2-minute perfusion with metabolic inhibitors ("chemical ischemia", grey bar). Dashed line indicates baseline E_M. The plots on the right illustrate changes in E_M (A_2) and maximal depolarization (ΔE_M; A_3). **B)** Isopotentiality recording in an astrocyte exposed to chemical ischemia (grey bars; B_1). The astrocyte depolarized from an initial E_M to peak E_M and subsequently recovered. The dashed line indicates the initial E_M recorded upon membrane rupture (arrowhead). The dot plot illustrates changes in E_M of all cells recorded; paired data

In review

are connected by lines (B_2). B_3 shows box plots comparing maximal changes in E_M in response to chemical ischemia in cell-attached mode (CA, see A_2) and in isopotentiality recordings. "Ctrl": peak E_M of astrocytes in isopotentiality measurements under control conditions (see Figure $1C_2$). The dashed line highlights the chemical ischemia-induced mean depolarization recorded in cell-attached mode. Box plots in A_3 and B_3 show individual data points (grey diamonds), mean (squares), median (horizontal line), SD (box), and min/max (whiskers). Significance levels are indicated by asterisks: $*p < 0.1$, $***p < 0.001$. *n.s.*: not significant.

Figure 3 | Effect of chemical ischemia on intercellular spread of Na^+. A) Na^+ spread during resting conditions. Regions of interest (ROIs) were drawn around somata of SR101-labeled neocortical astrocytes, which were loaded with the Na^+ indicator SBFI-AM (a_1-a_5; A_1). Changes in somatic $[Na^+]_i$ of astrocytes a_1-a_5 in response to brief electrical stimulation of astrocyte a_1, depicted as changes in somatic SBFI fluorescence (arrowhead, vertical dashed line; A_2). The graph in A_3 shows peak amplitudes of $[Na^+]_i$ increases in individual astrocytes (circles) relative to the amplitude of the directly stimulated cell versus the distance. Data from individual experiments were fit with mono-exponential decay functions (light grey lines). The bold black line shows the decay function of the average length constant (λ; $R^2 = 0.822$). **B)** Na^+ spread during chemical ischemia. ROIs were drawn around somata of SR101-labeled, SBFI-loaded astrocytes, which were loaded with the Na^+ indicator SBFI-AM (B_1). 2 min of chemical ischemia (grey box) induced a $[Na^+]_i$ increase in all astrocytes recorded from (b_1-b_4; B_2). At the time point when switching back to standard ACSF, astrocyte b_1 was subjected to electroporation (arrowhead, vertical dashed line), inducing an additional $[Na^+]_i$ increase in the stimulated (b_1) as well as in neighboring cells (b_2-b_4). The dashed red lines represent the extrapolated progression of chemical ischemia-induced Na^+ transients allowing the estimation of electroporation-induced additional Na^+ load (see text for details). The graph in B_3 shows peak amplitudes of $[Na^+]_i$ increases in individual astrocytes (circles) relative to the amplitude of the directly stimulated cell versus the distance. The electroporation was performed right after termination of metabolic stress. Light red lines refer to individual experiments. The bold red line shows the decay function of the average λ ($R^2 = 0.777$).

Figure 4 | Role of pH_i in alteration of gap junctional coupling. A) Measurement of pH_i. SR101-labeled astrocytes were loaded with the pH indicator BCECF (A_1). Changes in pH_i (depicted as relative changes in BCECF fluorescence) were recorded in response to a 2-minute chemical ischemia (A_2) as well as upon perfusion with low $[HCO_3^-]_e$ for 2 min (A_3) and for 5 min (A_4). Box plots illustrate peak acidification in astrocytes induced by the three different manipulations (A_5). **B-D)** Isopotentiality of astrocytes was recorded in slices treated for 2 min (B) or 5 min (C) with low $[HCO_3^-]_e$. The plots in B_2 and B_3 illustrate changes in E_M; paired data points derived from individual cells are connected by lines. Box plots in D show peak E_M in isopotentiality recordings in response to chemical ischemia and application of $[HCO_3^-]_e$ for 2 and 5 min. The box plots in A_5 and D show individual data points (grey diamonds), mean (squares), median (horizontal line), SD (box), and min/max (whiskers). Significance levels are indicated by asterisks: $*p < 0.05$, $**p < 0.01$, $***p < 0.001$. *n.s.*: not significant.

Figure 5 | Role of $[Ca^{2+}]_i$ in alteration of gap junctional coupling. A) Measurement of $[Ca^{2+}]_i$. SR101-labeled astrocytes were loaded with the Ca^{2+} indicator OGB-1 (A_1). Changes in $[Ca^{2+}]_i$ (depicted as relative changes in OGB-1 fluorescence) are shown for individual astrocytes in response to a 2-minute chemical ischemia (A_2) as well as a 2-minute chemical ischemia in the nominal absence of extracellular Ca^{2+} ("0 $[Ca^{2+}]_e$") (A_3) and in the presence of blockers of NCX (KB-R), NMDA receptors (AP5) as well as TRPV4 channels (HC) (A_4). Box plots depict changes in $[Ca^{2+}]_i$ directly after 2 min of chemical ischemia in control

Manuscript

condition, in the absence of $[Ca^{2+}]_e$, as well as in the presence of blockers of Ca^{2+} influx (A_5). **B-D)** Isopotentiality of astrocytes was recorded in 0 $[Ca^{2+}]_e$ (B) or with blockers of Ca^{2+} influx (C). Grey bars show the periods when slices were exposed for 2 min to chemical ischemia. The plots in B_2 and C_2 illustrate changes in E_M of all cells recorded. Data points derived from individual cells are connected by lines. The box plots depict peak E_M in isopotentiality recordings in response to chemical ischemia (see Figure 2B) and in cells exposed to reduction of Ca^{2+} influx (D). Box plots in A_5 and D show individual data points (grey diamonds), mean (squares), median (horizontal line), SD (box), and min/max (whiskers). Significance levels are indicated by asterisks: *$p < 0.05$, **$p < 0.01$, ***$p < 0.001$. *n.s.*: not significant.

In review

Figure 1.TIFF

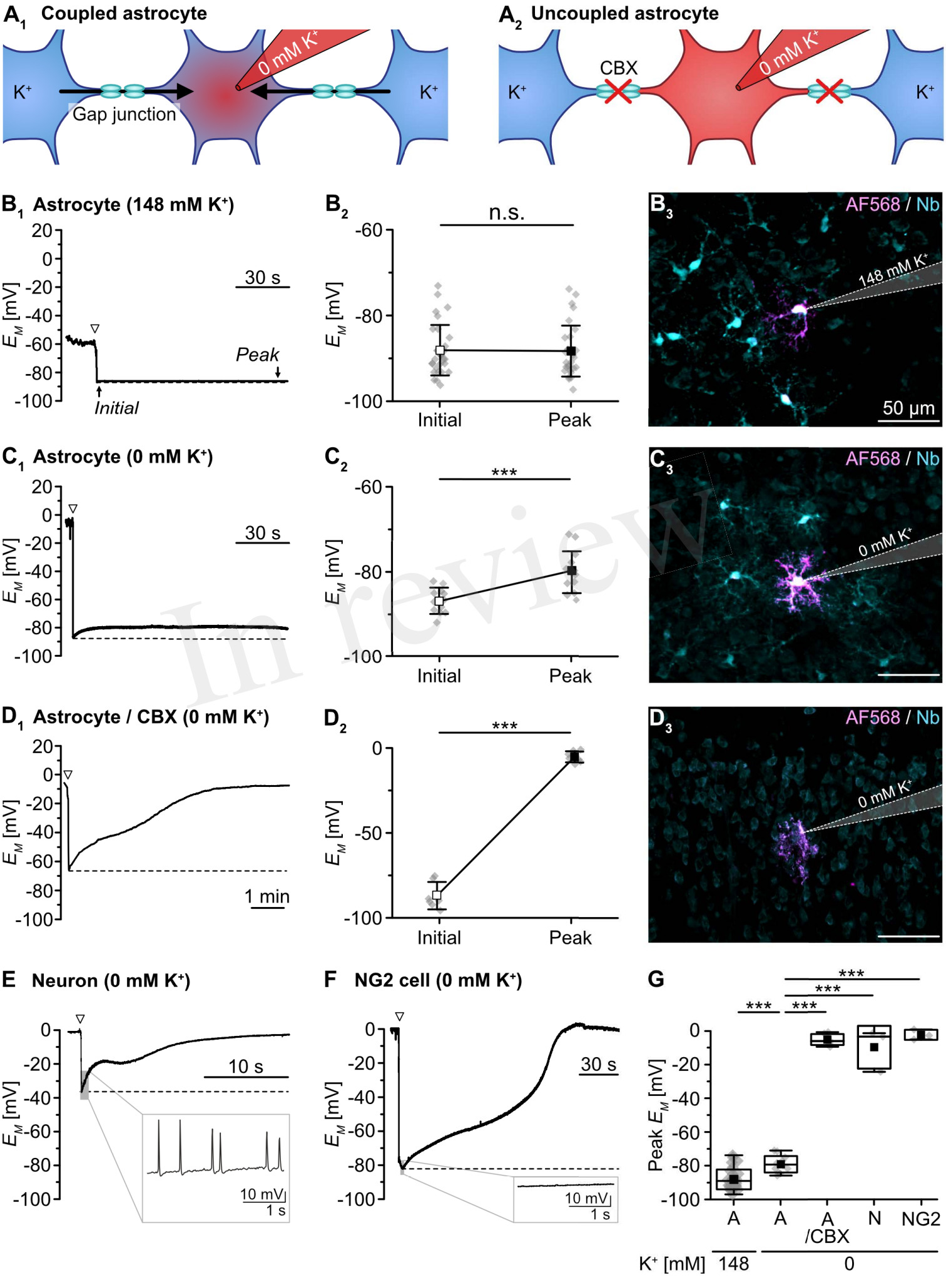

In review

Figure 2.TIFF

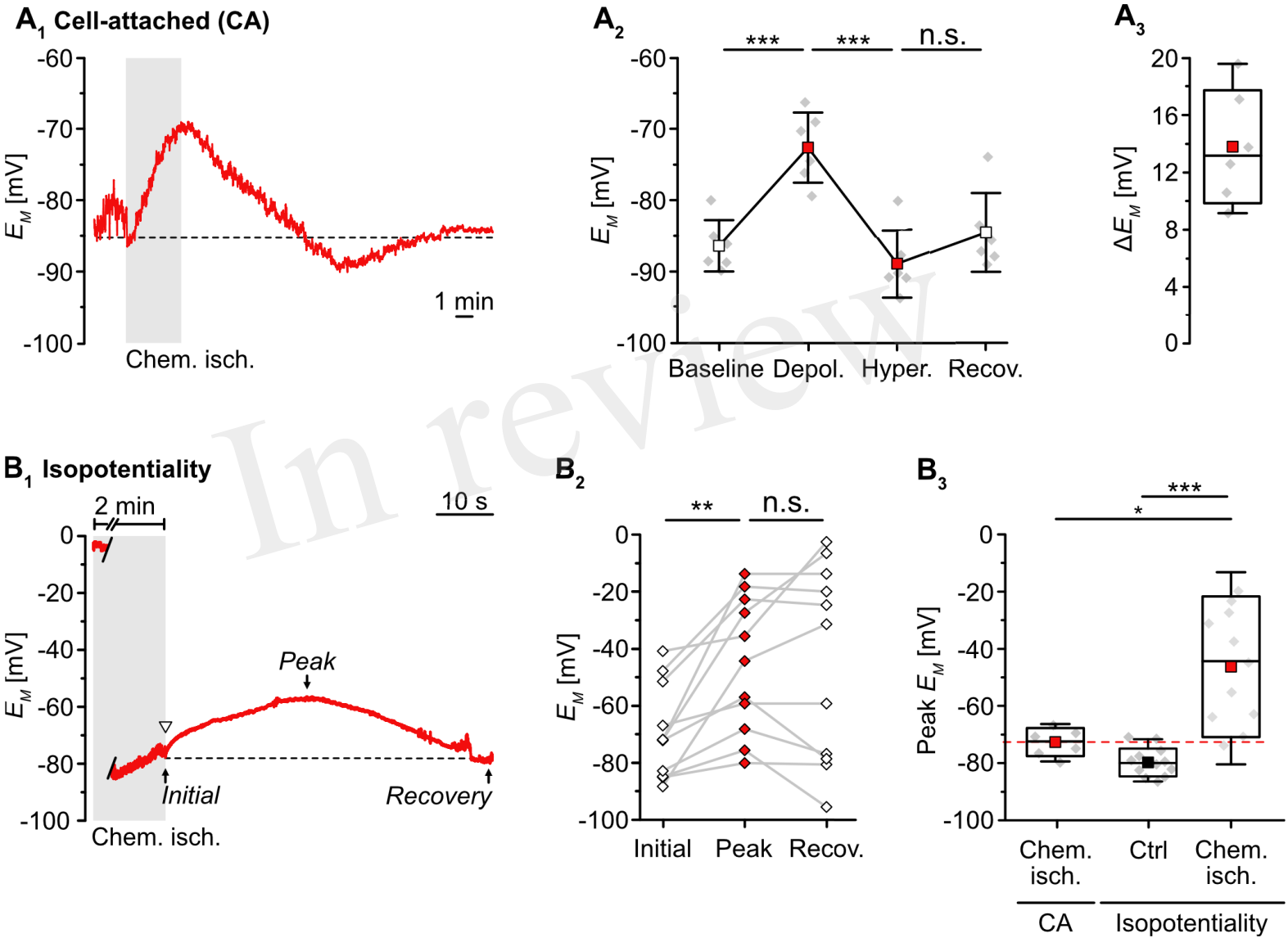

In review

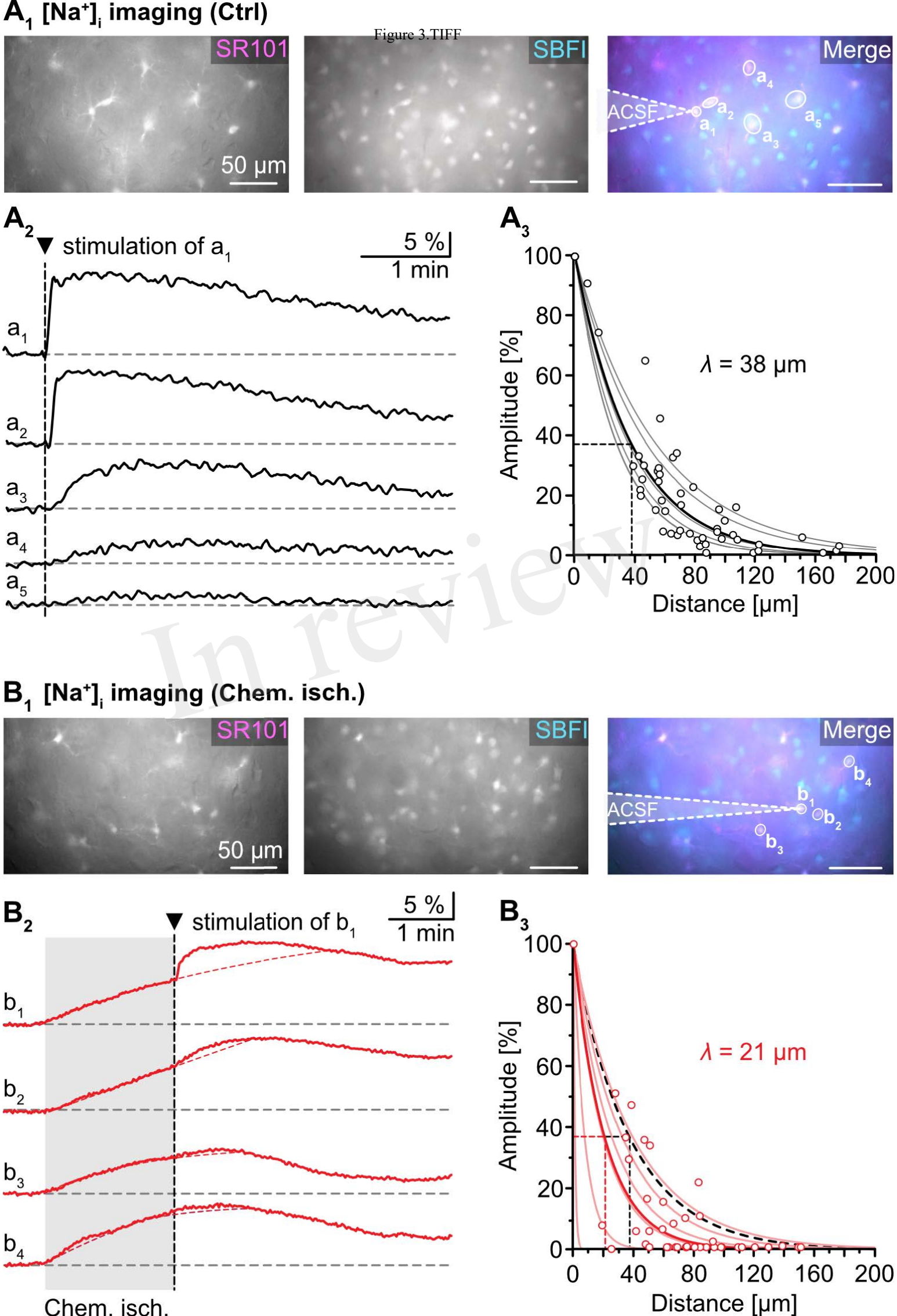

Figure 3.TIFF
In review

Figure 4.TIFF

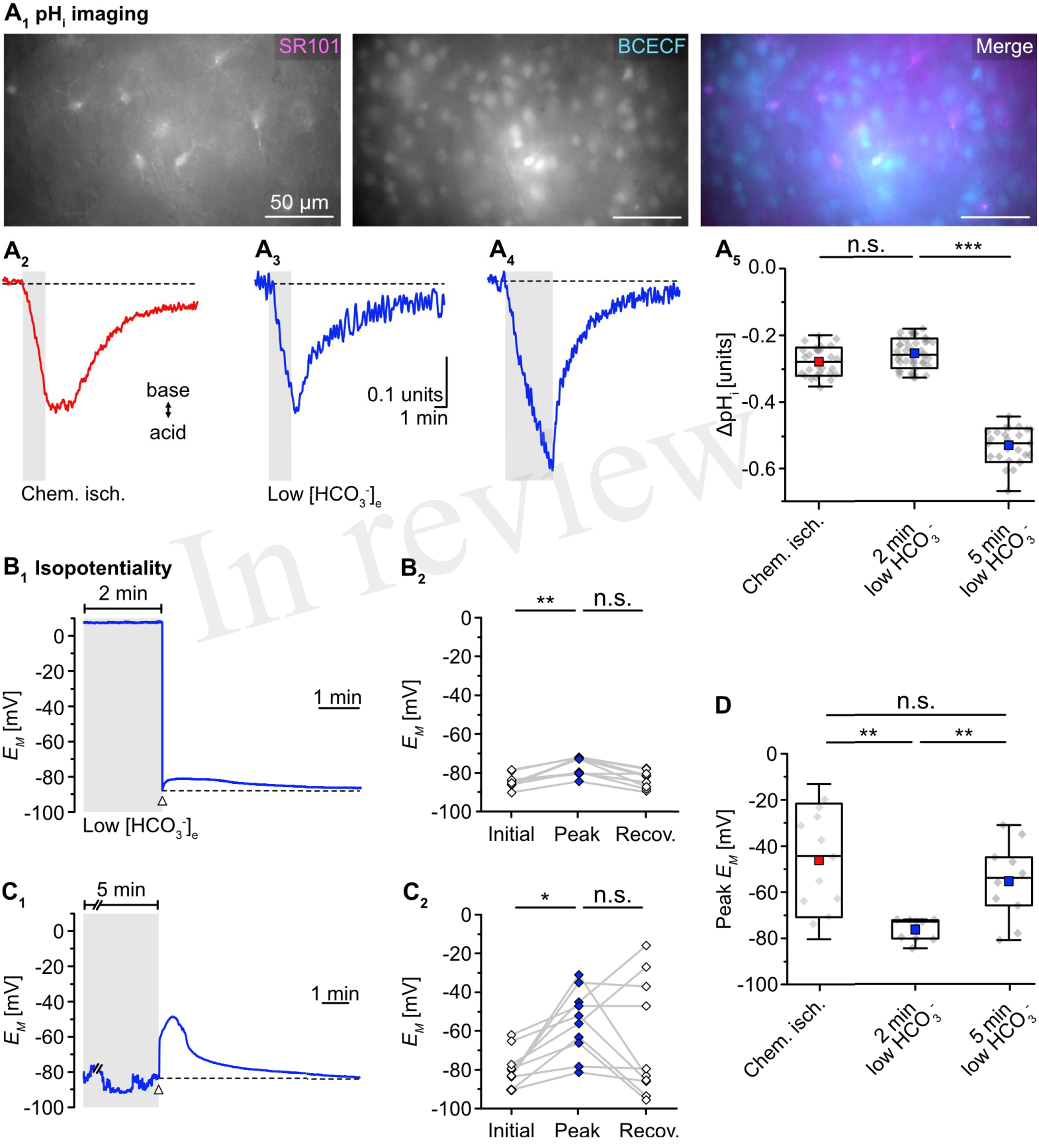

In review

Figure 5.TIFF

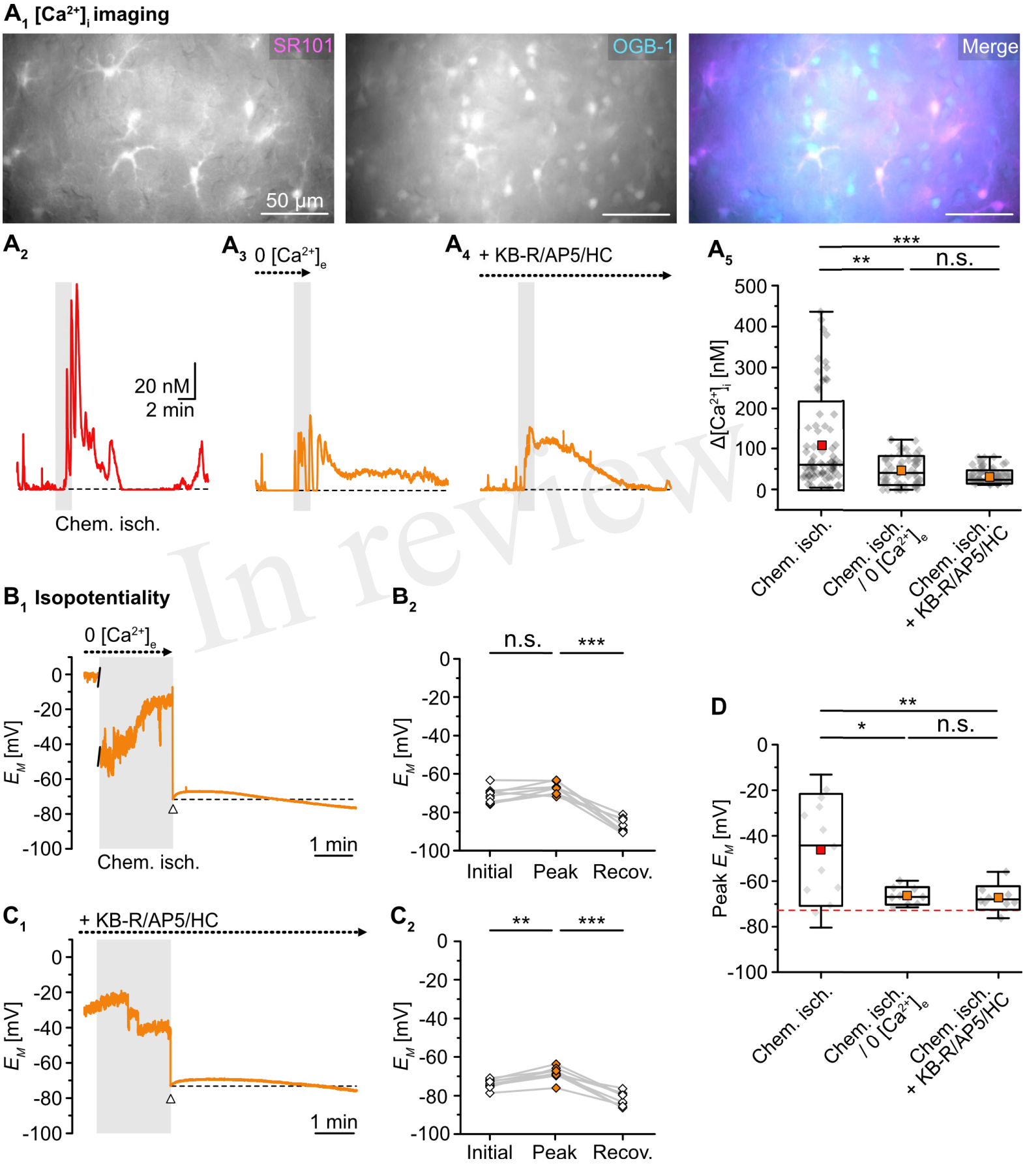

In review

Changes in Astroglial K^+ upon Brief Periods of Energy Deprivation in the Mouse Neocortex

Sara Eitelmann*, Jonathan Stephan*, Katharina Everaerts, Simone Durry, Nils Pape, Niklas Jonny Gerkau and Christine Rosemarie Rose

Institut für Neurobiologie, Heinrich-Heine-Universität Düsseldorf, Düsseldorf, Deutschland

Int J Mol Sci. 2022 Apr 27;23(9):4836. IF 2021: 6.2.

Eigener Beitrag

Experimente:
- Patch-Clamp-Messungen zur Berechnung der relativen Na^+/K^+-Permeabilität (α)

Analyse:
- E_M (Abbildung 2B) und pH_o (Abbildung 5A)
- Berechnung von α, $[K^+]_i$ (Abbildung 4B), $[HCO_3^-]_e$ und $[HCO_3^-]_i$ (Abbildung 5C-D) und Anionen-Lücke (Abbildung 6)
- Statistische Analyse aller Daten

Manuskript:
- Erstellung aller Abbildungen (Abbildung 1-7)
- Beitrag zur Konzeptualisierung und Methodik der Studie
- Beitrag zur Verfassung und Überarbeitung des Manuskripts

International Journal of
Molecular Sciences

MDPI

Article

Changes in Astroglial K^+ upon Brief Periods of Energy Deprivation in the Mouse Neocortex

Sara Eitelmann †, Jonathan Stephan †, Katharina Everaerts, Simone Durry, Nils Pape, Niklas J. Gerkau and Christine R. Rose *

Institute of Neurobiology, Heinrich Heine University Düsseldorf, Universitätsstraße 1, D-40225 Düsseldorf, Germany; sara.eitelmann@hhu.de (S.E.); jonathan.stephan@hhu.de (J.S.); katharina.everaerts@hhu.de (K.E.); simone.durry@hhu.de (S.D.); nils.pape@hhu.de (N.P.); niklas.gerkau@hhu.de (N.J.G.)

* Correspondence: rose@hhu.de

† These authors contributed equally to this work.

Abstract: Malfunction of astrocytic K^+ regulation contributes to the breakdown of extracellular K^+ homeostasis during ischemia and spreading depolarization events. Studying astroglial K^+ changes is, however, hampered by a lack of suitable techniques. Here, we combined results from fluorescence imaging, ion-selective microelectrodes, and patch-clamp recordings in murine neocortical slices with the calculation of astrocytic $[K^+]$. Brief chemical ischemia caused a reversible ATP reduction and a transient depolarization of astrocytes. Moreover, astrocytic $[Na^+]$ increased by 24 mM and extracellular $[Na^+]$ decreased. Extracellular $[K^+]$ increased, followed by an undershoot during recovery. Feeding these data into the Goldman–Hodgkin–Katz equation revealed a baseline astroglial $[K^+]$ of 146 mM, an initial K^+ loss by 43 mM upon chemical ischemia, and a transient K^+ overshoot of 16 mM during recovery. It also disclosed a biphasic mismatch in astrocytic Na^+/K^+ balance, which was initially ameliorated, but later aggravated by accompanying changes in pH and bicarbonate, respectively. Altogether, our study predicts a loss of K^+ from astrocytes upon chemical ischemia followed by a net gain. The overshooting K^+ uptake will promote low extracellular K^+ during recovery, likely exerting a neuroprotective effect. The resulting late cation/anion imbalance requires additional efflux of cations and/or influx of anions, the latter eventually driving delayed astrocyte swelling.

Keywords: astrocyte; potassium; sodium; pH; extracellular space; ischemia; imaging; ATeam; ion-sensitive microelectrodes; patch-clamp

check for updates

Citation: Eitelmann, S.; Stephan, J.; Everaerts, K.; Durry, S.; Pape, N.; Gerkau, N.J.; Rose, C.R. Changes in Astroglial K^+ upon Brief Periods of Energy Deprivation in the Mouse Neocortex. *Int. J. Mol. Sci.* **2022**, *23*, 4836. https://doi.org/10.3390/ijms23094836

Academic Editor: Isidro Ferrer

Received: 30 March 2022
Accepted: 24 April 2022
Published: 27 April 2022

Publisher's Note: MDPI stays neutral with regard to jurisdictional claims in published maps and institutional affiliations.

Copyright: © 2022 by the authors. Licensee MDPI, Basel, Switzerland. This article is an open access article distributed under the terms and conditions of the Creative Commons Attribution (CC BY) license (https://creativecommons.org/licenses/by/4.0/).

1. Introduction

A classical function of astrocytes is the regulation and maintenance of a low potassium concentration in the extracellular space ($[K^+]_o$) [1]. By taking up K^+ released from active neurons, astrocytes keep $[K^+]_o$ below the so-called ceiling level of about 10 mM [2–4]. This prevents detrimental accumulation of K^+ in the extracellular space, protecting neurons from excessive K^+-induced depolarization [5,6]. The mechanisms of astrocytic K^+ uptake involve plasma membrane transporters as well as K^+ channels [7,8]. Astrocytic Na^+/K^+-ATPase (NKA) apparently plays a predominant role, but the sodium-potassium-chloride cotransporter 1 (NKCC1) is likely to aid K^+ clearance upon more severe rises in $[K^+]_o$ [9,10].

Maintenance of $[K^+]_o$ by astrocytes is thus largely dependent on their NKA activity and on intact energy metabolism. In the core region of an ischemic stroke, failure of energy metabolism results in a breakdown of astrocyte K^+ regulation and $[K^+]_o$ homeostasis [5,6,11,12]. A failure of astrocytic K^+ uptake will not only hamper clearance of extracellular K^+, but will also cause a loss of K^+ from astrocytes, contributing to the rise in $[K^+]_o$ and promoting neuronal depolarization during energy failure [13,14]. As opposed to the ischemic core region, available energy resources in the neighboring penumbra may allow full recovery upon timely reperfusion [15]. The penumbra, however, is exposed to

repeated waves of spreading depolarizations initiating from the core tissue [16]. Spreading depolarizations impose additional stress onto the cells of the penumbra and promote the gradual expansion of the ischemic core [15,17,18]. They are characterized by transient accumulation of extracellular glutamate, cellular depolarization, loss of cellular ATP, and a reversible increase in intracellular Na^+ as well as Ca^{2+} concentrations [19,20]. A hallmark and one of the earliest signs of a developing spreading depolarization is an increase in $[K^+]_o$, suggesting that a disturbance in astrocytic K^+ regulation represents an important initial event [16,21].

Despite its high relevance for the pathogenesis of spreading depolarizations and cell damage upon brain ischemia, quantitative data on astrocytic $[K^+]_i$ during energy failure are extremely rare [12]. This is mostly due to technical hurdles. Available tools include ion-sensitive microelectrodes, which are mostly suited for the measurement of (low) $[K^+]_o$ [22]. A limited toolbox for fluorescence imaging with genetically-encoded or chemical K^+ indicator dyes exists [23–26], but these have not yet been successfully employed in astrocytes in situ.

As an alternative to direct measurement, former studies approached astroglial $[K^+]_i$ mathematically, exploiting the dominating plasma membrane permeability of astrocytes for K^+ (e.g., [14,27–32]). In the present study, we followed this approach to provide insights into changes in astroglial $[K^+]_i$ upon brief energy deprivation. We combined different imaging and electrophysiological methods in murine neocortical tissue slices with the calculation of $[K^+]_i$ using a simplified Goldman–Hodgkin–Katz (GHK) equation. Notably, we determined all parameters required experimentally, namely $[K^+]_o$, intracellular and extracellular Na^+ concentration ($[Na^+]_i$; $[Na^+]_o$), membrane potential (E_M), and relative Na^+ over K^+ permeability (α). This allowed us to estimate astrocytic $[K^+]_i$, as precisely as possible, significantly extending former studies using this strategy.

Our results show an initial rapid loss of K^+ from astrocytes upon brief energy restriction, confirming earlier reports. In addition, our study demonstrates a biphasic mismatch in the astrocytic Na^+/K^+ balance. The initial glial K^+ loss quantitatively overrides the ischemia-induced increase in $[Na^+]_i$, revealing a substantial negative anion gap during this phase. In contrast, during late recovery from energy depletion, our simulations uncover a transient net gain of astrocytic $[K^+]_i$, reversing the anion gap.

2. Materials and Methods

2.1. Preparation of Organotypic and Acute Tissue Slices

Acute parasagittal slices containing hippocampus and adjacent somatosensory cortex were obtained from wild type Balb/C mice of both genders at postnatal days (P)6–8 or P14–21. For preparation of organotypic tissue slice cultures, animals at P6–8 were decapitated, their brains immediately dissected and transferred into ice-cold standard artificial cerebrospinal fluid (ACSF) containing (in mM): 130 NaCl, 2.5 KCl, 1.25 NaH_2PO_4, 26 $NaHCO_3$, 2 $CaCl_2$, 1 $MgCl_2$, and 10 glucose; pH 7.4, bubbled with carbogen (95% O_2, 5% CO_2). The 250 µm-thick slices were then cut using a vibratome (HM650V, Microtome, Thermo Fisher Scientific, Waltham, MA, USA). Slices were transferred to Biopore membranes (Millicell standing insert, Merck Millipore, Burlington, VT, USA) and were kept in an incubator at the interface between humidified air containing 5% CO_2 and culture medium at 36 °C [33,34] until used in experiments.

For preparation of acute tissue slices of the neocortex, brains of mice at P14–21 were prepared and cut in a modified preparation ACSF, containing 0.5 mM $CaCl_2$ and 6 mM $MgCl_2$ to dampen glutamate-induced cellular excitation. To label astrocytes, slices were then incubated for 20 min at 34 °C in preparation ACSF containing 0.5–1 µM sulforhodamine (SR) 101, followed by another 10 min at 34 °C in SR101-free standard ACSF [35]. Afterward, slices were kept in standard ACSF at room temperature (20–22 °C) until used for experiments.

Experiments were performed in layers II/III of the somatosensory cortex and were carried out at room temperature. Slices were perfused with ACSF at a rate of 2.5 mL/min.

Transient chemical ischemia was induced by perfusing slices with glucose-free standard ACSF containing the cytochrome C oxidase inhibitor sodium azide (NaN_3; 5 mM) and the non-metabolizable glucose analog 2-deoxyglucose (2-DG; 2 mM) [19,36].

All chemicals were purchased from Merck/Sigma-Aldrich (St. Louis, MO, USA) or AppliChem (Darmstadt, Germany) if not stated otherwise.

2.2. Imaging of ATP

Imaging of intracellular ATP was performed in organotypic slice cultures using the FRET-sensor ATeam1.03^{YEMK} ("ATeam") [37]. In brief, 0.5 µL of a vector (AAV5/2) carrying the code for ATeam under the control of astrocyte-specific promotor GFAP was applied to the top of a slice after 1–3 days in culture as described before [34]. Slices were maintained in the incubator for a total of at least 10 days before performing experiments.

Transduced slices were transferred to an epifluorescence microscope (Nikon Eclipse FNI, Nikon, 40× water immersion objective, N.A. 0.8, Tokyo, Japan) equipped with a monochromator (Poly-V; Thermo Fisher Scientific/FEI, Planegg, Germany). ATeam expressed in astrocytes was excited at 435 nm, and images were acquired at 0.5 Hz with a CMOS camera (Orca 4 LT Plus, Hamamatsu Photonics, Herrsching, Germany) (Figure 1A). Emission was split at 500 nm (WVIEW GEMINI optic system; Hamamatsu Photonics, Herrsching, Germany) onto 2 band pass filters (483/32: imaging of eCFP/donor; 542/27: imaging of Venus/acceptor). Fluorescence was collected from regions of interest (ROIs) manually drawn around cell bodies, and the fluorescence ratio (Venus/eCFP) was calculated for individual ROIs. Subsequent analysis was performed offline employing "OriginPro 2021" Software (OriginLab Corporation, Northhampton, MA, USA). Changes in intracellular ATP levels are shown as percentage changes in the Venus/eCFP fluorescence ratio, normalized to the baseline fluorescence ratio before induction of chemical ischemia ("ATeam ratio [%]").

2.3. Imaging of Intracellular Na^+ and pH

For determination of intracellular ion concentrations in acutely isolated tissue slices, wide field imaging was performed using an upright microscope (Nikon Eclipse FN-1, Nikon, Fluor 40×/0.8 W water immersion objective, Tokyo, Japan) coupled to a Poly-V monochromator (Thermo Scientific/FEI). To measure $[Na^+]_i$, tissue slices were bolus-loaded with the membrane-permeable form of SBFI (SBFI-AM; sodium-binding benzofuran isophthalate-acetoxymethyl ester, 116.7 µM in the ejection pipette; ION Biosciences, San Marcos, TX, USA). SBFI was excited at 400 nm and its fluorescence detected above ~430 nm (409 beam splitter and 510/84 emission filter) [19]. Intracellular pH (pH_i) was determined upon loading of slices with BCECF (BCECF-AM; 2′,7′-Bis-(2-Carboxyethyl)-5-(and-6)-Carboxyfluorescein-acetoxy-methyl ester, 125 µM; A.G. Scientific, San Diego, CA, USA). BCECF was excited at 458 (isosbestic wavelength) and 488 nm (pH-sensitive wavelength), and its emission was recorded between 511 and 563 nm. Images were acquired at 0.5–1 Hz with an ORCA FLASH 4.0LT camera (Hamamatsu Photonics, Herrsching, Germany).

Fluorescence was collected from ROIs representing cell bodies of SR101-positive astrocytes and analyzed offline employing "OriginPro 2019/2021". SBFI-emission from individual ROIs was background corrected [38] and corrected for bleaching. For BCECF, the fluorescence ratio (F_{458}/F_{488}) was calculated after background correction. Changes in SBFI emission and BCECF ratio were converted into mM $[Na^+]$ and pH units, respectively, using established in situ calibration procedures [19,38,39].

Baseline $[Na^+]_i$ of layer II/III neocortical astrocytes was determined recently in our laboratory employing an approach introduced by Mondragao et al. [40,41]. This approach was adapted to determine baseline pH_i. In brief, slices were loaded with BCECF-AM, and the baseline ratio of a selected cell was recorded. Subsequently, this cell was subjected to whole-cell patch-clamp using a pipette solution with a pH of 7.3, which contained 0.5 mM BCECF. The initial baseline pH_i of the undisturbed cell was calculated from the

change in BCECF ratio upon membrane rupture and the known pH in pipette solution (and calibration parameters determined before).

2.4. Measurement of Extracellular K^+, Na^+, and pH

$[K^+]_o$, $[Na^+]_o$, and extracellular pH (pH_o) were measured in acute tissue slices using double-barreled ion-sensitive microelectrodes. These were prepared from two thin-walled borosilicate glass capillaries with filament (GC100F-15, GC150F-15; Harvard Apparatus, Holliston, MA, USA), glued and pulled out together as described before [22]. The tip of one capillary was silanized by exposure to vaporized hexamethyldisilazane (Fluka, Buchs, Switzerland) and filled with a liquid neutral ion carrier based on valinomycin for K^+ (Ionophore I, Cocktail B, Merck, Darmstadt, Germany), ETH 157 for Na^+ (Ionophore II, Cocktail A, Merck) or Hydrogen Ionophore I for pH (Cocktail A, 95291, Merck). Afterwards, ion-selective barrels were backfilled with 100 mM KCl (K^+-sensitive electrodes), 100 mM NaCl (Na^+), or HEPES (N-(2-hydroxyethyl)piperazine-N′-2-ethanesulfonic acid)-buffered saline (pH), respectively. HEPES-buffered saline contained (in mM): 125 NaCl, 3 KCl, 25 HEPES, 2 $MgSO_4$, 2 $CaCl_2$, 1.25 NaH_2PO_4, and 10 glucose; pH 7.4. Reference electrodes were filled with HEPES-buffered saline.

Calibration of K^+-sensitive microelectrodes was performed using salines composed of 25 mM HEPES and a total of 150 mM NaCl and KCl, in which $[K^+]$ was 0–10 mM and $[Na^+]$ adjusted accordingly. Na^+-sensitive electrodes were calibrated in salines composed of 25 mM HEPES, 3 mM KCl, and a total of 160 mM NaCl and *N*-methyl-D-glucamine chloride (NMDG-Cl), with $[Na^+]$ ranging from 70–160 mM and $[NMDG^+]$ adjusted to maintain osmolarity. Calibration of pH-sensitive microelectrodes was conducted in salines at a pH of 7.0 or 7.6, containing (in mM): 144.25 NaCl (pH 7.0)/108.48 NaCl (pH 7.6), 2.5 KCl, 1.25 NaH_2PO_4, and 12 $NaHCO_3$ (pH 7.0)/47.77 $NaHCO_3$ (pH 7.6), bubbled with carbogen. After calibration, electrodes were positioned in layer II/III at 40–60 µm below the slice surface and $[K^+]_o$, $[Na^+]_o$, or pH_o were recorded. Electrodes were calibrated again in the experimental bath directly after each experiment. Data were processed in "OriginPro 2021" and "MS Excel" (Microsoft Corporation, Redmond, WA, USA).

2.5. Patch-Clamp Recordings

To measure astrocytic membrane potential (E_M), patch-clamp recordings were performed at an upright microscope equipped with infrared differential interference contrast (E600FN, Nikon, 60× water immersion objective, N.A. 1.0, Tokyo, Japan) and an infrared video camera (XC-ST70CE, Hamamatsu Photonics, Herrsching, Germany) using an EPC10 amplifier and "PatchMaster" software (Harvard Bioscience/HEKA Elektronik, Lambrecht, Germany). Patch pipettes were pulled from borosilicate glass capillaries (GB150(F)-8P, Science Products, Hofheim am Taunus, Germany) at a vertical puller (PC-10 Puller, Narishige International, London, UK) and had a resistance of 3.5–4.5 MΩ.

For cell-attached recordings [42], pipettes were filled with either ACSF or standard pipette solution. The latter contained (in mM): 116 K-methansulfonate, 32 KCl, 10 HEPES, 8 NaCl, 4 Mg-ATP, and 0.4 Na_2-GTP; pH 7.3. The offset potential was corrected to account for the potential resulting from concentration differences between pipette solution and ACSF [42]. To record E_M in the cell-attached mode, seal resistance must be at least 100-fold higher than the membrane resistance (R_M) of the recorded cell [42]. R_M in cortical astrocytes was around 10 MΩ in 2–3 weeks old animals, and recordings were only accepted if the seal resistance was larger than 1 GΩ, which was continuously monitored using test pulses (−50 pA) every 30 s.

Whole-cell current-clamp recordings were performed to determine the relative Na^+ versus K^+ permeability of the plasma membrane ($\alpha = P_{Na}/P_K$) [43]. To this end, pipettes were filled with standard pipette solution. Voltage traces were sampled at 100 Hz. Measurements were rejected if the seal resistance exceeded 15 MΩ to ensure sufficient electrical and diffusional access to the patched cell. The liquid junction potential was not corrected. Data

Data were analyzed using "IGOR Pro" (WaveMetrics, Lake Oswego, OR, USA), "MS Excel", and "OriginPro 2021".

were analyzed using "IGOR Pro" (WaveMetrics, Lake Oswego, OR, USA), "MS Excel", and "OriginPro 2021".

2.6. Data Presentation and Statistics

Each set of experiments was performed on tissue slices taken from at least 3 different animals. Results given in the text represent mean ± standard deviation (SD). Data were illustrated in box plots showing individual data points (grey diamonds), mean (square), median (horizontal line), SD (box), and min/max (whiskers). Data were statistically analyzed using "WinSTAT" (R. Fitch Software, Bad Krozingen, Germany) and "OriginPro 2019/2021". Data were first tested for outliers. Thereafter, normal distribution was assessed using a Kolmogorov–Smirnov test. In case of normal distribution, results were assessed by two-tailed, paired or unpaired Student's *t*-tests. Otherwise, results were assessed by the Wilcoxon test and *U*-test (Mann–Whitney) for paired and unpaired data, respectively. *p* represents the error probability, * $p < 0.05$, ** $p < 0.01$, *** $p < 0.001$. *n* represents the number of cells or experiments per slice per animal. In case of two comparisons, data were statistically analyzed by the tests described above under post hoc Šidák correction (SC) of critical values [44]: * $p < 0.0253$, ** $p < 0.005$, *** $p < 0.0005$.

2.6. Data Presentation and Statistics

Each set of experiments was performed on tissue slices taken from at least 3 different animals. Results given in the text represent mean ± standard deviation (SD). Data were illustrated in box plots showing individual data points (grey diamonds), mean (square), median (horizontal line), SD (box), and min/max (whiskers). Data were statistically analyzed using "WinSTAT" (R. Fitch Software, Bad Krozingen, Germany) and "OriginPro 2019/2021". Data were first tested for outliers. Thereafter, normal distribution was assessed using a Kolmogorov–Smirnov test. In case of normal distribution, results were assessed by two-tailed, paired or unpaired Student's *t*-tests. Otherwise, results were assessed by the Wilcoxon test and *U*-test (Mann–Whitney) for paired and unpaired data, respectively. *p* represents the error probability, * $p < 0.05$, ** $p < 0.01$, *** $p < 0.001$. *n* represents the number of cells or experiments per slice per animal. In case of two comparisons, data were statistically analyzed by the tests described above under post hoc Šidák correction (SC) of critical values [44]: * $p < 0.0253$, ** $p < 0.005$, *** $p < 0.0005$.

3. Results

3. Results

3.1. Effect of Transient Energy Depletion on Intracellular ATP

The goal of the present study was to gain insight into changes in astrocytic $[K^+]_i$ upon transient energy depletion, simulating the situation in the ischemic penumbra. Energy failure was induced by transient inhibition of glycolysis and oxidative phosphorylation ("chemical ischemia") as described earlier [19,36]. To evaluate the effect of brief chemical ischemia on cellular ATP levels, we expressed the nanosensor ATeam1.03^{YEMK} ("ATeam") in organotypic tissue slices of the neocortex (Figure 1A) [34,37]. Perfusion of slices with the metabolic inhibitors for 2 min caused a well-detectable, reversible decrease in the ATeam ratio by 17.3 ± 5.3% of the baseline level determined in standard ACSF (n = 27 cells, 4 tissue slices, 3 animals) (Figure 1B,C; Table 1). Based on our recent calibrations using this sensor [45], these data imply a decline in the intracellular ATP concentration by about 1 mM in response to this manipulation. The ATeam ratio recovered slowly towards baseline, and 15 min after reperfusion with standard saline, ATeam levels were still about 3% lower than the initial baseline value.

3.1. Effect of Transient Energy Depletion on Intracellular ATP

The goal of the present study was to gain insight into changes in astrocytic $[K^+]_i$ upon transient energy depletion, simulating the situation in the ischemic penumbra. Energy failure was induced by transient inhibition of glycolysis and oxidative phosphorylation ("chemical ischemia") as described earlier [19,36]. To evaluate the effect of brief chemical ischemia on cellular ATP levels, we expressed the nanosensor ATeam1.03^{YEMK} ("ATeam") in organotypic tissue slices of the neocortex (Figure 1A) [34,37]. Perfusion of slices with the metabolic inhibitors for 2 min caused a well-detectable, reversible decrease in the ATeam ratio by 17.3 ± 5.3% of the baseline level determined in standard ACSF (n = 27 cells, 4 tissue slices, 3 animals) (Figure 1B,C; Table 1). Based on our recent calibrations using this sensor [45], these data imply a decline in the intracellular ATP concentration by about 1 mM in response to this manipulation. The ATeam ratio recovered slowly towards baseline, and 15 min after reperfusion with standard saline, ATeam levels were still about 3% lower than the initial baseline value.

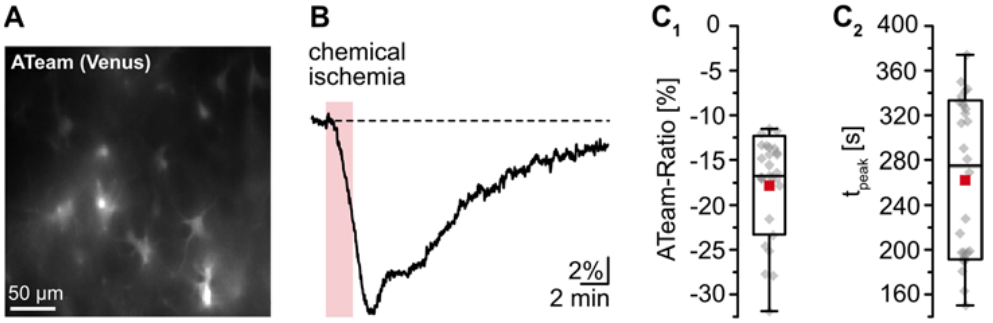

Figure 1. Reduction of astrocytic ATP levels by chemical ischemia for 2 min. (**A**) Image of the Venus fluorescence of ATeam, expressed under the GFAP promotor in an organotypic tissue slice. (**B**) Changes in the ATeam ratio of an individual astrocyte evoked by chemical ischemia (indicated by the red box). (**C**) Box plots of peak changes in astrocytic ATeam ratio (C_1) and the time-to-peak (C_2) upon chemical ischemia. Shown are individual data points (grey diamonds), means (squares), medians (horizontal lines), SDs (boxes), and min/max (whiskers).

Figure 1. Reduction of astrocytic ATP levels by chemical ischemia for 2 min. (**A**) Image of the Venus fluorescence of ATeam, expressed under the GFAP promotor in an organotypic tissue slice. (**B**) Changes in the ATeam ratio of an individual astrocyte evoked by chemical ischemia (indicated by the red box). (**C**) Box plots of peak changes in astrocytic ATeam ratio (C_1) and the time-to-peak (C_2) upon chemical ischemia. Shown are individual data points (grey diamonds), means (squares), medians (horizontal lines), SDs (boxes), and min/max (whiskers).

These results demonstrate that chemical ischemia induction for 2 min causes a transient increase in cellular ATP levels in astrocytes. Following experimental preparations, slices were perfused with the metabolic inhibitors for 2 min to result in moderate transient metabolic stress.

These results demonstrate that chemical ischemia induction for 2 min causes a transient increase in cellular ATP levels in astrocytes. Following experimental preparations, slices were perfused with the metabolic inhibitors for 2 min to result in moderate transient metabolic stress.

3.2. Changes of Ion Homeostasis and Astrocytic Membrane Potential during Chemical Ischemia

Owing to the lack of suitable techniques for quantitative experimental determination of $[K^+]_i$ in astrocytes in situ, we employed a combined empirical–theoretical approach. The latter exploits the dominating K^+ permeability of the plasma membrane of astrocytes, which, together with a minor permeability for Na^+, allows an approximation of their membrane potential (E_M) by a simplified GHK equation [27,43]:

$$E_M = \frac{RT}{F} \ln \frac{[K^+]_o + \alpha[Na^+]_o}{[K^+]_i + \alpha[Na^+]_i}, \quad (1)$$

where R is the universal gas constant, T is the absolute temperature, F is the Faraday constant, $[X^z]_{o/i}$ are respective ion concentrations outside and inside of the cell, and α is the relative membrane permeability for Na^+ versus K^+ (P_{Na}/P_K). Rearranging Equation (1) then enables the calculation of $[K^+]_i$:

$$[K^+]_i = \frac{[K^+]_o + \alpha[Na^+]_o}{e^{\frac{E_M F}{RT}}} - \alpha[Na^+]_i. \quad (2)$$

For a realistic approximation of $[K^+]_i$ using Equation (2), we determined all other parameters ($[Na^+]_i$, $[Na^+]_o$, $[K^+]_o$, E_M, and α) experimentally in astrocytes in acutely isolated tissue slices, thereby going beyond former studies using this approach (e.g., [14]).

Wide field imaging with the Na^+-sensitive fluorescent dye SBFI was employed to measure $[Na^+]_i$ [38]. Recent work from our laboratory showed that neocortical astrocytes exhibited an average baseline $[Na^+]_i$ of 12.1 mM [41]. Perfusion with metabolic inhibitors for 2 min caused a rapid increase in astrocytic $[Na^+]_i$ by 24.4 ± 7.2 mM ($p = 2 \times 10^{-29}$, *** after SC) (Figure 2A). Peak $[Na^+]_i$ was reached within 137 ± 21 s and $[Na^+]_i$ declined towards the initial baseline within 10–11 min after reperfusion ($p = 6 \times 10^{-28}$, *** after SC, $n = 34/4/4$) (Figure 2A_1,A_2). In the extracellular space, a baseline $[Na^+]_o$ of 157.4 ± 1.5 mM was determined using ion-sensitive microelectrodes [22]. In response to induction of chemical ischemia, $[Na^+]_o$ decreased by 1.9 ± 1.0 mM ($p = 0.003$, ** after SC) within 158 ± 24 s and then fully recovered within about 3 min upon washout of the drugs ($p = 0.002$, ** after SC; $n = 22/22/11$) (Figure 2B; data summarized in Table 1).

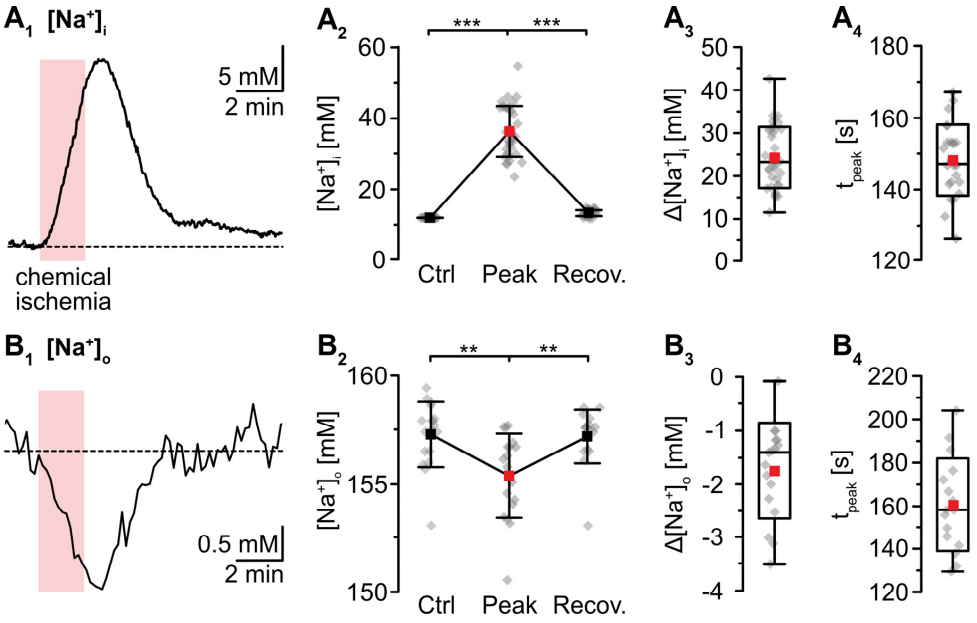

Figure 2. Changes in Na^+ induced by a chemical ischemia for 2 min. (**A**) Astrocytic $[Na^+]_i$. (**A$_1$**): $[Na^+]_i$ increase in an individual astrocyte. (**A$_2$**): Plot illustrating baseline $[Na^+]_i$ (data taken from [41]), peak changes in $[Na^+]_i$, and subsequent recovery of $[Na^+]_i$. Shown are individual data points (grey diamonds), means (squares), and SDs (whiskers). (**A$_3$**,**A$_4$**): Box plots illustrating peak changes in $[Na^+]_i$ (**A$_3$**) as well as the time-to-peak (**A$_4$**). (**B**) Same illustration as in (**A**) for changes in $[Na^+]_o$. (**B$_1$**): Individual measurement. (**B$_2$**): Plot illustrating baseline $[Na^+]_o$, peak changes in $[Na^+]_o$, and its subsequent recovery. (**B$_3$**,**B$_4$**): Box plots of peak changes in $[Na^+]_o$ (**B$_3$**) and the time-to-peak (**B$_4$**). Box plots in (**A$_3$**,**A$_4$**) and (**B$_3$**,**B$_4$**) show individual data points (grey diamonds), means (squares), medians (horizontal lines), SD (boxes), and min/max (whiskers). (**A$_2$**,**B$_2$**): ** $p < 0.005$, *** $p < 0.0005$ (Šidák corrected significance level).

K^+-sensitive microelectrodes were employed to analyze $[K^+]_o$, revealing a baseline of 2.7 ± 0.3 mM in layer II/III of acute tissue slices (Figure 3). Induction of chemical ischemia for 2 min resulted in a transient increase in $[K^+]_o$ by 1.2 ± 0.9 mM ($p = 2 \times 10^{-4}$, *** after SC; $n = 12/12/9$) (Figure 3A$_1$–A$_3$). The maximal $[K^+]_o$ increase was reached within 149 ± 26 s (Figure 3A$_4$). This was followed by a long-lasting undershoot of 0.6 ± 0.9 mM, after which $[K^+]_o$ slowly approached the initial baseline ($p = 5 \times 10^{-5}$, *** after SC) (Figure 3A$_2$).

For the determination of α (P_{Na}/P_K), the E_M of astrocytes was recorded in the whole-cell patch-clamp mode. In this configuration, astrocytic $[Na^+]_i$ and $[K^+]_i$ were determined by their respective concentrations in the pipette saline (see methods). α was calculated, rewriting Equation (1) as follows and inserting the experimentally determined $[Na^+]_o$ and $[K^+]_o$ (157.4 mM and 2.7 mM, see above):

$$\alpha = \frac{[K^+]_o + e^{\frac{E_M F}{RT}} * [K^+]_i}{e^{\frac{E_M F}{RT}} * [Na^+]_i - [Na^+]_o}, \quad (3)$$

revealing an α of 0.0100 ± 0.0031 in neocortical astrocytes.[1]

As mentioned, whole-cell patch-clamp results in a rapid dialysis of the recorded soma with the pipette saline. This, however, will also result in a partial clamping of intracellular ion concentrations during chemical ischemia, mitigating eventual changes in cellular membrane potentials [14]. To circumvent these effects, measurement of E_M induced by metabolic inhibition was performed in the cell-attached mode. After the formation of a GΩ seal, the recorded potential slowly shifted towards more negative values, attaining a stable value of -90.7 ± 5.1 mV within about 10–20 min ($n = 6/6/4$; not shown). Upon perfusion with metabolic inhibitors for 2 min, astrocytes transiently depolarized by

soma with the pipette saline. This, however, will also result in a partial clamping of intracellular ion concentrations during chemical ischemia, mitigating eventual changes in cellular membrane potentials [14]. To circumvent these effects, measurement of E_M induced by metabolic inhibition was performed in the cell-attached mode. After the formation of a GΩ seal, the recorded potential slowly shifted towards more negative values, attaining a stable value of −90.7 ± 5.1 mV within about 10–20 min (n = 6/6/4; not shown). Upon perfusion with metabolic inhibitors for 2 min, astrocytes transiently depolarized by 15.5 ± 3.8 mV (p = 0.003, ** after SC) (Figure 3B$_1$–B$_3$). The peak depolarization was reached after 201 ± 65 s (Figure 3B$_4$), where after E_M showed an undershoot by 4.8 ± 3.2 mV. Subsequently, E_M fully recovered to baseline within about 11 min after reperfusion with standard saline (n = 4 × 10^{-4}, *** after SC) (Figure 3B$_1$–B$_3$; data summarized in Table 1).

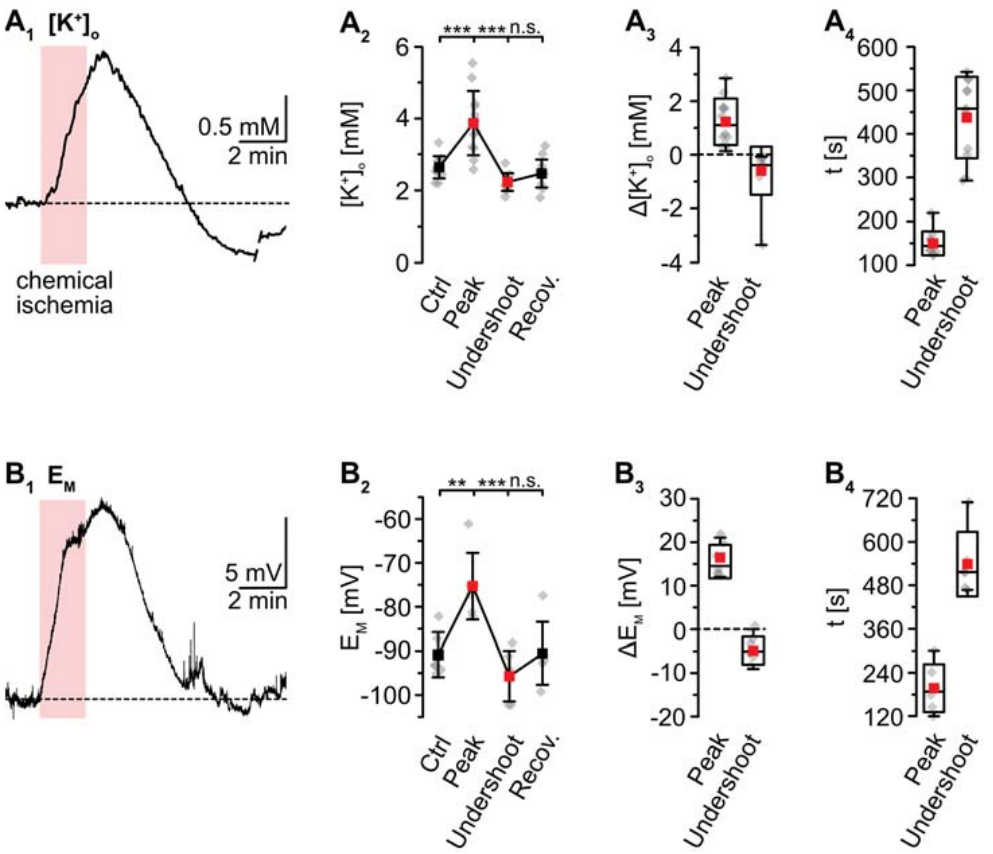

Figure 3. Ischemia-induced changes in $[K^+]_o$ and astrocytic membrane potential. (**A**) $[K^+]_o$. (**A$_1$**): Increase in $[K^+]_o$ in an individual measurement. (**A$_2$**): Plot illustrating baseline $[K^+]_o$, peak changes in $[K^+]_o$, undershoot and subsequent recovery. Shown are individual data points (grey diamonds), means (squares), and SDs (whiskers). (**A$_3$**,**A$_4$**): Box plots illustrating peak changes in $[K^+]_o$ (**A$_3$**) as well as the time-to-peak and time-to-undershoot (**A$_4$**). (**B**) Same illustration as in (**A**) for changes in astrocytic E_M. (**B$_1$**): Individual measurement. (**B$_2$**): Plot illustrating baseline E_M, peak changes in E_M, hyperpolarization, and subsequent recovery. (**B$_3$**,**B$_4$**): Box plots of peak changes in E_M (**B$_3$**) and the time-to-peak and time-to-undershoot (**B$_4$**). Box plots in (**A$_3$**,**A$_4$**) and (**B$_3$**,**B$_4$**) show individual data points (grey diamonds), means (squares), medians (horizontal lines), SDs (boxes), and min/max (whiskers). (**A$_2$**,**B$_2$**): ** $p < 0.005$, *** $p < 0.0005$ (Šidák corrected significance levels), n.s.: not significant.

3.3. Simulation of Changes in Astrocytic K^+ Concentration upon Transient Chemical Ischemia

To simulate the time course of astrocytic $[K^+]_i$, the individual traces of the experimentally determined parameters ($[Na^+]_i$, $[Na^+]_o$, $[K^+]_o$, E_M) were averaged (Figure 4A). The averaged $[Na^+]_o$ trace recovered to baseline within 2–3 min after washout of the inhibitors. As recordings were terminated after this period, the further course of $[Na^+]_o$ was set to this baseline (Figure 4A$_2$). In the following, $[K^+]_i$ was calculated for each time point using Equation (2). This revealed an average baseline of astrocytic $[K^+]_i$ of 146.1 mM (Figure 4B). Upon metabolic inhibition, $[K^+]_i$ decreased by 42.8 mM within 229 s to a minimum level of 103.4 mM. After this decline, $[K^+]_i$ slowly increased again, showing a transient overshoot of 16 mM that peaked roughly 6 min after washout. Finally, $[K^+]_i$ slowly recovered to a level close to the initial baseline, which was reached within about 18 min after reperfusion with standard ACSF (Figure 4B; data summarized in Table 1).

tion (2). This revealed an average baseline of astrocytic $[K^+]_i$ of 146.1 mM (Figure 4B). Upon metabolic inhibition, $[K^+]_i$ decreased by 42.8 mM within 229 s to a minimum level of 103.4 mM. After this decline, $[K^+]_i$ slowly increased again, showing a transient overshoot of 16 mM that peaked roughly 6 min after washout. Finally, $[K^+]_i$ slowly recovered to a level close to the initial baseline, which was reached within about 18 min after reperfusion with standard ACSF (Figure 4B; data summarized in Table 1).

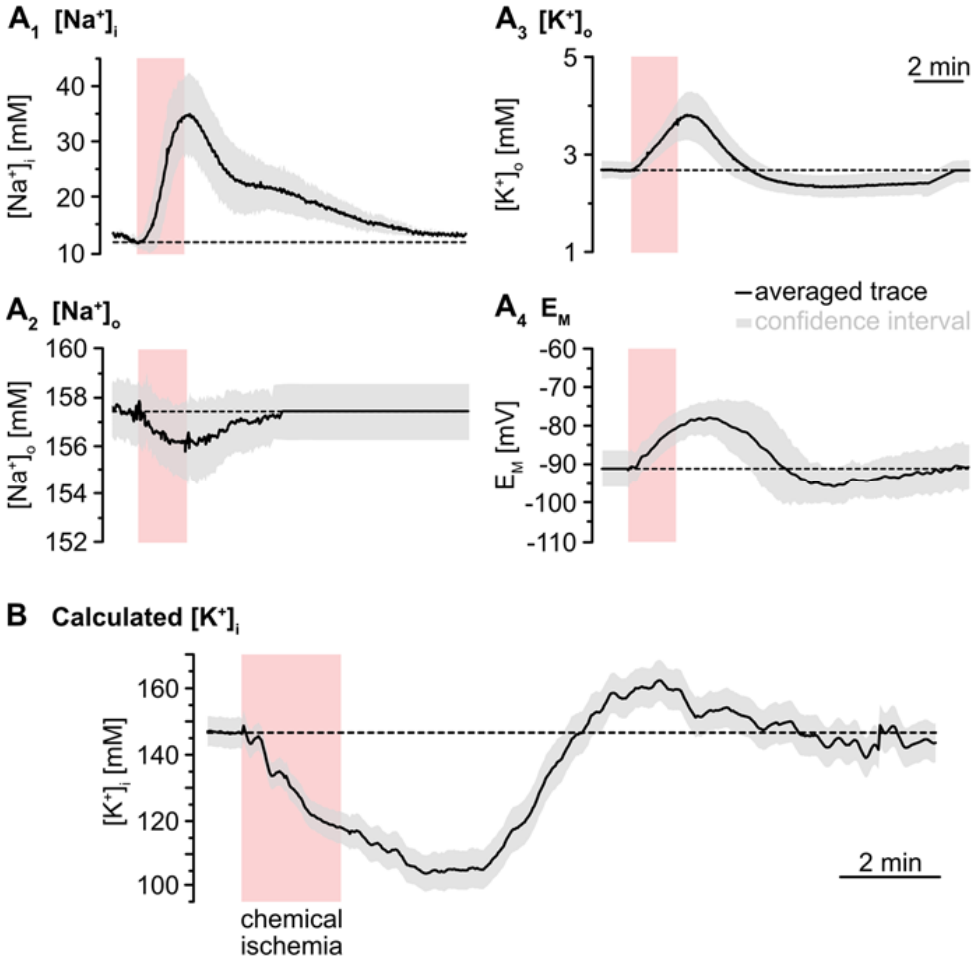

Figure 4. Simulation of ischemia-induced changes in astrocytic $[K^+]_i$. (**A**) Traces show averaged changes of $[Na^+]_i$, $[Na^+]_o$, $[K^+]_o$ and E_M. The grey envelopes show the 95% confidence intervals. (**B**) The change in astrocytic $[K^+]_i$ upon chemical ischemia was calculated from feeding the average traces shown in (**A**) into Equation (2). The grey envelope again depicts the 95% confidence interval, which was calculated from the individual confidence intervals given in (**A**).

3.4. Cation–Anion Balance during Transient Chemical Ischemia

Our results presented thus far indicate a mismatch between the calculated maximum loss of K^+ (43 mM) and the experimentally determined maximum Na^+ load of astrocytes (24 mM). This apparent cation imbalance requires additional transport of charged molecules across the membrane to maintain electroneutrality. One possibility is the passage of Cl^-, but recent work indicated that $[Cl^-]_i$ of neocortical astrocytes does not undergo significant changes in response to brief chemical ischemia [36]. An alternative candidate is HCO_3^-, for which astrocytes possess efficient transport mechanisms across the plasma membrane [46,47]. The $[HCO_3^-]$ is intimately linked to pH via the activity of carbonic anhydrases [48], and we thus studied extra- and intracellular pH to address this possibility.

pH-sensitive microelectrodes revealed a baseline pH_o of 7.35 ± 0.03 (n = 5/5/4). Chemical ischemia resulted in an alkaline shift of pH_o by 0.06 ± 0.02, which peaked at 101 ± 27 s (p = 0.016; * after SC; n = 5/5/4) (Figure 5A). The initial alkalinization was followed by acidification of pH_o to 7.27 ± 0.05 ($p = 8 \times 10^{-4}$, ** after SC), which peaked at 294 ± 44 s (n = 5/5/4) (Figure 5A). pH_o slowly recovered to baseline within 13–14 min after washout of the drugs. Astrocytes exhibited a baseline pH_i of 7.33 ± 0.26 (n = 8/5/4; not shown). pH_i dropped by 0.26 ± 0.06 units upon chemical ischemia ($p = 4 \times 10^{-43}$, *** after SC, n = 42/5/5) (Figure 5B). The peak acidification was reached at 237 ± 55 s, after

pH-sensitive microelectrodes revealed a baseline pH_o of 7.35 ± 0.03 (n = 5/5/4). Chemical ischemia resulted in an alkaline shift of pH_o by 0.06 ± 0.02, which peaked at 101 ± 27 s (p = 0.016; * after SC; n = 5/5/4) (Figure 5A). The initial alkalinization was followed by acidification of pH_o to 7.27 ± 0.05 ($p = 8 \times 10^{-4}$, ** after SC), which peaked at 294 ± 44 s (n = 5/5/4) (Figure 5A). pH_o slowly recovered to baseline within 13–14 min after washout of the drugs. Astrocytes exhibited a baseline pH_i of 7.33 ± 0.26 (n = 8/5/4; not shown). pH_i dropped by 0.26 ± 0.06 units upon chemical ischemia ($p = 4 \times 10^{-43}$, *** after SC, n = 42/5/5) (Figure 5B). The peak acidification was reached at 237 ± 55 s, after which pH_i slowly recovered. At 16–18 min after reperfusion, the pH_i was still slightly more acidic than the initial baseline ($p = 9 \times 10^{-36}$) (Figure 5B1,B2, data summarized in Table 1).

The Henderson–Hasselbalch equation, which describes the relation between pH and $[HCO_3^-]$ was solved for $[HCO_3^-]_i$ to enable calculation of changes in $[HCO_3^-]_i$ in response to chemical ischemia as shown in Figure 5C:

$$[HCO_3^-]_o = 10^{pH_o - pK_{S\,(CO_2)}} * [CO_2]. \quad (4)$$

Finally, we used Equation (5) to calculate $[HCO_3^-]_i$ (Figure 5D) as reported before [49]:

$$[HCO_3^-]_i = 10^{pH_i - pH_o} * [HCO_3^-]_o. \quad (5)$$

Int. J. Mol. Sci. 2022, 23, x FOR PEER REVIEW 10 of 18

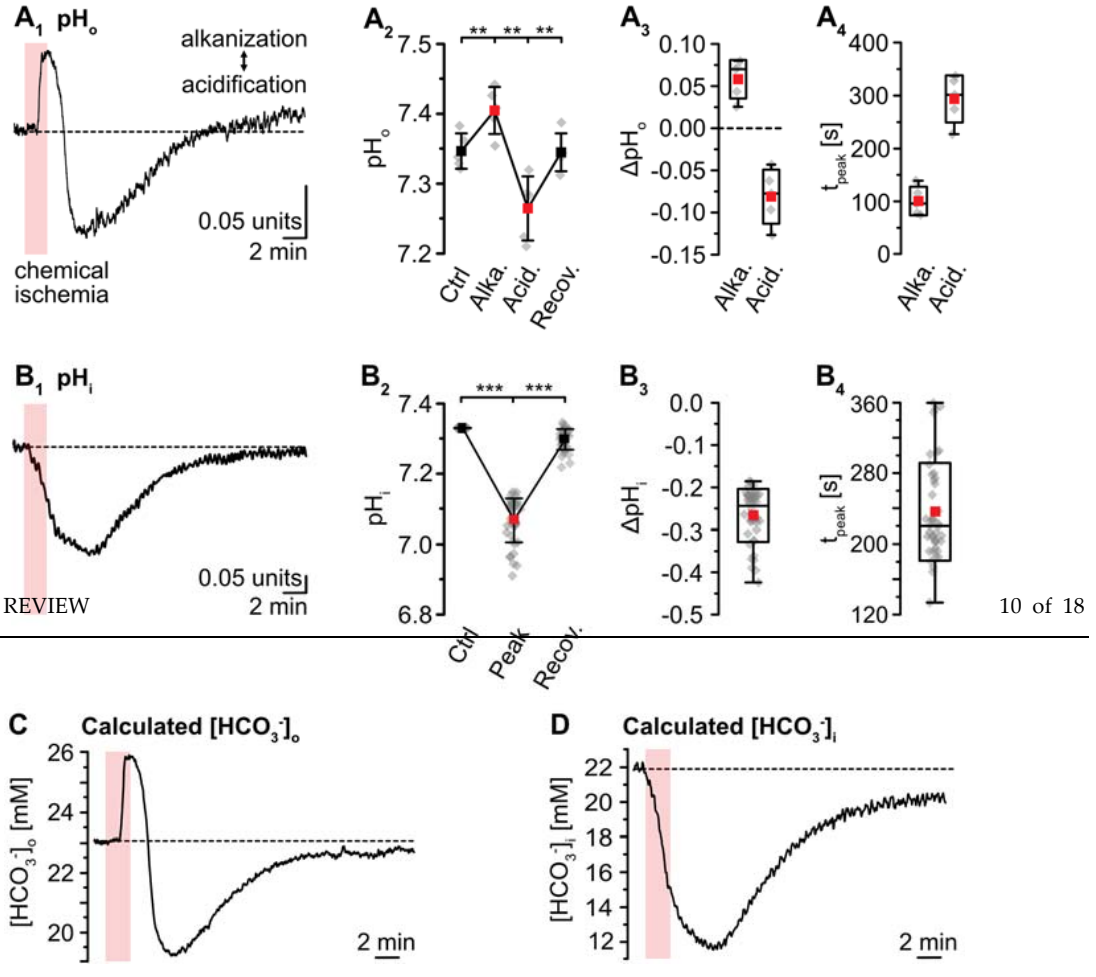

Figure 5. Ischemia-induced changes in pH and $[HCO_3^-]$. (**A**) pH_o. (**A1**): Biphasic change in pH_o in an individual experiment. (**A2**): Plot illustrating baseline pH_o, peak alkalinization, acidification, and subsequent recovery of pH_o. Shown are individual data points (grey diamonds), means (squares), and SDs (whiskers). (**A3**,**A4**): Box plots illustrating peak changes in pH_o (**A3**) as well as the time-to-peak (**A4**). (**B**) Same illustration as in (**A**) for changes in astrocytic pH_i. (**B1**): Individual measurement. (**B2**): Plot illustrating baseline pH_i, peak changes, and its subsequent recovery. (**B3**,**B4**): Box plots of peak changes in pH_i (**B3**) and the time-to-peak (**B4**). Box plots in (**A3**,**A4**) and (**B3**,**B4**) show individual datapoints (grey diamonds), means (squares), medians (horizontal lines), SDs (boxes), and min/max (whiskers). (**C**,**D**) Calculated change in $[HCO_3^-]_o$ and $[HCO_3^-]_i$, as derived from the Henderson–Hasselbalch equation and Equation (5), respectively. (**A2**,**B2**): ** $p < 0.005$, *** $p < 0.0005$ (Šidák corrected significance levels).

To reveal the presumed contribution of a movement of HCO_3^- to the cation–anion balance during transient chemical ischemia, we first subtracted the averaged traces of astrocytic $[Na^+]_i$ and $[K^+]_i$. This uncovered a biphasic anion gap, predicting an additional loss of anions during the initial decline in $[K^+]_i$, which turned into an anion gain during the overshoot in $[K^+]_i$ (Figure 6A). In a second step, we subtracted the calculated reduction in $[HCO_3^-]_i$ from the first curve, which reduced the initial anion gap by about 50% as shown

peak (**A4**). (**B**) Same illustration as in (**A**) for changes in astrocytic pH_i. (**B1**): Individual measurement. (**B2**): Plot illustrating baseline pH_i, peak changes, and its subsequent recovery. (**B3**,**B4**): Box plots of peak changes in pH_i (**B3**) and the time-to-peak (**B4**). Box plots in (**A3**,**A4**) and (**B3**,**B4**) show individual data points (grey diamonds), means (squares), medians (horizontal lines), SDs (boxes), and min/max (whiskers). (**C**,**D**) Calculated change in $[HCO_3^-]_o$ and $[HCO_3^-]_i$, as derived from the Henderson–Hasselbalch equation and Equation (5), respectively. (**A2**,**B2**): ** $p < 0.005$, *** $p < 0.0005$ (Šidák corrected significance levels).

To reveal the presumed contribution of a movement of HCO_3^- to the cation–anion balance during transient chemical ischemia, we first subtracted the averaged traces of astrocytic $[Na^+]_i$ and $[K^+]_i$. This uncovered a biphasic anion gap, predicting an additional loss of anions during the initial decline in $[K^+]_i$, which turned into an anion gain during the overshoot in $[K^+]_i$ (Figure 6A). In a second step, we subtracted the calculated reduction in $[HCO_3^-]_i$ from the first curve, which reduced the initial anion gap by about 50% as shown in Figure 6B. The ongoing acidification (and ongoing decrease in $[HCO_3^-]_i$), however, even aggravated the remaining anion gap in the second phase of recovery (Figure 6B).

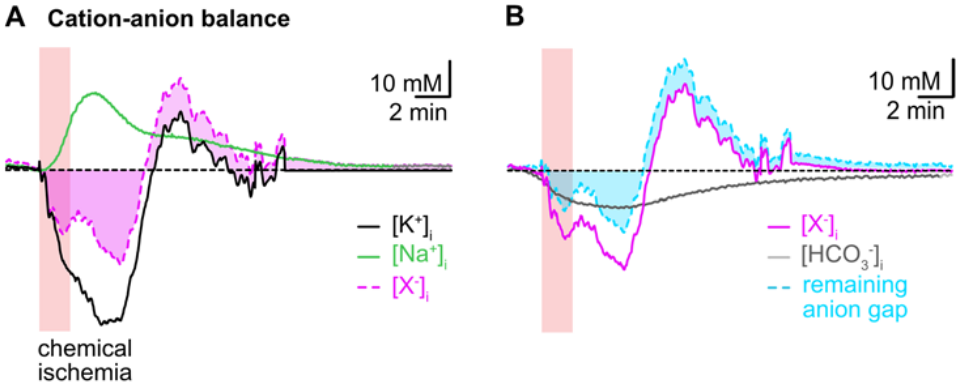

Figure 6. Intracellular cation–anion balance. (**A**) Subtraction of the averaged trace for changes in $[Na^+]_i$ (green trace) from that calculated for $[K^+]_i$ (black trace) reveals a biphasic anion gap (pink trace and area) induced by chemical ischemia. (**B**) Subtraction of the calculated changes in $[HCO_3^-]_i$ during chemical ischemia (grey trace) reduces the remaining anion gap in the initial phase and increases it in the second phase of recovery (cyan trace and area).

Taken together, these results indicate that changes in $[HCO_3^-]_i$ significantly contribute to the changes in the cation–anion balance of astrocytes induced by chemical ischemia. Flux of $[HCO_3^-]_i$ can, however, not compensate the observed intracellular cation/anion imbalance, suggesting additional movement of other charged molecules across the plasma membrane.

3.5. Summary of Results

Figure 7 and Table 1 summarize the data presented in this work. Our results demonstrate that brief chemical ischemia, induced by inhibition of cellular metabolism for 2 min, results in a transient decrease in the astrocytic ATP concentration. This is accompanied by a depolarization, an increase in $[Na^+]_i$, and an acidification of astrocytes. At the same time, $[Na^+]_o$ transiently decreases and $[K^+]_o$ increases followed by an undershoot in $[K^+]_o$, while pH_o undergoes a biphasic alkaline-acid shift. Calculation of astrocytic $[K^+]_i$ based on these experimentally determined parameters predicts an initial loss of astrocytic $[K^+]_i$, followed by a net, overshooting gain in $[K^+]_i$ during late recovery. Finally, our results show a mismatch of the intracellular cation–anion balance of astrocytes during and after chemical ischemia. This indicates a requirement for additional ion flux across the astrocytic membrane, which is most pronounced in the late recovery phase during which our data predict a net overshoot in $[K^+]_i$.

pH_o undergoes a biphasic alkaline-acid shift. Calculation of astrocytic $[K^+]_i$ based on these experimentally determined parameters predicts an initial loss of astrocytic $[K^+]_i$, followed by a net, overshooting gain in $[K^+]_i$ during late recovery. Finally, our results show a mismatch of the intracellular cation–anion balance of astrocytes during and after chemical ischemia. This indicates a requirement for additional ion flux across the astrocytic membrane, which is most pronounced in the late recovery phase during which our data predict a net overshoot in $[K^+]_i$.

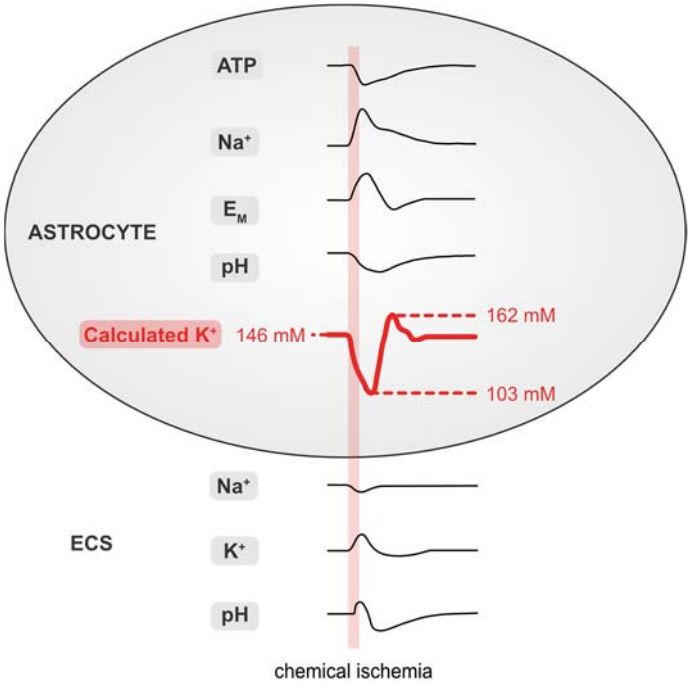

Figure 7. Summary of results. Schematized changes in extra- and intracellular ion concentrations upon chemical ischemia for 2 min. Values for $[K^+]_i$ were approximated from experimental traces using the GHK equation. ECS: extracellular space.

Table 1. Extra- and intracellular changes induced by chemical ischemia for 2 min.

Parameter	Control	Chemical Ischemia	Δ	*n*	*p*	
$[ATP]_o$ [%]	100	82.7 ± 5.3	−17.3 ± 5.3	27/4/3	n.a.	
$[Na^+]_o$ [mM]	157.4 ± 1.5	155.5 ± 1.9	−1.9 ± 1.0 (−1%)	22/22/11	3×10^{-3}	**
$[Na^+]_i$ [mM]	12.1 ± 0.3 §	36.5 ± 7.2	+24.4 ± 7.2 (+201%)	34/14/4	2×10^{-29}	***
$[K^+]_o$ [mM]	2.7 ± 0.3	3.9 ± 0.9	+1.7 ± 0.9 (+46%)	12/12/9	2×10^{-4}	***
$[K^+]_i$ [mM]	146.2	103.4	−42.8 (−29%)	n.a.	n.a.	
E_M [mV]	−90.7 ± 5.1	−75.2 ± 7.6	+15.5 ± 3.8 (−17%)	6/6/4	0.003	**
pH_o	7.35 ± 0.03	7.41 ± 0.03	+0.05 ± 0.03 (+1%)	5/5/4	0.016	*
pH_i	7.33 ± 0.26	7.07 ± 0.06	−0.26 ± 0.06 (−4%)	42/5/5	4×10^{-43}	***
$[HCO_3^-]_o$ [mM]	23.0	25.9	+2.9 (+13%)	n.a.	n.a.	
$[HCO_3^-]_i$ [mM]	22.1	11.6	−10.5 (−52%)	n.a.	n.a.	

Data show peak changes after a 2 minutes' chemical ischemia. Note that $[K^+]_o$ moreover undergoes an undershoot and that $[K^+]_i$ overshoots in the recovery phase as described in the results. Data are given as mean ± SD. *n*: number of cells or experiments per slice, per animal; *p*: error probability, asterisks depict significance levels after Sidak correction; * $p < 0.0253$, ** $p < 0.005$, *** $p < 0.0005$; n.a.: not applicable; §: from [41].

4. Discussion

4.1. Baseline $[K^+]_i$ of Astrocytes

While it is widely accepted that glial cells maintain a high $[K^+]_i$ [7,50], direct measurements of astrocytic $[K^+]_i$ are rare due to the lack of suitable techniques. Earlier estimates and measurements in several types of glial cells and based on different indirect methods predicted a baseline $[K^+]_i$ of 100–170 mM [6,27,28,51]. Values determined with ion-selective microelectrodes in rodent glial cells were generally lower [52–55], which may have been caused by a loss of K^+ due to impalement with the large-tip electrodes. Employing non-invasive imaging with the fluorescent K^+ indicator Asante Potassium Green-1, Rimmele et al. determined a $[K^+]_i$ of 133 mM in cultured rat astrocytes [23]. This dye, however,

has not been employed for studying $[K^+]_i$ in glial cells in more intact preparations, probably because it does not load well in astrocytes in brain tissue slices (unpublished observations, Rose laboratory). More recently, genetically encoded K^+ nanosensors were developed, which owing to their low apparent affinities for K^+, are more suitable for the determination of extracellular $[K^+]$ [24,25]. A sensor published by Shen et al. enabled the measurement of relative changes in $[K^+]_i$ in HEK cells [26], but its suitability for quantitative imaging of $[K^+]_i$ in brain tissue has not been established yet.

To gain information on $[K^+]_i$ and changes thereof in response to energy deprivation in astrocytes in situ, we, therefore, followed earlier approaches combining experimental determination of different cellular parameters with calculation of $[K^+]_i$ using the GHK equation. This strategy is based on the observation that mature astrocytes express a battery of different K^+ channels, including inwardly rectifying Kir4.1, the two-pore domain channels (TWIK-1 and TREK-2) as well as large-conductance calcium-activated K^+ channels (BK_{Ca}) [56]. Owing to their high K^+ permeability at rest [27,57], the membrane potential of astrocytes can be fairly well approximated by a modified GHK equation assuming an additional small Na^+ permeability [27,43]. Recent work has also demonstrated that short-term ischemic conditions neither alter the intrinsic properties of astrocytic K^+ channels nor affect the overall membrane conductance, suggesting that their depolarization largely arises from the accompanying changes in $[K^+]_o$ and $[K^+]_i$ [14,58].

The GHK equation evidently also allows for calculation of $[K^+]_i$, provided that all other parameters are known. Here, going beyond earlier reports, we not only measured $[K^+]_o$, $[Na^+]_o$ and E_M, but also $[Na^+]_i$ as well as the relative Na^+ permeability in our preparation experimentally, enabling a realistic approximation of $[K^+]_i$. We determined a relative membrane permeability for Na^+ versus K^+ (P_{Na}/P_K) of 0.01 in neocortical astrocytes, which is lower than that of astrocytes in the mouse hippocampal CA1 area (0.015; [43]). Under the given conditions and ion concentrations (e.g., a baseline $[K^+]_o$ of 2.7 mM), we obtained a baseline $[K^+]_i$ of 146 mM for neocortical astrocytes. This value is somewhat higher than that reported for astrocytes cultured from the mouse cortex (133 mM) [23]. As in the latter study, astrocytes were bathed in 5.4 mM $[K^+]_o$, they were most likely more depolarized, probably yielding a lower $[K^+]_i$ as compared to our study.

4.2. Changes in Astroglial $[K^+]_i$ during Energy Deprivation

A central function of astrocytes is the uptake of K^+ released by active neurons, thereby controlling and maintaining homeostasis of $[K^+]_o$ in the brain [7,9]. Consequently, several studies reported a rise in astrocytic $[K^+]_i$ in response to neuronal stimulation and/or a rise in $[K^+]_o$ [23,51,52,59]. Glial K^+ uptake is mainly mediated by the NKA, but other transporters such as the NKCC1 and/or channel-mediated influx may come into play depending on the amplitude and spatio-temporal properties of the $[K^+]_o$ elevation [9,10,60–62].

Breakdown of $[K^+]_o$ homeostasis is one of the first consequences of anoxic/ischemic conditions and a restriction in cellular energy supply [13,50,63]; whereas the ischemic core undergoes a complete breakdown of ion homeostasis and massive cell death, recovery is possible in the neighboring ischemic penumbra, which experiences a reduction in cerebral blood flow to 20–40% of normoxic conditions [64]. Repeated waves of spreading depolarizations, however, will impose additional transient ion loads and metabolic stress onto the already stressed cells of the penumbra [15–18]. Here, we mimicked ischemia-like conditions in the penumbra undergoing waves of spreading depolarizations by brief perfusion of tissue slices with metabolic inhibitors [19,36]. Noteworthy, this chemical ischemia does not represent a complete model of spreading depolarizations developing in the ischemic penumbra. Our experiments, however, confirm a rapid reduction of ATP in neocortical astrocytes after transient inhibition of metabolism, followed by a slow recovery [34]. In a recent study, we performed an in situ calibration of ATeam fluorescence [45]. This was achieved by exposure of organotypic tissue slices to the saponin ß-escin, resulting in a permeabilization of cellular plasma membranes for ATP. Defined changes in the [ATP] then resulted in defined changes in the ATeam FRET-ratio that followed Michaelis–Menten

kinetics, revealing an apparent K_D of 2.7 mM for ATeam1.03^{YEMK} in both neurons and astrocytes. A linear plot between 1 and 3 mM ATP showed that a 10% change in fluorescence ratio corresponded to a change in $[ATP]_i$ by 0.56 mM. Based on this calibration [45], astrocytic ATP exhibited an estimated decrease by about 1 mM in response to chemical ischemia for 2 min in the present study. Such transient, moderate reduction in cellular ATP is one of the hallmarks accompanying the generation of spreading depolarizations [65].

In addition, inhibition of cellular metabolism resulted in a transient decrease in $[Na^+]_o$, an increase in $[K^+]_o$, an increase in astrocytic $[Na^+]_i$, and a depolarization of astrocytes, confirming earlier observations [5,6,13,19,58,66,67]. All changes induced by a chemical ischemia for 2 min recovered towards baseline after washout of the inhibitors, with $[K^+]_o$ and glial E_M showing an additional undershoot below baseline and hyperpolarization, respectively [58,67]. As discussed above, ion changes were accompanied by a decrease and subsequent recovery of astrocytic ATP, suggesting a direct correlation between ATP levels and NKA activity, a phenomenon already reported from CA1 pyramidal neurons [68].

Earlier work suggested that the depolarization of astrocytes when exposed to brief periods of ischemic conditions is mainly due to a loss of K^+ from cells [14,58]. Our simulation based on the GHK equation supports this notion, indicating a decrease in astrocytic $[K^+]_i$ by about 43 mM upon brief inhibition of cellular energy production, most likely as a direct consequence of the decline in cellular ATP and the resulting decrease of NKA activity. Besides channel-mediated loss of K^+, activation of astrocytic glutamate transporters might, at least partly, contribute to the decline in astrocytic $[K^+]_i$ [19,23].

While initial K^+ efflux from astrocytes under ischemic conditions will aggravate the accumulation of extracellular K^+ induced by its release from neurons, our simulation also predicts a delayed gain of astrocytic K^+ during the late recovery phase. This phenomenon arises from the mismatch in the experimentally determined time courses of the undershoot in $[K^+]_o$ and the astrocytic hyper- and repolarization, respectively. It again suggests ongoing increased activation of the NKA following metabolic inhibition, probably because of the still-elevated $[Na^+]_i$ and/or in response to an increase in $[Ca^{2+}]_i$ [19,58,60,69]. In addition, astrocytic K^+ uptake might at least partly be mediated by increased activity of inward NKCC1 [11,36,70].

Notably, the overcompensating uptake of K^+ by astrocytes reduces $[K^+]_o$ below its initial baseline. The latter will exert a hyperpolarizing effect on neurons and reduce neuronal excitability [8,50], while at the same time increasing the driving force for astroglial glutamate uptake [71]. Astrocytes will thereby exert a neuroprotective role following transient energy depletion through a $[K^+]_o$-mediated dampening of network activity and reduction of neuronal ATP consumption, supporting the recovery of neurons from metabolic stress.

4.3. Astroglial Cation–Anion Balance during Energy Deprivation

The K^+ movements across the astrocytic membrane predicted by our simulation require the additional flux of ions to preserve electroneutrality [6]. While Na^+ influx compensates for about 50% of the predicted initial loss of K^+ from astrocytes, it does not fully counteract the simultaneous cation efflux, an observation also reported by earlier studies [6,67]. What is more, owing to its slow recovery, still elevated $[Na^+]_i$ even adds to the delayed predicted gain of K^+ in the second phase of recovery. This mismatch in the cellular cation–anion balance must be balanced by an additional net gain of cations, followed by additional cation loss in the second recovery phase and/or an initial net loss of anions, followed by a gain of anions. Besides loading with Na^+, astrocytes are subject to a transient increase in $[Ca^{2+}]_i$ [19] and $[H^+]_i$ (this study) during brief chemical ischemia. While this might reduce the anion gap in the first phase, the slow recovery from both Ca^{2+} signals and acidification result in its aggravation in the second phase.

A mobile anion which will contribute to the cation–anion balance is HCO_3^- [6]. Our experiments demonstrate a decrease in astrocytic pH_i and $[HCO_3^-]_i$, respectively, in response to chemical ischemia, significantly reducing the predicted imbalance in the first phase. The slow recovery from the intracellular acidification and ongoing decrease in

$[HCO_3^-]_i$, however, will again worsen the anion gap in the second recovery phase. While the initial charge imbalance may thus be compensated for through influx of additional cations (Ca^{2+}, H^+) and a reduction in $[HCO_3^-]_i$, these processes will later even increase the predicted anion gap.

Cl^- is another candidate for compensation of the predicted delayed charge imbalance. Earlier work has demonstrated rapid channel- and transporter-mediated movement of Cl^- across astrocytic membranes [72–74]. Accumulation of Cl^- moreover contributes to astrocyte swelling in ischemic conditions [11,75–78]. Conversely, a recent study employing fluorescence lifetime imaging in layer II/III astrocytes only reported negligible changes in their $[Cl^-]_i$ in response to a chemical ischemia for 2–5 min [36]. This was probably due to the simultaneous activation of different anion transporters mediating Cl^- accumulation (NKCC1) and Cl^- efflux (KCC's and glutamate transporters) [36]. An increase in astrocytic $[Cl^-]_i$ was, however, observed upon a 10 min' exposure to the metabolic inhibitors, showing that a net gain in Cl^- is indeed observed upon more severe conditions (i.e., a larger decline in cellular ATP and/or longer period of energy deprivation). On the other hand, earlier reports demonstrating an apparent mismatch between K^+ and Cl^- movement in astrocytes speculated that in addition to Cl^-, the net flux of lactate or other anionic osmolytes such as taurine, glutamate or aspartate might help maintaining the cellular cation–anion balance [11,51,79].

While these assumptions are thus supported by earlier work [11,51,79], it should be kept in mind that the proposed anion mismatch was not directly measured but inferred from the calculated $[K^+]_i$. Several factors could have biased our simulation. Among them is the influence of space clamp errors in patch-clamp measurements, a factor especially critical for astrocytes, which not only exhibit a very low input resistance but are also extensively coupled via gap junctions [1,35,56]. Moreover, experimentally determined changes in extracellular ion concentrations might represent underestimates of ion transients occurring in the intact tissue owing to the relatively large tip size of the ion-selective microelectrodes (around 1 µm) [22]. Finally, our intracellular ion measurements represent bulk measurements from cell bodies only, and changes in fine, diffusion-restricted astrocytic processes might be larger in amplitude as well [38,41].

With these considerations in mind, we conclude from our data that the predicted net gain of K^+ (and positive charge) by astrocytes in the late recovery phase from chemical ischemia will be accompanied by an additional efflux of cations and/or influx of anions. The overshooting uptake of K^+ by astrocytes will promote and aid the recovery of $[K^+]_o$, thereby exerting a dampening effect on neuronal excitability. Conversely, any net gain of osmolytes by astrocytes will eventually be accompanied by uptake of water, which will promote harmful cell swelling upon prolonged metabolic inhibition [11,75,80]. Identifying the nature of the additional ionic species or charged molecules transported across the plasma membrane is thus highly desirable to shed more light on the mechanisms of astrocytic swelling following brain ischemia [62,76].

Author Contributions: Conceptualization, S.E., J.S. and C.R.R.; methodology, S.E., J.S. and C.R.R.; validation, S.E., J.S. and C.R.R.; formal analysis and investigation, S.E., J.S., S.D., N.P., N.J.G. and K.E.; resources, C.R.R.; data curation, S.E., J.S., N.P., K.E. and S.D.; writing—original draft preparation, S.E., J.S. and C.R.R.; writing—review and editing, S.E., J.S., K.E., N.P., N.J.G. and C.R.R.; visualization, S.E.; supervision, J.S., N.J.G. and C.R.R.; project administration, J.S. and C.R.R.; funding acquisition, C.R.R. All authors have read and agreed to the published version of the manuscript.

Funding: This research was funded by grants from the Deutsche Forschungsgemeinschaft (DFG), Research Unit 2795 "Synapses under Stress" (Ro2327/13-1, 13-2, 14-1) and the Ilselore Luckow Foundation to C.R.R.

Institutional Review Board Statement: All procedures reported in this study were carried out in accordance with the institutional guidelines of the Heinrich Heine University Düsseldorf, as well as the European Community Council Directive (2010/63/EU) and were communicated to and approved by the animal welfare office of the animal care and use facility of the Heinrich Heine University

Düsseldorf (institutional act number: O52/05). To prepare brain slices, mice older than P10 were anaesthetized with CO_2. All animals were quickly decapitated, and their brains rapidly removed. In accordance with the German Welfare Act (TSchG; Section 4, paragraph 3), no additional approval for postmortem removal of brain tissue was necessary.

Informed Consent Statement: Not applicable.

Data Availability Statement: The data presented in this study are available on request from the corresponding author.

Acknowledgments: We thank Claudia Roderigo for excellent technical assistance.

Conflicts of Interest: The authors declare no conflict of interest. The funders had no role in the design of the study; in the collection, analyses, or interpretation of data; in the writing of the manuscript, or in the decision to publish the results.

References

1. Verkhratsky, A.; Nedergaard, M. Physiology of Astroglia. *Physiol. Rev.* **2018**, *98*, 239–389. [CrossRef] [PubMed]
2. Heinemann, U.; Lux, H.D. Ceiling of stimulus induced rises in extracellular potassium concentration in the cerebral cortex of cat. *Brain Res.* **1977**, *120*, 231–249. [CrossRef]
3. Hoppe, D.; Chvatal, A.; Kettenmann, H.; Orkand, R.K.; Ransom, B.R. Characteristics of activity-dependent potassium accumulation in mammalian peripheral nerve in vitro. *Brain Res.* **1991**, *552*, 106–112. [CrossRef]
4. Jendelova, P.; Sykova, E. Role of glia in K^+ and pH homeostasis in the neonatal rat spinal cord. *Glia* **1991**, *4*, 56–63. [CrossRef]
5. Somjen, G.G. *Ions in the Brain: Normal Function, Seizures, and Stroke*; Oxford University Press: New York, NY, USA, 2004.
6. Hansen, A.J. Effect of anoxia on ion distribution in the brain. *Physiol. Rev.* **1985**, *65*, 101–148. [CrossRef]
7. Kofuji, P.; Newman, E.A. Potassium buffering in the central nervous system. *Neuroscience* **2004**, *129*, 1045–1056. [CrossRef]
8. Bellot-Saez, A.; Kekesi, O.; Morley, J.W.; Buskila, Y. Astrocytic modulation of neuronal excitability through K^+ spatial buffering. *Neurosci. Biobehav. Rev.* **2017**, *77*, 87–97. [CrossRef]
9. Larsen, B.R.; Stoica, A.; MacAulay, N. Managing Brain Extracellular K^+ during Neuronal Activity: The Physiological Role of the Na^+/K^+-ATPase Subunit Isoforms. *Front. Physiol.* **2016**, *7*, 141. [CrossRef]
10. Hertz, L.; Song, D.; Xu, J.; Peng, L.; Gibbs, M.E. Role of the Astrocytic Na^+, K^+-ATPase in K^+ Homeostasis in Brain: K^+ Uptake, Signaling Pathways and Substrate Utilization. *Neurochem. Res.* **2015**, *40*, 2505–2516. [CrossRef]
11. Leis, J.A.; Bekar, L.K.; Walz, W. Potassium homeostasis in the ischemic brain. *Glia* **2005**, *50*, 407–416. [CrossRef]
12. van Putten, M.J.A.M.; Fahlke, C.; Kafitz, K.W.; Hofmeijer, J.; Rose, C.R. Dysregulation of astrocyte ion homeostasis and its relevance for stroke-induced brain damage. *Int. J. Mol. Sci.* **2021**, *22*, 5679. [CrossRef] [PubMed]
13. Erecinska, M.; Silver, I.A. Ions and energy in mammalian brain. *Prog. Neurobiol.* **1994**, *43*, 37–71. [CrossRef]
14. Du, Y.; Wang, W.; Lutton, A.D.; Kiyoshi, C.M.; Ma, B.; Taylor, A.T.; Olesik, J.W.; McTigue, D.M.; Askwith, C.C.; Zhou, M. Dissipation of transmembrane potassium gradient is the main cause of cerebral ischemia-induced depolarization in astrocytes and neurons. *Exp. Neurol.* **2018**, *303*, 1–11. [CrossRef] [PubMed]
15. Moskowitz, M.A.; Lo, E.H.; Iadecola, C. The science of stroke: Mechanisms in search of treatments. *Neuron* **2010**, *67*, 181–198. [CrossRef] [PubMed]
16. Pietrobon, D.; Moskowitz, M.A. Chaos and commotion in the wake of cortical spreading depression and spreading depolarizations. *Nat. Rev. Neurosci.* **2014**, *15*, 379–393. [CrossRef]
17. Shuttleworth, C.W.; Andrew, R.D.; Akbari, Y.; Ayata, C.; Balu, R.; Brennan, K.C.; Boutelle, M.; Carlson, A.P.; Dreier, J.P.; Fabricius, M.; et al. Which Spreading Depolarizations Are Deleterious To Brain Tissue? *Neurocrit. Care* **2020**, *32*, 317–322. [CrossRef]
18. Lauritzen, M.; Dreier, J.P.; Fabricius, M.; Hartings, J.A.; Graf, R.; Strong, A.J. Clinical relevance of cortical spreading depression in neurological disorders: Migraine, malignant stroke, subarachnoid and intracranial hemorrhage, and traumatic brain injury. *J. Cereb. Blood Flow Metab.* **2011**, *31*, 17–35. [CrossRef]
19. Gerkau, N.J.; Rakers, C.; Durry, S.; Petzold, G.C.; Rose, C.R. Reverse NCX Attenuates Cellular Sodium Loading in Metabolically Compromised Cortex. *Cereb. Cortex* **2018**, *28*, 4264–4280. [CrossRef]
20. Rakers, C.; Schmid, M.; Petzold, G.C. TRPV4 channels contribute to calcium transients in astrocytes and neurons during peri-infarct depolarizations in a stroke model. *Glia* **2017**, *65*, 1550–1561. [CrossRef]
21. Rossi, D.J.; Brady, J.D.; Mohr, C. Astrocyte metabolism and signaling during brain ischemia. *Nat. Neurosci.* **2007**, *10*, 1377–1386. [CrossRef]
22. Haack, N.; Durry, S.; Kafitz, K.W.; Chesler, M.; Rose, C.R. Double-barreled and concentric microelectrodes for measurement of extracellular ion signals in brain tissue. *J. Vis. Exp.* **2015**, *103*, e53058. [CrossRef] [PubMed]
23. Rimmele, T.S.; Chatton, J.Y. A novel optical intracellular imaging approach for potassium dynamics in astrocytes. *PLoS ONE* **2014**, *9*, e109243. [CrossRef] [PubMed]
24. Wellbourne-Wood, J.; Rimmele, T.S.; Chatton, J.Y. Imaging extracellular potassium dynamics in brain tissue using a potassium-sensitive nanosensor. *Neurophotonics* **2017**, *4*, 015002. [CrossRef] [PubMed]

25. Bischof, H.; Rehberg, M.; Stryeck, S.; Artinger, K.; Eroglu, E.; Waldeck-Weiermair, M.; Gottschalk, B.; Rost, R.; Deak, A.T.; Niedrist, T.; et al. Novel genetically encoded fluorescent probes enable real-time detection of potassium in vitro and in vivo. *Nat. Commun.* **2017**, *8*, 1422. [CrossRef] [PubMed]
26. Shen, Y.; Wu, S.Y.; Rancic, V.; Aggarwal, A.; Qian, Y.; Miyashita, S.I.; Ballanyi, K.; Campbell, R.E.; Dong, M. Genetically encoded fluorescent indicators for imaging intracellular potassium ion concentration. *Commun. Biol.* **2019**, *2*, 18. [CrossRef]
27. Kimelberg, H.K.; Bowman, C.; Biddlecome, S.; Bourke, R.S. Cation transport and membrane potential properties of primary astroglial cultures from neonatal rat brains. *Brain Res.* **1979**, *177*, 533–550. [CrossRef]
28. Dietzel, I.; Heinemann, U. Dynamic variations of the brain cell microenvironment in relation to neuronal hyperactivity. *Ann. N. Y. Acad. Sci.* **1986**, *481*, 72–86. [CrossRef]
29. Kalia, M.; Meijer, H.G.E.; van Gils, S.A.; van Putten, M.J.A.M.; Rose, C.R. Ion dynamics at the energy-deprived tripartite synapse. *PLoS Comput. Biol.* **2021**, *17*, e1009019. [CrossRef]
30. Ullah, G.; Wei, Y.; Dahlem, M.A.; Wechselberger, M.; Schiff, S.J. The Role of Cell Volume in the Dynamics of Seizure, Spreading Depression, and Anoxic Depolarization. *PLoS Comput. Biol.* **2015**, *11*, e1004414. [CrossRef]
31. Halnes, G.; Ostby, I.; Pettersen, K.H.; Omholt, S.W.; Einevoll, G.T. Electrodiffusive model for astrocytic and neuronal ion concentration dynamics. *PLoS Comput. Biol.* **2013**, *9*, e1003386. [CrossRef]
32. Breslin, K.; Wade, J.J.; Wong-Lin, K.; Harkin, J.; Flanagan, B.; Van Zalinge, H.; Hall, S.; Walker, M.; Verkhratsky, A.; McDaid, L. Potassium and sodium microdomains in thin astroglial processes: A computational model study. *PLoS Comput. Biol.* **2018**, *14*, e1006151. [CrossRef] [PubMed]
33. Stoppini, L.; Buchs, P.A.; Muller, D. A simple method for organotypic cultures of nervous tissue. *J. Neurosci. Methods* **1991**, *37*, 173–182. [CrossRef]
34. Lerchundi, R.; Kafitz, K.W.; Winkler, U.; Farfers, M.; Hirrlinger, J.; Rose, C.R. FRET-based imaging of intracellular ATP in organotypic brain slices. *J. Neurosci. Res.* **2019**, *97*, 933–945. [CrossRef] [PubMed]
35. Kafitz, K.W.; Meier, S.D.; Stephan, J.; Rose, C.R. Developmental profile and properties of sulforhodamine 101-labeled glial cells in acute brain slices of rat hippocampus. *J. Neurosci. Methods* **2008**, *169*, 84–92. [CrossRef] [PubMed]
36. Engels, M.; Kalia, M.; Rahmati, S.; Petersilie, L.; Kovermann, P.; van Putten, M.; Rose, C.R.; Meijer, H.G.E.; Gensch, T.; Fahlke, C. Glial chloride homeostasis under transient ischemic stress. *Front. Cell. Neurosci.* **2021**, *15*, 735300. [CrossRef]
37. Imamura, H.; Huynh Nhat, K.P.; Togawa, H.; Saito, K.; Iino, R.; Kato-Yamada, Y.; Nagai, T.; Noji, H. Visualization of ATP levels inside single living cells with fluorescence resonance energy transfer-based genetically encoded indicators. *Proc. Natl. Acad. Sci. USA* **2009**, *106*, 15651–15656. [CrossRef]
38. Langer, J.; Rose, C.R. Synaptically induced sodium signals in hippocampal astrocytes in situ. *J. Physiol.* **2009**, *587*, 5859–5877. [CrossRef]
39. Kelly, T.; Rose, C.R. Ammonium influx pathways into astrocytes and neurones of hippocampal slices. *J. Neurochem.* **2010**, *115*, 1123–1136. [CrossRef]
40. Mondragao, M.A.; Schmidt, H.; Kleinhans, C.; Langer, J.; Kafitz, K.W.; Rose, C.R. Extrusion versus diffusion: Mechanisms for recovery from sodium loads in mouse CA1 pyramidal neurons. *J. Physiol.* **2016**, *594*, 5507–5527. [CrossRef]
41. Ziemens, D.; Oschmann, F.; Gerkau, N.J.; Rose, C.R. Heterogeneity of activity-induced sodium transients between astrocytes of the mouse hippocampus and neocortex: Mechanisms and consequences. *J. Neurosci.* **2019**, *39*, 2620–2634. [CrossRef]
42. Perkins, K.L. Cell-attached voltage-clamp and current-clamp recording and stimulation techniques in brain slices. *J. Neurosci. Methods* **2006**, *154*, 1–18. [CrossRef] [PubMed]
43. Stephan, J.; Haack, N.; Kafitz, K.W.; Durry, S.; Koch, D.; Hochstrate, P.; Seifert, G.; Steinhauser, C.; Rose, C.R. Kir4.1 channels mediate a depolarization of hippocampal astrocytes under hyperammonemic conditions in situ. *Glia* **2012**, *60*, 965–978. [CrossRef] [PubMed]
44. Abdi, H. The Bonferroni and Šidák corrections for multiple comparisons. In *Encyclopedia of Measurement and Statistics*; Salkind, N., Ed.; Sage Publications: Thousand Oaks, CA, USA, 2007; pp. 103–107.
45. Lerchundi, R.; Huang, N.; Rose, C.R. Quantitative imaging of changes in astrocytic and neuronal adenosine triphosphate using two different variants of ATeam. *Front. Cell. Neurosci.* **2020**, *14*, 80. [CrossRef] [PubMed]
46. Deitmer, J.W.; Rose, C.R. Ion changes and signalling in perisynaptic glia. *Brain Res. Rev.* **2010**, *63*, 113–129. [CrossRef] [PubMed]
47. Majumdar, D.; Bevensee, M.O. Na-coupled bicarbonate transporters of the solute carrier 4 family in the nervous system: Function, localization, and relevance to neurologic function. *Neuroscience* **2010**, *171*, 951–972. [CrossRef] [PubMed]
48. Theparambil, S.M.; Ruminot, I.; Schneider, H.P.; Shull, G.E.; Deitmer, J.W. The electrogenic sodium bicarbonate cotransporter NBCe1 is a high-affinity bicarbonate carrier in cortical astrocytes. *J. Neurosci.* **2014**, *34*, 1148–1157. [CrossRef]
49. Kaila, K.; Saarikoski, J.; Voipio, J. Mechanism of action of GABA on intracellular pH and on surface pH in crayfish muscle fibres. *J. Physiol.* **1990**, *427*, 241–260. [CrossRef]
50. Somjen, G.G. Ion regulation in the brain: Implications for pathophysiology. *Neuroscientist* **2002**, *8*, 254–267. [CrossRef]
51. Walz, W.; Mukerji, S. KCl movements during potassium-induced cytotoxic swelling of cultured astrocytes. *Exp. Neurol.* **1988**, *99*, 17–29. [CrossRef]
52. Ballanyi, K.; Grafe, P.; ten Bruggencate, G. Ion activities and potassium uptake mechanisms of glial cells in guinea-pig olfactory cortex slices. *J. Physiol.* **1987**, *382*, 159–174. [CrossRef]

53. Grafe, P.; Ballanyi, K. Cellular mechanisms of potassium homeostasis in the mammalian nervous system. *Can. J. Physiol. Pharmacol.* **1987**, *65*, 1038–1042. [CrossRef] [PubMed]
54. Kettenmann, H.; Sonnhof, U.; Schachner, M. Exclusive potassium dependence of the membrane potential in cultured mouse oligodendrocytes. *J. Neurosci.* **1983**, *3*, 500–505. [CrossRef] [PubMed]
55. Buhrle, C.P.; Sonnhof, U. Intracellular ion activities and equilibrium potentials in motoneurones and glia cells of the frog spinal cord. *Pflug. Arch.* **1983**, *396*, 144–153. [CrossRef] [PubMed]
56. Zhou, M.; Du, Y.; Aten, S.; Terman, D. On the electrical passivity of astrocyte potassium conductance. *J. Neurophysiol.* **2021**, *126*, 1403–1419. [CrossRef]
57. Ransom, B.R.; Goldring, S. Ionic determinants of membrane potential of cells presumed to be glia in cerebral cortex of cat. *J. Neurophysiol.* **1973**, *36*, 855–868. [CrossRef]
58. Xie, M.; Wang, W.; Kimelberg, H.K.; Zhou, M. Oxygen and glucose deprivation-induced changes in astrocyte membrane potential and their underlying mechanisms in acute rat hippocampal slices. *J. Cereb. Blood Flow Metab.* **2008**, *28*, 456–467. [CrossRef]
59. Walz, W. Role of astrocytes in the clearance of excess extracellular potassium. *Neurochem. Int.* **2000**, *36*, 291–300. [CrossRef]
60. Ransom, C.B.; Ransom, B.R.; Sontheimer, H. Activity-dependent extracellular K^+ accumulation in rat optic nerve: The role of glial and axonal Na^+ pumps. *J. Physiol.* **2000**, *522 Pt 3*, 427–442. [CrossRef]
61. Sibille, J.; Pannasch, U.; Rouach, N. Astroglial potassium clearance contributes to short-term plasticity of synaptically evoked currents at the tripartite synapse. *J. Physiol.* **2014**, *592*, 87–102. [CrossRef]
62. MacAulay, N. Molecular mechanisms of K^+ clearance and extracellular space shrinkage-Glia cells as the stars. *Glia* **2020**, *68*, 2192–2211. [CrossRef]
63. Ekholm, A.; Katsura, K.; Kristian, T.; Liu, M.; Folbergrova, J.; Siesjo, B.K. Coupling of cellular energy state and ion homeostasis during recovery following brain ischemia. *Brain Res.* **1993**, *604*, 185–191. [CrossRef]
64. Murphy, T.H.; Corbett, D. Plasticity during stroke recovery: From synapse to behaviour. *Nat. Rev. Neurosci.* **2009**, *10*, 861–872. [CrossRef] [PubMed]
65. Mies, G.; Paschen, W. Regional changes of blood flow, glucose, and ATP content determined on brain sections during a single passage of spreading depression in rat brain cortex. *Exp. Neurol.* **1984**, *84*, 249–258. [CrossRef]
66. Rose, C.R.; Waxman, S.G.; Ransom, B.R. Effects of glucose deprivation, chemical hypoxia, and simulated ischemia on Na^+ homeostasis in rat spinal cord astrocytes. *J. Neurosci.* **1998**, *18*, 3554–3562. [CrossRef]
67. Muller, M.; Somjen, G.G. Na^+ and K^+ concentrations, extra- and intracellular voltages, and the effect of TTX in hypoxic rat hippocampal slices. *J. Neurophysiol.* **2000**, *83*, 735–745. [CrossRef]
68. Gerkau, N.J.; Lerchundi, R.; Nelson, J.S.E.; Lantermann, M.; Meyer, J.; Hirrlinger, J.; Rose, C.R. Relation between activity-induced intracellular sodium transients and ATP dynamics in mouse hippocampal neurons. *J. Physiol.* **2019**, *597*, 5687–5705. [CrossRef]
69. Wang, F.; Smith, N.A.; Xu, Q.; Fujita, T.; Baba, A.; Matsuda, T.; Takano, T.; Bekar, L.; Nedergaard, M. Astrocytes modulate neural network activity by Ca^{2+}-dependent uptake of extracellular K^+. *Sci. Signal.* **2012**, *5*, ra26. [CrossRef]
70. Kintner, D.B.; Wang, Y.; Sun, D. Role of membrane ion transport proteins in cerebral ischemic damage. *Front. Biosci.* **2007**, *12*, 762–770. [CrossRef]
71. Tyurikova, O.; Shih, P.Y.; Dembitskaya, Y.; Savtchenko, L.P.; McHugh, T.J.; Rusakov, D.A.; Semyanov, A. K^+ efflux through postsynaptic NMDA receptors suppresses local astrocytic glutamate uptake. *Glia* **2022**, *70*, 961–974. [CrossRef]
72. Wilson, C.S.; Mongin, A.A. The signaling role for chloride in the bidirectional communication between neurons and astrocytes. *Neurosci. Lett.* **2019**, *689*, 33–44. [CrossRef]
73. Woo, J.; Jang, M.W.; Lee, J.; Koh, W.; Mikoshiba, K.; Lee, C.J. The molecular mechanism of synaptic activity-induced astrocytic volume transient. *J. Physiol.* **2020**, *598*, 4555–4572. [CrossRef] [PubMed]
74. Benesova, J.; Rusnakova, V.; Honsa, P.; Pivonkova, H.; Dzamba, D.; Kubista, M.; Anderova, M. Distinct expression/function of potassium and chloride channels contributes to the diverse volume regulation in cortical astrocytes of GFAP/EGFP mice. *PLoS ONE* **2012**, *7*, e29725. [CrossRef]
75. Kahle, K.T.; Simard, J.M.; Staley, K.J.; Nahed, B.V.; Jones, P.S.; Sun, D. Molecular mechanisms of ischemic cerebral edema: Role of electroneutral ion transport. *Physiol. (Bethesda)* **2009**, *24*, 257–265. [CrossRef] [PubMed]
76. Kimelberg, H.K. Astrocytic swelling in cerebral ischemia as a possible cause of injury and target for therapy. *Glia* **2005**, *50*, 389–397. [CrossRef]
77. Risher, W.C.; Croom, D.; Kirov, S.A. Persistent astroglial swelling accompanies rapid reversible dendritic injury during stroke-induced spreading depolarizations. *Glia* **2012**, *60*, 1709–1720. [CrossRef]
78. Risher, W.C.; Andrew, R.D.; Kirov, S.A. Real-time passive volume responses of astrocytes to acute osmotic and ischemic stress in cortical slices and in vivo revealed by two-photon microscopy. *Glia* **2009**, *57*, 207–221. [CrossRef]
79. Hyzinski-Garcia, M.C.; Rudkouskaya, A.; Mongin, A.A. LRRC8A protein is indispensable for swelling-activated and ATP-induced release of excitatory amino acids in rat astrocytes. *J. Physiol.* **2014**, *592*, 4855–4862. [CrossRef]
80. Pasantes-Morales, H.; Vazquez-Juarez, E. Transporters and channels in cytotoxic astrocyte swelling. *Neurochem. Res.* **2012**, *37*, 2379–2387. [CrossRef]

Approaches to Study Gap Junctional Coupling

Jonathan Stephan[1], **Sara Eitelmann[1]** and Min Zhou[2]

[1] Institut für Neurobiologie, Heinrich-Heine-Universität Düsseldorf, Düsseldorf, Deutschland

[2] Department of Neuroscience, Wexner Medical Center, Ohio State University, Columbus, OH, United States

Front Cell Neurosci. 2021 Mar 10;15:640406. IF 2020: 6.147

Eigener Beitrag

- Erstellung von Abbildung 1
- Bearbeitung von vorveröffentlichten Abbildungen: Abbildung 2-5
- Recherche zur *tracer*-Kopplung und Erstellung der Tabelle 1
- Beitrag zur Verfassung und Überarbeitung des Manuskripts

frontiers in Cellular Neuroscience

REVIEW
published: 10 March 2021
doi: 10.3389/fncel.2021.640406

Approaches to Study Gap Junctional Coupling

Jonathan Stephan[1], Sara Eitelmann[1] and Min Zhou[2]**

[1] Institute of Neurobiology, Heinrich Heine University Düsseldorf, Düsseldorf, Germany, [2] Department of Neuroscience, Wexner Medical Center, Ohio State University, Columbus, OH, United States

Astrocytes and oligodendrocytes are main players in the brain to ensure ion and neurotransmitter homeostasis, metabolic supply, and fast action potential propagation in axons. These functions are fostered by the formation of large syncytia in which mainly astrocytes and oligodendrocytes are directly coupled. Panglial networks constitute on connexin-based gap junctions in the membranes of neighboring cells that allow the passage of ions, metabolites, and currents. However, these networks are not uniform but exhibit a brain region-dependent heterogeneous connectivity influencing electrical communication and intercellular ion spread. Here, we describe different approaches to analyze gap junctional communication in acute tissue slices that can be implemented easily in most electrophysiology and imaging laboratories. These approaches include paired recordings, determination of syncytial isopotentiality, tracer coupling followed by analysis of network topography, and wide field imaging of ion sensitive dyes. These approaches are capable to reveal cellular heterogeneity causing electrical isolation of functional circuits, reduced ion-transfer between different cell types, and anisotropy of tracer coupling. With a selective or combinatory use of these methods, the results will shed light on cellular properties of glial cells and their contribution to neuronal function.

Keywords: patch clamp, paired recordings, astrocyte syncytial isopotentiality, tracer coupling, wide field imaging

OPEN ACCESS

Edited by:
Christian Lohr,
University of Hamburg, Germany

Reviewed by:
Gerald Seifert,
University Hospital Bonn, Germany
Luc Leybaert,
Ghent University, Belgium

****Correspondence:***
Jonathan Stephan
jonathan.stephan@uni-duesseldorf.de
Min Zhou
Zhou.787@osu.edu

Specialty section:
This article was submitted to Non-Neuronal Cells, a section of the journal Frontiers in Cellular Neuroscience

Received: *11 December 2020*
Accepted: *03 February 2021*
Published: *10 March 2021*

Citation:
Stephan J, Eitelmann S and Zhou M (2021) Approaches to Study Gap Junctional Coupling. Front. Cell. Neurosci. 15:640406. doi: 10.3389/fncel.2021.640406

INTRODUCTION

Gap junction channels connect the cytosol of neighboring cells and allow the exchange of ions and small molecules, such as metabolites (Giaume et al., 2010, 2020). Gap junctions form, when two connexons in the membrane of neighboring cells align. Connexons in turn are hexamers that are formed by connexins (Cx; **Figure 1A**). There are 21 Cxs identified so far of which 11 are expressed by neurons and glial cells in the CNS that differ in their mass (Bedner et al., 2012) and expression profile (including developmental and cell type specificity) (Dahl et al., 1996; Kunzelmann et al., 1999; Nagy et al., 1999; Nagy and Rash, 2000; Augustin et al., 2016; Wadle et al., 2018). The composition of gap junctions with different connexons and Cxs defines their properties, for example selectivity and permeability (Bukauskas and Verselis, 2004; Harris, 2007; Abbaci et al., 2008). In addition, post-translational modifications further regulate gap junctional communication (Goodenough and Paul, 2009; Axelsen et al., 2013; Aasen et al., 2018). Homocellular coupling between astrocytes and oligodendrocytes is mediated by homotypic gap junctions (**Figure 1B**; Giaume and Theis, 2010; Maglione et al., 2010). Furthermore, heterocellular (panglial) coupling is observed between both cell types using heterotypic gap junctions (Wasseff and Scherer, 2011; Griemsmann et al., 2015; Augustin et al., 2016; Moshrefi-Ravasdjani et al., 2017; Claus et al., 2018; Wadle et al., 2018; Xin et al., 2019).

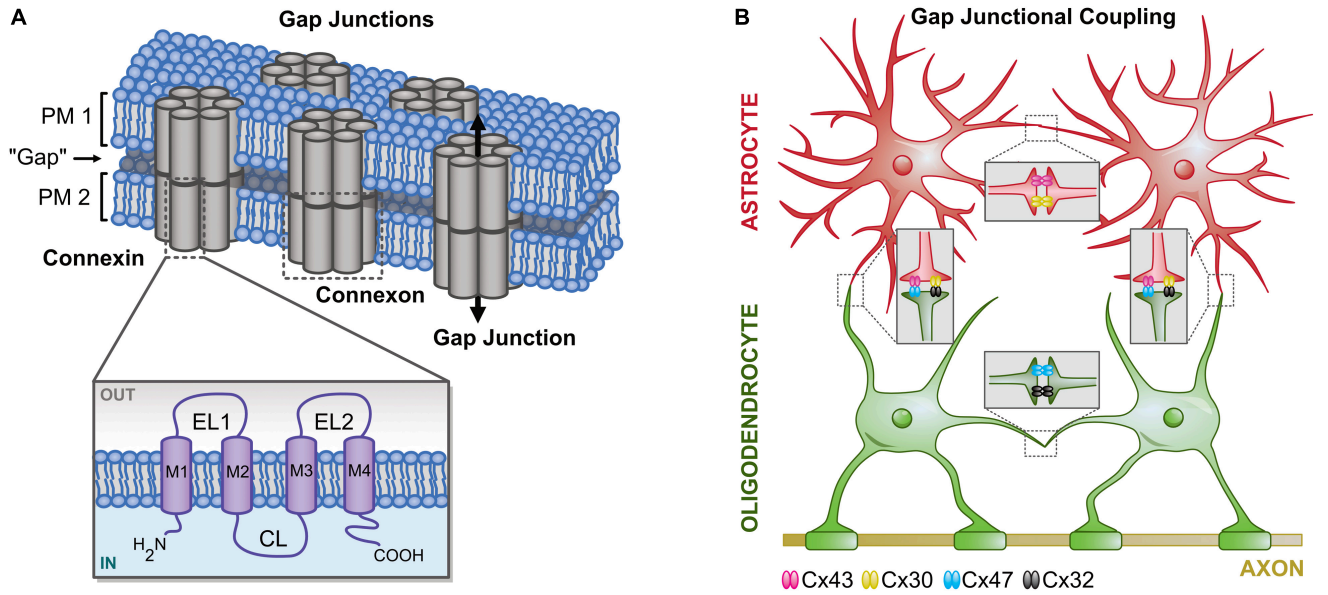

FIGURE 1 | Principle of gap junctional coupling. **(A)** Structural organization of gap junctions. Gap junctions are integral membrane proteins that connect the cytosol of neighboring cells. Two pairs of connexons (hexamers of connexins; Cx) form a pore enabling diffusion for ions and small molecules. EL, extracellular loop; CL, cytoplasmic loop; M, transmembrane helix. **(B)** (Pan-/)glial coupling. Astrocytes mainly express Cx43 and Cx30, whereas oligodendrocytes mainly express Cx47 and Cx32. Homotypic gap junctions couple astrocytes (Cx43:Cx43, Cx30:Cx30) and oligodendrocytes (Cx47:Cx47, C30:Cx30). Heterotypic gap junctions are formed by different connexons connecting astrocytes and oligodendrocytes (Cx43:Cx47, Cx30:Cx32).

In the corpus callosum, astrocytes and NG2 glia form panglial networks (Moshrefi-Ravasdjani et al., 2017). However, in many other brain regions—like the hippocampus, the cortex, and the medial nucleus of the trapezoid body—NG2 glia are neither tracer nor electrically coupled to other glial cells (Wallraff et al., 2004; Houades et al., 2008; Muller et al., 2009; Xu et al., 2014; Bedner et al., 2015; Griemsmann et al., 2015).

Gap junctional coupling is important for homeostasis of K^+ (Wallraff et al., 2006; Pannasch et al., 2011; Breithausen et al., 2020; MacAulay, 2020), Na^+ (Langer et al., 2012; Augustin et al., 2016; Moshrefi-Ravasdjani et al., 2017; Wadle et al., 2018), Cl^- (Egawa et al., 2013), and neurotransmitters (Pannasch et al., 2011; Chaturvedi et al., 2014). Furthermore, regulated gap junctional coupling is mandatory for activity-dependent redistribution of metabolites, such as glucose (Cruz et al., 2007; Rouach et al., 2008; Giaume et al., 2010). In addition, Cx expression and gap junctional communication are altered under pathophysiological conditions (Cotrina et al., 1998; Nakase et al., 2006; Giaume et al., 2010, 2019, 2020; Xu et al., 2010; Bedner et al., 2015; Lee et al., 2016; Wang Q. et al., 2020). Thus, the basic knowledge about glial gap junctional communication is fundamentally important for our further understanding of the complex neuron-glia interaction in healthy and diseased brains.

Astrocytes can be identified by several approaches. Many astrocytes express marker proteins such as GFAP, S100β, GLAST, or GLT-1 (Eng et al., 2000; Zhou et al., 2006; Kafitz et al., 2008; Schreiner et al., 2014). However, there are subpopulations of astrocytes, which for example do not express GFAP (Kafitz et al., 2008). Additionally, a fraction of NG2 glia are characterized by expression of GFAP and S100β (Nolte et al., 2001; Matthias et al., 2003; Karram et al., 2008). In 2004, the red fluorescent dye sulforhodamine (SR) 101 was introduced as a marker for astrocytes (Nimmerjahn et al., 2004), which allows the *a priori* identification of classical astrocytes in various brain regions, for example, in hippocampus, cortex, and auditory brainstem (Nimmerjahn et al., 2004; Kafitz et al., 2008; Stephan and Friauf, 2014; Ghirardini et al., 2018). Additionally, the use of SR101 is particularly advantageous in astrocyte imaging experiments as it can be combined with ion sensitive dyes such as Fura-2 and sodium-binding benzofuran isophthalate (SBFI; Kafitz et al., 2008; Langer et al., 2012).

Another approach for *a priori* identification of astrocytes is the utilization of reporter mice, such as GFAP-eGFP mice (Nolte et al., 2001). However, the transcript labels only a subset of astrocytes (Nimmerjahn et al., 2004) and, moreover, the transcript is also weakly expressed by NG2 glia (Matthias et al., 2003). Alternatively, ALDH1L1-eGFP mice can be used to identify astrocytes (Heintz, 2004; Yang et al., 2011). These reporter mice exhibit a more accurate labeling pattern of astrocyte populations (Cahoy et al., 2008). Aside this, reporter mice are available to *a priori* identify other glia, such as oligodendrocytes (PLP-GFP mice; Fuss et al., 2000) or NG2 glia (NG2-eYFP mice; Karram et al., 2008). It is worth mentioning that all these reporter mice are suitable to be combined with imaging of ion-sensitive dyes (Moshrefi-Ravasdjani et al., 2017).

A hallmark of classical astrocytes is their large K^+ conductance (Stephan et al., 2012), which results in a highly negative membrane potential (Zhou et al., 2006; Kafitz et al., 2008). Further, astrocyte properties are less

constant as the expression of many astrocyte-typical proteins is regulated during early postnatal development (Felix et al., 2020b). For example, the expression of inwardly rectifying k^+ channels ($Kir_{4.1}$) and two-pore domain K^+ channels (K_{2P}) increases (Seifert et al., 2009; Nwaobi et al., 2014; Lunde et al., 2015; Moroni et al., 2015; Olsen et al., 2015) causing a strong decrease in membrane resistance (R_M; Zhou et al., 2006; Kafitz et al., 2008; Stephan et al., 2012; Zhong et al., 2016). Simultaneously, the detectable amount of K_V channel-mediated currents decreases, which together alters the astrocytic current-voltage relationship from non-linear to linear (Zhou et al., 2006; Kafitz et al., 2008; Zhong et al., 2016). In contrast to NG2 glia, astrocytes do not express Na_V channels (Matthias et al., 2003; Zhou et al., 2006; Kafitz et al., 2008; Zhong et al., 2016).

ANALYSIS OF GAP JUNCTIONAL COUPLING

There are many different techniques available to study gap junctions. These include but are not limited to whole-cell patch-clamp (paired recordings, analysis of isopotentiality, tracer injection), genetic approaches (FRAP, PARIS, StarTrack, transgenic mice), imaging of ion-sensitive dyes (e.g., SBFI), and expression studies (immunohistochemistry, western blotting) (Abbaci et al., 2008; Giaume and Theis, 2010; Bedner et al., 2012; Langer et al., 2012; Griemsmann et al., 2015; Droguerre et al., 2019; Eitelmann et al., 2019; Gutierrez et al., 2019; Wu et al., 2019; Du et al., 2020; McCutcheon et al., 2020). Here, we focus on approaches to analyze gap junctional communication that can be implemented easily in most electrophysiology and imaging laboratories.

Patch Clamp-Based Approaches

Electrophysiological methods are commonly used to detect gap junctional coupling of cells. In 1966, the first evidence that astrocytes are intercellularly coupled was provided by an electrophysiological study of amphibian optic nerve by Kuffler et al. (1966). In their report, an elegant triple-sharp-electrode recording mode was used to reveal a "low-resistance connection" between neuroglia, which we know now as the gap junctional coupling of fibrous astrocytes in optic nerves. This electrophysiological method was continually used until the 1980s for glial physiology study. For example, Kettenmann and Ransom used it to record cultured astrocytes and oligodendrocytes, confirming that gap junctions were indeed the molecular identities for the functional coupling of these glial subtypes (Kettenmann and Ransom, 1988; Ransom and Kettenmann, 1990).

The advent of patch-clamp in the 1990s ushered electrophysiological studies into a new era. Since the patch-clamp system is able for simultaneous current injection and membrane potential recording, now only two electrodes are used for paired recording. Here, we will limit our discussion to this advanced paired recording mode and its application to analyze the functional connectivity of neighboring astrocytes. Until now, this technique has been used by several research laboratories for study of gap junctional coupling in native astrocytes in brain slices and freshly isolated astrocytes (Muller et al., 1996; Meme et al., 2009; Xu et al., 2010, 2014; Ma et al., 2016; Zhong et al., 2016; Kiyoshi et al., 2018). These studies demonstrated the paired recording mode as a highly sensitive method for revealing the functional coupling of astrocytes *in situ* and in pairs of freshly dissociated astrocytes. To address the electrical role of gap junctional coupling for astrocyte syncytium, a single electrode method was developed in 2016 with details described in the following "Astrocyte Syncytial Isopotentiality" section. Together with computational modeling, this method allows for monitoring dynamical changes in the coupling strength of an astrocyte syncytium (Ma et al., 2016; Kiyoshi et al., 2018). Another way to assess gap junctional coupling is to add a tracer to the internal solution of patch pipettes and to visualize gap junction-coupled cells. In the following section, we will first discuss the rationale, application, advantage, and limitation of the commonly used paired recording model and the newly developed syncytial isopotentiality measurement. Thereafter, we will highlight, how the addition of gap junction-permeable tracers to the pipette solution can be used to visualize cell-to-cell coupling and to subsequently analyze the topography of tracer-coupled networks.

Paired Recording Mode

The rationale behind the design of the paired recording model lies in the basic properties of gap junction channels. Gap junctions are large aqueous pores, 8–16 Å, filled with electrolytes that make them ideal electrical conductors for the flow of ionic currents between coupled cells (Weber et al., 2004). In the adjacent cells, the easiness of the ionic current flow is determined by the number of gap junctions aggregated on the plaques in the interface of the adjacent cells, or the intercellular gap junctional resistance (R_{gap}). Accordingly, the paired recording mode is designed to examine the R_{gap} through the passing of injected currents in one of the two coupled cells and to measure subsequently the size of remaining transjunctional voltage arriving at the second cell (**Figures 2A,B**; Bennett, 1966; Bennett et al., 1991; Ma et al., 2016). There are unique characteristics associated with paired recordings. It is known that the gap junctions formed by different Cxs differ in their permeability properties for endogenous compounds, therefore, differentially regulate the intercellular transfer of metabolites, i.e., glucose, and signaling molecules, such as ATP, glutamate, and IP_3 (Goldberg et al., 1999, 2002; Niessen et al., 2000). It is also known that Cxs vary in pore size and conductivity (∼30 to ∼300 pS) (Hille, 2001). However, the Cxs ubiquitously exhibit high selectivity to the major intracellular monovalent cation K^+ and Na^+ in the order of $K^+ > Na^+$ (Wang and Veenstra, 1997), and these ions are charge carriers that mediate current flow between coupled cells. Thus, independent of Cx isoforms, transjunctional voltage measurements stand out as an universal readout of gap junctional coupling (Veenstra et al., 1995; Veenstra, 1996). Additionally, paired recordings are featured by their high detection sensitivity conferred by the

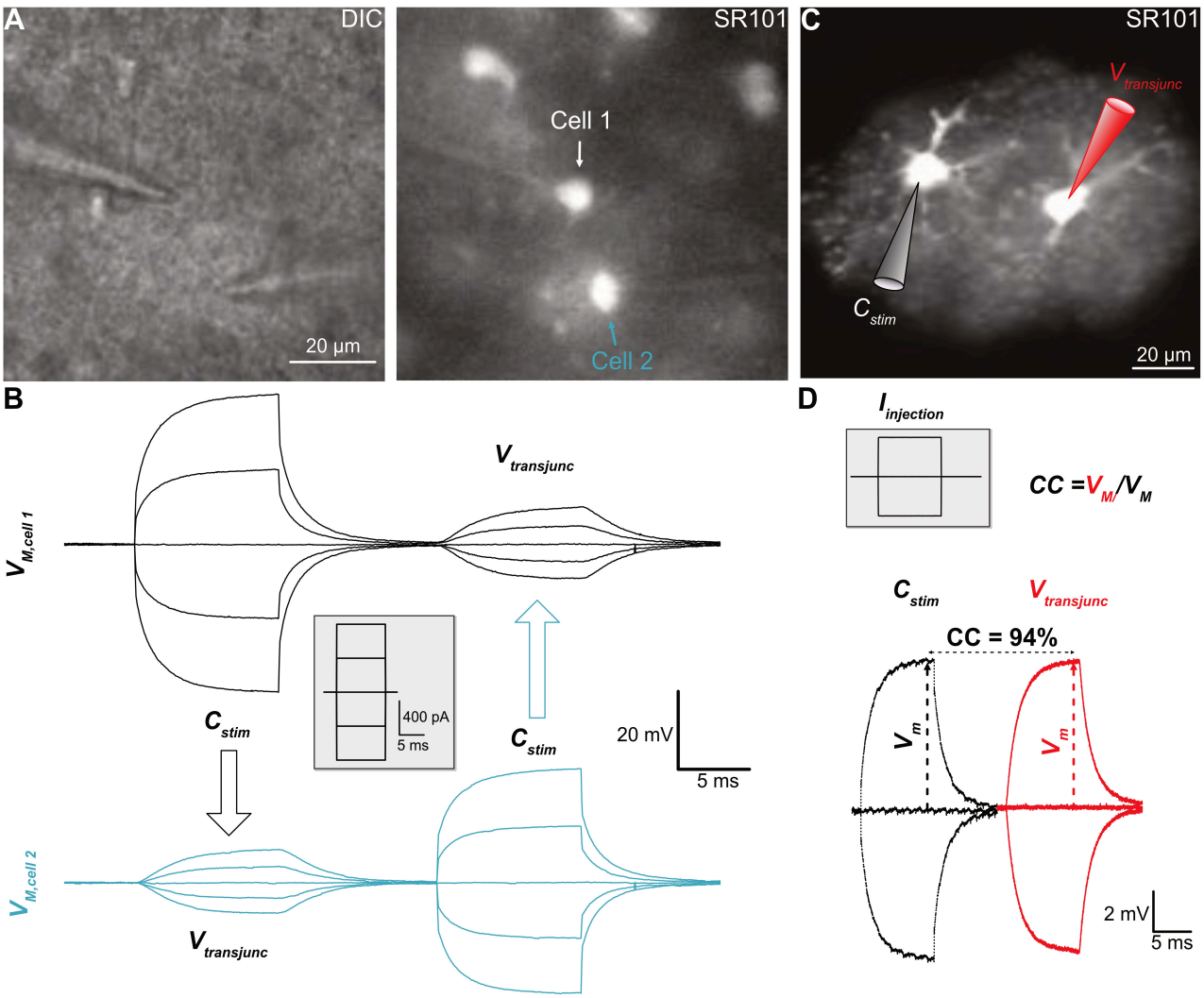

FIGURE 2 | Analysis of electrical coupling. **(A)** Paired recording of two neighboring astrocytes from hippocampal CA1 region. **(B)** In whole-cell current-clamp mode, the current steps, shown in the inset, were alternately delivered to one of the cells in a pair, termed the stimulated cell (C_{stim}), and that induced membrane potential changes in the C_{stim} meanwhile induced transjunctional voltages ($V_{transjunc}$) in the coupled neighbor. **(C)** A pair of freshly dissociated hippocampal astrocytes, identified by their SR101 staining, was recorded with K^+ free/Na^+ containing electrode solution. **(D)** The current injections into one of them induced comparable size of the membrane voltage displacements in both cells, indicating a strong coupling coefficient (*CC*) at an estimated value of 94%. Panels **(A)** and **(B)** modified from Zhong et al. (2016), and Panels **(C)** and **(D)** modified from Ma et al. (2016).

state-of-the-art electronic engineering technology of the patch-clamp amplifier, allowing detection of the ionic currents at the picoampere scale.

Experimentally, two adjacent astrocytes are sequentially recorded in whole-cell mode (**Figures 2A,B**). Subsequently, the current can be alternately injected into one of the recorded cells, defined as the stimulated cell ($C_{stim.}$), whereas the transjunctional voltage is recorded in the neighboring recipient cell ($C_{reci.}$). Although the R_{gap} can be calculated from the basic membrane properties and the current-induced membrane voltages, the coupling strength is commonly expressed as the coupling coefficient (*CC*)—the ratio of voltages measured from the $C_{reci.}/C_{stim.}$ The higher a *CC* value, the stronger the cell-to-cell coupling (Bennett, 1966; Bennett et al., 1991; Ma et al., 2016).

A major advantage of paired recordings is their high sensitivity, which is determined by the open probability that is universally high among gap junctions in the range of 0.6–0.9; whereas the sensitivity of tracer coupling is mostly determined by the pore selectivity that varies among gap junctions (Nielsen et al., 2012). Consequently, in simultaneous transjunctional voltage and dye coupling measurements, it is common to see measurable transjunctional voltages in an absence of detectable dye coupling (Murphy et al., 1983; Ransom and Kettenmann, 1990; Sontheimer et al., 1991; Xu et al., 2010). An example that paired recordings have a higher sensitivity was shown in a study carried out in hippocampal astrocytes *in situ* (Xu et al., 2010). Incubation of brain slices with a gap junction inhibitor, meclofenamic acid (MFA, 100 µM), was able to inhibit astrocyte

gap junctional coupling by 99% (Ma et al., 2016). Interestingly, in the presence of 100 μM MFA, the cross-diffusion of two tracers, Lucifer Yellow (LY) and biocytin, separately loaded into two recording electrodes, were completely inhibited, whereas the transjunctional voltages remained intact (Xu et al., 2010). In the barrel cortex, the Cx43 expression was found to be enriched within the barrels, but largely absent in the inter-barrel space (septa), and this was associated with a restricted dye coupling inside the barrels (Houades et al., 2006). To examine whether such segregated dye coupling indeed indicates a complete absence of gap junctional of astrocytes between barrels and their surrounding septa, the paired recording was carried out between a pair of astrocytes, one inside another outside of the barrel. The results showed that in the transjunctional voltage measurement, astrocytes do communicate inside and outside of the barrels and, therefore, are gap junctional coupled into a syncytium (Kiyoshi et al., 2018). Therefore, the existence of gap junctional coupling can be more sensitively inspected by this method.

Nevertheless, there are also technical challenges and limitations. First of all, still, only a handful of experimenters successfully employed paired recordings in their research. The technical complexity of paired recordings to monitor junctional coupling has limited more researchers to take advantage of this powerful tool in their glial physiology study. The second obstacle that impedes the application of paired recordings is the low R_M of astrocytes at an estimated level of 6.4 MΩ (Du et al., 2015). As a result, the "leaky" membrane shunts most of the injected currents, making it impossible to estimate the current passing through gap junctions resulting in erroneous *CC* calculation (Du et al., 2020). To make the matters worse, astrocytes are coupled into a syncytial network; each astrocyte is typically directly coupled to 7–9 nearest neighbors across the brain (Xu et al., 2010; Ma et al., 2016; Kiyoshi et al., 2018). Consequently, the injected currents to one of the recorded astrocytes should be redistributed into coupled astrocytes at unknown ratios (in a parallel electrical circuit) (Cotrina et al., 1998). Therefore, the leaking membrane and syncytial coupling make it next to impossible to calculate the actual *CC* in brain slice recordings. Consequently, rather low *CC* values in the range from 1.6% to 5.1% were reported from hippocampal astrocytes *in situ* (Meme et al., 2009; Xu et al., 2010).

To solve this problem, the innovative use of paired recordings was applied to freshly dissociated pairs of astrocytes to avoid extensive coupling. To circumvent the shunt of injected currents through abundantly expressed membrane K^+ channels, the physiological K^+ content in the electrode solution was substituted equimolarly by Na^+; hence, the electrode Na^+ equilibrating with the recorded pair of astrocytes will not leak through the membrane K^+ channels, and measured currents will therefore better reflect junctional coupling (**Figures 2C,D**). Under these conditions, a strong coupling *CC* of 94% was revealed. Based on this *CC*, there was an estimate of 2.000 gap junctions aggregated at the interface of two neighboring astrocytes, and a calculated R_{gap} at 4.3 MΩ (Ma et al., 2016), which is even lower than the astrocytic R_M of 6.4 MΩ (Du et al., 2015). These results together indicate that the electrical barrier between astrocytes is nearly absent. Recently, ultrastructural details of astrocyte-astrocyte contacts have been revealed that explain how such a low inter-astrocytic resistance could be biophysically achieved (Kiyoshi et al., 2020).

In summary, the rationale for paired recordings is based on an uniform feature of high open probability of gap junction channels for two intracellular monovalent cations, K^+ and Na^+. Therefore, it offers a rather universal readout to study the functional gap junctional coupling at high sensitivity. For brain slice studies, however, the paired recordings are most valuable for inspecting the existence of functional gap junctional coupling, but are of limited value for quantitative analysis of the *CC* between astrocytes due to the low R_M and syncytial coupling. Combinatory use of freshly dissociated pairs of astrocytes and non-physiological Na^+ or Cs^+ electrode solution is a powerful alternative to circumvent the above obstacles.

Astrocyte Syncytial Isopotentiality

As mentioned above, the R_{gap} between astrocytes is even lower than astrocytes' R_M, suggesting that two neighboring astrocytes are able to constantly equalize their membrane potentials and therefore electrically behave as one cell. By extension, the gap junction coupled astrocytes should then be able to balance their membrane potentials to comparable levels so that a syncytial isopotentiality could be achieved. In fact, this possibility was postulated in the past (Muller, 1996) and was discussed by Richard Orkand and his colleagues to be a necessity for the operation of K^+ spatial buffering in the brain (personal communication with Dr. Serguei Skatchkov). This syncytial isopotentiality was experimentally demonstrated in 2016 (Ma et al., 2016), and a system-wide existence of this feature in the astrocyte networks was confirmed soon after that (Huang et al., 2018; Kiyoshi et al., 2018; Wang W. et al., 2020).

The rationale for the methodological design is based on a basic feature of astrocytes. Physiologically, an astrocyte behaves as a perfect K^+ electrode (Kuffler et al., 1966; Ransom and Goldring, 1973). Therefore, one can experimentally substitute the intracellular K^+ concentration ($[K^+]_i$) through dialysis of the recorded cell with electrode solution containing equimolar (i.e. 140 mM) Na^+ (or Cs^+) (Ma et al., 2016; Wang W. et al., 2020). This, in turn, alters the V_M of the recorded astrocyte from K^+ equilibrium potential (E_K, -80 mV) to Na^+ equilibrium potential (E_{Na}, ∼ 0 mV) according to the prediction from the Goldman-Hodgkin-Katz (GHK) equation. In single freshly dissociated astrocytes, the V_M indeed shifts to ∼ 0 mV (**Figure 3A**) (Kiyoshi et al., 2018). However, should the R_{gap} be sufficiently low, the associated syncytium can then instantaneously act to compensate for the loss of physiological membrane potential (V_M) in the recorded cell, and the level of the compensation should be determined by the coupling strength and the number of directly nearest coupled neighbors (Ma et al., 2016; Kiyoshi et al., 2018).

Experimentally, the syncytial isopotentiality can be detected by the substitution of endogenous K^+ by a 140 mM Na^+/K^+-free electrode solution ($[Na^+]_P$) (**Figures 3A,B**) and recording the astrocyte in current-clamp mode. The breakthrough of the membrane patch shifted the V_M immediately to a resting membrane potential of -78 mV (**Figures 3A,B**). Over time, the V_M reaches a stationary level of -73 mV. This is in sharp contrast to the anticipated depolarization to 0 mV as predicted by the

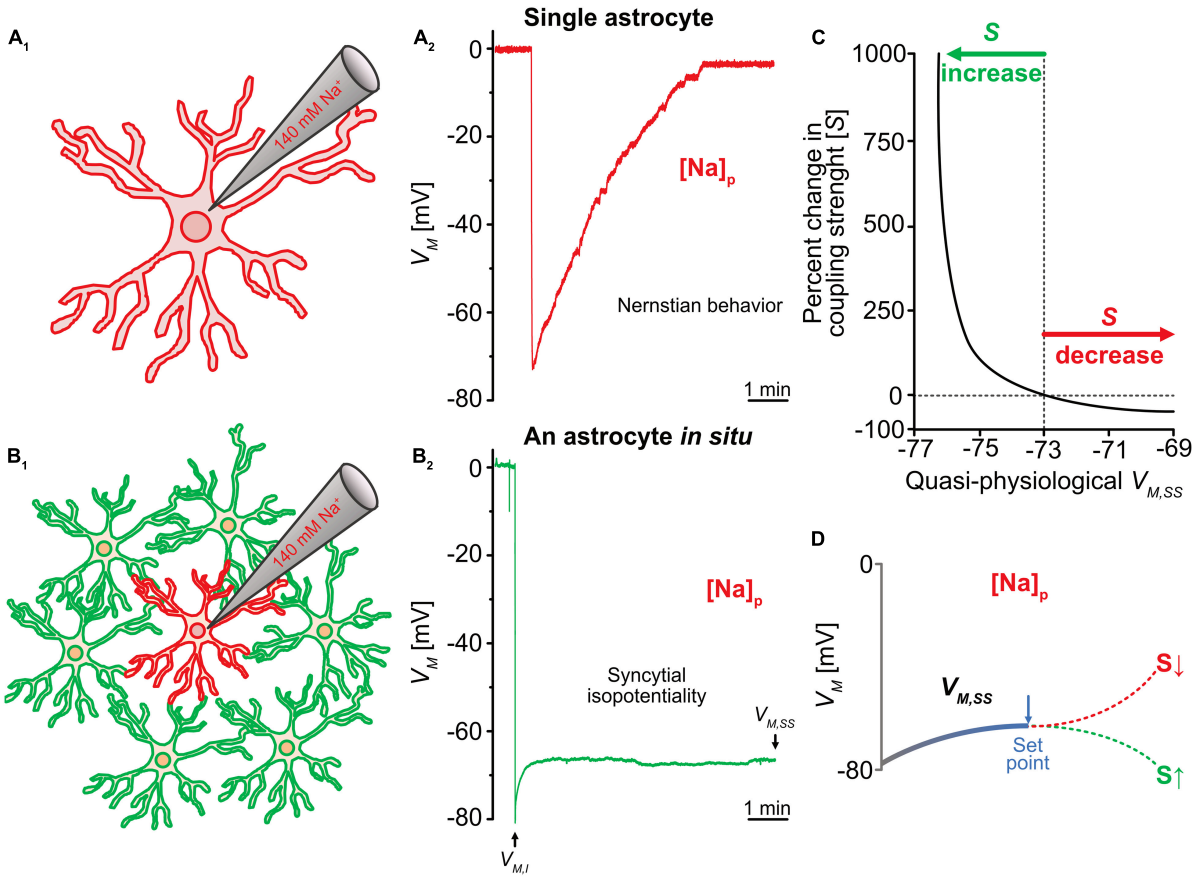

FIGURE 3 | Analysis of syncytial isopotentiality. **(A)** In a single freshly dissociated astrocyte, the K^+ free/Na^+ containing electrode solution ($[Na^+]_p$) progressively substituted the endogenous K^+ content in whole-cell recording, leading to a V_M depolarization toward 0 mV as predicated by Nernstian equation. **(B)** The V_M recorded from an astrocyte *in situ* with the $[Na^+]_p$ disobeys the Nernstian prediction. Instead, the steady-state V_M ($V_{M,SS}$) maintained at a quasi-physiological level as a result of voltage compensation by the physiological V_M of the coupled neighbors. **(C)** The relationship between $V_{M,SS}$ and coupling strength (*S*) predicted by computational modeling. **(D)** According to this modeling shown in **(C)**, the $V_{M,SS}$ can be shifted toward a more hyperpolarizing V_M of neighboring astrocytes due to a stronger syncytial coupling (*S*) or due to a weaker coupling strength (S), the $V_{M,SS}$ toward the GHK predication for the V_M of $[Na^+]_p$ at 0 mV. $V_{M,I}$ stands for initial V_M recorded immediately after break-in of cell membrane, reflecting the resting V_M of the recorded astrocyte. Figure modified from Kiyoshi et al. (2018).

GHK equation for K^+-free electrode solution (**Figure 3A**). The initial V_M recording ($V_{M,I}$) reflects the true resting V_M of an astrocyte (Ma et al., 2016; Kiyoshi et al., 2018). In hippocampal astrocyte syncytium, the steady-state V_M ($V_{M,SS}$) in $[Na^+]_P$ recordings is ~5 mV more depolarized than $V_{M,I}$.

The Ionic Mechanisms Engaged in the Establishment of $V_{M,SS}$

To biophysically explain how the quasi-physiological $V_{M,SS}$ is established, different size of syncytia, i.e., syncytia containing varying number of astrocytes, were used for $V_{M,SS}$ recordings, and computational modeling was used to simulate the underlying ionic mechanisms (Ma et al., 2016). The rupture of an astrocyte with $[Na^+]_p$ initiates dialysis of Na^+ to the recorded astrocyte and associated syncytium (**Figure 3B**$_1$). In the recorded cell, the Na^+ dialysis dissipates the endogenous K^+ content hence abolishes the physiological V_M established by the across membrane K^+ gradient. To the coupled syncytium, the Na^+ dialysis generates a Na^+ gradient and current flow across gap junctions that depolarizes neighboring astrocytes and hyperpolarizes the recorded cell. The latter is the major contributor to the quasi-physiological $V_{M,SS}$. Additionally, the dissipation of K^+ content in the recorded cell attracts an influx of K^+ from neighboring astrocytes. The accumulated K^+ has the potential to establish a hyperpolarizing potential in the recorded cell therefore additionally contributes to the totality of the quasi-physiological $V_{M,SS}$ (Ma et al., 2016). As shown in **Figure 3B**$_2$, these two ionic flows take approximately 5 min to reach a steady-state after rupture of whole-cell recording (**Figure 3B**$_2$).

How does the strength of syncytial isopotentiality influence the intensity of the Na^+ and K^+ current flows? As noted above, in the $[Na^+]_p$ recorded astrocyte, there are two ionic current flows in opposite directions and collectively contribute to the measured $V_{M,SS}$; the outward-going Na^+ current from recorded cell to the coupled cells, and inward-going K^+ current flow from the coupled astrocytes to the recorded cell. To simplify the analysis, we take the outward-going Na^+ ($I_{Na,out}$) to one of the coupled astrocytes as an example, the proximity of the potentials

in these two cells can be expressed as the difference of the voltages between the Na^+-loaded astrocyte (V_{Na}) and a coupled neighbor (V_N)

$$(V_N - V_{Na}) = R_{\text{gap}} * I_{\text{Na,out}}$$

where (V_N - V_{Na}) = 0 mV is a theoretically ideal isopotentiality achieved between the two cells. Assuming $I_{\text{Na,out}}$ is a constant determined by its chemical gradient down the neighboring cell, then a higher strength of isopotentiality, i.e., lower (V_N – V_{Na}), is correlated to a lower junctional resistance (R_{gap}). Secondly, as (V_N – V_{Na}) approaches the ideal isopotentiality of 0 mV, the $I_{Na,out}$ also diminishes to ∼ 0 pA. By extension, closer proximity of potentials between the recorded cell and its associated astrocytes, the less outward-going Na^+ current flow from $[Na^+]_p$ recorded astrocyte toward its associated syncytium.

Likewise, the intensity of the inward-going K^+ current ($I_{K,in}$) and syncytial coupling strength follows with the same relationship:

$$(V_N - V_{Na}) = R_{\text{gap}} * I_{K,in}$$

where the inward-going K^+ current is impeded by increasing proximity of the V_{Na} to V_N. It should be noted that K^+ cannot be substantially buildup due to efflux of K^+ through membrane K^+ channels in the $[Na^+]_p$ recorded astrocyte; consequently, less hyperpolarizing potential can be built up to make a significant contribution to the recorded $V_{M,\,SS}$.

In summary, we described a method that uses $[Na^+]_p$ to disrupt the continuity of a syncytial isopotentiality, and that in turn informs of the existence and the strength of the isopotentiality in an astrocyte syncytium. Biophysically, gap junctional ionic movement occurs during the equalization of the potential differences in a syncytium, therefore a strong syncytial isopotentiality means a less ionic movement inside a syncytium. Additionally, a larger syncytium has a greater capacity to minimize the ionic movement, which has been simulated in a computational model (Ma et al., 2016). Functionally, in the event of local extracellular environment changes, e.g., neuronal firing induced high K^+, syncytial isopotentiality provides a sustained driving force to individual astrocytes for high efficient K^+ uptake, spatial transfer and release of K^+ to regions where neuronal activity is low (Terman and Zhou, 2019).

$V_{M,SS}$ as a Functional Readout of Coupling Strength (S) of Syncytial Coupling

Based on the discussion above, the $V_{M,SS}$ is established and regulated by the R_{gap} and the number of astrocytes in a coupled syncytium, therefore can lean to a more hyperpolarizing V_M in the neighboring astrocytes, or a more depolarizing V_M established by intracellular Na^+. Thus, the $V_{M,SS}$ serves as a dynamic readout of the strength of syncytial coupling. To be able to quantitatively correlate the changes of $V_{M,SS}$ with *S*, a computational model has been established (**Figures 3C,D**) where a stronger syncytial coupling leads to a stronger compensation of the $V_{M,ss}$ towards the physiological V_M of neighboring astrocytes established by 140 mV $[K^+]_i$, whereas a weaker coupling shifts the $V_{M,ss}$ toward GHK predicted E_K for the Na^+ electrode solution. More details about the biophysical principles and assumptions used to build up this computational model are available in this publication (Kiyoshi et al., 2018). In addition, this model can be used for analysis of the dynamic change of coupling strength, for instance, during neuronal activation (Kiyoshi et al., 2018).

This method comprises several advantages. First, differing from paired recordings, $V_{M,SS}$ is measured from single electrode recordings. Second, this method allows for dynamic monitoring of the coupling strength of a syncytium over time. Third, this method can be incorporated with astrocyte syncytial anatomy studies. For example, ALDH1L1-eGFP reporter mice were use for *a priori* astrocyte identification and examination of syncytial isopotentiality across brain regions. Additionally, the recorded brain slices were then further processed with the tissue-clearing method (Susaki et al., 2014, 2015), i.e., depletion of the brain lipid content, for high-resolution confocal imaging study of the cellular morphology and spatial organization patterns of astrocytes (Kiyoshi et al., 2018). This study showed that in different layers of the visual cortex, the anatomy, in terms of cell density, interastrocytic distance and the number of the nearest neighbors vary in morphometric analysis. However, *S* does not differ between layers. Additionally, *S* of the visual cortex was found to be stronger than in the hippocampal CA1 region (Kiyoshi et al., 2018). Fourthly, this method can be incorporated with tracer coupling to map the directionality and spatial coupling of a syncytium (see also "Tracer Coupling"). For example, in the cerebellum, Bergmann glia and velate astrocytes are derived from the same progenitor pool but are strikingly different in their morphology (Kita et al., 2013). Bergmann glia are characterized by having their cell bodies arranged in rows alongside with the soma of Purkinje neurons and extension of their processes along the Purkinje cell layer toward the *pia* of the cerebellum. Velate astrocytes are cerebellar protoplasmic astrocytes that exhibit characteristic velate sheath processes and are more dispersed in arrangement (Chan-Palay and Palay, 1972). *S* is significantly weaker in Bergmann glia networks than those established by velate astrocytes at the granular layer. In the tracer coupling analysis, the injection of tracer revealed the coupling of Bergmann glia and velate astrocytes. Thus, despite a striking difference in syncytial anatomy, the syncytial isopotentiality occurs to syncytial networks established by both subtypes of astrocytes (Kiyoshi et al., 2018).

A limitation in this method is the inference of a syncytial isopotentiality based on biophysical principles and electrophysiological measurements. Significant progress has been made in the technique of genetically encoded voltage indicator (Kang et al., 2019). However, this state-of-the-art technique is still below the threshold to detect the subtle variation of voltages in an astrocyte syncytium, and therefore, future optimization of this technique is crucial to recruit advanced imaging techniques to study the physiology and pathology of astrocyte syncytial networks.

Tracer Coupling

Aside this direct measurement of cell-to-cell coupling, tracer coupling can be utilized to mimic diffusion within in the network. Tracers are usually loaded for several minutes into a single cell via the backfill of the patch pipette. Simultaneously, tracers diffuse within the gap junction network. The tracer concentration is highest in the patched cell and declines within the network with increasing distance as it diffuses. There are various tracers available comprising different advantages and disadvantages (**Table 1**; see also Abbaci et al., 2008). An often used tracer is LY (Kawata et al., 1983). It is a fluorescent dye that allows direct observation of diffusion within the network. Subsequently, LY labeling can be combined with immunohistochemistry to determine the identity of coupled cells (Binmoller and Muller, 1992; Konietzko and Muller, 1994). However, it comprises low permeability at gap junctions consisting of Cx30 (Rackauskas et al., 2007). As Cx30 expression increases during early postnatal development (Nagy et al., 1999; Griemsmann et al., 2015; Augustin et al., 2016; Wadle et al., 2018), LY will only highlight a fraction of coupling in more mature tissue. In addition, LY has a low solubility and tends to clog electrodes. As LY interferes with endogenous electrophysiological properties, it is rather not suitable to be combined with electrophysiological analyses (Tasker et al., 1991). Further fluorophores, e.g., Alexa Fluor (AF) dyes, can be used for tracing coupled cells as well (Han et al., 2013). Like LY, spreading of AF dyes can be assessed directly. However, they do not pass through Cx30 containing gap junctions and just insufficiently through other gap junctions requiring administration at high concentration (Weber et al., 2004). At lower concentrations, there is almost no diffusion to neighboring cells so that AF dyes can be used to label the patch-clamped cell (Augustin et al., 2016; Wadle et al., 2018; Eitelmann et al., 2019). Two other tracers, namely neurobiotin (Nb) and biocytin (Horikawa and Armstrong, 1988; Huang et al., 1992), are colorless and require fixation and further processing of the tissue. Thus, their diffusion cannot be assessed directly. The two tracers are recognized by streptavidin and avidin (Livnah et al., 1993). The latter ones can be linked to either fluorophores or enzymes. Using a fluorophore allows the combination with further immunohistochemical processing of the tissue (Schools

TABLE 1 | Commonly used tracers for analyzing gap junctional coupling.

Tracer	Mass [g/mol]	Fluorescence	Histology required	Advantage	Disadvantage	Reference(s)
LY 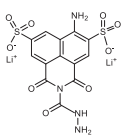	457	✓	✗	Direct imaging	Low Cx30-permeability Alteration of electrophysiological properties	Tasker et al., 1991 Kawata et al., 1983 Rackauskas et al., 2007
NB 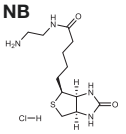	323	✗	(Strept-/) Avidin conjugates	Permeable through all astrocytic Cx	Background labeling of endogenous biotin	Huang et al., 1992 Livnah et al., 1993
Biocytin 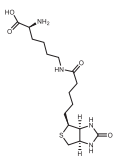	375	✗	(Strept-/) Avidin conjugates	Permeable through all astrocytic Cx	Background labeling of endogenous biotin	Horikawa and Armstrong, 1988 Livnah et al., 1993
2-NBDG 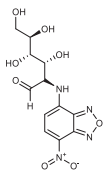	342	✓	✗	Imaging of glucose distribution	Degradation to non-fluorescent derivative	Yoshioka et al., 1996 Yamada et al., 2000
6-NBDG 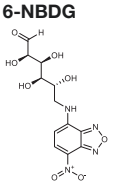	342	✓	✗	Imaging of glucose distribution		Speizer et al., 1985

LY, Lucifer Yellow; NB, neurobiotin; Cx, connexin; NBDG, deoxy-N-(7-nitrobenz-2-oxa-1,3-diazol-4-yl)-aminoglucose; AF, Alexa Fluor.

et al., 2006; Augustin et al., 2016; Eitelmann et al., 2019, 2020). Using peroxidases produces a light-stable product that is not sensitive to photo-bleaching (Konietzko and Muller, 1994; D'Ambrosio et al., 1998). Alternatively, fluorescent glucose analogues can be used (Speizer et al., 1985; Yamada et al., 2000). They allow to visualize activity-dependent, directed glucose redistribution in otherwise spherical networks (Rouach et al., 2008). However, it has to be kept in mind that, for example, 2-NBDG enters the glycolytic pathway and is degraded to a non-fluorescent derivative (Yoshioka et al., 1996).

Gap junctional coupling is not uniform, e.g., it was shown to increase developmentally (Binmoller and Muller, 1992; Schools et al., 2006; Houades et al., 2008; Langer et al., 2012; Griemsmann et al., 2015). Furthermore, there are many examples of spherical networks upon radial tracer diffusion in certain brain regions (Binmoller and Muller, 1992; Houades et al., 2006; Muller et al., 2009). However, in others—in particular in sensory systems—tracer spreading is unequal in different directions (Houades et al., 2008; Augustin et al., 2016; Claus et al., 2018; Condamine et al., 2018a; Wadle et al., 2018). There, network anisotropy strongly correlates with anatomical and functional organization of the underlying neuronal circuitry. The anisotropy of tracer spreading originates from astrocyte topography (Anders et al., 2014; Augustin et al., 2016; Ghezali et al., 2018; Wadle et al., 2018). Interestingly, in the lateral superior olive—a conspicuous nucleus in the auditory brainstem—absence of spontaneous cochlea-driven neuronal activity leading to disturbed neuronal circuitry (Hirtz et al., 2012; Muller et al., 2019) causes altered astrocyte topography followed by altered orientation of tracer-coupled networks (Eitelmann et al., 2020). In recent years, several different approaches were developed to analyze the anisotropy of tracer-coupled networks (**Figure 4**). Most approaches are able to reliably detect network anisotropy; however, some are working only in certain brain regions (Eitelmann et al., 2019). The different approaches rely on (1) distance of the farthest cells that are labeled, (2) labeling intensity, (3) position of all coupled cells, or (4) a combination of the aforementioned parameters. Most approaches use the ratio of the diffusion range and/or brightness

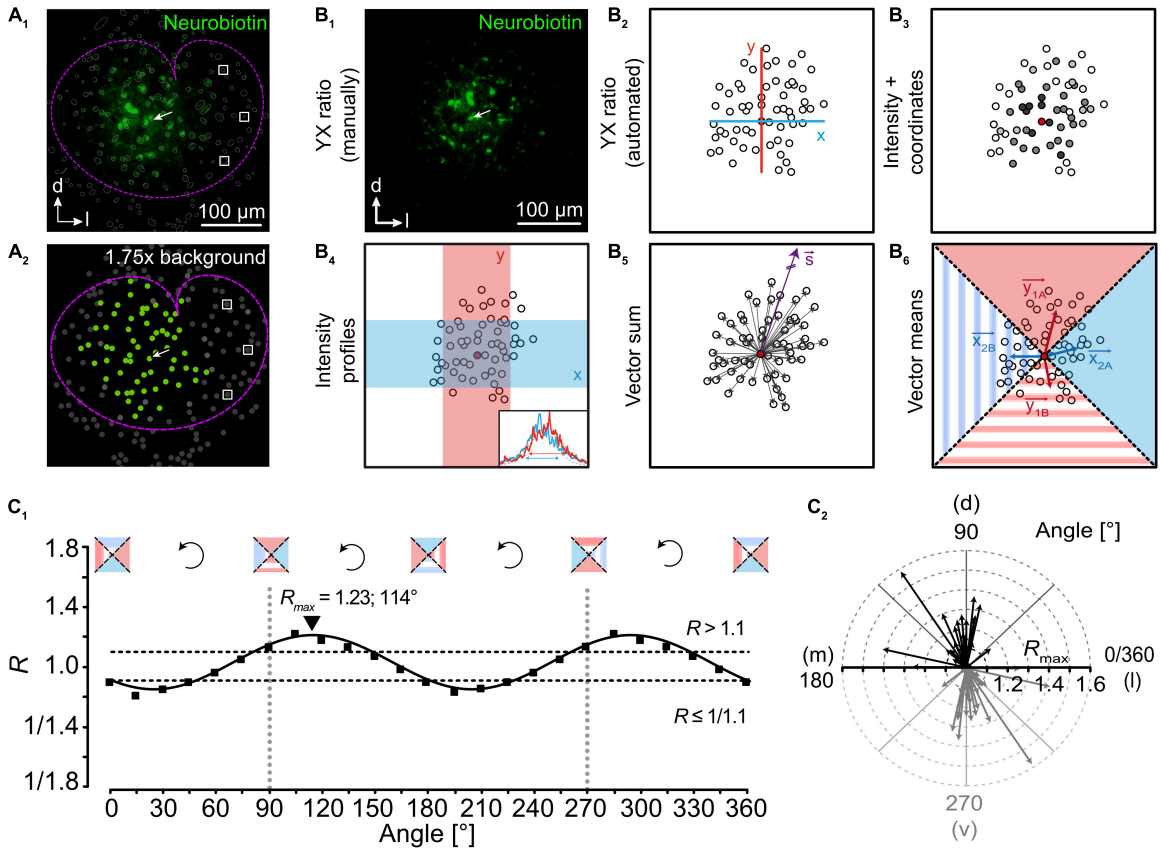

FIGURE 4 | Analysis of network topography. **(A)** Detection of coupled cells. Astrocytes in the lateral superior olive (outlined by dotted magenta line) form large tracer-coupled networks (**A_1**; green). All identified cells are encircled with a thin gray line. Semi-automated detection of coupled cells is achieved by determining background fluorescence levels of cells (white boxes) being far located from the tracer-filled cell (arrow). Setting a threshold allows for unbiased selection of coupled cells (**A_2**; green: coupled cells; gray: not coupled cells). **(B)** Approaches to study the topography of tracer-coupled networks. Anisotropy is often determined by the ratio of tracer spread (distance and/or intensity) in two directions that are orthogonal to each other **($B_{1-4,6}$)**. Alternatively, a purely vector-based approach can be used **(B_5)**. **(C)** In case of ratio-based analyses, rotation of the coordinate system allows the precise determination of maximal anisotropy and orientation (**C_1**; exemplarily shown for vector means, **B_6**). Afterward, results can be gathered in a radar diagram to denote the degree of anisotropy and orientation of networks **(C_2)**. Figure modified from Eitelmann et al. (2019).

of the tracer in two directions. The most convenient approach is to measure the extent of tracer spreading in two directions orthogonal to each other ("YX ratio"). Here, anisotropy is determined by the four outermost cells showing tracer signal (**Figure 4B**$_{1,2}$; Houades et al., 2006, 2008; Augustin et al., 2016; Ghezali et al., 2018; Wadle et al., 2018). However, since the tracer signal is declining with distance to the loaded cell, it can be difficult to determine the correct extension of the network. Alternatively, the product of network extension multiplied with the somatic tracer intensity for two directions orthogonal to each other can be calculated ("Intensity + coordinates"; **Figure 4B**$_3$; Anders et al., 2014). However, elevated somatic signal intensities

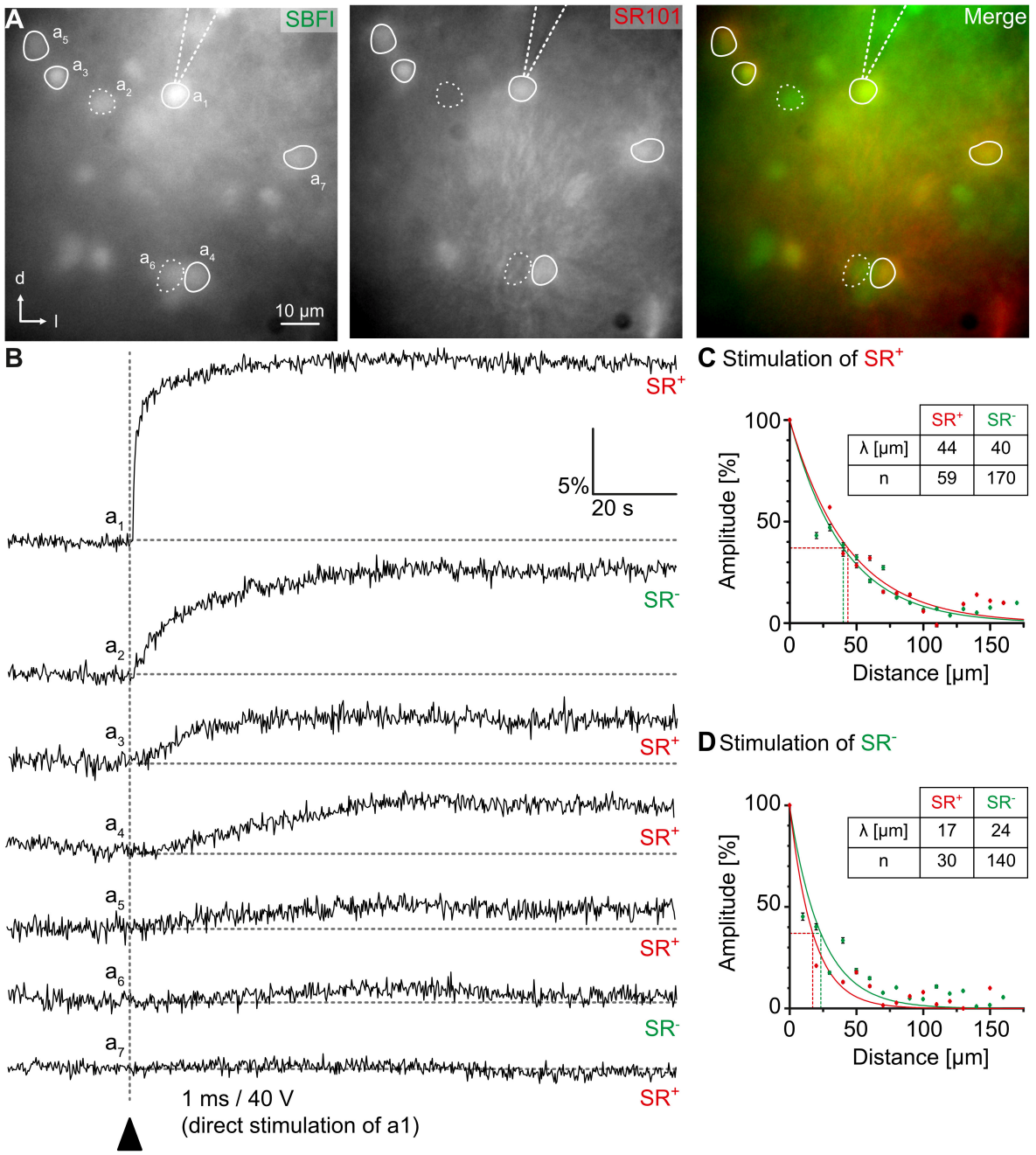

FIGURE 5 | Na^+ diffusion in glial networks. **(A)** Cells in the center of the inferior colliculus can be loaded with the fluorescent Na^+ indicator SBFI-AM (left). Astrocytes and *bona fide* oligodendrocytes can be distinguished by sulforhodamine (SR) 101-labeling. **(B)** Electrical stimulation results in Na^+ load of a single astrocyte (**a$_1$**). Subsequently, neighboring astrocytes (**a$_3$–a$_5$,a$_7$**; SR^+) and *bona fide* oligodendrocytes (**a$_2$,a$_6$**; SR^-), show elevated Na^+ transients as well. **(C,D)** Na^+ diffusion can be elicited by stimulation of both astrocytes **(C)** and *bona fide* oligodendrocytes **(D)**. The amplitude of Na^+ transients depends on the distance from the stimulated cell. Figure modified from Wadle et al. (2018).

due to expression of endogenous biotin (Bixel and Hamprecht, 2000; Yagi et al., 2002) might result in a distorted ratio. In another approach, the labeling intensity of somata and processes is analyzed to determine network anisotropy ("Intensity profiles"; **Figure 4B$_4$**; Claus et al., 2018). Here, intensity plot profiles of two rectangles orthogonal to each other and the ratio of respective full-width at half-maximum (FWHM) are calculated. However, cell number or individual positions are neglected and must be analyzed separately, if required. Finally, there are two vector-based approaches. The first calculates the "Vector sum" (**Figure 4B$_5$**; Condamine et al., 2018a,b). However, it only works in brain regions with defined borders, i.e., diffusion barriers resulting from reduced gap junction coupling. Examples of such brain regions are the trigeminal main sensory nucleus and the columns of the barrel cortex. In both, gap junction coupling is stronger within the nucleus and columns compared to areas outside. However, anisotropic tracer diffusion will be visualized only if the tracer is injected into an astrocyte that is not located in the center (Houades et al., 2008; Condamine et al., 2018a) as the "Vector sum" approach is not capable to detect the anisotropy of tracer-coupled networks if they are symmetric with respect to a point (Eitelmann et al., 2019). The second vector-based approach calculates the "Vector means" in four 90° sectors and the ratio of tracer extension is calculated (**Figure 4B$_6$**; Eitelmann et al., 2019, 2020). However, analyzing the anisotropy of tracer spreading using only two fixed axes might result in falsified results. For example, if an anisotropic network is turned by 45° from one of the two axes, all ratio-based approaches will postulate spherical network. Therefore, a subsequent analysis using a rotating coordinate system will not only determine the maximal anisotropy of a network, but will also define the preferred orientation (**Figure 4C**; Eitelmann et al., 2019). Taken together, heterogeneity of gap junctional coupling can be visualized excellently by tracer coupling studies. However, they often provide only a snap-shot of coupling using a non-physiological tracer.

Wide Field (Na^+) Imaging

Imaging of intracellular ion concentration can be a good tool to supplement tracer coupling studies. For the interpretation of ion diffusion within the gap junction network, it is beneficial to analyze the spread of ions that is less effected by signaling cascades. Thus, Ca^{2+} is a less suitable candidate as signaling to neighboring cells is generated by intra- and extracellular pathways (Giaume and Venance, 1998; Bernardinelli et al., 2004; Scemes and Giaume, 2006). However, intercellular Na^+ spread depends on gap junctional coupling as deletion of Cx43 and Cx30 prevents ion exchange between neighboring astrocytes (Wallraff et al., 2006; Langer et al., 2012). However, it has to be kept in mind that intracellular Na^+ is not completely independent from signaling cascades as it is linked to Ca^{2+} via the Na^+/Ca^{2+} exchanger (Felix et al., 2020a). For Na^+ imaging, cells are dye-loaded, e.g., with the membrane-permeable form of SBFI (SBFI-acetoxymethyl ester). After cleavage by endogenous esterases SBFI allows ratiometric imaging of $[Na^+]_i$ (**Figure 5**; Minta and Tsien, 1989; Meier et al., 2006). Na^+ load into a single cell can be achieved via direct electrical stimulation. This will result in Na^+ rise in the stimulated and in neighboring cells (**Figure 5B**; Langer et al., 2012; Augustin et al., 2016; Moshrefi-Ravasdjani et al., 2017; Wadle et al., 2018). Measuring the maximal $[Na^+]_i$ increase allows for the calculation of the length constant λ using a mono-exponential function (**Figures 5C,D**; Augustin et al., 2016; Moshrefi-Ravasdjani et al., 2017; Wadle et al., 2018), which demonstrates, how efficient Na^+ is redistributed and how strong gap junctional coupling is. It was shown that spatial spread of Na^+ between astrocytes was halfway far in the corpus callosum compared to other brain regions, i.e., hippocampus, lateral superior olive, and inferior colliculus (Langer et al., 2012; Augustin et al., 2016; Moshrefi-Ravasdjani et al., 2017; Wadle et al., 2018). Furthermore, Na^+ diffusion is stronger within homocellular networks. In contrast, in heterocellular (panglial) networks Na^+ redistribution is reduced (**Figure 5D**; Moshrefi-Ravasdjani et al., 2017; Wadle et al., 2018), which likely results from a lower permeability of connexons, which are incorporated into the heterotypic gap junction channels (Bedner et al., 2006). Taken together, imaging of ion sensitive dyes is a good supplement to tracer coupling studies to further characterize gap junctional communication.

CONCLUSION

Gap junctional communication between glial cells is important for ion and neurotransmitter homeostasis and ensures stabilization of their membrane potential. Though astrocytes throughout the brain share similar properties, they exhibit a considerable amount of region-dependent heterogeneity. To unravel these particular differences suitable approaches are necessary. In this review, we summarized and described well-established and recently developed methods that will allow electrophysiology and imaging laboratories to analyze gap junctional coupling in acute tissue slices.

AUTHOR CONTRIBUTIONS

JS and MZ designed the study. JS, MZ, and SE wrote the manuscript. SE designed and arranged the figures. All authors contributed to the article and approved the submitted version.

FUNDING

This study was supported by grants from the German Research Foundation (DFG Priority Program 1608 "Ultrafast and temporally precise information processing: Normal and dysfunctional hearing": STE 2352/2-1) to JS and the National Institute of Neurological Disorders and Stroke (RO1NS116059) to MZ.

ACKNOWLEDGMENTS

We acknowledge the support by the Heinrich Heine University Duesseldorf.

REFERENCES

Aasen, T., Johnstone, S., Vidal-Brime, L., Lynn, K. S., and Koval, M. (2018). Connexins: synthesis, post-translational modifications, and trafficking in health and disease. *Int J. Mol. Sci.* 19:1296. doi: 10.3390/ijms19051296

Abbaci, M., Barberi-Heyob, M., Blondel, W., Guillemin, F., and Didelon, J. (2008). Advantages and limitations of commonly used methods to assay the molecular permeability of gap junctional intercellular communication. *Biotechniques* 45, 56–62.

Anders, S., Minge, D., Griemsmann, S., Herde, M. K., Steinhauser, C., and Henneberger, C. (2014). Spatial properties of astrocyte gap junction coupling in the rat hippocampus. *Philos. Trans. R. Soc. Lond. B Biol. Sci.* 369:20130600. doi: 10.1098/rstb.2013.0600

Augustin, V., Bold, C., Wadle, S. L., Langer, J., Jabs, R., Philippot, C., et al. (2016). Functional anisotropic panglial networks in the lateral superior olive. *Glia* 64, 1892–1911. doi: 10.1002/glia.23031

Axelsen, L. N., Calloe, K., Holstein-Rathlou, N. H., and Nielsen, M. S. (2013). Managing the complexity of communication: regulation of gap junctions by post-translational modification. *Front. Pharmacol.* 4:130. doi: 10.3389/fphar.2013.00130

Bedner, P., Dupper, A., Huttmann, K., Muller, J., Herde, M. K., Dublin, P., et al. (2015). Astrocyte uncoupling as a cause of human temporal lobe epilepsy. *Brain* 138, 1208–1222. doi: 10.1093/brain/awv067

Bedner, P., Niessen, H., Odermatt, B., Kretz, M., Willecke, K., and Harz, H. (2006). Selective permeability of different connexin channels to the second messenger cyclic AMP. *J. Biol. Chem.* 281, 6673–6681. doi: 10.1074/jbc.m511235200

Bedner, P., Steinhauser, C., and Theis, M. (2012). Functional redundancy and compensation among members of gap junction protein families? *Biochim. Biophys. Acta* 1818, 1971–1984. doi: 10.1016/j.bbamem.2011.10.016

Bennett, M. V. (1966). Physiology of electrotonic junctions. *Ann. N. Y. Acad. Sci.* 137, 509–539. doi: 10.1111/j.1749-6632.1966.tb50178.x

Bennett, M. V., Barrio, L. C., Bargiello, T. A., Spray, D. C., Hertzberg, E., and Saez, J. C. (1991). Gap junctions: new tools, new answers, new questions. *Neuron* 6, 305–320. doi: 10.1016/0896-6273(91)90241-q

Bernardinelli, Y., Magistretti, P. J., and Chatton, J. Y. (2004). Astrocytes generate Na+-mediated metabolic waves. *Proc. Natl. Acad. Sci. U.S.A.* 101, 14937–14942. doi: 10.1073/pnas.0405315101

Binmoller, F. J., and Muller, C. M. (1992). Postnatal development of dye-coupling among astrocytes in rat visual cortex. *Glia* 6, 127–137. doi: 10.1002/glia.440060207

Bixel, M. G., and Hamprecht, B. (2000). Immunocytochemical localization of beta-methylcrotonyl-CoA carboxylase in astroglial cells and neurons in culture. *J. Neurochem.* 74, 1059–1067. doi: 10.1046/j.1471-4159.2000.0741059.x

Breithausen, B., Kautzmann, S., Boehlen, A., Steinhauser, C., and Henneberger, C. (2020). Limited contribution of astroglial gap junction coupling to buffering of extracellular K(+) in CA1 stratum radiatum. *Glia* 68, 918–931. doi: 10.1002/glia.23751

Bukauskas, F. F., and Verselis, V. K. (2004). Gap junction channel gating. *Biochim. Biophys. Acta* 1662, 42–60.

Cahoy, J. D., Emery, B., Kaushal, A., Foo, L. C., Zamanian, J. L., Christopherson, K. S., et al. (2008). A transcriptome database for astrocytes, neurons, and oligodendrocytes: a new resource for understanding brain development and function. *J. Neurosci.* 28, 264–278. doi: 10.1523/jneurosci.4178-07.2008

Chan-Palay, V., and Palay, S. L. (1972). The form of velate astrocytes in the cerebellar cortex of monkey and rat: high voltage electron microscopy of rapid Golgi preparations. *Z. Anat. Entwicklungsgesch* 138, 1–19. doi: 10.1007/bf00519921

Chaturvedi, R., Reddig, K., and Li, H. S. (2014). Long-distance mechanism of neurotransmitter recycling mediated by glial network facilitates visual function in *Drosophila*. *Proc. Natl. Acad. Sci. U.S.A.* 111, 2812–2817. doi: 10.1073/pnas.1323714111

Claus, L., Philippot, C., Griemsmann, S., Timmermann, A., Jabs, R., Henneberger, C., et al. (2018). Barreloid borders and neuronal activity shape panglial gap junction-coupled networks in the mouse thalamus. *Cereb. Cortex* 28, 213–222.

Condamine, S., Lavoie, R., Verdier, D., and Kolta, A. (2018a). Functional rhythmogenic domains defined by astrocytic networks in the trigeminal main sensory nucleus. *Glia* 66, 311–326. doi: 10.1002/glia.23244

Condamine, S., Verdier, D., and Kolta, A. (2018b). Analyzing the size, shape, and directionality of networks of coupled astrocytes. *J. Vis. Exp.* 4, 58116. doi: 10.3791/58116

Cotrina, M. L., Kang, J., Lin, J. H., Bueno, E., Hansen, T. W., He, L., et al. (1998). Astrocytic gap junctions remain open during ischemic conditions. *J. Neurosci.* 18, 2520–2537. doi: 10.1523/jneurosci.18-07-02520.1998

Cruz, N. F., Ball, K. K., and Dienel, G. A. (2007). Functional imaging of focal brain activation in conscious rats: impact of [(14)C]glucose metabolite spreading and release. *J. Neurosci. Res.* 85, 3254–3266. doi: 10.1002/jnr.21193

Dahl, E., Manthey, D., Chen, Y., Schwarz, H. J., Chang, Y. S., Lalley, P. A., et al. (1996). Molecular cloning and functional expression of mouse connexin-30,a gap junction gene highly expressed in adult brain and skin. *J. Biol. Chem.* 271, 17903–17910. doi: 10.1074/jbc.271.30.17903

D'Ambrosio, R., Wenzel, J., Schwartzkroin, P. A., Mckhann, G. M. II, and Janigro, D. (1998). Functional specialization and topographic segregation of hippocampal astrocytes. *J. Neurosci.* 18, 4425–4438. doi: 10.1523/jneurosci.18-12-04425.1998

Droguerre, M., Tsurugizawa, T., Duchene, A., Portal, B., Guiard, B. P., Deglon, N., et al. (2019). A new tool for in vivo study of astrocyte connexin 43 in brain. *Sci. Rep.* 9:18292.

Du, Y., Kiyoshi, C. M., Terman, D., and Zhou, M. (2020). "Analysis of the functional states of an astrocyte syncytium," in *Basic Neurobiology Techniques*, ed. N. Wright (New York, NY: Humana), 285–313. doi: 10.1007/978-1-4939-9944-6_12

Du, Y., Ma, B., Kiyoshi, C. M., Alford, C. C., Wang, W., and Zhou, M. (2015). Freshly dissociated mature hippocampal astrocytes exhibit passive membrane conductance and low membrane resistance similarly to syncytial coupled astrocytes. *J. Neurophysiol.* 113, 3744–3750. doi: 10.1152/jn.00206.2015

Egawa, K., Yamada, J., Furukawa, T., Yanagawa, Y., and Fukuda, A. (2013). Cl(-) homeodynamics in gap junction-coupled astrocytic networks on activation of GABAergic synapses. *J. Physiol.* 591, 3901–3917. doi: 10.1113/jphysiol.2013.257162

Eitelmann, S., Hirtz, J. J., and Stephan, J. (2019). A vector-based method to analyze the topography of glial networks. *Int. J. Mol. Sci.* 20:2821. doi: 10.3390/ijms20112821

Eitelmann, S., Petersilie, L., Rose, C. R., and Stephan, J. (2020). Altered gap junction network topography in mouse models for human hereditary deafness. *Int. J. Mol. Sci.* 21:7376. doi: 10.3390/ijms21197376

Eng, L. F., Ghirnikar, R. S., and Lee, Y. L. (2000). Glial fibrillary acidic protein: GFAP-thirty-one years (1969-2000). *Neurochem. Res.* 25, 1439–1451.

Felix, L., Delekate, A., Petzold, G. C., and Rose, C. R. (2020a). Sodium fluctuations in astroglia and their potential impact on astrocyte function. *Front. Physiol.* 11:871. doi: 10.3389/fphys.2020.00871

Felix, L., Stephan, J., and Rose, C. R. (2020b). Astrocytes of the early postnatal brain. *Eur. J. Neurosci.* [Epub ahead of print]. doi: 10.1111/ejn.14780

Fuss, B., Mallon, B., Phan, T., Ohlemeyer, C., Kirchhoff, F., Nishiyama, A., et al. (2000). Purification and analysis of in vivo-differentiated oligodendrocytes expressing the green fluorescent protein. *Dev. Biol.* 218, 259–274. doi: 10.1006/dbio.1999.9574

Ghezali, G., Calvo, C. F., Pillet, L. E., Llense, F., Ezan, P., Pannasch, U., et al. (2018). Connexin 30 controls astroglial polarization during postnatal brain development. *Development* 145:dev155275. doi: 10.1242/dev.155275

Ghirardini, E., Wadle, S. L., Augustin, V., Becker, J., Brill, S., Hammerich, J., et al. (2018). Expression of functional inhibitory neurotransmitter transporters GlyT1, GAT-1, and GAT-3 by astrocytes of inferior colliculus and hippocampus. *Mol. Brain* 11:4.

Giaume, C., Koulakoff, A., Roux, L., Holcman, D., and Rouach, N. (2010). Astroglial networks: a step further in neuroglial and gliovascular interactions. *Nat. Rev. Neurosci.* 11, 87–99. doi: 10.1038/nrn2757

Giaume, C., Saez, J. C., Song, W., Leybaert, L., and Naus, C. C. (2019). Connexins and pannexins in Alzheimer's disease. *Neurosci. Lett.* 695, 100–105. doi: 10.1016/j.neulet.2017.09.006

Giaume, C., and Theis, M. (2010). Pharmacological and genetic approaches to study connexin-mediated channels in glial cells of the central nervous system. *Brain Res. Rev.* 63, 160–176. doi: 10.1016/j.brainresrev.2009.11.005

Giaume, C., and Venance, L. (1998). Intercellular calcium signaling and gap junctional communication in astrocytes. *Glia* 24, 50–64. doi: 10.1002/(sici)1098-1136(199809)24:1<50::aid-glia6>3.0.co;2-4

Giaume, C. B., Naus, C. C., Saez, J. C., and Leybaert, L. (2020). Glial connexins and pannexins in the healthy and diseased brain. *Physiol. Rev.* 101, 93–145. doi: 10.1152/physrev.00043.2018

Goldberg, G. S., Lampe, P. D., and Nicholson, B. J. (1999). Selective transfer of endogenous metabolites through gap junctions composed of different connexins. *Nat. Cell Biol.* 1, 457–459. doi: 10.1038/15693

Goldberg, G. S., Moreno, A. P., and Lampe, P. D. (2002). Gap junctions between cells expressing connexin 43 or 32 show inverse permselectivity to adenosine and ATP. *J. Biol. Chem.* 277, 36725–36730. doi: 10.1074/jbc.m109797200

Goodenough, D. A., and Paul, D. L. (2009). Gap junctions. *Cold Spring Harb. Perspect. Biol.* 1:a002576.

Griemsmann, S., Hoft, S. P., Bedner, P., Zhang, J., Von Staden, E., Beinhauer, A., et al. (2015). Characterization of panglial gap junction networks in the thalamus, neocortex, and hippocampus reveals a unique population of glial cells. *Cereb. Cortex* 25, 3420–3433. doi: 10.1093/cercor/bhu157

Gutierrez, Y., Garcia-Marques, J., Liu, X., Fortes-Marco, L., Sanchez-Gonzalez, R., Giaume, C., et al. (2019). Sibling astrocytes share preferential coupling via gap junctions. *Glia* 67, 1852–1858. doi: 10.1002/glia.23662

Han, X., Chen, M., Wang, F., Windrem, M., Wang, S., Shanz, S., et al. (2013). Forebrain engraftment by human glial progenitor cells enhances synaptic plasticity and learning in adult mice. *Cell Stem Cell* 12, 342–353. doi: 10.1016/j.stem.2012.12.015

Harris, A. L. (2007). Connexin channel permeability to cytoplasmic molecules. *Prog. Biophys. Mol. Biol.* 94, 120–143. doi: 10.1016/j.pbiomolbio.2007.03.011

Heintz, N. (2004). Gene expression nervous system atlas (GENSAT). *Nat. Neurosci.* 7:483. doi: 10.1038/nn0504-483

Hille, B. (2001). *Ion Channels of Excitable Cells*. Sunderland, MA: Sinauer.

Hirtz, J. J., Braun, N., Griesemer, D., Hannes, C., Janz, K., Lohrke, S., et al. (2012). Synaptic refinement of an inhibitory topographic map in the auditory brainstem requires functional Cav1.3 calcium channels. *J. Neurosci.* 32, 14602–14616. doi: 10.1523/jneurosci.0765-12.2012

Horikawa, K., and Armstrong, W. E. (1988). A versatile means of intracellular labeling: injection of biocytin and its detection with avidin conjugates. *J. Neurosci. Methods* 25, 1–11. doi: 10.1016/0165-0270(88)90114-8

Houades, V., Koulakoff, A., Ezan, P., Seif, I., and Giaume, C. (2008). Gap junction-mediated astrocytic networks in the mouse barrel cortex. *J. Neurosci.* 28, 5207–5217. doi: 10.1523/jneurosci.5100-07.2008

Houades, V., Rouach, N., Ezan, P., Kirchhoff, F., Koulakoff, A., and Giaume, C. (2006). Shapes of astrocyte networks in the juvenile brain. *Neuron Glia Biol.* 2, 3–14. doi: 10.1017/s1740925x06000081

Huang, M., Du, Y., Kiyoshi, C., Wu, X., Askwith, C., Mctigue, D., et al. (2018). Syncytial isopotentiality: an electrical feature of spinal cord astrocyte networks. *Neuroglia* 1, 271–279. doi: 10.3390/neuroglia1010018

Huang, Q., Zhou, D., and Difiglia, M. (1992). Neurobiotin, a useful neuroanatomical tracer for in vivo anterograde, retrograde and transneuronal tract-tracing and for in vitro labeling of neurons. *J. Neurosci. Methods* 41, 31–43. doi: 10.1016/0165-0270(92)90121-s

Kafitz, K. W., Meier, S. D., Stephan, J., and Rose, C. R. (2008). Developmental profile and properties of sulforhodamine 101–Labeled glial cells in acute brain slices of rat hippocampus. *J. Neurosci. Methods* 169, 84–92. doi: 10.1016/j.jneumeth.2007.11.022

Kang, B. E., Lee, S., and Baker, B. J. (2019). Optical consequences of a genetically-encoded voltage indicator with a pH sensitive fluorescent protein. *Neurosci. Res.* 146, 13–21. doi: 10.1016/j.neures.2018.10.006

Karram, K., Goebbels, S., Schwab, M., Jennissen, K., Seifert, G., Steinhauser, C., et al. (2008). NG2-expressing cells in the nervous system revealed by the NG2-EYFP-knockin mouse. *Genesis* 46, 743–757. doi: 10.1002/dvg.20440

Kawata, M., Sano, Y., Inenaga, K., and Yamashita, H. (1983). Immunohistochemical identification of lucifer yellow-labeled neurons in the rat supraoptic nucleus. *Histochemistry* 78, 21–26. doi: 10.1007/bf00491107

Kettenmann, H., and Ransom, B. R. (1988). Electrical coupling between astrocytes and between oligodendrocytes studied in mammalian cell cultures. *Glia* 1, 64–73. doi: 10.1002/glia.440010108

Kita, Y., Kawakami, K., Takahashi, Y., and Murakami, F. (2013). Development of cerebellar neurons and glias revealed by in utero electroporation: golgi-like labeling of cerebellar neurons and glias. *PLoS One* 8:e70091. doi: 10.1371/journal.pone.0070091

Kiyoshi, C. M., Aten, S., Arzola, E. P., Patterson, J. A., Taylor, A. T., Du, Y., et al. (2020). Ultrastructural view of astrocyte-astrocyte and astrocyte-synapse contacts within the hippocampus. *BioRxiv* doi: 10.1101/2020.10.28.358200

Kiyoshi, C. M., Du, Y., Zhong, S., Wang, W., Taylor, A. T., Xiong, B., et al. (2018). Syncytial isopotentiality: a system-wide electrical feature of astrocytic networks in the brain. *Glia* 66, 2756–2769. doi: 10.1002/glia.23525

Konietzko, U., and Muller, C. M. (1994). Astrocytic dye coupling in rat hippocampus: topography, developmental onset, and modulation by protein kinase C. *Hippocampus* 4, 297–306. doi: 10.1002/hipo.450040313

Kuffler, S. W., Nicholls, J. G., and Orkand, R. K. (1966). Physiological properties of glial cells in the central nervous system of amphibia. *J. Neurophysiol.* 29, 768–787. doi: 10.1152/jn.1966.29.4.768

Kunzelmann, P., Schroder, W., Traub, O., Steinhauser, C., Dermietzel, R., and Willecke, K. (1999). Late onset and increasing expression of the gap junction protein connexin30 in adult murine brain and long-term cultured astrocytes. *Glia* 25, 111–119. doi: 10.1002/(sici)1098-1136(19990115)25:2<111::aid-glia2>3.0.co;2-i

Langer, J., Stephan, J., Theis, M., and Rose, C. R. (2012). Gap junctions mediate intercellular spread of sodium between hippocampal astrocytes in situ. *Glia* 60, 239–252. doi: 10.1002/glia.21259

Lee, C. Y., Dallerac, G., Ezan, P., Anderova, M., and Rouach, N. (2016). Glucose tightly controls morphological and functional properties of astrocytes. *Front. Aging Neurosci.* 8:82. doi: 10.3389/fnagi.2016.00082

Livnah, O., Bayer, E. A., Wilchek, M., and Sussman, J. L. (1993). Three-dimensional structures of avidin and the avidin-biotin complex. *Proc. Natl. Acad. Sci. U.S.A.* 90, 5076–5080. doi: 10.1073/pnas.90.11.5076

Lunde, L. K., Camassa, L. M., Hoddevik, E. H., Khan, F. H., Ottersen, O. P., Boldt, H. B., et al. (2015). Postnatal development of the molecular complex underlying astrocyte polarization. *Brain Struct. Funct.* 220, 2087–2101. doi: 10.1007/s00429-014-0775-z

Ma, B., Buckalew, R., Du, Y., Kiyoshi, C. M., Alford, C. C., Wang, W., et al. (2016). Gap junction coupling confers isopotentiality on astrocyte syncytium. *Glia* 64, 214–226. doi: 10.1002/glia.22924

MacAulay, N. (2020). Molecular mechanisms of K(+) clearance and extracellular space shrinkage-Glia cells as the stars. *Glia* 68, 2192–2211.

Maglione, M., Tress, O., Haas, B., Karram, K., Trotter, J., Willecke, K., et al. (2010). Oligodendrocytes in mouse corpus callosum are coupled via gap junction channels formed by connexin47 and connexin32. *Glia* 58, 1104–1117. doi: 10.1002/glia.20991

Matthias, K., Kirchhoff, F., Seifert, G., Huttmann, K., Matyash, M., Kettenmann, H., et al. (2003). Segregated expression of AMPA-type glutamate receptors and glutamate transporters defines distinct astrocyte populations in the mouse hippocampus. *J. Neurosci.* 23, 1750–1758. doi: 10.1523/jneurosci.23-05-01750.2003

McCutcheon, S., Stout, R. F. Jr., and Spray, D. C. (2020). The dynamic Nexus: gap junctions control protein localization and mobility in distinct and surprising ways. *Sci. Rep.* 10:17011.

Meier, S. D., Kovalchuk, Y., and Rose, C. R. (2006). Properties of the new fluorescent Na+ indicator CoroNa Green: comparison with SBFI and confocal Na+ imaging. *J. Neurosci. Methods* 155, 251–259. doi: 10.1016/j.jneumeth.2006.01.009

Meme, W., Vandecasteele, M., Giaume, C., and Venance, L. (2009). Electrical coupling between hippocampal astrocytes in rat brain slices. *Neurosci. Res.* 63, 236–243. doi: 10.1016/j.neures.2008.12.008

Minta, A., and Tsien, R. Y. (1989). Fluorescent indicators for cytosolic sodium. *J. Biol. Chem.* 264, 19449–19457. doi: 10.1016/s0021-9258(19)47321-3

Moroni, R. F., Inverardi, F., Regondi, M. C., Pennacchio, P., and Frassoni, C. (2015). Developmental expression of Kir4.1 in astrocytes and oligodendrocytes of rat somatosensory cortex and hippocampus. *Int. J. Dev. Neurosci.* 47, 198–205. doi: 10.1016/j.ijdevneu.2015.09.004

Moshrefi-Ravasdjani, B., Hammel, E. L., Kafitz, K. W., and Rose, C. R. (2017). Astrocyte sodium signalling and panglial spread of sodium signals in brain white matter. *Neurochem. Res.* 42, 2505–2518. doi: 10.1007/s11064-017-2197-9

Muller, C. M. (1996). "Gap-junctional communication in mammalian cortical astrocytes: development, modifiability and possible functions," in *Gap Junctions in the Nervous System*, eds D. C. Spary and R. Dermietzel (Austin, TX: RG Landes Company), 203–212. doi: 10.1007/978-3-662-21935-5_12

Muller, J., Reyes-Haro, D., Pivneva, T., Nolte, C., Schaette, R., Lubke, J., et al. (2009). The principal neurons of the medial nucleus of the trapezoid body and NG2(+) glial cells receive coordinated excitatory synaptic input. *J. Gen. Physiol.* 134, 115–127. doi: 10.1085/jgp.200910194

Muller, N. I. C., Sonntag, M., Maraslioglu, A., Hirtz, J. J., and Friauf, E. (2019). Topographic map refinement and synaptic strengthening of a sound localization circuit require spontaneous peripheral activity. *J. Physiol.* 597, 5469–5493. doi: 10.1113/jp277757

Muller, T., Moller, T., Neuhaus, J., and Kettenmann, H. (1996). Electrical coupling among Bergmann glial cells and its modulation by glutamate receptor activation. *Glia* 17, 274–284. doi: 10.1002/(sici)1098-1136(199608)17:4<274::aid-glia2>3.0.co;2-#

Murphy, A. D., Hadley, R. D., and Kater, S. B. (1983). Axotomy-induced parallel increases in electrical and dye coupling between identified neurons of Helisoma. *J. Neurosci.* 3, 1422–1429. doi: 10.1523/jneurosci.03-07-01422.1983

Nagy, J. I., Patel, D., Ochalski, P. A., and Stelmack, G. L. (1999). Connexin30 in rodent, cat and human brain: selective expression in gray matter astrocytes, co-localization with connexin43 at gap junctions and late developmental appearance. *Neuroscience* 88, 447–468. doi: 10.1016/s0306-4522(98)00191-2

Nagy, J. I., and Rash, J. E. (2000). Connexins and gap junctions of astrocytes and oligodendrocytes in the CNS. *Brain Res. Brain Res. Rev.* 32, 29–44. doi: 10.1016/s0165-0173(99)00066-1

Nakase, T., Yoshida, Y., and Nagata, K. (2006). Enhanced connexin 43 immunoreactivity in penumbral areas in the human brain following ischemia. *Glia* 54, 369–375. doi: 10.1002/glia.20399

Nielsen, M. S., Axelsen, L. N., Sorgen, P. L., Verma, V., Delmar, M., and Holstein-Rathlou, N. H. (2012). Gap junctions. *Compr. Physiol.* 2, 1981–2035.

Niessen, H., Harz, H., Bedner, P., Kramer, K., and Willecke, K. (2000). Selective permeability of different connexin channels to the second messenger inositol 1,4,5-trisphosphate. *J. Cell Sci.* 113(Pt 8), 1365–1372.

Nimmerjahn, A., Kirchhoff, F., Kerr, J. N., and Helmchen, F. (2004). Sulforhodamine 101 as a specific marker of astroglia in the neocortex in vivo. *Nat. Methods* 1, 31–37. doi: 10.1038/nmeth706

Nolte, C., Matyash, M., Pivneva, T., Schipke, C. G., Ohlemeyer, C., Hanisch, U. K., et al. (2001). GFAP promoter-controlled EGFP-expressing transgenic mice: a tool to visualize astrocytes and astrogliosis in living brain tissue. *Glia* 33, 72–86. doi: 10.1002/1098-1136(20010101)33:1<72::aid-glia1007>3.0.co;2-a

Nwaobi, S. E., Lin, E., Peramsetty, S. R., and Olsen, M. L. (2014). DNA methylation functions as a critical regulator of Kir4.1 expression during CNS development. *Glia* 62, 411–427. doi: 10.1002/glia.22613

Olsen, M. L., Khakh, B. S., Skatchkov, S. N., Zhou, M., Lee, C. J., and Rouach, N. (2015). New insights on astrocyte ion channels: critical for homeostasis and neuron-glia signaling. *J. Neurosci.* 35, 13827–13835. doi: 10.1523/jneurosci.2603-15.2015

Pannasch, U., Vargova, L., Reingruber, J., Ezan, P., Holcman, D., Giaume, C., et al. (2011). Astroglial networks scale synaptic activity and plasticity. *Proc. Natl. Acad. Sci. U.S.A.* 108, 8467–8472. doi: 10.1073/pnas.1016650108

Rackauskas, M., Verselis, V. K., and Bukauskas, F. F. (2007). Permeability of homotypic and heterotypic gap junction channels formed of cardiac connexins mCx30.2, *Cx*40, Cx43, and Cx45. *Am. J. Physiol. Heart Circ. Physiol.* 293, H1729–H1736.

Ransom, B. R., and Goldring, S. (1973). Ionic determinants of membrane potential of cells presumed to be glia in cerebral cortex of cat. *J. Neurophysiol.* 36, 855–868. doi: 10.1152/jn.1973.36.5.855

Ransom, B. R., and Kettenmann, H. (1990). Electrical coupling, without dye coupling, between mammalian astrocytes and oligodendrocytes in cell culture. *Glia* 3, 258–266. doi: 10.1002/glia.440030405

Rouach, N., Koulakoff, A., Abudara, V., Willecke, K., and Giaume, C. (2008). Astroglial metabolic networks sustain hippocampal synaptic transmission. *Science* 322, 1551–1555. doi: 10.1126/science.1164022

Scemes, E., and Giaume, C. (2006). Astrocyte calcium waves: what they are and what they do. *Glia* 54, 716–725. doi: 10.1002/glia.20374

Schools, G. P., Zhou, M., and Kimelberg, H. K. (2006). Development of gap junctions in hippocampal astrocytes: evidence that whole cell electrophysiological phenotype is an intrinsic property of the individual cell. *J. Neurophysiol.* 96, 1383–1392. doi: 10.1152/jn.00449.2006

Schreiner, A. E., Durry, S., Aida, T., Stock, M. C., Ruther, U., Tanaka, K., et al. (2014). Laminar and subcellular heterogeneity of GLAST and GLT-1 immunoreactivity in the developing postnatal mouse hippocampus. *J. Comp. Neurol.* 522, 204–224. doi: 10.1002/cne.23450

Seifert, G., Huttmann, K., Binder, D. K., Hartmann, C., Wyczynski, A., Neusch, C., et al. (2009). Analysis of astroglial K+ channel expression in the developing hippocampus reveals a predominant role of the Kir4.1 subunit. *J. Neurosci.* 29, 7474–7488. doi: 10.1523/jneurosci.3790-08.2009

Sontheimer, H., Waxman, S. G., and Ransom, B. R. (1991). Relationship between Na+ current expression and cell-cell coupling in astrocytes cultured from rat hippocampus. *J. Neurophysiol.* 65, 989–1002. doi: 10.1152/jn.1991.65.4.989

Speizer, L., Haugland, R., and Kutchai, H. (1985). Asymmetric transport of a fluorescent glucose analogue by human erythrocytes. *Biochim. Biophys. Acta* 815, 75–84. doi: 10.1016/0005-2736(85)90476-6

Stephan, J., and Friauf, E. (2014). Functional analysis of the inhibitory neurotransmitter transporters GlyT1, GAT-1, and GAT-3 in astrocytes of the lateral superior olive. *Glia* 62, 1992–2003. doi: 10.1002/glia.22720

Stephan, J., Haack, N., Kafitz, K. W., Durry, S., Koch, D., Hochstrate, P., et al. (2012). Kir4.1 channels mediate a depolarization of hippocampal astrocytes under hyperammonemic conditions in situ. *Glia* 60, 965–978. doi: 10.1002/glia.22328

Susaki, E. A., Tainaka, K., Perrin, D., Kishino, F., Tawara, T., Watanabe, T. M., et al. (2014). Whole-brain imaging with single-cell resolution using chemical cocktails and computational analysis. *Cell* 157, 726–739. doi: 10.1016/j.cell.2014.03.042

Susaki, E. A., Tainaka, K., Perrin, D., Yukinaga, H., Kuno, A., and Ueda, H. R. (2015). Advanced CUBIC protocols for whole-brain and whole-body clearing and imaging. *Nat. Protoc.* 10, 1709–1727. doi: 10.1038/nprot.2015.085

Tasker, J. G., Hoffman, N. W., and Dudek, F. E. (1991). Comparison of three intracellular markers for combined electrophysiological, morphological and immunohistochemical analyses. *J. Neurosci. Methods* 38, 129–143. doi: 10.1016/0165-0270(91)90163-t

Terman, D., and Zhou, M. (2019). Modeling the role of the astrocyte syncytium and K+ buffering in maintaining neuronal firing patterns. *Opera Med. Physiol.* 5, 7–16.

Veenstra, R. D. (1996). Size and selectivity of gap junction channels formed from different connexins. *J. Bioenerg. Biomembr.* 28, 327–337. doi: 10.1007/bf02110109

Veenstra, R. D., Wang, H. Z., Beblo, D. A., Chilton, M. G., Harris, A. L., Beyer, E. C., et al. (1995). Selectivity of connexin-specific gap junctions does not correlate with channel conductance. *Circ. Res.* 77, 1156–1165. doi: 10.1161/01.res.77.6.1156

Wadle, S. L., Augustin, V., Langer, J., Jabs, R., Philippot, C., Weingarten, D. J., et al. (2018). Anisotropic panglial coupling reflects tonotopic organization in the inferior colliculus. *Front. Cell Neurosci.* 12:431. doi: 10.3389/fncel.2018.00431

Wallraff, A., Kohling, R., Heinemann, U., Theis, M., Willecke, K., and Steinhauser, C. (2006). The impact of astrocytic gap junctional coupling on potassium buffering in the hippocampus. *J. Neurosci.* 26, 5438–5447. doi: 10.1523/jneurosci.0037-06.2006

Wallraff, A., Odermatt, B., Willecke, K., and Steinhauser, C. (2004). Distinct types of astroglial cells in the hippocampus differ in gap junction coupling. *Glia* 48, 36–43. doi: 10.1002/glia.20040

Wang, H. Z., and Veenstra, R. D. (1997). Monovalent ion selectivity sequences of the rat connexin43 gap junction channel. *J. Gen. Physiol.* 109, 491–507. doi: 10.1085/jgp.109.4.491

Wang, Q., Wang, W., Aten, S., Kiyoshi, C. M., Du, Y., and Zhou, M. (2020). Epileptiform neuronal discharges impair astrocyte syncytial isopotentiality in acute hippocampal slices. *Brain Sci.* 10:208. doi: 10.3390/brainsci10040208

Wang, W., Kiyoshi, C. M., Du, Y., Taylor, A. T., Sheehan, E. R., Wu, X., et al. (2020). TREK-1 null impairs neuronal excitability, synaptic plasticity, and cognitive function. *Mol. Neurobiol.* 57, 1332–1346. doi: 10.1007/s12035-019-01828-x

Wasseff, S. K., and Scherer, S. S. (2011). Cx32 and Cx47 mediate oligodendrocyte:astrocyte and oligodendrocyte:oligodendrocyte gap junction coupling. *Neurobiol. Dis.* 42, 506–513. doi: 10.1016/j.nbd.2011.03.003

Weber, P. A., Chang, H. C., Spaeth, K. E., Nitsche, J. M., and Nicholson, B. J. (2004). The permeability of gap junction channels to probes of different size is dependent on connexin composition and permeant-pore affinities. *Biophys. J.* 87, 958–973. doi: 10.1529/biophysj.103.036350

Wu, L., Dong, A., Dong, L., Wang, S. Q., and Li, Y. (2019). PARIS, an optogenetic method for functionally mapping gap junctions. *eLife* 8:e43366.

Xin, W., Schuebel, K. E., Jair, K. W., Cimbro, R., De Biase, L. M., Goldman, D., et al. (2019). Ventral midbrain astrocytes display unique physiological features and sensitivity to dopamine D2 receptor signaling. *Neuropsychopharmacology* 44, 344–355. doi: 10.1038/s41386-018-0151-4

Xu, G., Wang, W., Kimelberg, H. K., and Zhou, M. (2010). Electrical coupling of astrocytes in rat hippocampal slices under physiological and simulated ischemic conditions. *Glia* 58, 481–493.

Xu, G., Wang, W., and Zhou, M. (2014). Spatial organization of NG2 glial cells and astrocytes in rat hippocampal CA1 region. *Hippocampus* 24, 383–395. doi: 10.1002/hipo.22232

Yagi, T., Terada, N., Baba, T., and Ohno, S. (2002). Localization of endogenous biotin-containing proteins in mouse Bergmann glial cells. *Histochem. J.* 34, 567–572.

Yamada, K., Nakata, M., Horimoto, N., Saito, M., Matsuoka, H., and Inagaki, N. (2000). Measurement of glucose uptake and intracellular calcium concentration in single, living pancreatic beta-cells. *J. Biol. Chem.* 275, 22278–22283. doi: 10.1074/jbc.m908048199

Yang, Y., Vidensky, S., Jin, L., Jie, C., Lorenzini, I., Frankl, M., et al. (2011). Molecular comparison of GLT1+ and ALDH1L1+ astrocytes in vivo in astroglial reporter mice. *Glia* 59, 200–207. doi: 10.1002/glia.21089

Yoshioka, K., Saito, M., Oh, K. B., Nemoto, Y., Matsuoka, H., Natsume, M., et al. (1996). Intracellular fate of 2-NBDG, a fluorescent probe for glucose uptake activity, in *Escherichia coli* cells. *Biosci. Biotechnol. Biochem.* 60, 1899–1901. doi: 10.1271/bbb.60.1899

Zhong, S., Du, Y., Kiyoshi, C. M., Ma, B., Alford, C. C., Wang, Q., et al. (2016). Electrophysiological behavior of neonatal astrocytes in hippocampal stratum radiatum. *Mol. Brain* 9:34.

Zhou, M., Schools, G. P., and Kimelberg, H. K. (2006). Development of GLAST(+) astrocytes and NG2(+) glia in rat hippocampus CA1: mature astrocytes are electrophysiologically passive. *J. Neurophysiol.* 95, 134–143. doi: 10.1152/jn.00570.2005

Conflict of Interest: The authors declare that the research was conducted in the absence of any commercial or financial relationships that could be construed as a potential conflict of interest.

Copyright © 2021 Stephan, Eitelmann and Zhou. This is an open-access article distributed under the terms of the Creative Commons Attribution License (CC BY). The use, distribution or reproduction in other forums is permitted, provided the original author(s) and the copyright owner(s) are credited and that the original publication in this journal is cited, in accordance with accepted academic practice. No use, distribution or reproduction is permitted which does not comply with these terms.

Altered Gap Junction Network Topography in Mouse Models for Human Hereditary Deafness

Sara Eitelmann[1,2], Laura Petersilie[2], Christine Rosemarie Rose[2] and Jonathan Stephan[1,2]

[1] Arbeitsgruppe Tierphysiologie, Technische Universität Kaiserslautern, Kaiserslautern, Deutschland

[1] Institut für Neurobiologie, Heinrich-Heine-Universität Düsseldorf, Düsseldorf, Deutschland

Int J Mol Sci. 2020 Oct 6;21(19):7376. IF 2020: 5.924.

Wichtige Anmerkung: Alle Experimente und Analysen von Abbildung 2-5 wurden von mir selbst im Rahmen meiner Diplomarbeit in der Arbeitsgruppe Tierphysiologie an der Technischen Universität Kaiserslautern durchgeführt.

Eigener Beitrag während Promotion

Analyse:
- Analyse der immunhistochemischen Färbungen (Abbildung 1)
- Statistische Analyse aller Daten

Manuskript:
- Erstellung aller Abbildungen (Abbildung 1-5)
- Beitrag zur Konzeptualisierung und Methodik der Studie
- Beitrag zur Verfassung und Überarbeitung des Manuskripts

International Journal of
Molecular Sciences

MDPI

Article

Altered Gap Junction Network Topography in Mouse Models for Human Hereditary Deafness

Sara Eitelmann [1,2], Laura Petersilie [2], Christine R. Rose [2] and Jonathan Stephan [1,2,*]

[1] Animal Physiology Group, Department of Biology, University of Kaiserslautern, Erwin Schrödinger-Straße 13, D 67663 Kaiserslautern, Germany; sara.eitelmann@uni-duesseldorf.de
[2] Institute of Neurobiology, Heinrich Heine University Düsseldorf, Universitätsstraße 1, D 40225 Düsseldorf, Germany; laura.petersilie@hhu.de (L.P.); rose@uni-duesseldorf.de (C.R.R.)
* Correspondence: jonathan.stephan@uni-duesseldorf.de; Tel.: +49-211-81-13486

Received: 21 August 2020; Accepted: 2 October 2020; Published: 6 October 2020

Abstract: Anisotropic gap junctional coupling is a distinct feature of astrocytes in many brain regions. In the lateral superior olive (LSO), astrocytic networks are anisotropic and oriented orthogonally to the tonotopic axis. In $Ca_V1.3$ knock-out (KO) and otoferlin KO mice, where auditory brainstem nuclei are deprived from spontaneous cochlea-driven neuronal activity, neuronal circuitry is disturbed. So far it was unknown if this disturbance is also accompanied by an impaired topography of LSO astrocyte networks. To answer this question, we immunohistochemically analyzed the expression of astrocytic connexin (Cx) 43 and Cx30 in auditory brainstem nuclei. Furthermore, we loaded LSO astrocytes with the gap junction-permeable tracer neurobiotin and assessed the network shape and orientation. We found a strong elevation of Cx30 immunoreactivity in the LSO of $Ca_V1.3$ KO mice, while Cx43 levels were only slightly increased. In otoferlin KO mice, LSO showed a slight increase in Cx43 as well, whereas Cx30 levels were unchanged. The total number of tracer-coupled cells was unaltered and most networks were anisotropic in both KO strains. In contrast to the WTs, however, LSO networks were predominantly oriented parallel to the tonotopic axis and not orthogonal to it. Taken together, our data demonstrate that spontaneous cochlea-driven neuronal activity is not required per se for the formation of anisotropic LSO astrocyte networks. However, neuronal activity is required to establish the proper orientation of networks. Proper formation of LSO astrocyte networks thus necessitates neuronal input from the periphery, indicating a critical role of neuron-glia interaction during early postnatal development in the auditory brainstem.

Keywords: astrocytes; auditory brainstem; lateral superior olive; gap junctions; voltage-activated calcium channel 1.3; otoferlin; spontaneous activity; deafness

1. Introduction

In many brain regions, astrocytes and oligodendrocytes form large panglial gap junction (GJ)-mediated networks [1–4]. In the hippocampus, where only few oligodendrocytes are located [1,5], networks mainly consist of astrocytes [6]. GJ networks exhibit a heterogeneous topography throughout the CNS. In particular areas, astrocytes are unequally interconnected to each other leading to an anisotropic network topography. Such limitations are present, for example, in sensory systems, which exhibit a strong anatomo-functional organization. In the barrel cortex and the barreloid thalamus, tracer coupling is restricted to the barrels [7,8]. Moreover, anisotropic tracer spread is present in the lateral superior olive (LSO) and the inferior colliculus (IC) [1,2,9]—two nuclei of the auditory brainstem, in which tracer-coupled networks are oriented orthogonally to the tonotopic axis. Both LSO and IC are tonotopically organized [10–12] and principal neurons refer to this organization, as their dendritic trees exhibit a narrow morphology with an orientation orthogonal to the tonotopic

axis [13–17]. The correlation of astrocyte network anisotropy with the topography of principal neurons suggests that they are causally linked to each other, though the mechanism is still unknown.

Before hearing onset, which takes place at around postnatal day 12 in mice, circuits undergo substantial refinement [10,18,19]. In the superior olivary complex (SOC) of some species, namely rats and gerbils, but not in mice, principal neurons in the medial nucleus of the trapezoid (MNTB) change their synaptic phenotype from GABAergic towards glycinergic [20–22]. Furthermore, the number of MNTB–LSO projections decreases within the first two postnatal weeks, and MNTB–LSO synapses become consolidated [22,23]. This developmental refinement requires spontaneous cochlea-driven neuronal activity [24–26]. Even interfering with cholinergic efferent signaling onto hair cells in the cochlea alters spontaneous cochlea-driven neuronal activity and causes disturbed tonotopic map formation and impairment of sound source localization [27,28]. Mutations in various genes, for example coding for the voltage-activated calcium channel (Ca_V) 1.3 or the calcium sensor otoferlin in inner hair cells of the cochlea, cause hereditary deafness [29–32]. For both deafness genes, mouse models are available: Ca_V1.3 knock-out (KO) mice [33] and otoferlin KO mice [34]. In these mice, the auditory brainstem lacks spontaneous cochlea-driven neuronal activity, which in the SOC results in malformed nuclei and impaired circuit formation, i.e., reduced refinement and strengthening of MNTB–LSO synapses as well as impaired reorganization of the dendrite topography of LSO principal neurons [26,35,36]. In the wild type (WT), LSO astrocyte networks are anisotropic and predominantly oriented orthogonally to the tonotopic axis, thus correlating with dendrite topography and tonotopy. It has been suggested that network anisotropy might be beneficial for directed redistribution of, e.g., ions to limit crosstalk between neighboring isofrequency bands [1]. Accordingly, any impairment of network anisotropy and preferential orientation would further undermine tonotopic information processing. However, it was unknown so far if astrocytes and astrocytic networks are affected in the two KOs models.

Our results show that LSO astrocytes assessed at postnatal days 10–12 maintain an electrophysiologically earlier developmental phenotype in Ca_V1.3 KO and otoferlin KO mice. The expression of connexin (Cx) 43 and Cx30 was increased, but the degree of GJ coupling was unaltered. However, network topography was strongly altered in Ca_V1.3 KO and otoferlin KO mice. Most networks were anisotropic, but in contrast to the WT, networks were now predominantly oriented parallel (and not orthogonal) to the tonotopic axis. Thus, our data show that spontaneous cochlea-driven neuronal activity is not only mandatory for proper formation of neuronal circuitry, but in addition is required for proper orientation of astrocyte networks in the LSO.

2. Results

2.1. Expression of Cx43 and Cx30 in the Auditory Brainstem

In Ca_V1.3 KO and otoferlin KO mice, neuronal circuitry and nuclei topography are altered in the auditory brainstem [26,35,36]. To assess putative changes in astrocytic coupling, we first analyzed the expression of Cx43 and Cx30 in the SOC containing the MNTB, superior paraolivary nucleus (SPN), and the LSO. As observed before, immunohistochemistry directed against Cx43 and Cx30 resulted in punctate labeling of auditory brainstem nuclei, whereas Cx levels outside of the nuclei, e.g. in the internuclear space, were low (Figure 1Aa–Cb; [1]). Compared to the WT, expression of Cx43 was increased in the SPN from both KO models (Ca_V1.3 KO: $p = 0.020$; otoferlin KO: $p = 0.010$) and in the LSO from otoferlin KO ($p = 0.006$; Figure 1D). Cx30 levels were elevated in the SPN ($p = 0.001$) and LSO ($p < 0.001$) from Ca_V1.3 KO, but not from the otoferlin KO (Figure 1E). Cx43 and Cx30 levels were not significantly altered in MNTB from either KO model as compared to the WT (Figure 1D–E).

It was previously shown that deprivation of spontaneous cochlea-driven neuronal activity alters nuclei topography [35]. Thus, we analyzed the size of nuclei and found a 50% smaller coronal nucleus area for the SPN and LSO in both KO models ($p < 0.001$ for all comparisons), however, the coronal MNTB area was not altered (Figure 1F). Notably, the LSO in the Ca_V1.3 KO lost its typical kidney-like

shape (Figure 1B; [35]), whereas this topography was maintained in the otoferlin KO (Figure 1C). Thus, our initial results indicated that astrocytic GJ coupling might be altered due to altered Cx expression and nucleus size.

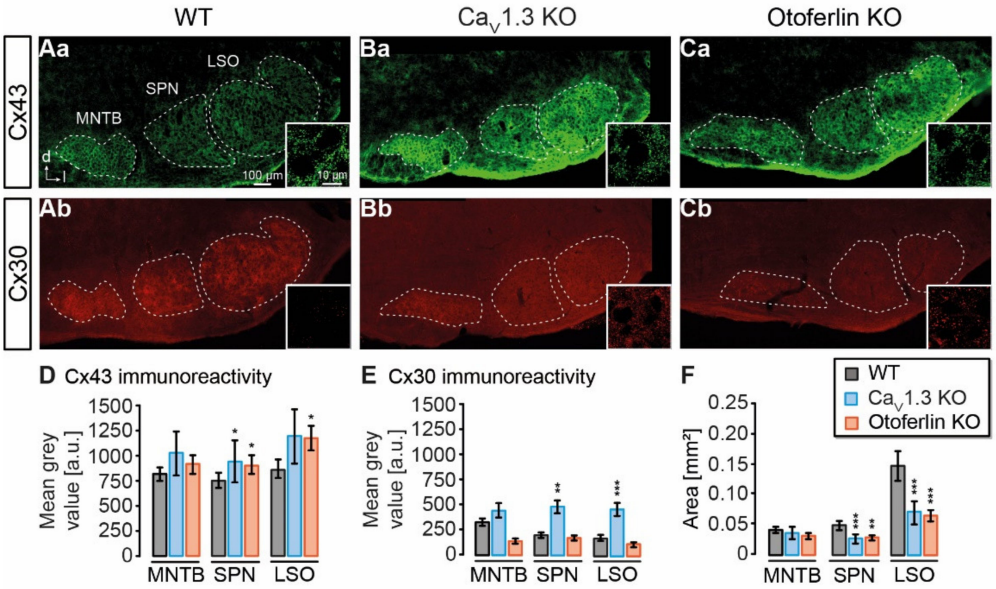

Figure 1. Expression of astrocyte-related connexins in the superior olivary complex (SOC). (**A**–**C**), widefield images showing immunoreactivity of Cx43 and Cx30 in the mouse SOC from the wild type (WT) (**Aa** (Cx43), **Ab** (Cx30)), CaV1.3 knock-out (KO) (**Ba** (Cx43), **Bb** (Cx30)) and otoferlin KO (**Ca** (Cx43), **Cb** (Cx30)). Regions used for mean grey value und area analysis are indicated with dashed lines. Insets: Close ups showing the punctate Cx labeling in the lateral superior olive (LSO) center. (**D**), mean grey values of Cx43 immunofluorescence. Cx43 levels were increased in the SPN from both KO models and in the LSO from otoferlin KO. (**E**), mean grey values of Cx30 immunofluorescence. Cx30 was elevated in the SPN and LSO of Ca$_V$1.3 KO. (**F**), area of nuclei in the SOC. SPN and LSO from both KO models exhibited a reduced area compared to the WT. Mean grey values were background subtracted. (**D**–**F**) show mean ± SD. Significance levels in panels (**D**–**F**) were Šidák corrected for two comparisons. The sample size is given in the text of Section 4.2. * $p < 0.025$, ** $p < 0.005$, *** $p < 0.0005$.

2.2. Electrophysiological Properties of LSO Astrocytes

To investigate the effect of reduced spontaneous neuronal activity on astrocytic GJ coupling in the auditory brainstem, we chose the LSO as a model region. In previous studies we could show that LSO astrocyte networks are predominantly anisotropic and oriented orthogonally to the tonotopic axis [1,9]. LSO astrocytes were a priori identified using sulforhodamine (SR) 101-labeling [37]. In the WT and both KO models, astrocytes were brightly labeled and were more numerous within the LSO as compared to the area around the nucleus. Analogous to the results from the immunohistochemistry experiment, the astrocyte distribution reflected the typical kidney-like shape of the LSO from the WT and otoferlin KO, and in the Ca$_V$1.3 KO astrocytes occupied an elliptic area (Figure 2Aa,Ba,Ca). As described above, the LSO size was reduced in both KO models. In the WT, astrocytes in the LSO center preferentially exhibited a dorsoventral orientation, which is roughly orthogonal to the tonotopic axis (Figure 2Aa; [1]). In contrast, astrocytes in the LSO center from both KO models appeared to be oriented in mediolateral direction, which approximately reflects the tonotopic axis (Figure 2Ba,Ca).

Neuronal circuitry in both KO models shows impaired development, but it was unknown, if the loss of spontaneous cochlea-driven neuronal activity interferes with astrocyte development. We patch-clamped individual LSO astrocytes and characterized their basic electrophysiological properties. Astrocytes from the WT exhibited a highly negative membrane potential (−82.9 ± 4.0 mV, $n = 63$) and a very low membrane resistance (3.7 ± 2.5 MΩ, $n = 63$), which is typical for LSO

astrocytes [1,37]. LSO astrocytes from both KO models did not differ in their membrane potential ($Ca_V1.3$ KO: −83.2 ± 4.8 mV, n = 21, p = 0.814; otoferlin KO: −79.0 ± 8.1 mV, n = 17, p = 0.413) or membrane resistance ($Ca_V1.3$ KO: 3.5 ± 1.5 MΩ, n = 21, p = 0.833; otoferlin KO: 3.7 ± 1.7 MΩ, n = 17, p = 0.991).

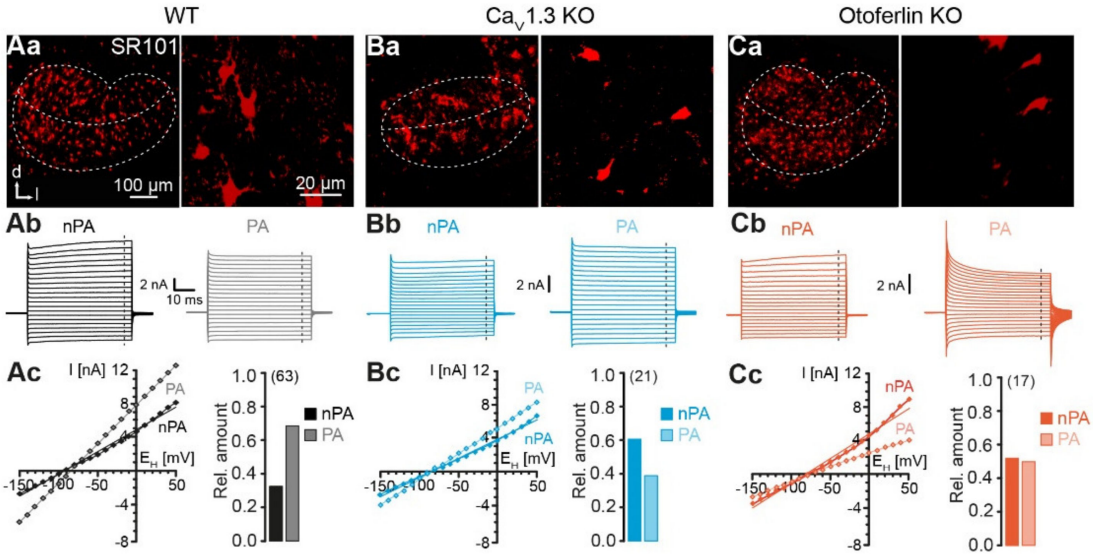

Figure 2. Identification and characterization of LSO astrocytes. (**A**–**C**), identification of astrocytes in the LSO. Confocal images of SR101-labeled astrocytes in the LSO (**left**). SR101-labeling was independent from genetic modification of mouse strains (**Aa**,**Ba**,**Ca**). The border of the LSO and the tonotopic axis are highlighted with dashed lines. In the WT and otoferlin KO mice, the LSO displayed the typical kidney-like shape (**Aa**,**Ca**). In Cav1.3 KO mice, the LSO was elliptic (**Ba**). Higher magnification of SR101-labeled astrocytes in the center of the LSO (**right**). Electrophysiological characterization of astrocytes (**Ab**–**Cc**). Astrocytes were recorded in voltage-clamp mode and step-wise hyper- and depolarized. Non-passive astrocytes (nPA) expressed time- and voltage-dependent outward currents (**left**). Passive astrocytes (PA) exhibited only ohmic currents (**right**) (**Ab**,**Bb**,**Cb**). Current-voltage (*I*/*V*) relationship was determined at the end of the voltage steps (dashed lines in **Ab**,**Bb**,**Cb**). Due to the presence of outward currents, nPAs and PAs exhibited non-linear and linear *I*/*V* relationships, respectively (**left**) (**Ac**,**Bc**,**Cc**). Relative amount of n/PAs (**right**). The number of analyzed cells is given in parentheses. The WT data (**Aa**–**Ac**) were part of [9]. Panels Aa left, Ab right, and parts of Ac left were reused from that publication.

We next hyper- and depolarized astrocytes from the WT and the two KO models to analyze the expression of inward and outward currents (Figure 2Ab,Bb,Cb). According to their elicited current traces, astrocytes could be classified as non-passive astrocytes (nPAs) and passive astrocytes (PAs). Astrocytes mainly showing voltage-activated outward currents resulting in a non-linear current-voltage (*I*/*V*) relationship were designated as nPAs. In turn, astrocytes that primarily expressed ohmic currents and hence displayed a preferentially linear *I*/*V* relationship, represented PAs. Both astrocytes subtypes are present in the WT and both KO models (Figure 2Ab,Cb). In the WT, most astrocytes exhibited a non-passive phenotype (nPA/PA: 32%/68%, n = 63; Figure 2Ac). Interestingly, the relative proportion shifted from PAs towards nPAs in both KO models. In $Ca_V1.3$ KO, there are more nPAs than PAs (62%/38%, n = 21, $p < 0.001$, X^2 test; Figure 2Bc). In the otoferlin KO, there is an almost equal amount of nPAs and PAs (nPA/PA: 53%/47%, n = 17, $p < 0.001$, X^2 test; Figure 2Cc). Thus, our data indicate that astrocytes in KO models do not undergo the normal postnatal transition from nPAs, expressing voltage-activated K^+ channels, towards PAs, predominantly expressing inwardly rectifying and leak K^+ channels, and thus partially maintain a phenotype characteristic of an earlier developmental stage [38,39].

2.3. Unaltered LSO Astrocyte Network Properties

Astrocyte coupling increases during postnatal development, which results in larger networks containing more cells [40,41]. As the percentage of astrocytes that maintained an electrophysiologically earlier developmental phenotype (nPAs) was increased in KO models, we next investigated, if coupling of LSO astrocytes was altered, too. During whole-cell recording the patch-clamped astrocytes were loaded with GJ-permeable tracer neurobiotin. Subsequent tracer visualization revealed labeling of coupled cells, whose brightness declined exponentially with increased distance to the patched cell (Figure 3Aa–Cc). Notably, the LSO borders did not restrict the tracer diffusion.

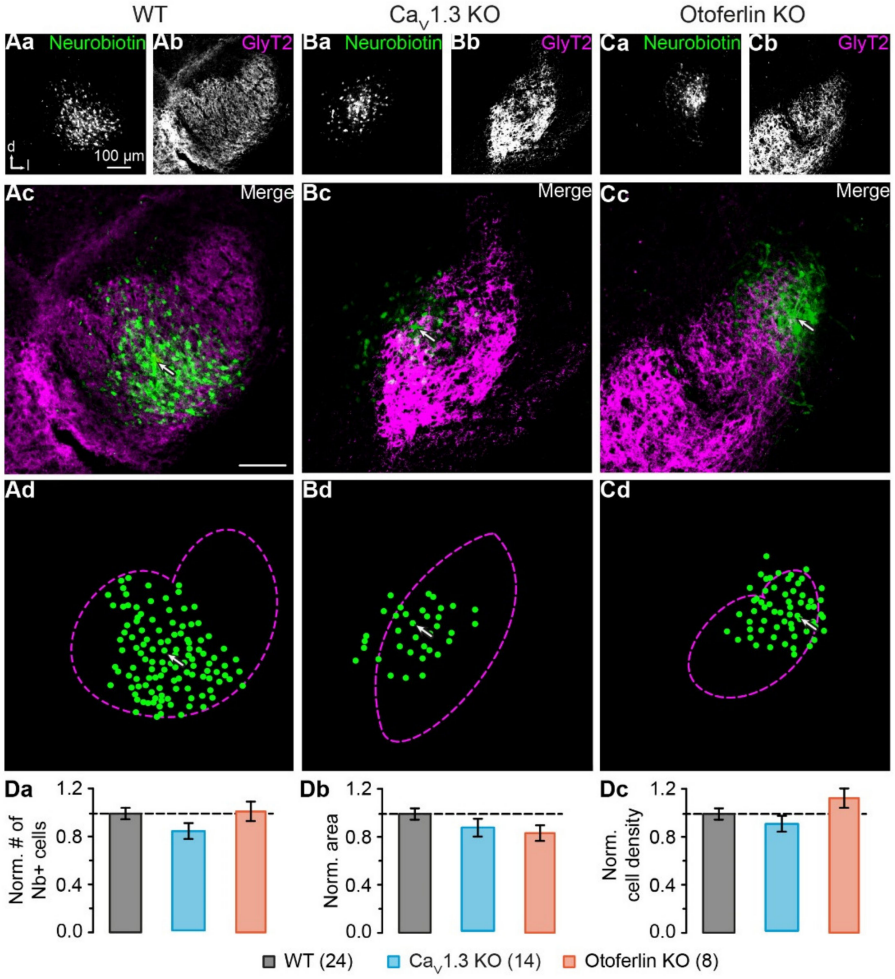

Figure 3. Reconstruction of LSO astrocyte networks. (**A**–**C**), tracer-coupled networks of the WT, $Ca_V1.3$ KO, and otoferlin KO mice. The tracer neurobiotin diffused from the patch-clamped astrocyte into coupled cells (**Aa**–**Ac**,**Ba**–**Bc**,**Ca**–**Cc**). Immunohistochemical labeling for glycine transporter (GlyT) 2 highlighted the LSO (**Ab**,**Bb**,**Cb**) and allowed the localization of the network within the nucleus (**Ac**,**Bb**,**Cc**). Cells with fluorescence intensity of at least 1.75-fold background intensity were transferred to a schematized representation and are displayed by green dots (**Ad**,**Bb**,**Cd**). The dotted magenta lines indicate the LSO border as derived from GlyT2 labeling (**Ab**,**Bb**,**Cb**). The arrows in (**Ac**,**Ad**,**Bc**,**Bd**,**Cc**,**Cd**) mark the patched cell. (**D**), network properties. Values were normalized to the WT data, indicated with the dashed line. There were no differences between the number of coupled cells (**Da**), network area (**Db**), or density of coupled cells (**Dc**). The WT data (**Aa**–**Ad**) were part of [9]. Panel (**Aa**–**Ac**) was reused from that publication. (**Da**–**Dc**) show mean ± SD. Number of slices is given in parentheses.

The semi-automated intensity-based cell detection [9] showed that networks did not differ significantly in basic properties between WT and KO models, i.e. cell number (WT: 64 ± 15, n = 24; $Ca_V1.3$ KO: 54 ± 12, n = 14, p = 0.468; otoferlin KO: 65 ± 14, n = 8, p = 0.129; Figure 3Da), area (WT: 0.043 ± 0.009 mm^2, n = 24; $Ca_V1.3$ KO: 0.039 ± 0.007 mm^2, n = 14, p = 0.513; otoferlin KO: 0.036 ± 0.007 mm^2, n = 8, p = 0.644; Figure 3Db), and cell density (WT: 1484 ± 331 cells/mm^2, n = 24; $Ca_V1.3$ KO: 1398 ± 331 cells/mm^2, n = 14, p = 0.493; otoferlin KO: 1816 ± 384 cells/mm^2, n = 8, p = 0.137; Figure 3Dc). Thus, in contrast to the electrophysiological phenotype, the network size in both KO models was unchanged and did thereby not reflect the properties of an earlier developmental stage.

2.4. Disturbed LSO Astrocyte Network Topography

LSO astrocyte networks are predominantly orthogonal to the tonotopic axis [1,9]. We next analyzed, if this preferential orientation is maintained in KO models. Network anisotropy was analyzed using our vector-based approach with subsequent meta-analysis [9]. Therefore, we applied a sinusoidal fit to the data to calculate the shape (R_{max}) and orientation (α) relative to the dorsoventral axis (Figure 4Aa,Ba,Ca). In case of anisotropic tracer-coupled networks comprising two axes of symmetry, rotating the coordinate system resulted in a ratio that oscillates two times per full turn (Figure 4Aa,Ba). In contrast, spherical networks with more than two axes of symmetry oscillated with a considerably higher frequency (Figure 4Ca).

As expected (cf. [1]), the WT LSO astrocyte networks were predominantly anisotropic and oriented orthogonally to the tonotopic axis (71%, 17/24; Figure 4Ab,Db). Only 13% (3/24) of the WT tracer-coupled networks were spherical and 17% (4/24) were anisotropic with a preferential orientation parallel to the tonotopic axis (Figure 4Ab,Db). Similar to this, most LSO astrocyte networks in $Ca_V1.3$ KO and otoferlin KO mice were anisotropic (Figure 4Bb,Cb). However, tracer-coupled networks in both KO models showed a different predominant orientation. Half of the networks in $Ca_V1.3$ KO (7/14) and otoferlin KO mice (4/8) were oriented parallel to the tonotopic axis (Figure 4Bb,Cb,Db). Less were spherical ($Ca_V1.3$: 29%, 4/14; Figure 4Bb,Db; Otof: 25%, 2/8; Figure 4Cb,Db) or oriented orthogonally to the tonotopic axis ($Ca_V1.3$ KO: 21%, 3/14; Figure 4Bb,Db; otoferlin KO: 25%, 2/8; Figure 4Cb,Db). Thus, the predominant direction of tracer spread and, accordingly, the preferred orientation of LSO astrocytes networks turned in both KO models by 90°, as compared to the WT. As a consequence, there might be increased gap junction-related cross-talk along the tonotopic axis (Figure 5).

Taken together, our results show that deprivation of spontaneous cochlea-driven neuronal activity does not per se distort astrocyte coupling in the LSO. However, LSO astrocyte network orientation is largely altered.

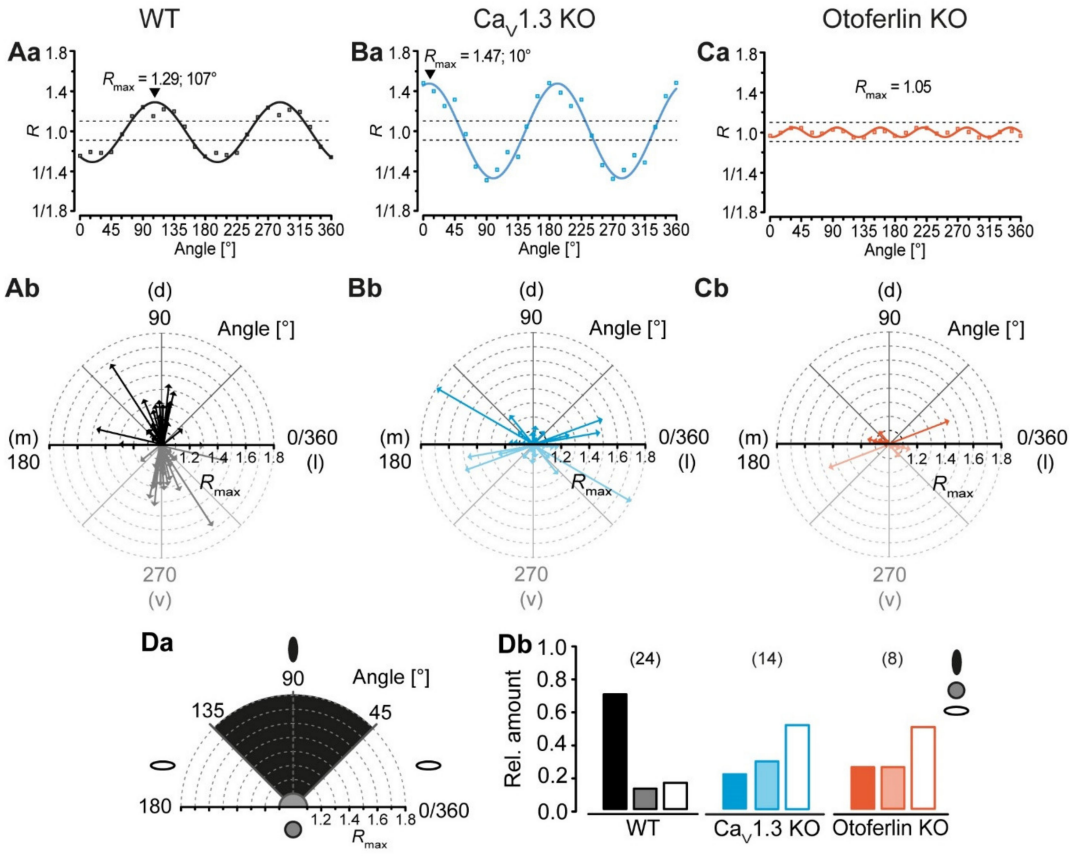

Figure 4. LSO astrocyte networks show a disturbed topography in Ca$_V$1.3 KO and otoferlin KO mice. (**A**–**C**), analysis of network topography. The coordinate system was step wise rotated and the ratio of tracer extent was calculated using the vector means approach. The anisotropy and orientation of networks in the center of the LSO were determined using a sinusoidal function (**Aa**–**Ca**). Shown, are representative sinusoidal fits of the anisotropic networks that were oriented orthogonally (WT; Aa) and parallel to the tonotopic axis (Ca$_V$1.3 KO; Ba) as well as a fit of an isotropic network with no preferential orientation (otoferlin KO; Ca). (**Aa**–**Ca**) refer to networks shown in Figure 3Aa–Cd. Radar diagrams displaying the anisotropy (R_{max} > 1.1: anisotropic; R_{max} ≤ 1.1: isotropic) and orientation α of tracer-coupled networks (**Ab**–**Cb**). The mediolateral (m-l) axis resembles the tonotopic axis, the dorsoventral (d–v) axis resembles the orientation of isofrequency bands, which are oriented orthogonal to the tonotopic axis. In WT mice, most tracer-coupled networks showed a preferential orientation orthogonal to the tonotopic axis (d–v; 45 ≤ α < 135°) (**Ab**). In contrast, the majority of anisotropic astrocyte networks in Ca$_V$1.3 KOs and otoferlin KOs were aligned parallel to the tonotopic axis (m-l; α < 45° and α ≥ 135°) (**Bb**–**Cb**). (**D**), classification of networks. Astrocyte networks were affiliated to three classes by their shape R_{max} and orientation α (class 1, black ellipse: anisotropic and oriented orthogonally to tonotopic axis; class 2, grey circle: isotropic; class 3: anisotropic and oriented parallel to the tonotopic axis; **Da**). In WT mice, most LSO astrocyte networks were categorized into class 1. In contrast, tracer-coupled networks in KOs were predominantly affiliated to class 3 (**Db**). The WT data (**Aa**–**Ab**) were already part of the following study: [9]. Panel Ab was reused from that publication.

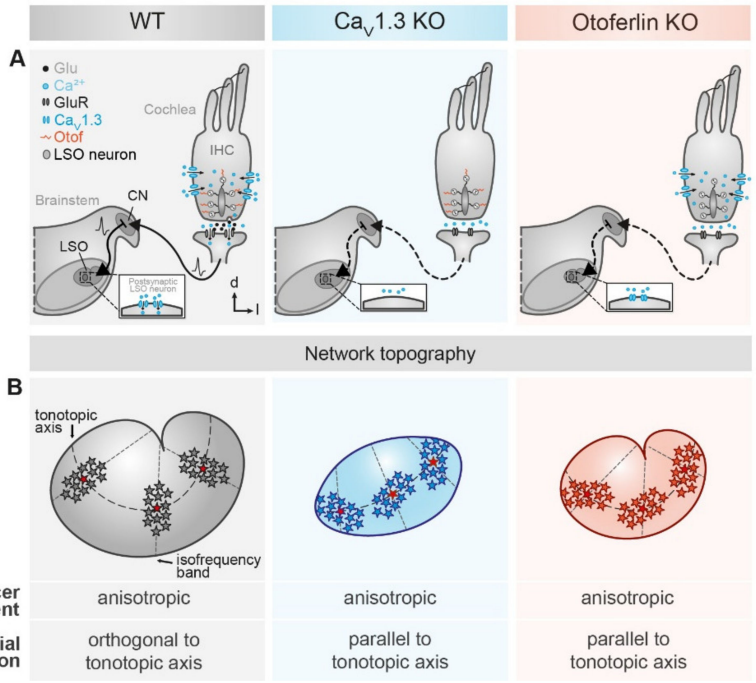

Figure 5. Summary of LSO astrocyte network topography in mouse models for human hereditary deafness. (**A**) schematic drawings depicting the subcellular modifications of the different mouse models. Compared to the WT (**left**), absence of $Ca_V1.3$ (**middle**) and otoferlin (**right**) from cochlear inner hair cells prevents Ca^{2+} entry into the inner hair cell and Ca^{2+} detection, respectively. Subsequently, exocytotic glutamate release is inhibited. Thereby, spontaneous activity of inner hair cells does not result in vesicle fusion, synaptic transmission, and subsequent activation of the auditory pathway. (**B**) main result of network analysis. LSO astrocyte networks are preferentially anisotropic and oriented orthogonally to the tonotopic axis (**left**). By contrast, networks in $Ca_V1.3$ KO (**middle**) and otoferlin KO mice (**right**) are predominantly oriented parallel to the tonotopic axis. Furthermore, the area of the LSO is reduced in both KO models. Moreover, the kidney-like shape of the LSO is lost in the $Ca_V1.3$ KO.

3. Discussion

In the present study, we have investigated the influence of absent spontaneous cochlea-driven neuronal activity on gap junctional tracer coupling in LSO astrocytes. To do so, we used two mouse models of hereditary deafness—a $Ca_V1.3$ KO and an otoferlin KO. As we have previously demonstrated a strong anatomo-functional correlation between neuronal circuitry and glial GJ network topography, we hypothesized that the altered neuronal circuitry in these two mouse models is also reflected in altered astrocytic networks. Our data show that the expression of astrocytic Cx is partially increased in the LSO, but the extent of tracer coupling is not altered. Most GJ networks are still anisotropic, but are oriented along the tonotopic axis in the KOs, thus correlating with the disturbed neuronal circuitry.

3.1. Connexin Expression in KO Models

GJ coupling depends on Cx expression levels. In the barrel cortex, high Cx expression within barrels correlates with strong GJ coupling, whereas lower Cx levels in the septa between the barrels result in weaker coupling [7,42]. Furthermore, Cx expression is upregulated during development [1,2,43,44], which increases GJ coupling [40,41]. Accordingly, loss of spontaneous cochlea-driven neuronal activity leading to impaired developmental maturation of neuronal circuitry [25,26,35,36] might have kept Cx expression in the LSO at an earlier developmental state as well. Here, we even found moderately increased Cx levels in the LSO, while the nucleus area was reduced in $Ca_V1.3$ KO and otoferlin KO mice (Figure 1; [35]). However, neither the increase in Cx levels nor the reduced nucleus size affected the size of tracer-coupled networks (Figure 3).

3.2. Activity-Dependent Alteration of Astrocyte Network Topography

LSO astrocytes in the two KO models exhibited similar basic membrane properties as reported earlier for the WT, namely a very negative membrane potential and a low membrane resistance [1,37]. Thus, expression of Kir and K_2P channels, which set both membrane potential and membrane resistance [45], is independent from spontaneous cochlea-driven neuronal activity. However, LSO astrocytes in both KO models exhibited more often a non-linear *I/V* relationship (Figure 2), which is indicative of partially impaired development, as they stayed in an earlier developmental state (cf. [38,39]). There was no significant alteration of network size, which is a bit surprising as Cx levels were moderately increased. Moreover, most tracer-coupled networks were anisotropic in both KO models (Figure 4). However, the disturbed refinement of neuronal circuitry is paralleled by an altered network orientation. Whereas networks in the WT were predominantly oriented orthogonally to the tonotopic axis [1,9], networks in KO models were predominantly oriented parallel to the tonotopic axis (Figure 4). Thus, spontaneous cochlea-driven neuronal activity per se is not required for the formation of anisotropic LSO astrocyte networks. However, it drives astrocytes and networks to be predominantly oriented orthogonally to the tonotopic axis.

3.3. Mechanism Underlying the Altered Network Topography

There must be at least two mechanisms in the LSO directing, on the one hand, network anisotropy and on the other hand, network orientation. In the two KO models used, loss of spontaneous cochlea-driven neuronal activity only interferes with network orientation, but not with network anisotropy per se (Figure 4). Anisotropic tracer coupling is present in different brain regions and can have different origins. In the barrel cortex and barreloid thalamus, anisotropy of glial GJ networks arises from restricted coupling across the barrels [7,8]. So far, such restrictions were not found in the LSO, since GJ networks cross nuclear borders [1]. In contrast, network anisotropy in the hippocampus and in the LSO originates from anisotropic topography of astrocyte processes [1,9,46,47]. The astrocyte polarization in the hippocampus depends on a non-channel function of Cx30 [46]. However, polarization of astrocytes and subsequent orientation of GJ networks in the LSO must be independent from Cx30 as it is virtually absent at the early postnatal stage (P10–12) investigated in this study [1]. Moreover, it is rather unlikely that the slightly elevated Cx30 expression in the $Ca_V1.3$ KO interferes with GJ network orientation, as there is no elevation of Cx30 expression in the otoferlin KO (Figure 1) and both KO models show the same alteration of GJ network orientation (Figure 4).

Astrocyte morphology correlates with topography of GJ networks in the auditory brainstem [1,2]. The changed orientation of astrocyte processes in the LSO in both KO models is likely to be responsible for the alteration of preferred GJ network orientation (Figures 2 and 4). However, the following question needs to be answered: What is the link between the lack of spontaneous cochlea-driven neuronal activity and alteration of astrocyte and GJ network topography?

3.4. Signaling between Astrocytes and Neurons

Spontaneous cochlea-driven neuronal activity is not only important for postnatal refinement of neuronal circuitry and dendrite topography [26,35,36], but is also required for the formation of GJ networks that are oriented predominantly orthogonally to the tonotopic axis. However, the interplay between astrocytes and neurons during this early postnatal phase is not clear as we do not know who signalizes whom to mature. There are basically two opposing possibilities: (1) Astrocyte topography and subsequent GJ network orientation precede and induce neuronal refinement, or (2) neuronal circuitry directs astrocytes and subsequently GJ networks to arrange properly. Another aspect is the question—until which point do the astrocyte and network maturation processes require cochlea-driven neuronal activity? This question can be addressed in future studies using, for example, the $Pou4f3^{DTR}$ mouse line, in which inner hair cells can be ablated by injection of diphtheria toxin [48].

In the avian auditory brainstem astrocyte-secreted factors are required to modulate dendrite topography and synapse distribution [49,50]. Therefore, the absence of spontaneous cochlea-driven neuronal activity likely does not induce neuronal refinement directly, but requires astrocyte–neuron signaling. However, GJ networks are affected themselves. This suggests that there must be in addition a communication between neurons and astrocytes, whose absence renders GJ network orientation in the KO models. This idea is further supported by the fact that the knocked-out targets, namely $Ca_V1.3$ and otoferlin, are localized in neurons and inner hair cells, respectively, but not in astrocytes [51,52]. In contrast, the still maintained preferred anisotropic topography of GJ networks indicates that this is an intrinsic property of LSO astrocytes and is independent from spontaneous cochlea-driven neuronal activity.

3.5. Conclusion

Taken together, our results demonstrate that spontaneous cochlea-driven neuronal activity is not exclusively mandatory for the proper formation of neuronal circuitry, but in addition, is crucial for the proper formation of GJ networks. Hence, GJ network topography reflects disturbed neuronal topography in the investigated mouse models. The signaling path between astrocytes and neurons has to be further analyzed.

4. Materials and Methods

Experiments were performed on WT C57BL/6 mice, $Ca_V1.3$ KO mice [33] and otoferlin KO mice [34] of both genders at postnatal days 10–12 in accordance with the German law for conducting animal experiments. Animals were bred at a 12 h day/night cycle and received food and water ad libitum. Breeding was approved by the regional council of Rhineland-Palatinate (23 177-07/G 15-2-076; 24 August 2016). In accordance with the German animal welfare act (TSchG), no additional approval for post mortem removal of brain tissue was necessary. All chemicals were purchased from Sigma-Aldrich (St. Louis, MO, USA) or AppliChem (Darmstadt, Germany), if not stated otherwise.

4.1. Genotyping

At 3–5 days after birth and directly after preparation of brain tissue, a tail biopsy was taken. First, biopsies were digested in 200 µL 25 mM NaOH and 0.2 mM ethylenediaminetetraacetic acid (EDTA) for 1 h at 95° Celcius (C) at 300 rpm in a twitter (Thriller, Peqlab, VWR, Darmstadt, Germany) to isolate the DNA. Afterwards, 200 µL 40 mM tris(hydroxymethyl)aminomethane (Tris)—HCl, pH 5, was added to neutralize the solution and products were centrifuged for 9–10 min at 15–20 °C at 13,000 rpm (Biofuge fresco, Heraeus, Thermo Fisher Scientific, Waltham, MA, USA). For the following polymerase chain reaction (PCR), 200 µL of the supernatant was decanted, since this contained the DNA. The PCR solution contained the master mix (Table 1) as well as the decanted supernatant. PCR protocols were performed as listed in Table 1. For otoferlin PCR, a restriction enzyme was used to determine genotypes. Therefore, a second digestion was performed with a solution containing 3 µL autoclaved H_2O, 1 µL 10× NEB 3 enzyme buffer and 1 µL BGI II-enzyme (Biolabs, Frankfurt am Main, Germany) times the samples plus 5 µL of the PCR product.

Next, visualization of the DNA bands in the gel was achieved by adding 4 µL sample buffer (40 mM Tris, 20 mM acetic acid, 1 mM EDTA with 40% glycerol and Xylene cyanol). Then, 5 µL DNA ladder (Hyperladder Bio-33040, Bioline, Meridian Biosciences, Memphis, TN, USA) was loaded into the first lane of each 1.5% agarose gel (1.5% agarose and 0.001% EtBr diluted in tris-acetate-EDTA buffer). The other lanes were filled with 14 µL of each probe and were run for 30–35 min at 90–95 V. To develop the gel and visualize the bands, gels were put into a chamber (Biometra Tl1, LTF Labortechnik, Wasserburg, Germany).

Table 1. Master mixes for PCR solutions and protocols used for genotyping of WT and KO mice.

Geno-Type	H_2O	5× PCR Buffer	Forward Primer	Reverse Primer	Taq Poly-Merase	PCR Protocol	Amplicon Size (bp)
WT	7.7 µL	4.0 µL	2.0 µL, 5 pmol/µL, 5′-GCA AAC TAT GCA AGA GGC ACC AGA-3′	2.0 µL, 5 pmol/µL, 5′-TAC TTC CAT TCC ACT ATA CTA ATG CAG GCT-3′	0.3 µL	2 min 92 °C; 20 s 52 °C; 30 s 72 °C; 30 cycles (20 s 92 °C; 20 s 52 °C; 30 s 72 °C); 7 min 72 °C; 15 °C cool down	300
CaV1.3 KO	7.9 µL	4.0 µL	2.0 µL, 5 pmol/µL, 5′-TTC CAT TTG TCA CGT CCT GCA CCA-3′	2.0 µL, 5 pmol/µL, 5′-TAC TTC CAT TCC ACT ATA CTA ATG CAG GCT-3′	0.1 µL	2 min 92 °C; 20 s 52 °C; 30 s 72 °C; 43 cycles (25 s 92 °C; 20 s 52 °C; 30 s 72 °C); 7 min 72 °C; 15 °C cool down	450
Otoferlin KO	7.9 µL	4.0 µL	0.5 µL, 10 pmol/µL, 5′-TAC TGC CCA CAT GAG CTT TG-3′	0.5 µL, 10 pmol/µL, 5′-CAG AGG AAT CCA GCT GAA GG-3′	0.1 µL	2 min 95 °C; 30 s 95 °C; 34 cycles (20 s 57 °C; 30 s 72 °C); 5 min 72 °C; 15 °C cool down	186/163 (WT), 349 (KO)

4.2. Immunohistochemistry

Animal perfusion and tissue preparations were performed as described earlier [1]. The tissue was subsequently processed for Cx43 and Cx30 antibody labeling. Tissues were transferred to phosphate buffered saline (PBS) and cut into 25–30 µm thick slices using a microtome (HM650V, Microtome, Microm International GmbH, Thermo Fisher Scientific, Waltham, MA, USA). Slices were mounted on glass slides (SuperFrost Plus, VWR, Darmstadt, Germany) for on-slide labeling. Unspecific binding sites were blocked with 0.25% triton X-100 and 2% normal goat serum (NGS; Gibco, Thermo Fisher Scientific, Waltham, MA, USA) for 1 h at room temperature (RT). Primary antibodies (rabbit anti-connexin 43, C6219, Sigma-Aldrich, St. Louis, MO, USA; rabbit anti-connexin 30, 700258, Invitrogen, Thermo Fisher Scientific, Waltham, MA, USA) were diluted 1:500 in 0.25% triton X-100 and 2% NGS and applied over night at +4 °C. Since both Cx antibodies were raised in the same host species, stainings were performed on separate sets of fixed slices. After washing with 0.25% triton X-100 and 2% NGS, tissue slices were incubated with secondary antibody (Alexa Fluor (AF) 488 goat anti-rabbit, A-11034, Invitrogen, Thermo Fisher Scientific, Waltham, MA, USA) diluted 1:100 in 2% NGS for 70 min at RT. After washing with PBS, slices were provided with coverslips in 10% DABCO (Fluka, Sigma-Aldrich, St. Louis, MO, USA) in MOWIOL (Calbiochem, Merck, Darmstadt, Germany).

Overview images were documented using a motorized upright widefield microscope (Nikon Eclipse 90i: Plan Fluor 10×/0.30, Nikon Instruments, Tokio, Japan) equipped with a DS-Q1Mc camera (Nikon Instruments, Tokio, Japan) and a FITC filter set (EX: 465–495 nm; DM: 505 nm; BA: 515–555 nm). All settings were kept constant when comparing immunolabeled areas and stainings. High-resolution images showing the center of auditory brainstem nuclei were taken on a motorized confocal laser scanning microscope (Nikon Eclipse C1 mounted at an E600FN: Plan Apo VC 60x/1.40 Oil, Nikon Instruments, Tokio, Japan). Fluorophores were detected with an Argon laser (excitation: 488 nm; emission collected at >515 nm; Melles Griot, Bensheim, Germany) in combination with EZ-C1 3.91 Silver Version software (Nikon Instruments, Tokio, Japan). A minimum of 3 slices were analyzed per nucleus and genotype: WT (Cx43/30): n = 3–5/3–8; $Ca_V1.3$ KO: n = 19–23/11–12; otoferlin KO: n = 5/6–8. The number of slices used for the analysis of nucleus area is the cumulated number of slices used for Cx43 and Cx30 for each nucleus and genotype. Selection and documentation of slices was done blind. For background correction of signal intensities, negative controls were performed and resulting mean background levels for each nucleus were subtracted.

4.3. Preparation of Acute Tissue Slices

Acute coronal brainstem slices were prepared as described earlier [37]. In brief, brains were quickly dissected after decapitation and transferred into ice-cold cutting solution containing (in mM): 26 $NaHCO_3$, 1.25 NaH_2PO_4, 2.5 KCl, 1 $MgCl_2$, 2 $CaCl_2$, 260 D-glucose, 2 Na-pyruvate, and 3 myo-inositol, pH 7.4, bubbled with carbogen (95% O_2, 5% CO_2). Thereafter, slices were transferred to artificial cerebrospinal fluid (ACSF) containing (in mM): 125 NaCl, 25 $NaHCO_3$, 1.25 NaH_2PO_4, 2.5 KCl, 1 $MgCl_2$, 2 $CaCl_2$, 10 D-glucose, 2 Na-pyruvate, 3 myo-inositol, and 0.44 ascorbic acid, pH 7.4, bubbled with carbogen. 270-µm-thick slices were cut using a vibratome (VT1200 S, Leica, Wetzlar, Germany). For a priori identification of astrocytes, slices were incubated for 30 min at 37 °C in 0.5–1 µM SR101 dissolved in ACSF and washed for another 30 min at 37 °C in SR101-free ACSF. Afterwards, slices were kept at RT until experiments were performed.

4.4. Electrophysiology and Tracer Loading

Whole-cell patch-clamp experiments were performed at RT with an upright microscope equipped with infrared differential interference contrast (Eclipse FN1, Nikon Instruments, 60× water immersion objective, N.A. 1.0, Tokio, Japan) and an infrared video camera (XC-ST70CE, Hamamatsu, Shizuoka, Japan) using a patch-clamp EPC10 amplifier and "PatchMaster" software (HEKA Elektronik, Lambrecht, Germany). The pipette solution contained (in mM): 140 K-gluconate, 5 EGTA (glycol-bis(2-aminoethylether)-N,N′,N′,N′-tetraacetic acid), 10 HEPES (*N*-(2-hydroxyethyl)piperazine-*N*′-2-ethanesulfonic acid), 1 $MgCl_2$, 2 Na_2ATP, and 0.3 Na_2GTP, pH 7.3. The pipette solution additionally contained a cocktail of the GJ-impermeable dye AF568 (100 µM, Invitrogen, Thermo Fisher Scientific, Waltham, MA, USA) and the GJ-permeable tracer neurobiotin (1%, Vector Laboratories, Inc., Peterborough, UK) to mark the patched cell and label the coupling network, respectively [1,2]. Patch pipettes were pulled from borosilicate glass capillaries (GB150(F)-8P, Science Products, Hofheim am Taunus, Germany) using a horizontal puller (P-87, Sutter Instruments, Novato, CA, USA) and had a resistance of 2–8 MΩ.

Astrocytes were patched in the central part of the LSO, where the mediolateral and dorsoventral axes are roughly tangential and orthogonal to the tonotopic axis, respectively. Astrocytes were recorded in voltage-clamp mode and held at −85 mV, which is close to their resting membrane potential [1,37]. The (fast) pipette capacitance was compensated. In standard whole-cell configuration the total input resistance (R_{In}) consists of membrane resistance (R_M) and series resistance (R_S) that are arranged in series [53]. They were calculated from currents recorded during hyperpolarizing voltage steps (ΔU = 5 mV). R_{In} is given by (Equation (1)):

$$R_{In} = \frac{U_2 - U_1}{I_2 - I_1} \quad (1)$$

with U_1 is −85 mV, U_2 is −90 mV. I_1 and I_2 are the recorded steady-state currents at U_1 and U_2, respectively. R_S was calculated by (Equation (2)):

$$R_S = \frac{U_2 - U_1}{I_{peak} - I_1} \quad (2)$$

with U_1, U_2, and I_2 are the same parameters as given in Equation (1) and I_{peak} is the maximal current at the initial phase when clamping from U_1 to U_2. Finally, R_M was calculated by (Equation (3); [54]):

$$R_M = R_{In} - R_S \quad (3)$$

Measurements were rejected if the R_S exceeded 15 MΩ to ensure sufficient electrical and diffusional access to the patched cell [55]. The liquid junction potential was not corrected. Astrocytes were characterized by applying a standard step protocol ranging from −150 mV to +50 mV with 10 mV

increments and step duration of 50 ms to determine their *I/V* relationship. The resulting current traces were sampled at 50 kHz and online filtered at 2.9 kHz. Data were analyzed using "IGOR Pro" software (WaveMetrics, Lake Oswego, OR, USA).

4.5. Visualization of Coupled Cells

GJ networks and nucleus boundaries were visualized as described earlier [1,9]. Fixed slices were processed at RT. First, slices were washed three times in PBS (containing NaCl, Na_2HPO_4*$2H_2O$, NaH_2PO_4*H_2O; pH 7.4). Membrane permeabilization was achieved by incubation in 0.25% triton X-100 for 30 min. Thereafter, slices were washed again in PBS. Neurobiotin was identified by incubating slices for 3 h with avidin AF488 (50 µg/mL, Invitrogen, Thermo Fisher Scientific, Waltham, MA, USA) and slices were washed again. Since tracer coupling differs within and dorsal to the LSO [1], glycine transporter (GlyT) 2-staining was used to identify the relative position of the patched cell and the network within the LSO. Avidin-labeled slices were again permeabilized for 30 min in 0.25% triton X-100. Unspecific binding sites were blocked for 1 h in a solution containing 2% bovine serum albumin (BSA), 11.1% NGS (PAA laboratories, Cölbe, Germany), and 0.3% triton X-100. The slices were then incubated overnight (about 20 h) at +4 °C with primary antibody (rabbit anti-GlyT2, AB1773, Millipore, Burlington, MA, USA) diluted 1:2000 in 1% BSA, 1% NGS, and 0.3% triton X-100. The next steps were performed at RT. After washing in PBS, slices were incubated for 90 min with the secondary antibody (goat anti-rabbit AF647, A-21450, Invitrogen, Thermo Fisher Scientific, Waltham, MA, USA) diluted 1:300 in 1% BSA, 1% NGS, and 0.3% triton X-100. Finally, slices were washed in PBS and mounted in 2.5% Dabco on glass slides.

SR101-labeling, network tracing and immunohistochemical stainings were documented at a confocal microscope (Zeiss LSM700: EC Plan-Fluor 10x/0.3; Plan-Apochromat 63x/1.4 Oil) in combination with ZEN software (Zeiss, Oberkochen, Germany), respectively. Fluorophores were detected as follows (excitation wavelength/filtered emission wavelength): AF488 (488 nm/505–530 nm), AF568 (543 nm/>560 nm), AF647 (639 nm/>640 nm), and SR101 (561 nm/580–620 nm). To improve the quality of confocal micrographs and reduce background fluorescence, a Kalman filter was used (averaging of four identical image sections). Images were processed using "FIJI" software [56].

4.6. Analysis of Network Topography

To avoid unconscious experimenter-based corruption of data, coupled cells were identified using an intensity-based detection method [9]. Only cells surpassing a threshold of 1.75 times background intensity were incorporated in the analysis (Figure 3Ad,Bb,Cd). Subsequent vector-based calculation of network topography was used for an automated analysis [9]. Here, the network was divided into four 90° sectors and the sum vector for each sector was calculated. The length of these vectors was normalized to the number of cells in each sector. *R* is the quotient of the normalized *y* value and the normalized *x* value (Equation (4)):

$$R = \frac{\frac{\left|\vec{y_{1A}}\right|}{n_{1A}} + \frac{\left|\vec{y_{1B}}\right|}{n_{1B}}}{\frac{\left|\vec{x_{2A}}\right|}{n_{2A}} + \frac{\left|\vec{x_{2B}}\right|}{n_{2B}}} \quad (4)$$

where $\left|\vec{y_{1A}}\right|$, $\left|\vec{y_{1B}}\right|$, $\left|\vec{x_{2A}}\right|$, $\left|\vec{x_{2B}}\right|$ are the absolute values of the sum vectors of the sectors 1A, 1B, 2A, and 2B, respectively, and n_{1A}, n_{1B}, n_{2A} and n_{2B} are the number of cells in respective sectors. Then, the coordinate system was rotated and the ratio was recalculated in 15° steps. A sinusoidal function (Figure 4Aa,Ba,Ca; Equation (5)) was fitted to the data:

$$R = A_0 + A\sin(\omega\alpha + (\varphi + \frac{3}{4}\pi)) \quad (5)$$

where A_0 is the offset, ω is the circular frequency, α is the angle and φ is the phase shift. The highest Ratio ($R_{max} = A_0 + A$) of the fit reveals the angle of maximal anisotropy of a single network. Therefore,

networks were classified into three groups depending on R_{max} and their preferential orientation α (Figure 4Da): (1) $R_{max} > 1.1$ and $45° < \alpha \leq 135°$, anisotropic and orthogonal to the tonotopic axis, (2) $R_{max} \leq 1.1$, round and (3) $R_{max} > 1.1$ and $0° \leq \alpha < 45°$ or $135° < \alpha \leq 180°$, anisotropic and parallel to the tonotopic axis.

4.7. Statistics

Results are provided as mean ± SD. Data were statistically analyzed using WinSTAT (R. Fitch Software, Bad Krozingen, Germany) and tested for normal distribution with the Kolmogorov–Smirnov test. In case of normal distribution, results were assessed by two-tailed, unpaired Student's *t*-tests. Otherwise, results were assessed by a Mann–Whitney *U*-test. Differences in distribution of classes were analyzed between the WT and the two mouse models using a X^2 test. *p* represents the error probability, * $p < 0.05$, ** $p < 0.01$, *** $p < 0.001$. *n* represents the number of recorded cells or analyzed networks (/slices). In case of multiple comparisons data were statistically analyzed by the tests described above under post hoc Šidák correction of critical values [57]: two comparisons: Figure 1D–F and Figure 3D: * $p < 0.025$, ** $p < 0.005$, *** $p < 0.0005$.

4.8. Additional Information

The WT data, as well as Figure 2Aa left, Ab right, and parts of Ac, Figure 3Aa–Ac, and Figure 4Ab were taken from [9] in accordance to the terms and conditions of the Creative Commons Attribution (CC BY) license (http://creativecommons.org/licenses/by/4.0/).

Author Contributions: Conceptualization, J.S.; methodology, S.E., L.P., and J.S.; validation, J.S.; formal analysis, S.E.; investigation, S.E. and L.P.; resources, J.S. and C.R.R.; data curation, S.E. and L.P.; writing—original draft preparation, S.E. and J.S.; writing—review and editing, S.E., C.R.R., and J.S.; visualization, S.E.; supervision, J.S.; project administration, J.S.; funding acquisition, C.R.R. and J.S. All authors have read and agreed to the published version of the manuscript.

Funding: This study was supported by institutional funding (TU Kaiserslautern) and the GERMAN RESEARCH FOUNDATION (DFG Priority Program 1608 "Ultrafast and temporally precise information processing: Normal and dysfunctional hearing": STE 2352/2-1; Priority Program 1757 "Functional Specializations of Neuroglia as Critical Determinants of Brain Activity": RO 2327/8-2).

Acknowledgments: We thank Eckhard Friauf for critical comments on the manuscript. Additionally, we thank Ralph Reiss for genotyping, and Tina Kehrwald and Simone Durry for preparing transgenic mice and immunohistochemical processing of the tissue, respectively.

Conflicts of Interest: The authors declare no conflict of interest.

Abbreviations

ACSF	Artificial cerebrospinal fluid
AF	Alexa fluor
BSA	Bovine serum albumin
Ca_V	Voltage-activated calcium channel
Cx	Connexin
EDTA	Ethylenediaminetetraacetic acid
EGTA	Glycol-bis(2 aminoethylether)-N,N′,N′,N′-tetraacetic acid
GJ	Gap junction
GlyT	Glycine transporter
HEPES	N (2 hydroxyethyl)piperazine-N′ 2 ethanesulfonic acid
IC	Inferior colliculus
KO	Knock-out
LSO	Lateral superior olive
MNTB	Medial nucleus of the trapezoid body
NGS	Normal goat serum

nPA	Non-passive astrocyte
PA	Passive astrocyte
PBS	Phosphate buffered solution
PCR	Polymerase chain reaction
R	Ratio
RT	Room temperature
SOC	Superior olivary complex
SPN	Superior paraolivery nucleus
SR101	Sulforhodamine 101
Tris	Tris(hydroxymethyl)aminomethane
WT	Wild type

References

1. Augustin, V.; Bold, C.; Wadle, S.L.; Langer, J.; Jabs, R.; Philippot, C.; Weingarten, D.J.; Rose, C.R.; Steinhauser, C.; Stephan, J. Functional anisotropic panglial networks in the lateral superior olive. *Glia* **2016**, *64*, 1892–1911. [CrossRef] [PubMed]
2. Wadle, S.L.; Augustin, V.; Langer, J.; Jabs, R.; Philippot, C.; Weingarten, D.J.; Rose, C.R.; Steinhauser, C.; Stephan, J. Anisotropic Panglial Coupling Reflects Tonotopic Organization in the Inferior Colliculus. *Front. Cell. Neurosci.* **2018**, *12*, 431. [CrossRef] [PubMed]
3. Maglione, M.; Tress, O.; Haas, B.; Karram, K.; Trotter, J.; Willecke, K.; Kettenmann, H. Oligodendrocytes in mouse corpus callosum are coupled via gap junction channels formed by connexin47 and connexin32. *Glia* **2010**, *58*, 1104–1117. [CrossRef] [PubMed]
4. Moshrefi-Ravasdjani, B.; Hammel, E.L.; Kafitz, K.W.; Rose, C.R. Astrocyte Sodium Signalling and Panglial Spread of Sodium Signals in Brain White Matter. *Neurochem. Res.* **2017**, *42*, 2505–2518. [CrossRef] [PubMed]
5. Griemsmann, S.; Hoft, S.P.; Bedner, P.; Zhang, J.; von Staden, E.; Beinhauer, A.; Degen, J.; Dublin, P.; Cope, D.W.; Richter, N.; et al. Characterization of Panglial Gap Junction Networks in the Thalamus, Neocortex, and Hippocampus Reveals a Unique Population of Glial Cells. *Cereb. Cortex* **2015**, *25*, 3420–3433. [CrossRef] [PubMed]
6. Wallraff, A.; Kohling, R.; Heinemann, U.; Theis, M.; Willecke, K.; Steinhauser, C. The impact of astrocytic gap junctional coupling on potassium buffering in the hippocampus. *J. Neurosci.* **2006**, *26*, 5438–5447. [CrossRef]
7. Houades, V.; Koulakoff, A.; Ezan, P.; Seif, I.; Giaume, C. Gap junction-mediated astrocytic networks in the mouse barrel cortex. *J. Neurosci.* **2008**, *28*, 5207–5217. [CrossRef]
8. Claus, L.; Philippot, C.; Griemsmann, S.; Timmermann, A.; Jabs, R.; Henneberger, C.; Kettenmann, H.; Steinhauser, C. Barreloid Borders and Neuronal Activity Shape Panglial Gap Junction-Coupled Networks in the Mouse Thalamus. *Cereb. Cortex* **2018**, *28*, 213–222. [CrossRef]
9. Eitelmann, S.; Hirtz, J.J.; Stephan, J. A Vector-Based Method to Analyze the Topography of Glial Networks. *Int. J. Mol. Sci.* **2019**, *20*, 2821. [CrossRef]
10. Kandler, K.; Clause, A.; Noh, J. Tonotopic reorganization of developing auditory brainstem circuits. *Nat. Neurosci.* **2009**, *12*, 711–717. [CrossRef]
11. Huang, C.M.; Fex, J. Tonotopic organization in the inferior colliculus of the rat demonstrated with the 2-deoxyglucose method. *Exp. Brain Res.* **1986**, *61*, 506–512. [CrossRef]
12. Merzenich, M.M.; Reid, M.D. Representation of the cochlea within the inferior colliculus of the cat. *Brain Res.* **1974**, *77*, 397–415. [CrossRef]
13. Rietzel, H.J.; Friauf, E. Neuron types in the rat lateral superior olive and developmental changes in the complexity of their dendritic arbors. *J. Comp. Neurol.* **1998**, *390*, 20–40. [CrossRef]
14. Malmierca, M.S.; Blackstad, T.W.; Osen, K.K. Computer-assisted 3-D reconstructions of Golgi-impregnated neurons in the cortical regions of the inferior colliculus of rat. *Hear. Res.* **2011**, *274*, 13–26. [CrossRef]
15. Sanes, D.H.; Song, J.; Tyson, J. Refinement of dendritic arbors along the tonotopic axis of the gerbil lateral superior olive. *Brain Res. Dev. Brain Res.* **1992**, *67*, 47–55. [CrossRef]
16. Bal, R.; Green, G.G.; Rees, A.; Sanders, D.J. Firing patterns of inferior colliculus neurons-histology and mechanism to change firing patterns in rat brain slices. *Neurosci. Lett.* **2002**, *317*, 42–46. [CrossRef]

17. Ghirardini, E.; Wadle, S.L.; Augustin, V.; Becker, J.; Brill, S.; Hammerich, J.; Seifert, G.; Stephan, J. Expression of functional inhibitory neurotransmitter transporters GlyT1, GAT-1, and GAT-3 by astrocytes of inferior colliculus and hippocampus. *Mol. Brain* **2018**, *11*, 4. [CrossRef]
18. Kandler, K.; Gillespie, D.C. Developmental refinement of inhibitory sound-localization circuits. *Trends Neurosci.* **2005**, *28*, 290–296. [CrossRef]
19. Friauf, E.; Krächan, E.G.; Müller, N.I.C. Lateral superior olive. In *The Oxford Handbook of the Auditory Brainstem*; Kandler, K., Ed.; Oxford University Press: New York, NY, USA, 2019; pp. 328–394. [CrossRef]
20. Kotak, V.C.; Korada, S.; Schwartz, I.R.; Sanes, D.H. A developmental shift from GABAergic to glycinergic transmission in the central auditory system. *J. Neurosci.* **1998**, *18*, 4646–4655. [CrossRef]
21. Nabekura, J.; Katsurabayashi, S.; Kakazu, Y.; Shibata, S.; Matsubara, A.; Jinno, S.; Mizoguchi, Y.; Sasaki, A.; Ishibashi, H. Developmental switch from GABA to glycine release in single central synaptic terminals. *Nat. Neurosci.* **2004**, *7*, 17–23. [CrossRef]
22. Fischer, A.U.; Muller, N.I.C.; Deller, T.; Del Turco, D.; Fisch, J.O.; Griesemer, D.; Kattler, K.; Maraslioglu, A.; Roemer, V.; Xu-Friedman, M.A.; et al. GABA is a modulator, rather than a classical transmitter, in the medial nucleus of the trapezoid body-lateral superior olive sound localization circuit. *J. Physiol.* **2019**, *597*, 2269–2295. [CrossRef] [PubMed]
23. Kim, G.; Kandler, K. Elimination and strengthening of glycinergic/GABAergic connections during tonotopic map formation. *Nat. Neurosci.* **2003**, *6*, 282–290. [CrossRef] [PubMed]
24. Tritsch, N.X.; Yi, E.; Gale, J.E.; Glowatzki, E.; Bergles, D.E. The origin of spontaneous activity in the developing auditory system. *Nature* **2007**, *450*, 50–55. [CrossRef] [PubMed]
25. Sanes, D.H.; Takacs, C. Activity-dependent refinement of inhibitory connections. *Eur. J. Neurosci.* **1993**, *5*, 570–574. [CrossRef]
26. Muller, N.I.C.; Sonntag, M.; Maraslioglu, A.; Hirtz, J.J.; Friauf, E. Topographic map refinement and synaptic strengthening of a sound localization circuit require spontaneous peripheral activity. *J. Physiol.* **2019**, *597*, 5469–5493. [CrossRef]
27. Clause, A.; Kim, G.; Sonntag, M.; Weisz, C.J.; Vetter, D.E.; Rubsamen, R.; Kandler, K. The precise temporal pattern of prehearing spontaneous activity is necessary for tonotopic map refinement. *Neuron* **2014**, *82*, 822–835. [CrossRef]
28. Clause, A.; Lauer, A.M.; Kandler, K. Mice Lacking the Alpha9 Subunit of the Nicotinic Acetylcholine Receptor Exhibit Deficits in Frequency Difference Limens and Sound Localization. *Front. Cell. Neurosci.* **2017**, *11*, 167. [CrossRef]
29. Choi, B.Y.; Ahmed, Z.M.; Riazuddin, S.; Bhinder, M.A.; Shahzad, M.; Husnain, T.; Riazuddin, S.; Griffith, A.J.; Friedman, T.B. Identities and frequencies of mutations of the otoferlin gene (OTOF) causing DFNB9 deafness in Pakistan. *Clin. Genet.* **2009**, *75*, 237–243. [CrossRef]
30. Duman, D.; Sirmaci, A.; Cengiz, F.B.; Ozdag, H.; Tekin, M. Screening of 38 genes identifies mutations in 62% of families with nonsyndromic deafness in Turkey. *Genet. Test. Mol. Biomark.* **2011**, *15*, 29–33. [CrossRef]
31. Baig, S.M.; Koschak, A.; Lieb, A.; Gebhart, M.; Dafinger, C.; Nurnberg, G.; Ali, A.; Ahmad, I.; Sinnegger-Brauns, M.J.; Brandt, N.; et al. Loss of Ca(v)1.3 (CACNA1D) function in a human channelopathy with bradycardia and congenital deafness. *Nat. Neurosci.* **2011**, *14*, 77–84. [CrossRef]
32. Iwasa, Y.; Nishio, S.Y.; Yoshimura, H.; Kanda, Y.; Kumakawa, K.; Abe, S.; Naito, Y.; Nagai, K.; Usami, S. OTOF mutation screening in Japanese severe to profound recessive hearing loss patients. *BMC Med. Genet.* **2013**, *14*, 95. [CrossRef] [PubMed]
33. Platzer, J.; Engel, J.; Schrott-Fischer, A.; Stephan, K.; Bova, S.; Chen, H.; Zheng, H.; Striessnig, J. Congenital deafness and sinoatrial node dysfunction in mice lacking class D L-type Ca^{2+} channels. *Cell* **2000**, *102*, 89–97. [CrossRef]
34. Longo-Guess, C.; Gagnon, L.H.; Bergstrom, D.E.; Johnson, K.R. A missense mutation in the conserved C2B domain of otoferlin causes deafness in a new mouse model of DFNB9. *Hear. Res.* **2007**, *234*, 21–28. [CrossRef] [PubMed]
35. Hirtz, J.J.; Boesen, M.; Braun, N.; Deitmer, J.W.; Kramer, F.; Lohr, C.; Muller, B.; Nothwang, H.G.; Striessnig, J.; Lohrke, S.; et al. Cav1.3 calcium channels are required for normal development of the auditory brainstem. *J. Neurosci.* **2011**, *31*, 8280–8294. [CrossRef]

36. Hirtz, J.J.; Braun, N.; Griesemer, D.; Hannes, C.; Janz, K.; Lohrke, S.; Muller, B.; Friauf, E. Synaptic refinement of an inhibitory topographic map in the auditory brainstem requires functional Cav1.3 calcium channels. *J. Neurosci.* **2012**, *32*, 14602–14616. [CrossRef]
37. Stephan, J.; Friauf, E. Functional analysis of the inhibitory neurotransmitter transporters GlyT1, GAT-1, and GAT-3 in astrocytes of the lateral superior olive. *Glia* **2014**, *62*, 1992–2003. [CrossRef]
38. Kafitz, K.W.; Meier, S.D.; Stephan, J.; Rose, C.R. Developmental profile and properties of sulforhodamine 101–Labeled glial cells in acute brain slices of rat hippocampus. *J. Neurosci. Methods* **2008**, *169*, 84–92. [CrossRef] [PubMed]
39. Zhou, M.; Schools, G.P.; Kimelberg, H.K. Development of GLAST(+) astrocytes and NG2(+) glia in rat hippocampus CA1: Mature astrocytes are electrophysiologically passive. *J. Neurophysiol.* **2006**, *95*, 134–143. [CrossRef]
40. Langer, J.; Stephan, J.; Theis, M.; Rose, C.R. Gap junctions mediate intercellular spread of sodium between hippocampal astrocytes in situ. *Glia* **2012**, *60*, 239–252. [CrossRef]
41. Schools, G.P.; Zhou, M.; Kimelberg, H.K. Development of gap junctions in hippocampal astrocytes: Evidence that whole cell electrophysiological phenotype is an intrinsic property of the individual cell. *J. Neurophysiol.* **2006**, *96*, 1383–1392. [CrossRef]
42. Kiyoshi, C.M.; Du, Y.; Zhong, S.; Wang, W.; Taylor, A.T.; Xiong, B.; Ma, B.; Terman, D.; Zhou, M. Syncytial isopotentiality: A system-wide electrical feature of astrocytic networks in the brain. *Glia* **2018**, *66*, 2756–2769. [CrossRef] [PubMed]
43. Kunzelmann, P.; Schroder, W.; Traub, O.; Steinhauser, C.; Dermietzel, R.; Willecke, K. Late onset and increasing expression of the gap junction protein connexin30 in adult murine brain and long-term cultured astrocytes. *Glia* **1999**, *25*, 111–119. [CrossRef]
44. Nagy, J.I.; Patel, D.; Ochalski, P.A.; Stelmack, G.L. Connexin30 in rodent, cat and human brain: Selective expression in gray matter astrocytes, co-localization with connexin43 at gap junctions and late developmental appearance. *Neuroscience* **1999**, *88*, 447–468. [CrossRef]
45. Felix, L.; Stephan, J.; Rose, C.R. Astrocytes of the early postnatal brain. *Eur. J. Neurosci.* **2020**. [CrossRef]
46. Ghezali, G.; Calvo, C.F.; Pillet, L.E.; Llense, F.; Ezan, P.; Pannasch, U.; Bemelmans, A.P.; Etienne Manneville, S.; Rouach, N. Connexin 30 controls astroglial polarization during postnatal brain development. *Development* **2018**, *145*, dev155275. [CrossRef] [PubMed]
47. Anders, S.; Minge, D.; Griemsmann, S.; Herde, M.K.; Steinhauser, C.; Henneberger, C. Spatial properties of astrocyte gap junction coupling in the rat hippocampus. *Philos. Trans. R Soc. Lond. B Biol. Sci.* **2014**, *369*, 20130600. [CrossRef] [PubMed]
48. Golub, J.S.; Tong, L.; Ngyuen, T.B.; Hume, C.R.; Palmiter, R.D.; Rubel, E.W.; Stone, J.S. Hair cell replacement in adult mouse utricles after targeted ablation of hair cells with diphtheria toxin. *J. Neurosci.* **2012**, *32*, 15093–15105. [CrossRef]
49. Korn, M.J.; Koppel, S.J.; Cramer, K.S. Astrocyte-secreted factors modulate a gradient of primary dendritic arbors in nucleus laminaris of the avian auditory brainstem. *PLoS ONE* **2011**, *6*, e27383. [CrossRef]
50. Korn, M.J.; Koppel, S.J.; Li, L.H.; Mehta, D.; Mehta, S.B.; Seidl, A.H.; Cramer, K.S. Astrocyte-secreted factors modulate the developmental distribution of inhibitory synapses in nucleus laminaris of the avian auditory brainstem. *J. Comp. Neurol.* **2012**, *520*, 1262–1277. [CrossRef]
51. Xu, J.H.; Long, L.; Tang, Y.C.; Hu, H.T.; Tang, F.R. Ca(v)1.2, Ca(v)1.3, and Ca(v)2.1 in the mouse hippocampus during and after pilocarpine-induced status epilepticus. *Hippocampus* **2007**, *17*, 235–251. [CrossRef]
52. Schug, N.; Braig, C.; Zimmermann, U.; Engel, J.; Winter, H.; Ruth, P.; Blin, N.; Pfister, M.; Kalbacher, H.; Knipper, M. Differential expression of otoferlin in brain, vestibular system, immature and mature cochlea of the rat. *Eur. J. Neurosci.* **2006**, *24*, 3372–3380. [CrossRef] [PubMed]
53. Hamill, O.P.; Marty, A.; Neher, E.; Sakmann, B.; Sigworth, F.J. Improved patch-clamp techniques for high-resolution current recording from cells and cell-free membrane patches. *Pflugers. Arch.* **1981**, *391*, 85–100. [CrossRef] [PubMed]
54. Stephan, J.; Haack, N.; Kafitz, K.W.; Durry, S.; Koch, D.; Hochstrate, P.; Seifert, G.; Steinhauser, C.; Rose, C.R. Kir4.1 channels mediate a depolarization of hippocampal astrocytes under hyperammonemic conditions in situ. *Glia* **2012**, *60*, 965–978. [CrossRef] [PubMed]
55. Pusch, M.; Neher, E. Rates of diffusional exchange between small cells and a measuring patch pipette. *Pflugers. Arch.* **1988**, *411*, 204–211. [CrossRef] [PubMed]

56. Schindelin, J.; Arganda-Carreras, I.; Frise, E.; Kaynig, V.; Longair, M.; Pietzsch, T.; Preibisch, S.; Rueden, C.; Saalfeld, S.; Schmid, B.; et al. Fiji: An open-source platform for biological-image analysis. *Nat. Methods* **2012**, *9*, 676–682. [CrossRef]
57. Abdi, H. The Bonferroni and Šidák corrections for multiple comparisons. In *Encyclopedia of Measurement and Statistics*; Salkind, N., Ed.; Sage Publications: Thousand Oaks, CA, USA, 2007; pp. 103–107.

© 2020 by the authors. Licensee MDPI, Basel, Switzerland. This article is an open access article distributed under the terms and conditions of the Creative Commons Attribution (CC BY) license (http://creativecommons.org/licenses/by/4.0/).

Danksagung

Zuallererst möchte ich bei Prof. Christine Rose dafür bedanken, dass sie mir die Chance gegeben hat, als „externe“ meine Promotion in einem neuen Institut zu beginnen. Ich hoffe es hat sich in den bisschen mehr als 3 Jahren herausgestellt, dass du nicht „die Katze im Sack gekauft hast“. Des Weiteren danke ich Prof. Patrick Küry für die Übernahme des zweiten Gutachtens.

Als nächstes möchte ich gerne Jona für die nun langjährige Unterstützung danken. Dann möchte ich gerne mich noch bei Karl bedanken, ohne dich als Säule des Instituts würde nichts laufen. Genauso geht noch ein großer Dank an Claudia und Simone.

Zudem möchte ich noch dem Chaoten-Verein aus dem Institut bedanken. Insbesondere danke ich hierbei Laura und Jan; ohne euch wäre das alles emotional und wissenschaftlich viel schwieriger gelaufen. Ich bin wirklich froh, dass ihr ein Teil dieser Reise wart.

Zum Schluss möchte ich noch meinem Vater danken, da du mir gezeigt hast, dass man so gut wie alles lernen kann, solange man die nötige Zeit und Kraft investiert. Und meinem Freund Phil; danke, dass du in meinem Leben die Stütze bist, die ich so oft brauche.

Für meine Mutter.

Danke, dass du mir die Leidenschaft für Zahlen und Rätsel weitergegeben hast. Du konntest es leider nicht mehr miterleben, aber ich habe es geschafft.

Eidesstaatliche Erklärung

Ich versichere an Eides Statt, dass die Dissertation von mir selbständig und ohne unzulässige fremde Hilfe unter Beachtung der „Grundsätze zur Sicherung guter wissenschaftlicher Praxis an der Heinrich-Heine-Universität Düsseldorf“ erstellt worden ist.

Diese Arbeit wurde weder ganz noch teilweise bei einem anderen Prüfungsamt zur Erlangung eines akademischen Grades eingereicht.

Ort, Datum	Unterschrift